

A large, faint watermark of a university seal is visible in the upper right corner of the red background. The seal features a central figure, possibly a saint or scholar, surrounded by ornate scrollwork and the Latin word "SIGILLUM" at the top.

Wenhui Zhou

**Development of Porous
Nanomaterial-Based Drug
Delivery Systems for Precision
Cancer Therapy**



Wenhui Zhou

Born 1991, Shiyan, China

Previous studies and degrees

Master of Medicine, Southern Medical University, 2017

Bachelor of Medicine, Hubei University of Medicine, 2014



Development of Porous Nanomaterial-Based Drug Delivery Systems for Precision Cancer Therapy

Wenhui Zhou

Pharmaceutical Sciences Laboratory
Faculty of Science and Engineering
Åbo Akademi University
Åbo, Finland, 2024

Supervisor:**Professor Hongbo Zhang**

Pharmaceutical Sciences Laboratory
Åbo Akademi University

Finland

Turku Bioscience Centre
University of Turku and Åbo Akademi University
Finland

Co-Supervisors:**Professor Jing Feng**

Shanghai Fengxian District Central Hospital
Southern Medical University
China

Professor Tapani Viitala

Pharmaceutical Sciences Laboratory
Åbo Akademi University
Finland

Reviewers:**Professor Karsten Haupt**

CNRS Enzyme and Cell Engineering Laboratory
Université de Technologie de Compiègne
France

Associate professor Alexandra Teleki

Department of Pharmacy
Uppsala University
Sweden

Opponent:**Professor Karsten Haupt**

CNRS Enzyme and Cell Engineering Laboratory
Université de Technologie de Compiègne
France

ISBN 978-952-12-4380-6 (Print)

ISBN 978-952-12-4381-3 (Digital)

Painosalama Oy, Turku, Finland 2024

To my family

Abstract

As science and technology progressively evolve, traditional cancer treatments (such as chemotherapy, conventional surgery and radiation) are no longer sufficient to meet the growing demand for precision cancer therapy. Precision cancer therapy, a more personalized and efficient cancer diagnostic and treatment technology, is gaining increasing attention. Correspondingly, there is a growing variety of multifunctional nanomaterials being extensively used in the field of nanomedicine to meet the needs of precision cancer therapy. The doctoral thesis focus on the development of novel porous nanomaterial-based drug delivery systems, particularly mesoporous silica nanoparticles (MSNs) and metal-organic framework nanoparticles (MOFs) for precise cancer treatment.

The thesis starts with a extensive review of the application of nanotechnology in precision cancer therapy and the most advanced research progress on tumor treatment using porous nanomaterials. This is followed by the results part which is divided into two main sections based on five related articles, detailing our research works of precision cancer treatment using MSNs and MOFs as drug delivery systems. The first section of the results mainly focuses on the use of mesoporous silica encapsulated gold nanorods (Au@MSNs) with photothermal response capabilities for cancer therapy. By surface modification and various drug loading, the Au@MSNs were found to exhibit controlled drug release properties and enabling multiple treatment combinations. Additionally, the Au@MSNs were further encapsulated into injectable GelMA hydrogel microspheres using microfluidic technology, which enabled sustainable drug release and multi-drug generated synergistic treatments. The second section of the results focuses on research works involving MOFs for precision cancer therapy. In this section, different MOFs were prepared and used in the intracellular delivery of chemotherapy drugs and nucleic acid drugs for glioblastoma (GBM) and ovarian cancer therapy. Particularly, surface modification and encapsulating of MOFs in GelMA facilitated blood brain barrier (BBB) penetration, as well as sustainable drug release and multi-drug generated synergistic treatments.

The thesis work comprehensively covers the synthesis, detailed characterization, *in vitro* and *in vivo* evaluations of MSNs and MOFs for cancer therapy. Moreover, it demonstrates the main strategies used for the research in nano-system structure design for precision cancer therapy. It is envisioned that this thesis work will make a substantial contribution to the field of nanomedicines for precision cancer therapy with the potential to significantly advance the fight against cancers.

Keywords

Mesoporous silica nanoparticles (MSNs), metal-organic framework nanoparticles (MOFs), precision cancer therapy, photodynamic therapy (PDT), photothermal therapy (PTT), nanomedicine, surface modification, combination cancer therapy

Sammanfattning

Med förbättringen av människans livskvalitet och teknologiska utvecklingar blir traditionella cancerbehandlingar, såsom kirurgi och radio-kemoterapi, gradvis otillräckliga för att möta kraven på precision i cancerterapi. Precision i cancerterapi, en mer personlig och effektiv diagnostik och behandlingsteknik för cancer, får alltmer uppmärksamhet. Multifunktionella nanomaterial används därför i större utsträckning inom nanomedicinområdet för att möta behoven av precision i cancerterapi. Denna doktorsavhandling fokuserar sig på utvecklingen av nya porösa nanomaterialbaserade läkemedelstillförselsystem, särskilt mesoporösa kiseldioxidnanopartiklar (MSNs) och metall-organiska ramverksnanopartiklar (MOFs) för precisionsbehandling av cancer.

Avhandlingen inleds med en omfattande översikt över användningen av nanoteknik i precisionscancerterapi och den senaste forskningsutvecklingen inom tumörbehandling med porösa nanomaterial. Därefter behandlas resultaten i två huvudsektioner baserade på två till tre relaterade artiklar och där forskningen om precisionscancerbehandling med MSNs och MOFs som läkemedelstillförselsystem utförlig presenteras och diskuteras. Den första sektionen av resultaten fokuserar främst på användningen av mesoporösa kiseldioxidinneslutna guldnanostavar (Au@MSNs) med fototermisk responsförmåga för cancerterapi. Genom ytmodifiering och olika läkemedelsbelastningar visade det sig att Au@MSNs uppvisade kontrollerad läkemedelsfrisättning och möjliggjorde flera behandling kombinationer. Dessutom inkapslades Au@MSNs i injicerbara GelMA-hydrogelmikrosfärer med mikrofluidikteknik, vilket möjliggör hållbar läkemedelsfrisättning och synergistiska behandlingar genererade av flera läkemedel. Den andra sektionen av resultaten fokuserar på forskningsarbeten som involverar MOFs för precisionscancerterapi. I denna sektion förbereddes och användes olika MOFs för intracellulär leverans av kemoterapiläkemedel och nukleinsyraläkemedel för behandling av glioblastom (GBM) och äggstockscancer. Särskilt användes ytmodifiering och GelMA-inkapsling för att realisera blod-hjärnbarriärpenetration, hållbar läkemedelsfrisättning och synergistiska behandlingar genererade av flera läkemedel.

Avhandlingen täcker hela kedjan från syntes till detaljerad karakterisering, samt *in vitro*- och *in vivo*-utvärderingsresultat av MSNs och MOFs för cancerterapi. Dessutom demonstreras ytterligare de huvudsakliga forskningsstrategierna som använts i avhandlingen för nanosystemstrukturens design för precisionscancerterapi. Denna avhandling förutses göra ett väsentligt bidrag till fältet gällande nanomedicin för precisionsbehandling av cancer med potential att avsevärt främja kampen mot cancer.

Nyckelord

Mesoporösa kiseldioxidnanopartiklar (MSNs), metall-organiska ramverksnanopartiklar (MOFs), precisionscancerterapi, fotodynamisk terapi

(PDT), fototermisk terapi (PTT), nanomedicin, ytförändring,
kombinationscancerterapi

Table of contents

Abstract	i
Sammanfattning	iii
Table of contents	v
List of original publications	viii
Contribution of the author	ix
Supplementary publications	x
Abbreviations	xi
1. Introduction	1
2. Literature review	2
2.1. Current state of cancer therapy	2
2.1.1. Surgical therapy	2
2.1.2. Chemotherapy	3
2.1.3. Molecular targeted therapy	5
2.1.4. Gene therapy	7
2.2. Nanomaterials in precision cancer therapy	11
2.2.1. Nanomaterials for drug delivery	12
2.2.2. Nanomaterials enhancing the treatment specificity	13
2.2.3. Future directions and unexplored potentials.....	13
2.3. Overview of porous nanomaterials in precision cancer therapy.....	14
2.3.1. Introduction to porous nanomaterials.....	14
2.3.2. Representative types of porous nanomaterials.....	16
2.3.3. Applications of MSN and MOF in precision cancer therapy	19
2.4. Challenges and opportunities in the use of porous nanomaterials for precision cancer therapy	21
2.4.1. Challenges in clinical application	22
2.4.2. Opportunities.....	23
3. Hypothesis and objective of the work	24
4. Materials and methods	25
4.1. Cell line and culturing.....	25

4.2. Nanomaterial synthesis and characterization.....	25
4.1.1. Prodrug synthesis and characterization.....	25
4.1.2. Preparation and characterization of Au NRs and Au@MSNs.....	25
4.1.3. Preparation and characterization of ZrTCP and ZIF-8 NPs	26
4.1.4. Surface modifications and characterization of NPs	26
4.1.5. GelMA microhydrogel preparation and characterization	26
4.3. <i>In vitro</i> experimental protocols	26
4.3.1. Cellular uptake and lysosomal escape assay	26
4.3.2. Cytotoxicity assay	26
4.3.3. Cell death detection assay	26
4.3.4. Western blot assay	27
4.3.5. Real time PCR assay	27
4.4. <i>In vivo</i> experimental protocols.....	27
4.4.1. Tumour mouse model.....	27
4.4.2. <i>In vivo</i> live imaging.....	27
4.4.3. Histological analysis	27
4.5. Data analysis.....	27
5. Results and discussion.....	28
5.1. Overview of the thesis work.....	28
5.2. Design of NPs for precision cancer therapy.....	29
5.2.1. Cancer therapy NPs combining multiple functions (paper I, II, IV & V)	30
5.2.2. NPs with stimuli-responsive drug release (paper I & V)	30
5.2.3. Cell membrane biomimetic modification of NPs (paper II & IV)	30
5.2.4. Microgelation of NPs (paper II & V).....	30
5.2.5. NPs for targeting the immunogenic cell death (ICD) pathway (paper II)	31
5.2.6. NPs for gene therapy (paper III & IV)	31
5.2.7. NPs for targeting the cell pyroptosis pathway (paper V)	31
5.3. Multifunctional MSNs for precision cancer therapy (papers I & II).....	31
5.3.1. Preparation and characterization of multifunctional Au@MSNs.....	31

5.3.2. Cellular interactions.....	35
5.3.3. Preparation and characterization of GelMA microhydrogels.....	38
5.3.4. <i>In vitro</i> anti-tumor activity.....	39
5.3.5. Biodistribution and <i>in vivo</i> anti-tumor activity	44
5.4. MOFs for precision cancer therapy (papers III, IV & V)	48
5.4.1. Preparation and characterization of multifunctional MOFs (paper III, IV & V).....	48
5.4.2. Cellular interactions.....	50
5.4.3. GelMA microhydrogel preparation and characterization	52
5.4.4. <i>In vitro</i> anti-tumor activity.....	53
5.4.5. Biodistribution and <i>in vivo</i> anti-tumor activity	57
6. Conclusion and future perspectives.....	63
6.1. Summary of key findings.....	63
6.2. Future directions and recommendations.....	63
Acknowledgements	65
References	67
Original publications	77

List of original publications

1. Co-delivery CPT and PTX prodrug with a photo/thermo-responsive nanoplatform for triple-negative breast cancer therapy

Wenhui Zhou, Xiaodong Ma, Jie Wang, Xiaoyu Xu, Oliver Koivisto, Jing Feng, Tapani Viitala, Hongbo Zhang*. *Smart Medicine* **2022**;1:e20220036

2. Minimally invasive injection of biomimetic Nano@Microgel for in situ ovarian cancer treatment through enhanced photodynamic reactions and photothermal combined therapy

Xiaodong Ma, **Wenhui Zhou**, Rong Zhang, Cancan Zhang, Jiaqi Yan, Jing Feng, Jessica M. Rosenholm, Tingyan Shi*, Xian Shen*, Hongbo Zhang*. *Materials Today Bio* **2023**; 100663.

3. Biomineralization of *in vitro* transcribed messenger RNA by organic frameworks for gene supplementary and restoring expression (Manuscript)

Wenhui Zhou, Chang Liu, Jiaqi Yan, Xiaoyu Xu, Jessica M. Rosenholm, Tapani Viitala, Jing Feng*, Hongbo Zhang*

4. Exploiting the warburg effect: Co-delivery of metformin and FOXK2 siRNA for ovarian cancer therapy

Wenhui Zhou, Xiaodong Ma, Jianpeng Xiao, Xiaohui He, Chang Liu, Xiaoyu Xu, Tapani Viitala, Jing Feng*, Hongbo Zhang*. *Small Science* **2024**; 2300192.

5. Boosting glioblastoma therapy with targeted pyroptosis induction

Xinggang Fang, Zhuo Chen, **Wenhui Zhou**, Tongfei Li, Man Wang, Yujiu Gao, Shinan Ma, Ying Feng, Shiming Du, Peimin Lan, Hanyu Chen, Jiarui Wei, Sisi Zhang, Zixiang Li, Xinglin Liu, Hongbo Zhang*, Xingrong Guo*, Jie Luo*. *Small* **2023**; 2207604

Contribution of the author

1. In the first article, the author served as a main researcher of the project, mainly undertaking tasks such as experimental design, data collection and analysis, writing and revising of the manuscript.
2. In the second article, the author was a key participant in the project, mainly working on the cellular-level data collection and analysis and contributed to the writing and revising of the manuscript.
3. In the third article, the author was responsible for the experimental design, data collection and analysis, and the writing and revising of the manuscript.
4. In the fourth article, as the main researcher for the project, the author carried out the experimental design, collected and analyzed data at the cellular level and partially at the material level, and was involved in the writing, and revising.
5. In the fifth article, as a major contributor to the project, the author was involved in the experimental design, data analysis, manuscript revision, and partly in the submission process.

Supplementary publications

1. Metabolism -Regulating Nanozyme System for Advanced Nanocatalytic Cancer Therapy

Chang Liu, Xiaoyu Xu, Yongyang Chen, Miao Yin, Ermei Mäkilä, **Wenhui Zhou**, Wenmei Su, Hongbo Zhang. *Small* **2024**

2. Co-delivery of paclitaxel prodrug, gemcitabine and porphine by micelles for pancreatic cancer treatment via chemo-photodynamic combination therapy

Qiwei Wu, Xiaodong Ma, **Wenhui Zhou**, Rong Yu, Jessica M Rosenholm, Weizhong Tian, Lirong Zhang, Dongqing Wang, Hongbo Zhang. *Pharmaceutics* **2022**, 14, 2280. (Co-first author)

3. Reregulated mitochondrial dysfunction reverses cisplatin resistance microenvironment in colorectal cancer

Yonghui Wang, Xiaodong Ma, **Wenhui Zhou**, Chang Liu, Hongbo Zhang. *Smart Medicine* **2022**. 1 (1), e20220013

4. In vivo kidney allograft endothelial specific scavengers for on-site inflammation reduction under antibody-mediated rejection

Chang Liu, Pengpeng Yan, Xiaoyu Xu, **Wenhui Zhou**, Dhayakumar Rajan Prakash, Shuqi Wang, Junnian Zhou, Rending Wang, Hongfeng Huang, Jianghua Chen, Hongbo Zhang, Jia Shen. *Small* **2022**. 18 (36), 2106746.

5. Combination of photothermal, prodrug and tumor cell camouflage technologies for triple-negative breast cancer treatment

Lirong Zhang, Xiaodong Ma, **Wenhui Zhou**, Qiwei Wu, Jiaqi Yan, Xiaoyu Xu, Bhawana Ghimire, Jessica M Rosenholm, Jing Feng, Dongqing Wang, Hongbo Zhang. *Materials Today Advances* **2022**. 13, 100199. (Co-first author)

6. Self-assembly of DNA nanogels with endogenous microRNA toehold self-regulating switches for targeted gene regulation therapy

Jiaqi Yan, Haixia Zou, **Wenhui Zhou**, Xiaowan Yuan, Zhijun Li, Xiaodong Ma, Chang Liu, Yonghui Wang, Jessica M Rosenholm, Wenguo Cui, Xiangmeng Qu, Hongbo Zhang. *Biomaterials Science* **2022**. 10 (15), 4119-4125. (Co-first author)

7. Delivery of therapeutic oligonucleotides in nanoscale

Lei Wu, **Wenhui Zhou**, Lihua Lin, Anhong Chen, Jing Feng, Xiangmeng Qu, Hongbo Zhang, Jun Yue. *Bioactive Materials* **2022**. 7, 292-323. (Co-first author)

8. Improving the knock-in efficiency of the MOF-encapsulated CRISPR/Cas9 system through controllable embedding structures

Chang Liu, Xiaoyu Xu, Oliver Koivisto, **Wenhui Zhou**, Guillaume Jacquemet, Jessica M Rosenholm, Hongbo Zhang. *Nanoscale* **2021**. 13 (39), 16525-16532.

Abbreviations

2-MIM	2-methylimidazole
AE	Aloe emodin
ATCC	American Type Culture Collection
AuNRs	Gold Nanorods
BBB	Blood brain barrier
CASP3	Caspase-3
CCK-8	Cell Counting Kit-8
CM	Cell membrane
CPT	Cisplatin
Cy 5.5	Cyanine5.5 NHS ester
DAPI	4',6-diamidino-2-phenylindole
DCF	2',7'-Dichlorofluorescein
DCFH-DA	2',7'-Dichlorofluorescein diacetate
DLS	Dynamic light scattering
DMEM	Dulbecco's modified eagle's medium
DMF	Dimethylformamide
DSPE	1,2-Distearoyl-sn-glycero-3-phosphoethanolamine
EGFP	Enhanced green fluorescent protein
FOXK2	Forkhead box protein K2
GBM	Glioblastoma
GelMA	Gelatin methacryloyl
GEM	Gemcitabine
GSDME	Gasdermin E
GSH	Glutathione
HAADF	High-angle annular dark field scanning electron microscope
HMGB1	High mobility group box 1 protein
ICD	Immunogenic cell death
ICG	Indocyanine green
IVIS	<i>In vivo</i> imaging system
LDH	Lactate dehydrogenase
Met	Metformin
MFI	Mean fluorescent intensity
MOF	Metal organic frameworks
MOFs	Metal organic framework nanoparticles
mRNA	Messenger RNA
MSN	Mesoporous silica
MSNs	Mesoporous silica nanoparticles
NPs	Nanoparticles
PBS	Phosphate-buffered saline
PDT	Photodynamic therapy
PEG	Polyethylene glycol
PLGA	Poly(lactic-co-glycolic acid)

PLR	Poly(L-arginine hydrochloride)
p(NIPAM-co-MAAC)	Poly(N-isopropylacrylamide-co-methacrylic acid)
PTT	Photothermal therapy
PTX	Paclitaxel
PVDF	Polyvinylidene fluoride
RT	Room temperature
SEM	Scanning electron microscope
siRNA	Short interference RNA
T CPP	Tetrakis (4-carboxyphenyl) porphyrin
TEM	Transmission electron microscopy
THPP	Tetraphenylporphyrin
TME	Tumor microenvironment
Tf	Transferrin
TfR	Transferrin receptor
WB	Western blot
ZIFs	Zeolitic imidazolate framework nanoparticles
ZrTCP	ZrTCP nanparticles

1. Introduction

With the development of oncology, nanomedicine has emerged as a frontier in the quest for more effective cancer treatments. My research in this thesis is mainly focused on the use of the most advanced porous nanomaterials, including mesoporous nanomaterials (MSN) and metal-organic frameworks (MOF) for the development of multifunctional drug delivery nanosystems for targeted cancer therapy. The research work goes beyond conventional therapy methods, introducing multifunctional nanocarriers that are advanced in the enhancing of drug loading capacity, target specificity, and reduced systemic toxicity. These advanced characters are key to precision oncology, offering new hope and strategies in the fight against cancer.

The challenge of delivering cancer therapeutics efficiently and safely remains a significant obstacle in the field. The new treatment modalities often grapple with the dual challenge of co-delivering a range of therapeutics while ensuring a responsive release in the tumor microenvironment. My research work seeks to provide more creative designs of smart nanocarriers by cleverly using MSNs and MOFs for cancer therapy. In this thesis, I specially focused on developing nanosystemss that can synergistically combine photothermal therapy (PTT), photodynamic therapy (PDT) with traditional chemotherapy and emerging gene therapy. Meanwhile, nanoparticle modification methods such as cell membrane biomimetic coatings and conjugating targeting ligands are also used to increase the delivery efficiency and decrease the side effects. By combining these methods, the aim is to offer more efficient and safer nanoplatforms for use in precision cancer therapy.

The research work is based on the common challenges arising in clinical cancer treatments, and I propose solutions from both tumor biology and nanomedicine. The main challenge involves the flexible application of MSN and MOF nanomaterials to design and fabricate multifunctional drug delivery nanocarriers suited for precision cancer therapy. These nanocarriers are designed to fulfill a dual objective: synergistically employing various approaches to effectively eliminate tumor cells and enhancing the targeted delivery to tumor cells while minimizing toxic side effects. A particular consideration in the design process of these nanocarriers is the co-loading of multiple cancer treatment drugs and the targeted approach towards tumor cells.

This research is set against the backdrop of breast, ovarian cancer and glioma, and delves into the potential of synthesized multifunctional nanocarriers for effective co-loading, controlled release of chemotherapeutic agents, and nucleic acids, as well as their responsiveness to specific tumor cell microenvironment conditions. The study involves rigorous evaluations of the therapeutic effectiveness and toxicity at both cell and animal levels. The results of this research are expected to contribute substantially to the field of nanomedicine, particularly in advancing the methodologies and strategies for cancer treatment, thereby marking a significant step forward in the ongoing battle against this pervasive disease.

2. Literature review

2.1. Current state of cancer therapy

Over the past few decades, there has been a transformative progress in cancer treatment methods. The evolution of these treatments encompasses a broad range of approaches, from surgical interventions to complex gene therapies. This evolution reflects a general shift towards precision oncology in cancer treatment, aiming for personalized treatment plans based on the unique characteristics of each patient and the molecular profile of the tumor. Here, I will briefly summarize the most representative and commonly used methods (including surgery, chemotherapy, molecular targeted therapy, and gene therapy) for cancer therapy (Figure 1) and outline their main advantages and disadvantages.

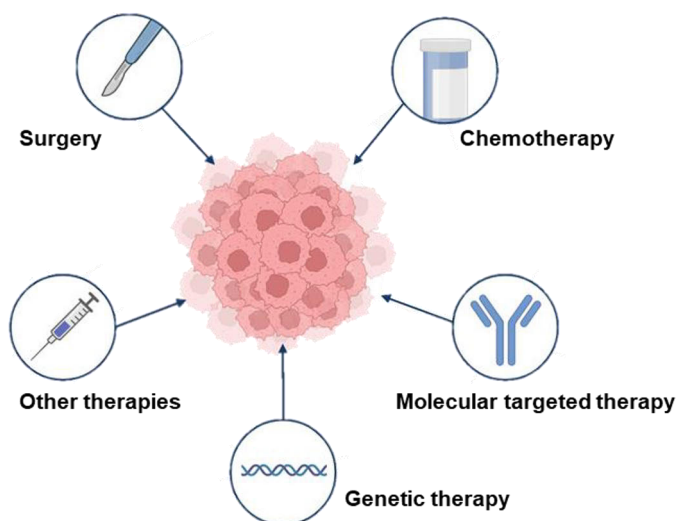


Figure 1. Principal options for cancer therapy.

2.1.1. Surgical therapy

Surgical therapy remains an indispensable and key method in the treatment of cancer, and it mainly relies on the efficacy of removing physical tumor tissue. Especially in the treatment of solid tumors, surgery often serves as the primary choice. In recent years, advancements in the understanding of tumor biology and technological progresses have significantly enhanced the precision and effectiveness of surgical techniques (GlobalSurg and Surgery 2022). Traditional open surgeries, characterized by larger incisions, have been the standard for many years. However, the emergence of minimally invasive surgery, including laparoscopic and robotic-assisted techniques, has revolutionized cancer surgical practices (Jayne et al., 2019). Compared to traditional open surgeries, minimally invasive surgery offer smaller incisions, reduced pain, quicker recovery, and lower risk of complications (Derdeyn et al., 2014). The emergence of robotic-assisted surgeries, particularly the da Vinci surgical system, is renowned for its

enhanced precision and control, greatly aiding in the accuracy of complex procedures (Hussein et al., 2023).

Current surgical approaches are increasingly tailored to specific tumor types and stages. For example, in early-stage breast cancer, breast-conserving surgery is often preferred over mastectomy due to its effectiveness and preservation of residual tissue (Moo et al., 2018). In colorectal cancer, advances in total mesorectal excision have significantly reduced recurrence rates and improved patient quality of life (Keller et al., 2020). Additionally, surgical intervention plays a crucial role in cancer diagnosis and staging, essential for planning subsequent treatment strategies (Goldstein and Mascitelli 2011; Singhal 2016).

Despite significant advancements in cancer surgical techniques, there are still some challenges remaining, such as effectively addressing tumors intertwined with vital structures or in areas difficult to reach surgically (Wyld et al., 2015). Interestingly, the integration of surgery with the principles of precision medicine is an evolving field, for example, the techniques of intraoperative imaging and fluorescence-guided surgery to improve tumor visualization while protecting healthy tissue have been established (Singhal 2016). The concept of personalized surgery by utilizing the genetic and molecular profiling of tumors is also emerging for tailoring surgical interventions to the individual needs of patients (Chiappetta et al., 2023).

Overall, due to the effectiveness and limitations of surgical indications for cancer, future integration with other treatment modalities like chemotherapy and radiotherapy is likely, thus continually evolving towards more personalized treatment strategies to achieve the best outcomes with minimal impact on the physical and mental well-being of the patient (Kaur et al., 2023).

2.1.2. Chemotherapy

Chemotherapy, which relies on chemical drugs to inhibit the growth and survival of tumor cells is one of the most common and crucial methods in cancer treatment. It has changed significantly from the earliest single-agent chemotherapies to the current synergistic combination therapies involving multiple drugs. This development in cancer chemotherapy has progressively adapted to the principles of precision oncology, personalized treatments to effectively target specific characteristics of tumors.

The mechanisms and classes of chemotherapy drugs for cancer treatment are diverse (Figure 2) (Anand et al., 2023). For example, alkylating agents like cyclophosphamide work by adding alkyl groups to DNA, causing cross-linking that prevents DNA replication and transcription. Antimetabolites such as 5-fluorouracil disrupt the synthesis of DNA and RNA by mimicking their natural building blocks, ultimately inhibiting the proliferative ability of cancer cells (Alvarez et al., 2012). While platinum-based drugs like cisplatin induce intrastrand DNA crosslinks, leading to cell apoptosis (Dasari and Tchounwou 2014). Each of these drug categories exploits the rapid division and certain metabolic characteristics of cancer cells. Precision oncology demands the use of specific chemotherapy drugs based on the genetic profile of the tumor during treatment. For example, in breast cancer, tumors overexpressing the HER2/neu gene respond well to trastuzumab (Herceptin) (Slamon et al., 2001). In colorectal

cancer, the efficacy of drugs like cetuximab and panitumumab depends on the KRAS mutation status of the tumor (Karapetis et al., 2008). These findings highlight the shift from traditional, indiscriminate chemotherapy to more individualized chemotherapy regimens based on genetic markers.

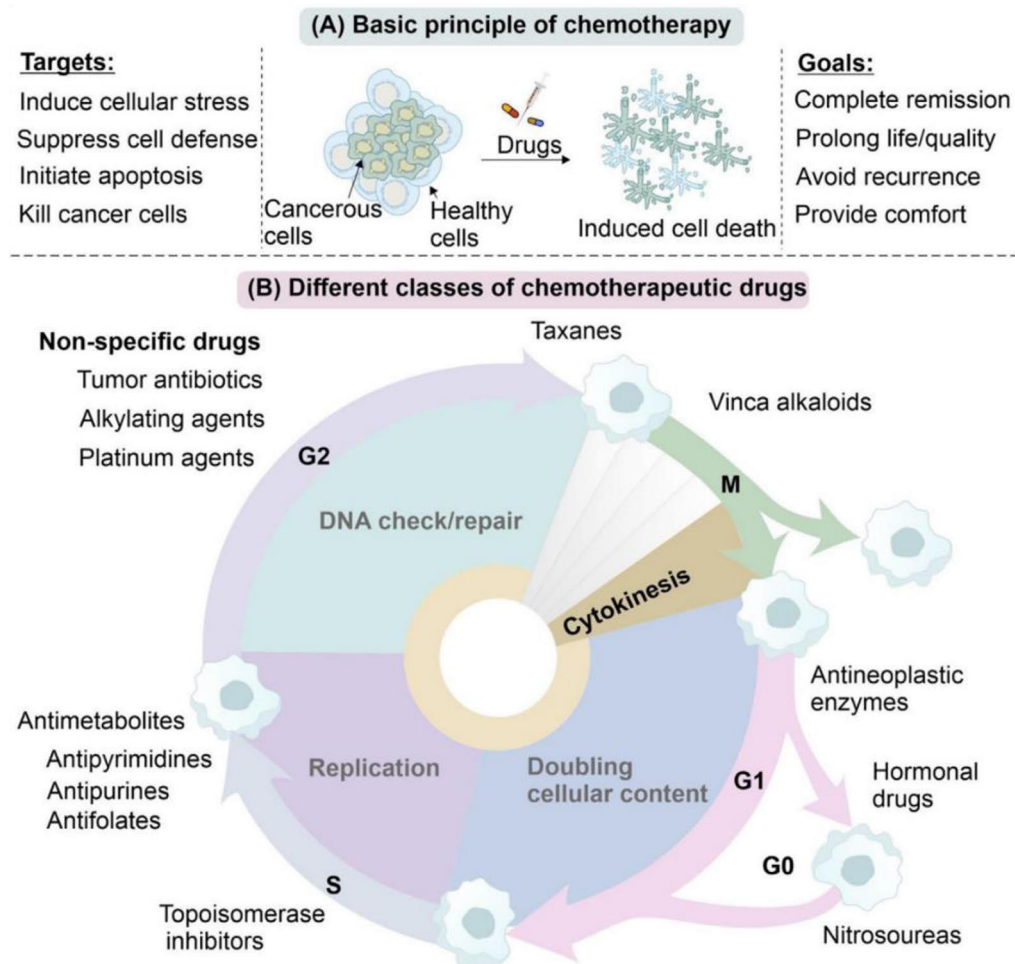


Figure 2. Approaches and various drug classes in cancer chemotherapy. (Copyright 2023, Elsevier)

However, drug resistance of tumor cells remains a formidable challenge in cancer therapy. Mechanisms of drug resistance in tumor cells include increased drug efflux, mutation of drug targets, and enhanced DNA repair. For example, the overexpression of efflux pumps like P-glycoprotein leads to reduced intracellular concentrations of drugs, thereby diminishing their efficacy (Wu et al., 2014). Currently, there are many strategies used to overcome drug resistance, such as the use of drug combinations of multiple drugs or targeted therapies against certain drug resistance mechanisms. For example, the success of PARP inhibitors in overcoming platinum-resistance in ovarian cancers represents a significant advancement in this area (Fong et al., 2009). Additionally, the side effects of

chemotherapy drugs are another major concern, often limiting their use. These effects range from short-term effects like nausea and hair loss to long-term risks such as cardiotoxicity and secondary cancers. Therefore, the development of targeted therapies that specifically attack cancer cells while sparing normal cells is crucial to reduce these side effects. Additionally, advancements in supportive care, such as the use of granulocyte colony-stimulating factor (G-CSF) to manage neutropenia, have also shown to improve the patient outcomes after chemotherapy (Trueman 2009).

Combination chemotherapy, which use more than one chemical drug to treat cancer at the same time to realize better therapeutic effect holds great promise for future cancer therapy. The main advantage of this treatment method is that it is based on the different anti-tumor mechanisms of multiple chemical drugs. Thus, the simultaneous use of multiple drugs can achieve enhanced tumor cell killing effects through multiple pathways or mechanisms (Pomeroy et al., 2022). For example, the combined use of taxol, doxorubicin, and cyclophosphamide (also called TAC method) is the most common choice for breast cancer therapy (Fisusi and Akala 2019) while the combination of taxol and cisplatin is the best choice for lung cancer treatment (Wu et al., 2017). However, the efficiency of combination chemotherapy is critically determined by factors such as drug-drug interactions, the cell cycle specificity of the drug, and the variability in cellular responses to drugs (Mayer and Janoff 2007). For example, in the combined use of taxol and cisplatin for cancer treatment, cisplatin can delay the excretion of taxol, exacerbating adverse reactions (Parker et al., 1993). Therefore, it is necessary to administer taxol before cisplatin during combination treatment.

In general, the role of chemotherapy in cancer treatment is increasingly becoming a part of multimodal therapy strategies. In particular, the combination of chemotherapy with newer treatments such as targeted therapy and immunotherapy is becoming more and more common. This method not only has significant advantages in enhancing the therapy efficacy but also in reducing the side effects associated with traditional chemotherapy (Pomeroy et al., 2022). Additionally, innovations in drug delivery are showing promise in enhancing the tumor tissue specificity and tolerability of chemotherapy drugs (Cheng et al., 2021). Ongoing research and clinical trials are continuously refining and enhancing the role of new chemotherapy methods for comprehensive cancer treatments. In conclusion, although chemotherapy remains a vital component of cancer treatment, its role is still evolving in the era of precision medicine. This evolution, based on genetic profiling, offers personalized approaches and hope for more effective and less toxic treatment methods.

2.1.3. Molecular targeted therapy

Molecular targeted therapy represents a significant advancement in precision cancer therapy. It indicates the changing of conventional extensive cytotoxic chemotherapy to more precise, targeted cancer treatments. This method is based on the development of targeted drugs, such as small molecules or antibodies, designed to block or activate specific molecular pathways that are essential for cancer cell growth and survival (Figure 3) (Fernandez-Rozadilla et al., 2021; Hainaut and Plymoth 2013; Hanahan and Weinberg 2011).

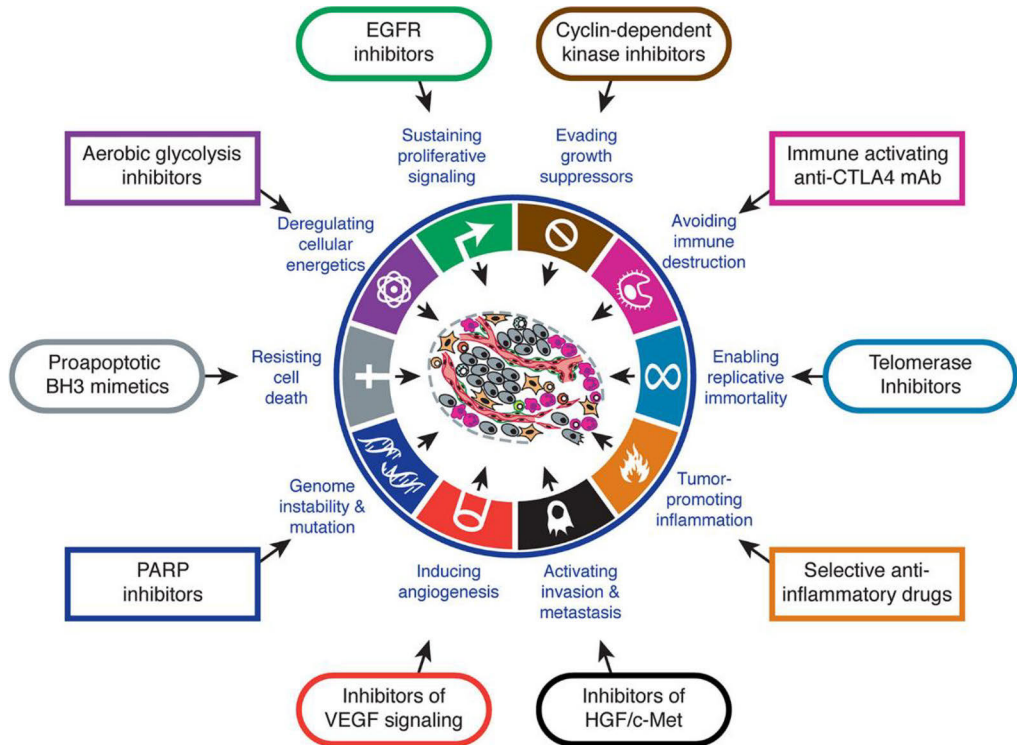


Figure 3. Key characteristics of tumors and their corresponding targeted treatment strategies. (Copyright 2011, Elsevier)

One of the key aspects of molecular target therapy is the identification of target molecules that are predominantly expressed or mutated in cancer cells. For example, the discovery of the BCR-ABL tyrosine kinase in chronic myeloid leukemia (CML) led to the development of imatinib (Gleevec), a drug that specifically inhibits this kinase. This inhibition compound has significantly improved the prognosis of CML patients (Topaly et al., 2001). Another example is the targeting of the epidermal growth factor receptor (EGFR) in various cancers. In non-small cell lung cancer (NSCLC), mutations in the EGFR gene can be used to predict the response of tumor cells to tyrosine kinase inhibitors like gefitinib and erlotinib, making NSCLC treatment more personalized (Fukui et al., 2010). Another key aspect for successful targeted cancer therapy is the use of monoclonal antibodies in molecular targeting. For example, trastuzumab (Herceptin), targeting the HER2/neu receptor, has become a standard treatment for breast cancer patients with overexpression of this receptor (Swain et al., 2023). Similarly, bevacizumab (Avastin), which inhibits vascular endothelial growth factor (VEGF), has been used in the treatment of various cancers including colorectal and non-small cell lung cancer (Hurwitz et al., 2004).

However, the drug resistance to molecular targeted therapies is a growing concern. The mechanisms of resistance are diverse, including secondary mutations in the target protein, activation of alternative signalling pathways, and phenotypic changes in cancer cells, such as epithelial-to-mesenchymal transition

(EMT). Addressing the problem of drug resistance relies on a deeper understanding of these mechanisms and the development of second- and third-generation inhibitors or combination therapies (He et al., 2021). Furthermore, while the side effects of molecular targeted therapies are generally less severe than traditional chemotherapy, they can still be significant. These include skin reactions, hypertension, and gastrointestinal symptoms, which need to be managed carefully to ensure patient compliance and quality of life (Paleari 2022).

In summary, molecular targeted therapy offers a more personalized and effective option for cancer treatment, marking the advent of the era of personalized oncology. However, resistance in cancer cells and side effects of drugs are significant limitations of molecular targeted therapy. The future direction of molecular targeted therapy lies in continually searching and finding new targets and developing drugs with higher specificity and efficacy, a process being accelerated by advances in genomics and proteomics. Additionally, combining molecular targeted therapy with other treatments such as immunotherapy is a promising area, showing significant advantages in enhancing treatment efficacy and for overcoming drug resistance (Jin et al., 2023).

2.1.4. Gene therapy

Gene therapy for cancer represents the most advanced direction in personalized oncology. This method mainly utilizes therapeutic nucleic acid molecules to edit, restore, or silence the expression of tumor-associated genes, aiming to treat cancer (Figure 4). Since the first gene therapy trials in the 1990s, the field has witnessed significant developments and is emerging as promising treatments for

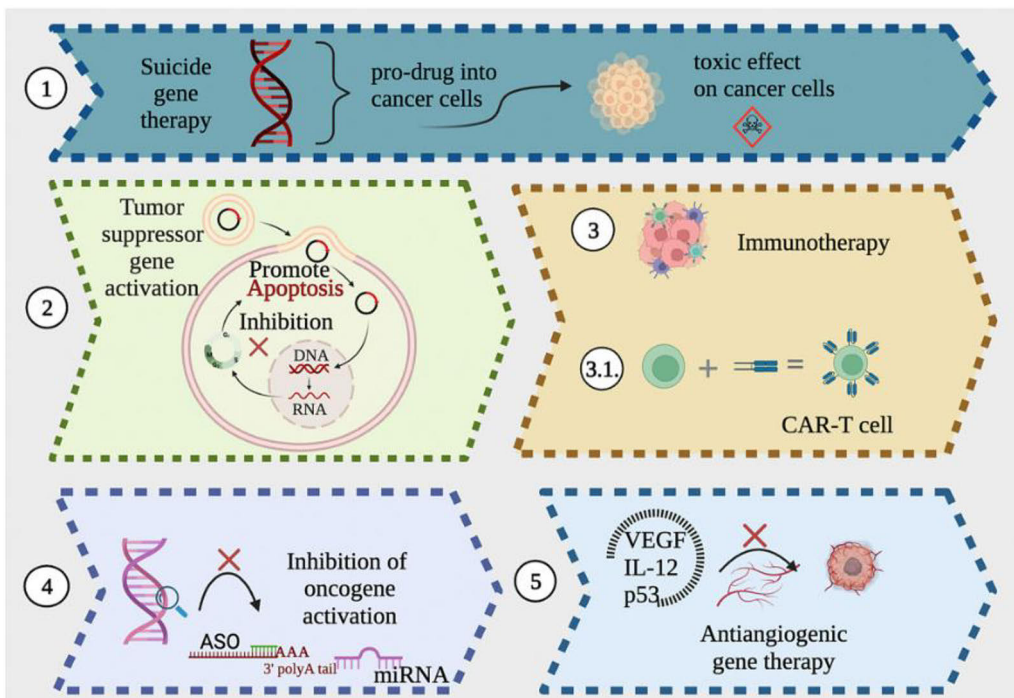


Figure 4. Concepts of cancer gene therapy and their main categories. (Copyright 2023, John Wiley and Sons)

various cancers (Cesur-Ergun and Demir-Dora 2023; Dunbar et al., 2018). There are several gene therapy medicines have already been approved all over the world (Figure 5). The core principle of cancer gene therapy is to correct genetic abnormalities driving the progression of cancer. The main strategies include gene replacement, gene silencing, gene supplementation, and genetic materials generated immunotherapy, each targeting different aspects during tumor progression (Das et al., 2015). The development of efficient and safe gene delivery systems, such as viral and non-viral vectors, is crucial for advancing gene therapy from pre-clinical research to clinical applications (Bender 2018; Collins and Gottlieb 2019).

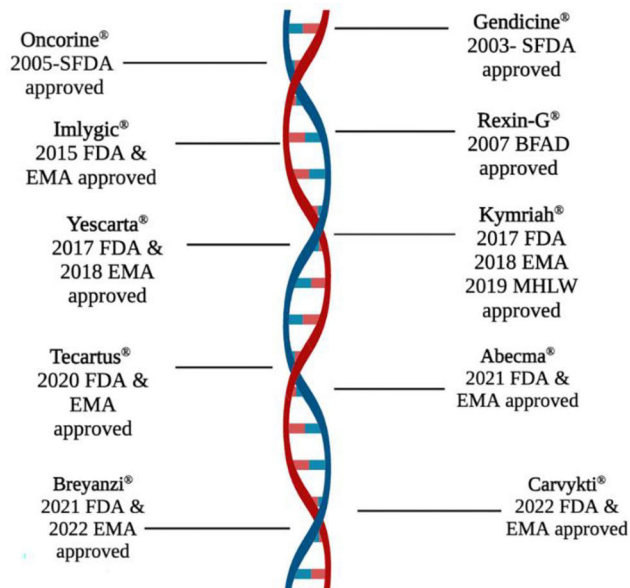


Figure 5. Worldwide approved cancer gene medicines up to 2023. (Copyright 2023, John Wiley and Sons)

2.1.4.1. Gene supplementary therapy

Gene supplementary therapy involves adding specific gene fragments to cancer cells or cell in the surrounding environment to induce cell death or inhibit tumor growth. This approach is particularly effective for tumor cells lacking certain critical genes or pathways necessary for normal cellular function.

One of the most prominent applications of gene supplementary therapy is the co-delivery of a prodrug-activating gene with a prodrug to cancer cells. For example, the herpes simplex virus thymidine kinase (HSV-TK) gene can be delivered alongside the prodrug ganciclovir to tumor cells. Once inside of the tumor cells, the HSV-TK enzyme converts ganciclovir into a toxic metabolite, selectively killing dividing cancer cells (Sawdon et al., 2021). Clinical trials have demonstrated the potential of this method for glioblastoma and prostate cancer treatments (Wang et al., 2023). Another example of using gene supplementation therapy is the use of tumor suppressor genes. The introduction of genes like p53, which are often mutated or deleted in various cancers, can help in inducing apoptosis in cancer cells. Adenoviral-mediated p53 gene therapy has been tested in various cancers,

particularly demonstrating significant therapeutic effects in lung and head and neck cancers (Hong et al., 2014; Hughes et al., 2015). Additionally, gene supplementation therapy is also used in the inhibition of tumor angiogenesis, where genes that inhibit the formation of new blood vessels necessary for tumor growth are introduced. Angiostatin and endostatin have for example been used to inhibit angiogenesis in solid tumors (Li et al., 2018; Scappaticci et al., 2001).

However, despite the extraordinary potential of gene therapy in treating various tumors, the limitations due to the exogenous nature and instability of therapeutic nucleic acid molecules restrict its widespread application. Overall, the effectiveness of gene supplementation therapy depends on efficient delivery of genes to target cells and the sustained expression of the therapeutic genes. Advances in gene carrier technology, such as the development of targeted viral vectors and non-viral systems like liposomes and NPs, are decisive factors in enhancing the effectiveness of the gene (Paunovska et al., 2022; Zu and Gao 2021).

2.1.4.2. Gene replacement therapy

Gene replacement therapy aims to replace or repair mutant genes that are crucial in the progression of cancer. The treatment is particularly suitable for cancers where single-gene mutations play a central role. Common oncogenic targets for gene replacement include mutated genes like p53 and PTEN. The gene p53, known for its tumor-suppressing properties, often undergoes mutations in diverse types of cancer. Restoring its normal function can induce cell cycle arrest and apoptosis in cancer cells. The delivering of wild-type p53 with adenoviral vectors have shown promising anti-tumor results in clinical trials for the treatment of lung, head, and neck cancers (Guan et al., 2009; Hong et al., 2014; Nemunaitis et al., 2000). Additionally, the replacement of BRCA1/2 has been regarded as a good strategy for the treatment of breast cancer. Mutations in BRCA1 and BRCA2 genes are associated with an increased risk of breast and ovarian cancers (Sun et al., 2017). Restoring the expression of normal BRCA1 and BRCA2 through replacement therapy can reinstate normal DNA repair mechanisms and inhibit tumor growth (Koller and Bauer 2021).

Currently, gene replacement therapy faces challenges in delivery and expression efficiency of the therapeutic gene, potential off-target effects and immune responses. However, it is encouraging that advancements in vector technology and gene editing tools like CRISPR/Cas9 are continually enhancing the precision and efficiency of gene replacement therapy (Chen et al., 2019; Sharma et al., 2021).

2.1.4.3. Gene silencing therapy

Gene silencing therapy is one of the most common methods in tumor gene therapy, aiming to treat tumors by targeting and inhibiting the expression of overexpressed or aberrant genes in cancer cells. By utilizing small molecules like siRNA and antisense oligonucleotides (ASOs), this therapy is effective in treating genetic disorders, certain cancers, and viral infections.

The core of this therapy is the RNA interference (RNAi) technology. RNAi employs short hairpin RNA (shRNA) or small interfering RNA (siRNA) to target and degrade the mRNA of oncogenes, thereby suppressing their expression. For

example, targeting oncogenes, such as MYC and KRAS has been shown to have significant anti-tumor activity in liver and lung cancers (McKeown and Bradner 2014; Pecot et al., 2014; Tian et al., 2021). Another key component of gene silencing therapy is the use of antisense oligonucleotides. These short DNA or RNA strands bind to specific mRNA molecules, effectively preventing their translation into proteins. Clinical trials have demonstrated the effectiveness of antisense oligonucleotides targeting the Bcl-2 oncogene in the treatments for lymphoma and leukemia, showing their potential to induce apoptosis in cancer cell (Tekedereli et al., 2013). Moreover, gene silencing therapy also involves epigenetic modulation. This includes the use of drugs or genetic tools to alter the epigenetic landscape of cancer cells, thereby silencing oncogenes. For example, DNA methyltransferase inhibitors and histone deacetylase inhibitors have been approved for the treatment of certain blood cancers (Jones and Baylin 2007).

Overall, gene silencing therapies focus more on the regulation of oncogenes while preserving the function of other normal genes. Despite challenges in precise drug delivery, off-target effects, and maintaining gene silencing and long-term drug safety, this therapy offers a more precise and less invasive alternative to traditional tumor treatments.

2.1.4.4. Genetic materials-based immunotherapy

Immunotherapy is a revolutionary method for cancer treatment. It utilizes the immune system of the body to recognize and eliminate cancer cells. Gene therapy plays a crucial role in enhancing the effectiveness of immunotherapeutic strategies. Here, we primarily explore tumor immunotherapy related to gene therapy.

Chimeric antigen receptor (CAR) T-cell therapy is the best example of gene therapy-based immunotherapy. It involves genetical modification of T cells from the patient to express CARs specifically targeting cancer cells. CAR-T cell therapies, such as tisagenlecleucel for treating acute lymphoblastic leukemia and axicabtagene ciloleucel for diffuse large B-cell lymphoma, have shown significant results in treating certain blood cancers (Jones and Baylin 2007; Neelapu et al., 2018; Sterner and Sterner 2021). Tumor-infiltrating lymphocytes (TILs) is another important example of gene therapy in immunotherapy. TILs, extracted from the tumor tissue of a patient, are genetically modified to enhance their activity and then reinfused back to the body of the patient. This method enhances the natural ability of T cells to fight cancer cells. Clinical trials using TIL therapy have shown encouraging outcomes in melanoma and cervical cancer (Feldman et al., 2015; Geukes Foppen et al., 2015; Rosenberg et al., 2011). Moreover, gene therapy is also being used to augment the efficacy of checkpoint inhibitors, which are drugs that unleash an immune response against cancer. For example, gene therapy approaches that increase the expression of PD-L1 in tumor cells can enhance the response to PD-1/PD-L1 inhibitors (Jiang et al., 2019). Furthermore, gene therapy also plays a significant role in the field of cancer vaccines. Cancer vaccines are designed to elicit an immune response against specific tumor antigens. Gene therapy techniques can be used to create vaccines that more effectively present these antigens to the immune system. For example, researchers have used gene therapy technology to successfully develop the

prostate cancer vaccine Sipuleucel-T, which targets the prostatic acid phosphatase (PAP) antigen (McNeel et al., 2009; McNeel et al., 2019).

Immunotherapy, particularly when combined with gene therapy, offers a highly personalized approach to cancer treatment. However, challenges such as identifying certain targets, managing immune-related adverse effects, and ensuring long-term efficacy still remain.

2.2. Nanomaterials in precision cancer therapy

Medical nanomaterials, referring to medical application materials with sizes ranging from 1 to 100 nm, have demonstrated broad application prospects in the field of tumor treatment due to their unique physical, chemical, and biological properties. Specifically, the main role of nanomaterials in tumor therapy lies in their ability to precisely deliver therapeutic drug molecules to critical sites of the tumor, such as within tumor cells or the tumor microenvironment, thereby significantly enhancing treatment efficacy while reducing toxic side effects on normal tissues (Figure 6). This precise drug delivery approach offers new hope and possibilities for tumor treatment.

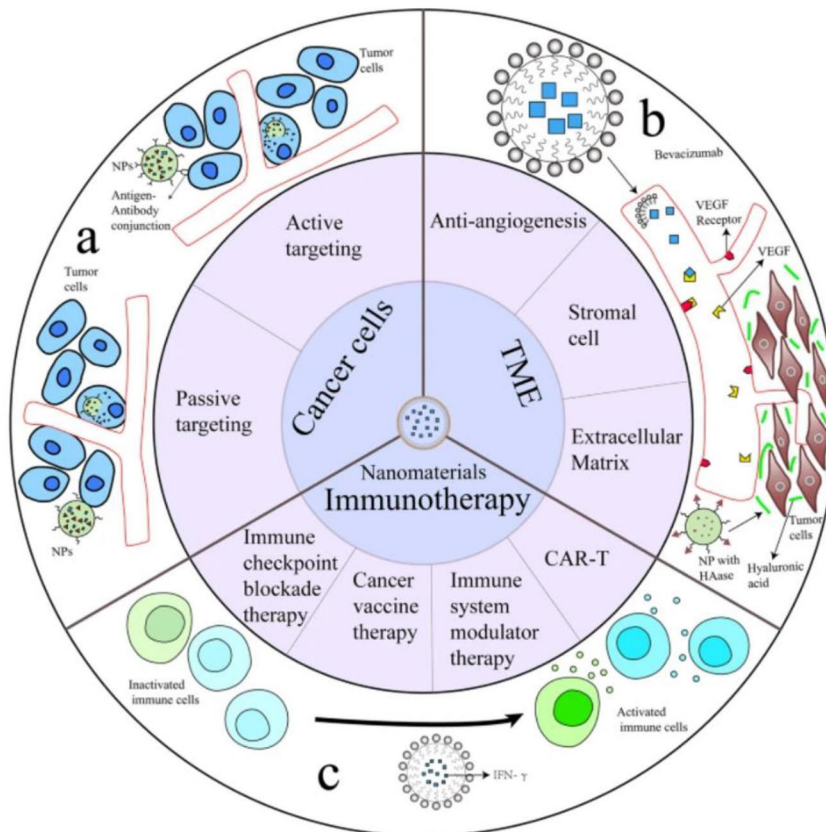


Figure 6. Overview of nanomaterials in the application of cancer therapy. (Copyright 2021, Springer Nature)

2.2.1. Nanomaterials for drug delivery

The use of nanomaterials in drug delivery has significantly advanced the treatment of cancer, addressing several critical challenges in traditional chemotherapy (Figure 7) (Cheng et al., 2021; Gavas et al., 2021).

Firstly, nanomaterials can enhance drug solubility and biocompatibility. NPs have been pivotal in enhancing the solubility and bioavailability of hydrophobic drugs. For example, the development of solid lipid NPs (SLNs) and nanostructured lipid carriers (NLCs) has enabled the encapsulation of lipophilic drugs like all-trans-retinoic acid (ATRA), improving their bioavailability and therapeutic efficacy (Muller et al., 2000). Similarly, dendrimer-based nanocarriers have been used to enhance the solubility of poorly soluble drugs like camptothecin, showing a significant increase in bioavailability (Hsu et al., 2017; Sk and Kojima 2015).

Secondly, nanomaterials enable the co-delivery of multiple drugs. Nanocarriers capable of co-delivering two or more drugs have been developed to provide a synergistic therapeutic effect. This strategy is particularly useful in overcoming drug resistance. For example, NPs co-delivering doxorubicin and paclitaxel have shown to enhance efficacy in killing cancer cells resistant to either drug alone (Aghebbati-Maleki et al., 2020; Cheng et al., 2013; Luo et al., 2020).

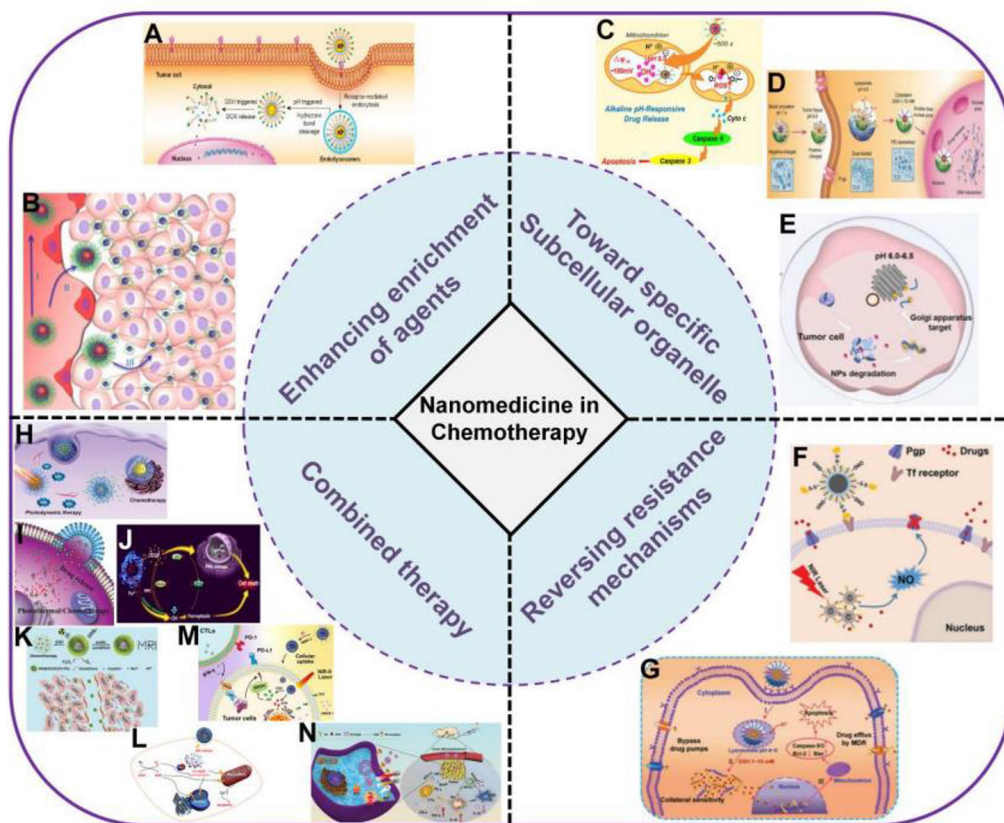


Figure 7. Concept of nanomedicine in cancer therapy. (Copy right, 2021, Ivyspring International Publisher)

Furthermore, nanomaterials exhibit unique advantages in traversing biological barriers such as cell membranes. NPs can overcome biological barriers, enhancing drug delivery to tumor sites (Mitchell et al., 2021). The use of NPs that cross the blood-brain barrier (BBB) is particularly significant in the treatment of brain tumors, where the BBB poses a major challenge. For example, polysorbate 80-coated NPs loaded with drugs like doxorubicin have shown promise in crossing the BBB and delivering drugs to brain tumors (Lockman et al., 2002; Zhou et al., 2018).

2.2.2. Nanomaterials enhancing the treatment specificity

The application of nanomaterials in cancer therapy has also significantly enhanced the treatment specificity and reduced the off-target toxicity. The enhanced treatment specificity is mainly relying on the modification of the materials for targeted drug delivery and stimuli-responsive drug release.

The use of NPs in drug delivery has been instrumental in reducing the off-target toxicity of chemotherapeutic agents. Nanoparticle formulations allow for higher drug concentrations at the tumor site with reduced systemic exposure. For example, liposomal formulations of doxorubicin, such as Doxil®, have been shown to reduce cardiotoxicity, a significant side effect of free doxorubicin, due to their preferential accumulation in the tumor tissue (O'Brien et al., 2004).

Targeted nanoparticle delivery systems have been developed to specifically target cancer cells, thereby reducing toxicity to healthy cells. This, because NPs offer the unique advantage of being able to specifically target cancer cells, sparing healthy tissues. This is achieved through surface modifications with ligands or antibodies that bind to overexpressed receptors on cancer cells. For example, gold NRs functionalized with anti-EGFR antibodies have shown increased specificity in targeting EGFR-overexpressing cancer cells, thereby enhancing the therapeutic efficacy and reducing side effects (El-Sayed et al., 2006). Additionally, aptamer-functionalized NPs have emerged as a novel targeting strategy, offering high specificity and affinity for target cancer cells (Farokhzad et al., 2004; Sousa de Almeida et al., 2021). A notable advancement in this area is the development of liposomes conjugated with transferrin or folate, which target receptors overexpressed in certain types of cancers, thereby enhancing drug delivery to tumor cells while minimizing systemic toxicity (Luque-Michel et al., 2017; Peer et al., 2007; Raj et al., 2021).

Moreover, advanced nanocarriers can respond to specific stimuli in the tumor microenvironment (such as lower pH, high concentration of ROS), ensuring drug release at the target site (Kaushik et al., 2022). This approach minimizes systemic exposure and reduces side effects. pH-sensitive liposomes that release their payload in the acidic environment of tumors are an excellent example of this technology (Ding et al., 2022). The pH-responsive liposomes remain stable in the circulation but release the drug in response to the acidic pH in the tumor microenvironment (Nowag and Haag 2014).

2.2.3. Future directions and unexplored potentials

The advancement of nanotechnology holds great potential for propelling the rapid development of precision cancer therapy. The following directions are considered

promising to further enhance the efficacy, specificity, and safety of cancer therapies.

Firstly, developing multi-functional NPs capable of delivering a combination of therapeutic agents simultaneously is a promising area. These NPs can carry chemotherapeutics, gene therapy agents, and immunotherapeutics in a single platform, allowing for a multi-pronged attack on cancer cells. For instance, NPs designed for co-delivery of chemotherapeutic drugs and siRNA have shown potential in simultaneously attacking cancer cells and silencing drug resistance genes (Du et al., 2015; Kanasty et al., 2013; Li et al., 2019).

Next, personalized medicine is being taken to a new level with nanotechnology. Tailoring nanoparticle therapy based on the specific tumor profile of a patient, including genetic and epigenetic characteristics, could significantly enhance treatment outcomes. This approach involves developing NPs that are responsive to the unique molecular signatures of the cancer of an individual, thereby maximizing efficacy and minimizing toxicity (Lammers et al., 2012; Nair 2020; Nicolini et al., 2012).

Moreover, the integration of nanotechnology with immuno-oncology is an exciting frontier. NPs can be used to deliver immunomodulators directly to the tumor microenvironment, enhancing the immune response against cancer cells. For example, NPs loaded with immune checkpoint inhibitors, such as PD-1/PD-L1 antibodies, have shown potential in enhancing the efficacy of immunotherapy (Jiang et al., 2019).

Additionally, nanotechnology also offers significant potential in cancer diagnosis and monitoring. The development of NPs for use in imaging and as biosensors could enable earlier detection of cancers and more precise monitoring of treatment responses. Gold NPs and quantum dots are being explored for their ability to enhance imaging contrast and detect cancer biomarkers with high sensitivity (Hutter and Maysinger 2011; Ou et al., 2020).

Finally, the use of NPs to overcome drug resistance in cancer therapy is a critical area of research. NPs can be engineered to bypass efflux pumps, deliver drugs to intracellular targets, or co-deliver drugs and genetic material to reverse resistance mechanisms. This strategy could significantly improve the effectiveness of treatments against drug-resistant cancers (Wei et al., 2021; Wu et al., 2017).

2.3. Overview of porous nanomaterials in precision cancer therapy

2.3.1. Introduction to porous nanomaterials

Porous nanomaterials, a class of solids with rich microstructures (Figure 8), have found widespread applications across various fields including adsorption separation, analytics, catalysis, energy storage, and biology. Their use in medicine marks a significant breakthrough in material science, especially in areas such as drug delivery and cancer therapy (Li et al., 2022). Porous nanomaterials are characterized by their nanoscale pores and extensive surface area, and they are primarily distinguished by their ability to interact at the molecular level. The

structure and morphology of these materials, including size and shape, are pivotal to their drug loading capacity and influencing the controlled release of therapeutic agent (Baeza et al., 2017; Tieu et al., 2019). The multifunctionality of porous nanomaterials, particularly in surface modifications, enables a broad spectrum of biomedical applications. They can, through surface engineering, achieve targeted drug delivery to specific tissues or cells, thereby minimizing systemic toxicity. Pioneering works by Slowing, Vallet-Regí, and others provide comprehensive insights into their roles in controlled drug release, gene transfection, and various medical challenges, ranging from targeted drug delivery to imaging (Slowing et al., 2008; Vallet-Regi et al., 2017). The adaptability and customization potential of these materials underscore their value in advanced medical treatments and diagnostics.

The interactions between nanomaterials and biological systems are often complex, and porous nanomaterials can be engineered to perform specific tasks. For example, to interact with specific cell types or respond to special physiological conditions, which is crucial in cancer therapy. This specificity in targeting and minimal side effects exemplify the practical applications in clinical settings (Tang et al., 2012). Currently, as porous nanomaterials continue to evolve in oncology, efforts to integrate targeting, drug delivery, and diagnostic imaging into a single platform are promising new directions. This multifunctionality offers a more efficient and effective disease management approach, especially in oncology (Tarn et al., 2013).

In summary, the introduction of porous nanomaterials has ushered in a new era in medical science. Their unique properties and multifunctional applications place them at the forefront of research and development in drug delivery and cancer therapy. The continuous explorations and innovations in this field hold the promise of unlocking new possibilities in medical treatments and diagnostics, leading to more effective and personalized medical solutions.

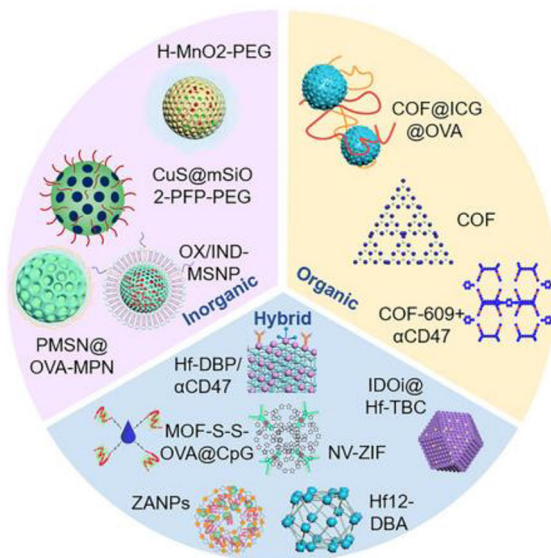


Figure 8. Main categories of porous nanomaterials in biomedicine. (Copyright 2022, Springer Nature)

2.3.2. Representative types of porous nanomaterials

The main types of mesoporous nanomaterials include mesoporous silica (MSN), mesoporous carbon, mesoporous metal oxides, mesoporous metal-organic frameworks (MOF), porous polymers and carbon-based nanomaterials. Here, the focus will be on MSN, MOF and porous polymers and carbon-based nanomaterials, which are the most used in nanomedicine.

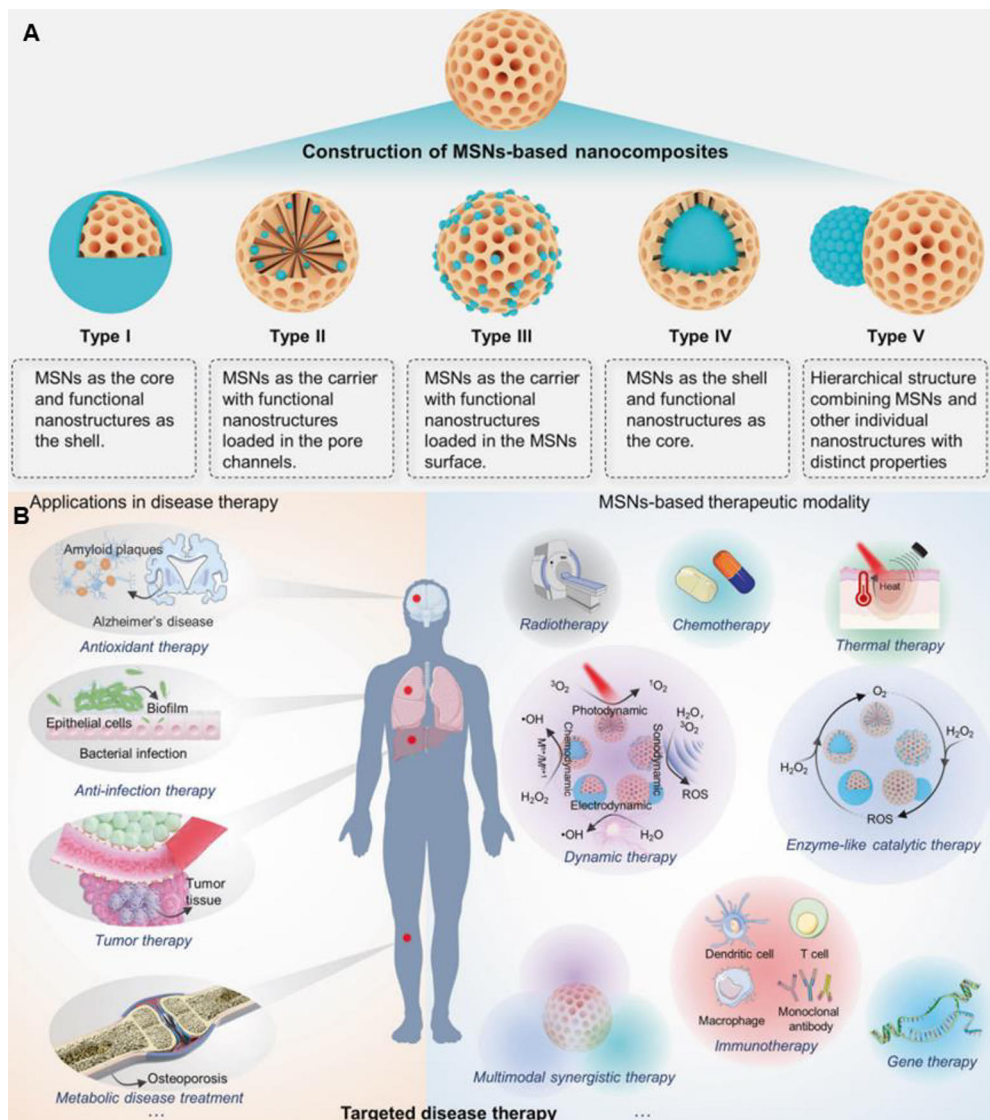


Figure 9. Sbtypes of MSNs-based nanocomposites and their applications in biomedicine. (Copyright 2023, Springer Nature)

2.3.2.1. Mesoporous silica NPs (MSNs)

MSNs are star materials in the emerging nanomedicines field for drug delivery and cancer treatment. Owing to their good biocompatibility, high drug loading efficiency, and the capability for personalized fabrication, MSNs have emerged as

ideal drug delivery carriers and are widely explored for precision cancer therapy (Figure 9) (Vallet-Regi et al., 2001) (Tang et al., 2012). MSNs, made from mesoporous silica material, possess highly ordered pore structures with diameters ranging from 2 to 50 nm. This pore structure significantly increases the effective surface area of MSNs, endowing them with robust drug loading capacity (Tang et al., 2012; Tarn et al., 2013). The encapsulation of drugs in MSNs mainly relies on physical adsorption of drug molecules on the surface of the mesoporous material, as well as covalent linkage via functional groups on the MSN surface. The release of encapsulated drugs can be precisely controlled through stimuli-responsive cleavage of these covalent bonds. For example, MSNs modified with pH-sensitive groups can achieve stimulus-responsive drug release in the acidic microenvironment of cancer tissues, greatly benefiting targeted tumor therapy while minimizing the impact on healthy tissues. This stimuli-responsive drug release and surface modifiability significantly enhance the potential of MSNs in precision medicine (Xu et al., 2023). Furthermore, MSNs demonstrate strong adaptability as drug carriers, efficiently encapsulating a range of bioactive components with therapeutic effects, including small molecules, ligands, nucleic acids, and biomacromolecule (Barkat et al., 2021; Xu et al., 2023), further highlighting their significant role in tumor treatment.

2.3.2.2. Metal-organic framework NPs (MOFs)

MOFs represent another significant class of porous nanomaterials, known for their unique structural and functional characteristics. MOFs are composed of metal ions or clusters coordinated to organic ligands, forming a highly porous, crystalline framework (Figure 10) (Kampouraki et al., 2019; Singh et al., 2021). This structure endows MOFs with an exceptionally high surface area, crucial for drug loading applications. The diverse functions of MOFs are established on their tunable pore sizes and functionalizable surfaces, allowing for the encapsulation of a diverse range of drug molecules (Gao et al., 2021; Rezaee et al., 2022; Yang and Yang 2020).

The mechanism of drug delivery in MOFs typically involves the physical or chemical adsorption of drug molecules within their porous structure. Due to their highly ordered and customizable framework, MOFs can be engineered to release drugs in response to specific stimuli, such as changes in pH, temperature, or the presence of specific enzymes (Pantwalawalkar et al., 2023; Wang et al., 2020). This stimuli-responsive release capability positions MOFs as an attractive option for targeted drug delivery, particularly in the context of cancer therapy where targeted and controlled drug release is needed.

The research on MOFs in drug delivery has been expansive. A study by Horcajada et al. highlighted the potential of MOFs in encapsulating and releasing drugs, showcasing their high drug loading capacity and the possibility for controlled release (Horcajada et al., 2010). Research by Wu and Zhou, on the other hand, delved into the design and functionalization strategies of MOFs for targeted drug delivery, emphasizing their growing importance in precision medicine and offering new avenues for the development of more effective and patient-specific therapies (Wu and Yang 2017).

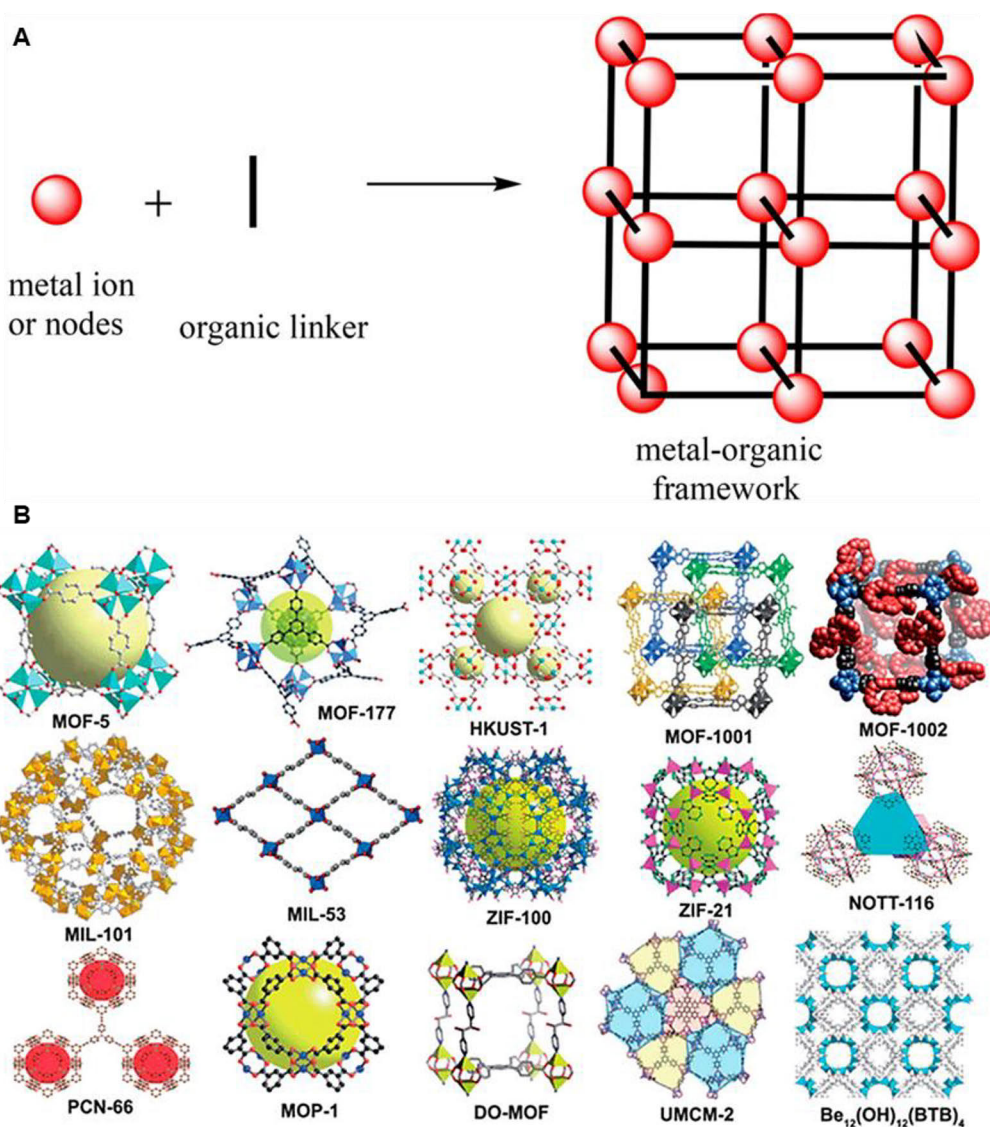


Figure 10. A. The schematic of MOFs formation; B. Representative MOFs structures. (Copyright 2021, Springer Nature; Copyright 2019, MDPI)

2.3.2.3 Porous polymer and carbon-based nanomaterials

Porous polymer and carbon-based nanomaterials offer unique advantages in drug delivery due to their inherent stability, biocompatibility, and potential for surface modification (Li et al., 2022; Qin and Li 2020; Sajjadi et al., 2021). These materials can be engineered to exhibit stimuli-responsive drug release behaviors, crucial for targeted therapy with minimal side effects. The structural diversity of these materials also facilitates the conjugation of various targeting ligands, enhancing the specificity and efficacy of cancer treatments (Le and Doan 2023; Mahor et al., 2021).

Recent advancements in the design and synthesis of these materials have opened new possibilities for their application in precision cancer therapy (Weng et al., 2020). For example, porous carbon nanomaterials have been explored for their ability to deliver drugs and imaging agents specifically to tumor sites, while porous polymer nanomaterials have shown promise in providing controlled release of therapeutic agents in response to specific stimuli, such as pH changes or enzymatic activity in the tumor microenvironment. Debnath et al. has also explored the use of porous carbon nanomaterials in drug delivery, demonstrating their potential in targeted cancer therapy (Debnath and Srivastava 2021). Additionally, Li et al. provided insights into the biomedical applications of porous polymer nanomaterials, discussing their advancing roles in drug delivery and therapeutic applications (Li et al., 2022).

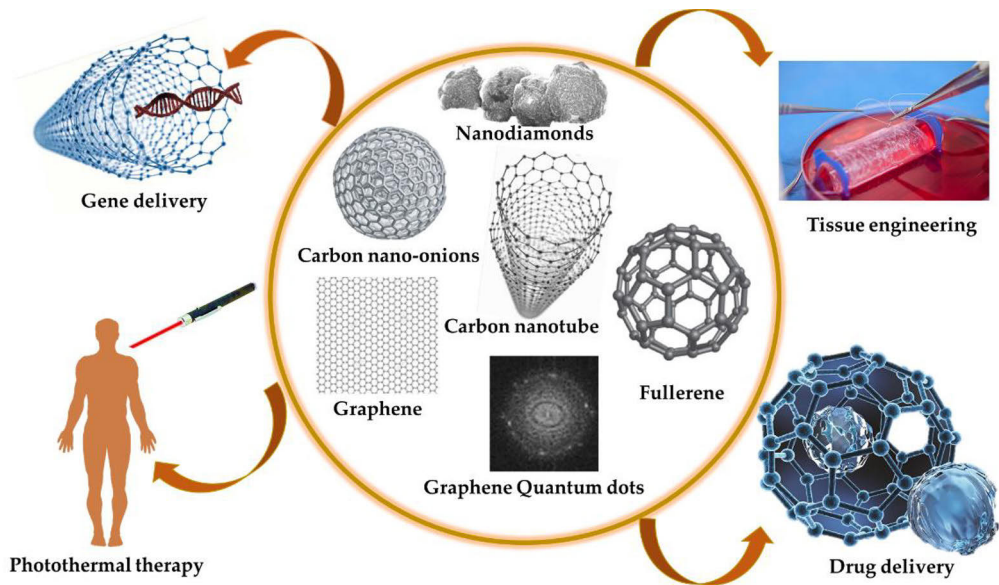


Figure 11. Subtypes of carbon-based nanomaterials and their biomedical applications. (Copyright 2021, MDPI)

2.3.3. Applications of MSN and MOF in precision cancer therapy

In recent years, porous nanomaterials represented by MSNs and MOFs have become star nanomaterials in precision cancer treatment due to their huge drug loading capacity, modifiable surface, and customizable preparation method (Figure 11). In particular, they have provided a more intelligent drug delivery system design strategy by their powerful payload and stimulus responsiveness in the field for tumor therapeutics. In addition, due to the good physicochemical properties and biocompatibility, MSN and MOF are also widely used in tumor imaging and can significantly reduce side effects related to systemic drug distribution.

2.3.3.1. Multifunctional drug delivery system

One of the most promising aspects of MSN and MOF nanomaterials is that they have high specific surface area and pore structure, which enable them to realize

multiple functions via drug loading and surface modifications. Surface modifications of porous nanomaterials can be used to enhance their biocompatibility, targeting ability, and overall efficacy in drug delivery. The modification of surface properties can be achieved through various methods, including functionalization with specific ligands, coating with biocompatible polymers, or attaching targeting moieties. Li et al. demonstrated the effective targeting of breast cancer cells using MSNs functionalized with folate, which binds to the folate receptors overexpressed in many cancer types (Li et al., 2016).

Another key characteristic is their capacity to be engineered to release drugs in response to specific internal or external triggers (Figure 12) (Pantwalawalkar et al., 2023). This includes environmental stimuli such as pH, temperature, or enzymatic activity, thereby enhancing the precision and effectiveness of the therapy. For example, MSNs have been utilized to deliver chemotherapeutic agents directly to tumor cells, releasing the drug in response to the acidic tumor microenvironment. This approach has shown promise in enhancing the efficacy of the drug while reducing its systemic toxicity. Key studies in this area include research by Fang et al., who explored the controlled drug release capabilities of MSNs, and Lawson et al., who demonstrated the use of MOFs in targeted drug delivery (Gupta et al., 2023; Lawson et al., 2021). One of the most researched areas in this domain is pH-sensitive porous nanomaterials. These materials are designed to remain stable under normal physiological conditions but release their drug payload in response to the acidic microenvironment of tumor tissues. Benová et al. demonstrated the use of mesoporous silica NPs with pH-sensitive gates, showing controlled release of the drug in acidic conditions prevalent in cancerous tissue (Benová et al., 2021).

2.3.3.2. Targeted therapy and imaging

In addition to their roles in drug delivery, porous nanomaterials are instrumental in targeted therapy and imaging in cancer treatment. By functionalizing these materials with specific targeting molecules, they can selectively accumulate in tumor tissues, thereby enhancing the specificity and efficacy of the treatment. The incorporation of imaging agents into these materials enables real-time monitoring of drug delivery and tumor response, providing invaluable insights into the effectiveness of the treatment method.

This dual functionality not only improves the efficacy of cancer therapy but also aids in the early detection and diagnosis of tumors. MSNs, for example, have been used to deliver imaging agents to tumor sites, allowing for the visualization of the size, shape, and response of the tumor to treatment. MOFs have also been explored for their potential in multimodal imaging, combining the delivery of therapeutic agents with imaging capabilities to provide a comprehensive approach to cancer treatment. A study by Kesse et al. exemplifies this approach, showcasing the use of MSNs in targeted therapy and imaging (Kesse et al., 2019). Another significant contribution in this area is the research by Demir et al., which highlights the potential of MOFs in multimodal imaging and targeted drug delivery (Demir Duman and Forgan 2021).

In summary, the advancements in porous nanomaterials have opened new avenues in the field of precision cancer therapy. These advanced features enhance the efficacy of drug delivery systems and provide a pathway for more precise and targeted cancer therapy. As research in this area continues to grow, it is anticipated that these materials will play a significant role in the advancement of precision medicine.

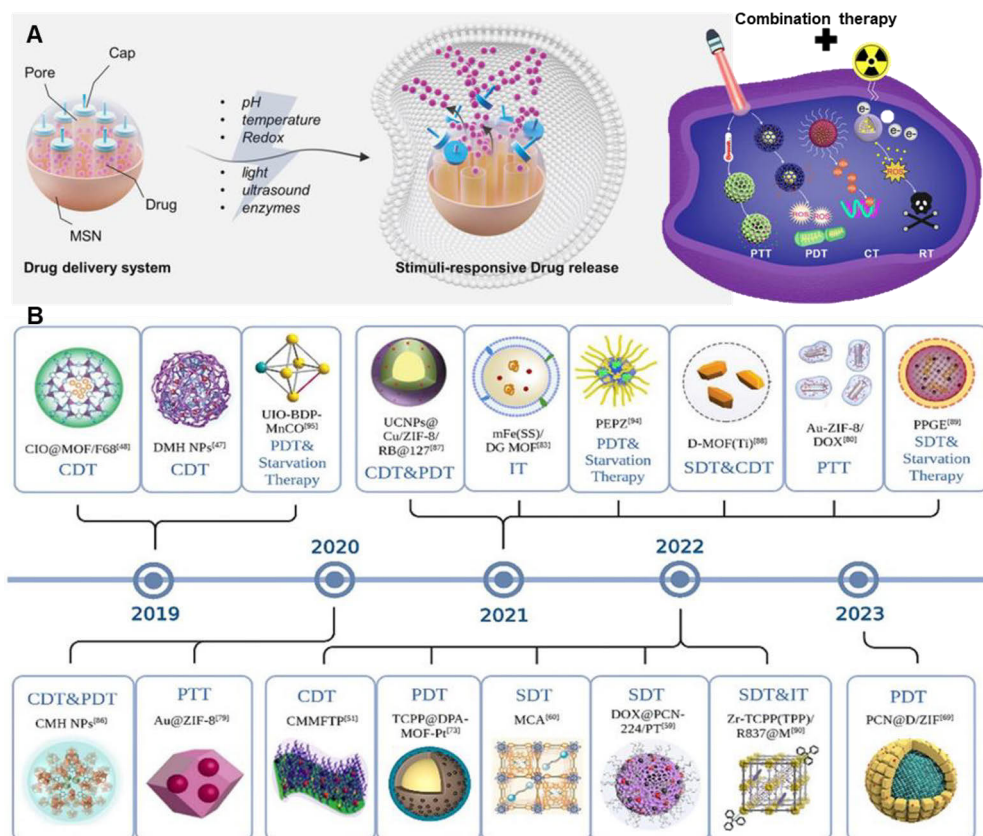


Figure 12. Biomedical applications of MSN and MOF nanomaterials. (Copyright 2023, Springer Nature; Copyright 2023, Royal Society of Chemistry)

2.4. Challenges and opportunities in the use of porous nanomaterials for precision cancer therapy

Porous nanomaterials have shown considerable promise in precision cancer therapy, offering a platform for targeted and controlled drug delivery. However, there are still some challenges that need to be addressed and solved to fully realize their potential in clinical applications (Figure 13). Meanwhile, these challenges also present opportunities for the improvement in cancer therapy. By addressing issues such as biocompatibility, targeting accuracy, and manufacturing scalability, porous nanomaterials can be optimized to enhance the efficacy and safety of cancer treatments.

2.4.1. Challenges in clinical application

2.4.1.1. Biocompatibility and toxicity

A main concern in the clinical application of porous nanomaterials is their biocompatibility and potential toxicity. Tarn et al. emphasize the need for comprehensive studies to evaluate the long-term effects and interactions of these materials with biological systems, particularly the impact of surface modifications and particle size on cellular responses (Tarn et al., 2013). Further research by He et al. addresses the biodegradability and clearance of mesoporous silica NPs, highlighting the importance of particle size and PEGylation in their biodistribution and excretion profiles (He et al., 2011). Additional concerns about cytotoxic effects were raised by Zhang et al., particularly regarding surface modifications (Zhang et al., 2022).

2.4.1.2. Stability and degradability

The stability and degradability of porous nanomaterials in physiological conditions are critical for their functionality and safety. They ensure the structural integrity of these materials for effective drug delivery, and also securing their safe clearance from the body to prevent potential accumulation and side effects, which is a complex balance. Lerida-Viso et al. discuss this challenge, emphasizing the need for materials that strike a balance between stability and biodegradability to prevent long-term accumulation in the body (Lerida-Viso et al., 2023).

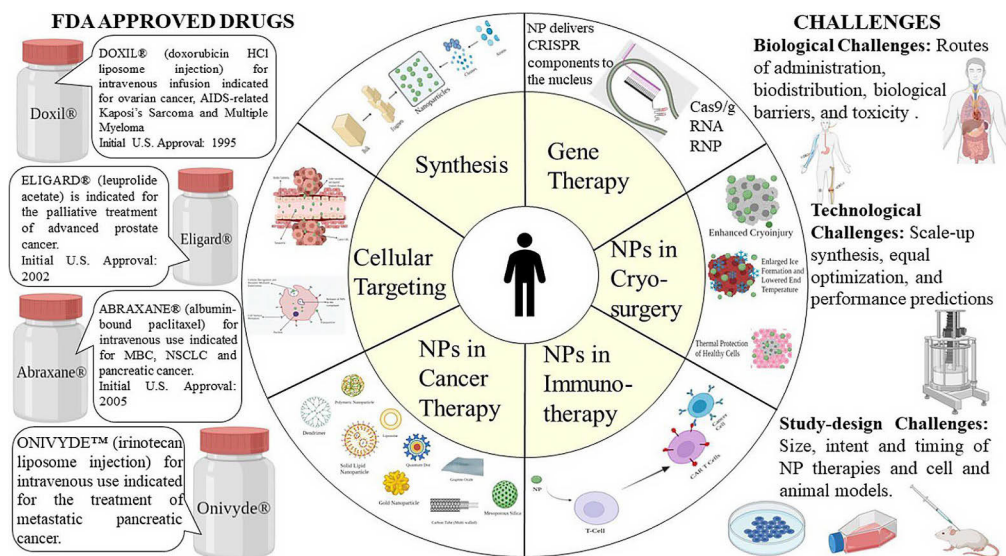


Figure 13. Approved cancer therapy nanomedicines and the main challenges in their successful clinical application. (Copyright 2021, Springer Nature)

2.4.1.3. Scalability of synthesis

Achieving scalable and reproducible synthesis methods for porous nanomaterials is a significant barrier to clinical adoption. The complexity of the synthesis of these materials often hinders the consistency in production, quality, and functionality across large batches. Janjua et al. delve into the challenges and

potential solutions for scalable synthesis, highlighting the economic and technical aspects of mass-producing mesoporous silica NPs (Janjua et al., 2023).

2.4.2. Opportunities

2.4.2.1. Targeted and controlled drug delivery

The precision in drug delivery achievable with porous nanomaterials significantly improves the treatment efficacy. This approach minimizes the impact on healthy tissues and reducing side effects at the same time. Chen et al. demonstrated the potential of dual-targeted mesoporous silica NPs in delivering drugs specifically to cancer cells, significantly enhancing treatment efficacy (Chen and Liu 2016).

2.4.2.2. Personalized treatment approaches

Aligning with personalized medicine principles, porous nanomaterials allow for tailoring drug delivery systems to individual patient profiles. Xu et al. developed customizable metal-organic frameworks that can be adapted for individual patient needs in cancer therapy, showcasing the potential for personalized treatment approaches (Liu et al., 2021; Xu et al., 2022).

2.4.2.3. Combination therapy

Combining multiple drugs into a single carrier, porous nanomaterials offer an effective approach in cancer treatment. This strategy targets various aspects of cancer simultaneously, potentially leading to more comprehensive treatments. Liu et al. highlighted the use of mesoporous silica NPs for co-delivering chemotherapeutic drugs and immune-boosting agents, illustrating their potential in combination therapy (Huang et al., 2023; Liu et al., 2022).

3. Hypothesis and objective of the work

The central hypothesis of this thesis is founded on the premise that advanced porous nanomaterials, particularly MSN and MOF, hold the key to revolutionizing drug delivery systems in precision cancer therapy. These advanced nanocarriers are anticipated to significantly enhance the precision, efficacy, and safety of cancer treatments. By offering targeted drug delivery directly to tumor cells and allowing for the controlled release of therapeutics in response to specific conditions within the tumor microenvironment, these systems are expected to bridge critical gaps in current cancer treatment methodologies, especially in delivering and releasing drugs in a controlled manner, thereby improving treatment outcomes.

In pursuit of the hypothesis, the first objective focuses on the synthesis and characterization of these advanced porous nanomaterial-based carriers. Emphasis is placed on optimizing the structural and surface properties of mesoporous silica and MOFs to maximize their drug loading capacity, stability, and biocompatibility. The goal is to engineer these nanocarriers to be highly efficient in encapsulating and delivering a range of cancer therapeutics, including chemotherapeutic agents and genetic materials. This step is crucial in tailoring the nanocarriers for specific applications in precision cancer therapy. Following this, the second objective revolves around the functional evaluation of these nanocarriers. This includes assessing their targeted delivery capabilities, responsiveness to tumor-specific stimuli such as pH and temperature variations, and the potential to co-deliver multiple therapeutic agents. A key aspect of this evaluation is to explore the synergistic effects of combining photothermal therapy with traditional chemotherapy or gene therapy strategies using these multifunctional nanocarriers.

The final objective extends to the validation of the effectiveness of these nanocarrier systems through in-depth *in vitro* and *in vivo* studies. These studies aim to demonstrate the ability of the nanocarriers to specifically target tumor cells, thereby reducing the side effects commonly associated with cancer treatments and enhancing therapeutic outcomes. Successful validation would underscore the clinical relevance of these developed drug delivery systems, aligning seamlessly with the overarching theme of the thesis: developing cutting-edge drug delivery systems for precision cancer therapy. This approach not only aims to address the current limitations in cancer therapy but also contributes significantly to the field of precision medicine, where treatment strategies are tailored to individual patient needs, optimizing therapeutic efficacy while minimizing adverse effects.

4. Materials and methods

4.1. Cell line and culturing

The cells used in this work were mainly purchased from ATCC (American Type Culture Collection, Manassas, VA, USA), and were cultured with their recommended cell culture medium. All the cells were tested for and verified not to have any mycoplasma contamination. All the cell lines used in this work are summarized in Table 1.

Table 1. Cell lines used in this work:

Cell line	Tissue	Source
HEK293	Kidney of human embryo	https://www.atcc.org/products/crl-1573
Hela	Human cervix adenocarcinoma	https://www.atcc.org/products/crm-ccl-2
SKOV3	Human ovary adenocarcinoma	https://www.atcc.org/products/htb-77
OVCAR3	Human ovary adenocarcinoma	https://www.atcc.org/products/htb-161
MDA-MB-231	Human breast adenocarcinoma	https://www.atcc.org/products/crm-htb-26
MCF 10A	Human breast tissue	https://www.atcc.org/products/crl-10317
4T1	Mouse breast cancer	https://www.atcc.org/products/crl-2539
PANC1	Human pancreas carcinoma	https://www.atcc.org/products/crl-1469
GL261	Mouse brain glioblastoma	https://www.dsmz.de/collection/catalogue/details/culture/ACC-802
U-87 MG	Human brain glioblastoma	https://www.atcc.org/products/htb-14

4.2. Nanomaterial synthesis and characterization

4.1.1. Prodrug synthesis and characterization

The prodrug PTX-SS-COOH used in this work was prepared according to our previous work (Zhang et al., 2022). Briefly, PTX and 3,3'-Dithiodipropionic acid (DTDP) are linked via condensation reaction of hydroxyl group and carboxyl group under N-(3-dimethylaminopropyl)-N-ethylcarbodiimide hydrochloride (EDC·HCl) and 4-dimethylaminopyridine (DMAP) environments. The synthesized PTX-SS-COOH prodrug was purified by silica gel column chromatography and characterized by ¹H NMR spectroscopy.

4.1.2. Preparation and characterization of Au NRs and Au@MSNs

Gold nanorods (Au NRs) and Au@MSNs were synthesized using a seed-mediated growth method. The formation process involved a series of reactions, including

the addition of specific reagents like CTAB, H₂AuCl₄, and NaBH₄. The NPs were characterized by DLS and TEM microscopy.

4.1.3. Preparation and characterization of ZrTCP and ZIF-8 NPs

ZrTCP NPs were synthesized by combining Zr⁴⁺ with the photosensitizer TCPP in a benzoic acid/DMF mixture, followed by heating and centrifugation. The ZIF-8 NPs were prepared using a self-assembly method involving zinc nitrate, 2-methylimidazole, and aloe-emodin or PLR&mRNA mixture. Characterization of both types of NPs was conducted using TEM and DLS.

4.1.4. Surface modifications and characterization of NPs

Two different surface modification methods of NPs were used in this work. The first one was to wrap the Au@MSN or ZIF-8 NPs with functional polymers. The coating was realized by mixing the polymers (p(NIPAM-co-MAAc) or PEG-PLGA-Tf) with NPs in a water solution overnight under stirring conditions and characterized by TEM. The other surface modification method of NPs was to wrap the Au@MSN or ZrTCP NPs with cancer cell derived cell membrane. The wrapping process was done by mixing the NPs with the cell membrane isolated from SKOV3 cells in water solution at 4°C overnight under stirring condition and characterized by TEM.

4.1.5. GelMA microhydrogel preparation and characterization

The injectable GelMA microhydrogel was prepared with a microfluidic chip. Briefly, the NPs and combined drugs are first mixed with GelMA and the crosslinker in water solution used as an internal flow solution. 5% Span 80 dissolved in mineral oil was used as an external flow solution. Next, different sizes of GelMA microhydrogels were prepared by injecting the internal flow solution to the external flow solution under different flow ratios and fixed by UV light. Finally, the GelMA microhydrogels were collected and characterized by confocal microscopy, TEM, and SEM.

4.3. *In vitro* experimental protocols

4.3.1. Cellular uptake and lysosomal escape assay

Cultured tumor cells were initially exposed to various NPs for pre-set durations, and then the cells were selectively labelled with LysoTracker and DAPI, followed by fixing with 4% PFA. Finally, the cells were harvested and analysed by flow cytometry and imaged by confocal microscopy. The fluorescence intensity was quantified by Image J software.

4.3.2. Cytotoxicity assay

The cytotoxicities of NPs were evaluated by the effects on the cell viability. Briefly, cultured tumor cells were initially exposed to various NPs for pre-set durations, and then the cell viabilities were tested by WST-1 or CCK-8 assay.

4.3.3. Cell death detection assay

The effect of NPs on cell survival was measured by Calcein AM/PI staining and Annexin V/PI staining analysis assays. Briefly, cells after treatment with NPs were harvested and stained with Annexin V/PI or stained with Calcein AM/PI directly

in the cell culture dish. Then Annexin V positive cells were analysed with a flow Cytometer, and Calcein AM/PI positive cells were observed and imaged with confocal microscopy.

4.3.4. Western blot assay

The protein samples were collected after cells were treated with different NPs for 24-72 hours. The protein expression level was analysed with Bio-Rad Mini-PROTEAN Tetra Vertical Electrophoresis and Blotting Cells according to their standard protocols.

4.3.5. Real time PCR assay

The total RNA of treated cells were firstly extracted with Trizol reagent, and reverse transcribed into cDNA. Next, quantitative PCR was used to quantify mRNA levels of genes related to apoptosis, cell cycle, and other pathways affected by the nanoparticle treatments.

4.4. *In vivo* experimental protocols

4.4.1. Tumour mouse model

The subcutaneous tumor mice model was established by inoculating a certain number of logarithmic growth phase tumor cells into the subcutaneous fat pad of the mice. Meanwhile, the mouse brain glioma orthotopic model and the ovarian cancer orthotopic tumor model were formed by respectively implanting a certain number of logarithmic growth phase tumor cells into the cranial and ovarian tissues.

4.4.2. *In vivo* live imaging

At indicated time points, the mice were anesthetized or sacrificed to obtain the tumor tissues and main organs (including heart, liver, spleen, lung and kidney) for bioluminescence and fluorescence imaging with an *in vivo* imaging system.

4.4.3. Histological analysis

At the endpoint of the experiment, all of the animals were sacrificed, and tumor tissues and main organs (including heart, liver, spleen, lung and kidney) were collected for histological examination (including H&E, Ki67, TUNEL, FOXP2 staining).

4.5. Data analysis

The SPSS software was utilized for the statistical analysis of the data. Appropriate statistical tests, such as one-way ANOVA or Student's t-test, were used for making comparisons. The level of statistical significance was set at $p < 0.05$. Graphs and charts were used to visually represent data findings, and all experiments were conducted in triplicates to ensure reproducibility and reliability of results.

5. Results and discussion

5.1. Overview of the thesis work

The primary objective of this research was to explore advanced, multifunctional drug delivery carriers for precision oncology, leveraging the unique properties of mesoporous nanomaterials in terms of modifiability, drug delivery efficiency, and biocompatibility. Utilizing nanoscale self-assembly, prodrug concepts, and microfluidic-assisted techniques, this work is pioneering new avenues in tumor therapy.

The thesis research commenced with the successful synthesis of gold nanorods coated with mesoporous silica, exhibiting photothermal responsiveness, using a seed growth method. This facilitated the co-loading of multiple chemotherapeutic agents and enabled tumor-cell-responsive drug release. The application of infrared light triggered a combined therapeutic approach, integrating chemotherapy, photothermal, and photodynamic treatments.

In parallel, this work capitalized on the environmental responsiveness, high drug-loading efficiency, and customizability of MOFs. I successfully developed various MOFs responsive to intracellular environments. These NPs efficiently delivered traditional small molecule drugs and nucleic acid-based therapeutics (siRNA and mRNA), achieving targeted therapy specific to tumor signaling pathways.

Furthermore, recognizing the broad potential of microfluidic technology in the biosciences, drug-releasing microhydrogels based on mesoporous silica and/or MOFs were synthesized. This approach, involving in situ intratumoral injection, not only ensured effective tumor therapy but also substantially reduced the potential organ toxicity and dosage requirements associated with intravenous administration of nanomaterials.

Overall, this work underscores the efficacy of multifunctional nanocarrier systems in enhancing cancer treatment. It emphasizes the importance of diverse carrier platforms for optimizing therapeutic strategies, setting a precedent for future innovations in cancer therapy. This comprehensive study followed a structured workflow (as shown in Figure 14), integrating various nanotechnology and biomedical concepts to achieve its goals.

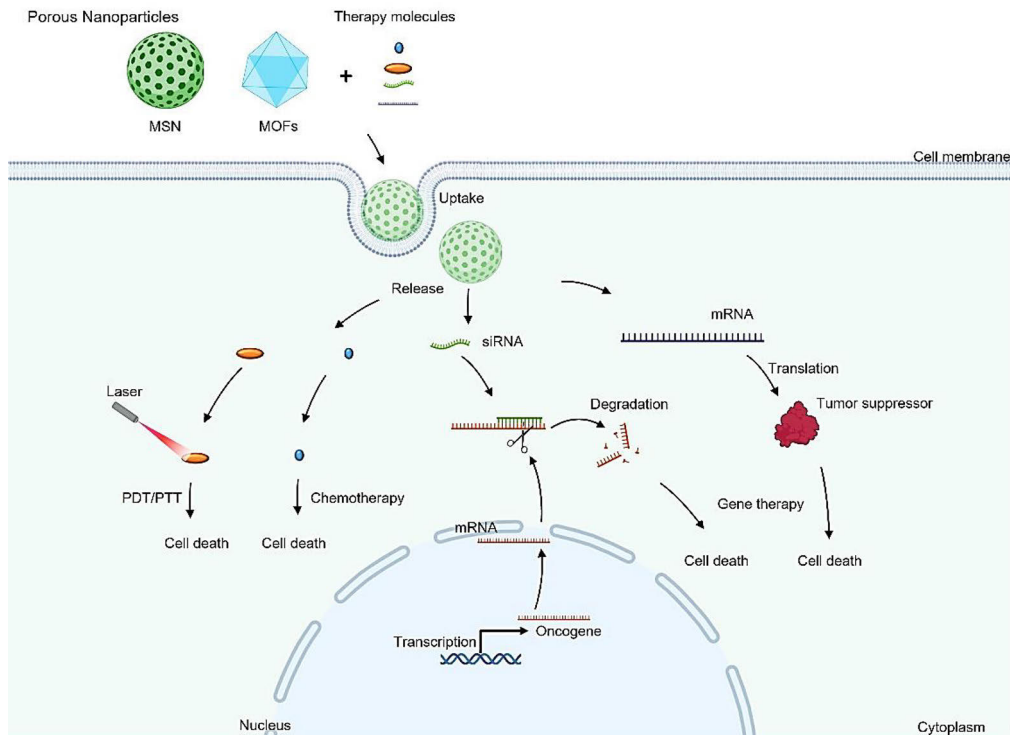


Figure 14. Schematic diagram of the thesis work.

5.2. Design of NPs for precision cancer therapy

To maximize the advantages of MSN and MOF nanomaterials for the precise treatment of cancers, several smart nanostructure designs and surface modification strategies were employed. These methods enable the prepared MSNs and MOFs to synergistically combat tumors through the combination of multiple therapy methods. This section focuses on the details of these designs and modifications, which are also summarized in Table 2.

Table 2. The summaries of NPs' design and surface modification strategies

Paper	Nanomaterials	NPs	Cargo	Modification	Function
I	MSN	Au@MSNs	PTX-SS-COOH, CPT	p(NIPAM-co-MAAc) coating	combination chemotherapy, PTT
II			THPP	Ter ligand, cell membrane coating	ER targeting, PTT, PDT, ICD targeting
III		ZIF-8	mRNA	PLR	protein expression
IV	MOF	ZrTCP	siRNA	cell membrane coating	gene therapy
V		ZIF-8	AE	Tf-PEG-PLGA coating	pyroptosis targeting

5.2.1. Cancer therapy NPs combining multiple functions (paper I, II, IV & V)

The first strategy used in this work was to combine chemotherapy, PTT and/or PDT with one NP design. To achieve the goal, Au@MSNs which enables PTT were prepared. Next, the prodrug PTX-SS-COOH was linked to the surface of the Au@MSNs before loading the chemotherapy drug CPT into the MSN pores. Thus, the combination of PTX, CPT and PTT for cancer treatment was realized (paper I). The combination of PTT and PDT was also enabled by loading the photosensitizer THPP into the pores of the Au@MSNs (paper II). To realize the combination of multiple therapy methods with MOFs, the photosensitizer TCPP was used as a ligand during the preparation of ZrTCP NPs, and the combination of gene therapy and PDT was achieved after siRNA loading (paper IV).

5.2.2. NPs with stimuli-responsive drug release (paper I & V)

Stimuli-responsive drug release is one of the most important advantages of nanomedicine that can help to enhance the specificity of drugs and reducing the side effect. Therefore, to enable controlled drug release from MSNs, PTX was linked to the surface of Au@MSNs via an -SS- group, which can be catalyzed by the high levels of ROS (reactive oxygen species) present in tumor cells. Moreover, a thermo-responsive polymer, p(NIPAM-co-MAAc), was applied as a coating on the surface of Au@MSNs loaded with both CPT and PTX. This resulted in the creation of Au@MSNs capable of photothermal-controlled and ROS-responsive drug release, as detailed in Paper I.

5.2.3. Cell membrane biomimetic modification of NPs (paper II & IV)

The biomimetic modification of NP surfaces with cellular membranes involves the coating of the NPs with natural or synthetic cell membrane materials, creating cell-mimicking NPs. These NPs exhibit many biological functions which are typical of normal cells due to their high similarity to natural cell membrane structures. For instance, they utilize the proteins and polysaccharides on the cell membrane surface to evade immune system detection. Compared to unmodified NPs, these biomimetically modified NPs have demonstrated extended circulation times within the body. Additionally, the cell membrane coating strategy enhances the tumor-targeting capabilities of the NPs. Different sources of cell membranes can impart diverse therapeutic effects against tumors (Wu et al., 2023; Zhang et al., 2021).

In this work, ovarian cancer SKOV3 cell-derived membranes were used to coat Au@MSN-Ter/THPP NPs, thus forming SKOV3 cell-mimicking Au@MSN-Ter/THPP@CM NPs.

A cell biomimetic strategy was also use in the design of ZrTCP NPs for precise cancer therapy. For this, cell membranes derived from ovarian cancer SKOV3 cells were utilized to encapsulate ZrTCP NPs loaded with FOXK2 siRNA, thus forming ZrTCP@siFOXK2 NPs.

5.2.4. Microgelation of NPs (paper II & V)

In past decades, gelatin methacryloyl (GelMA) hydrogels have gained increasing attention in fields such as drug delivery and tissue repair, owing to their excellent

biocompatibility and straightforward synthesis process. Particularly in drug delivery, their biodegradable nature plays a crucial role in controlled drug release and targeted local delivery. In this work, microfluidic technology was used to wrap the drug loaded Au@MSNs or ZrTCP NPs into GelMA microhydrogels. Different sizes of GelMA hydrogel microspheres were prepared by changing the flow speed ratio of the reaction. These microgelated NPs enabled combined therapies and sustained drug release.

5.2.5. NPs for targeting the immunogenic cell death (ICD) pathway (paper II)

Immunogenic cell death (ICD) is a distinct type of cell demise that activates the immune system and synergizes with immunotherapy. To activate the ICD pathway, I first functionalized the surface of Au@MSNs with an ER (endoplasmic reticulum) targeting ligand. The resulting Au@MSN-Ter/THPP@CM@GelMA/CAT microspheres exhibited the capability to initiate a cascade reaction, leading to augmented photodynamic therapy effects and the subsequent activation of the ICD pathway.

5.2.6. NPs for gene therapy (paper III & IV)

Gene therapy is one of the most promising methods for cancer therapy. However, the delivery of therapeutic nucleic acid drugs to cancer cells, specifically solid tumors remain a big challenge. Therefore, the efficiency of RNA (siRNA and mRNA) delivery with ZrTCP and ZIF-8 NPs was tested and used for combined cancer therapy in this work.

5.2.7. NPs for targeting the cell pyroptosis pathway (paper V)

Pyroptosis pathway is a programmed cell death pathway that is mediated by DSDM (gasdermin). The promotion of pyroptosis in cancer cells has been regarded as a good choice for cancer therapy. In this work, a pyroptosis activator AE (aloeemodin) was encapsulated in ZIF-8 NPs, which enabled the induction of the GBM cell death via the pyroptosis pathway.

5.3. Multifunctional MSNs for precision cancer therapy (papers I & II)

In this section, mesoporous silica-coated gold rod NPs were employed to achieve multifunctionality of the mesoporous silica nanomaterials through surface modification and prodrug technology. This included a detailed exposition on the synthesis, characterization, and evaluation of the antitumor efficacy of these multifunctional mesoporous silica nanomaterials.

5.3.1. Preparation and characterization of multifunctional Au@MSNs

5.3.1.1. Morphology and physicochemical properties

To achieve multifunctionality in mesoporous silica nanomaterials and maximize their potential as drug carriers, Au@MSNs were developed by using a seed growth method. This innovative approach allows the co-loading of various

chemotherapeutic drugs or tumor cell-targeting ligands through the mesoporous channels and surface modifications of these gold nanorod NPs (Au NRs). As illustrated in Figure 15, the synthesized Au NRs exhibit a regular rod-like structure, with a size of 65 nm (Figure 15 A). After coating with mesoporous

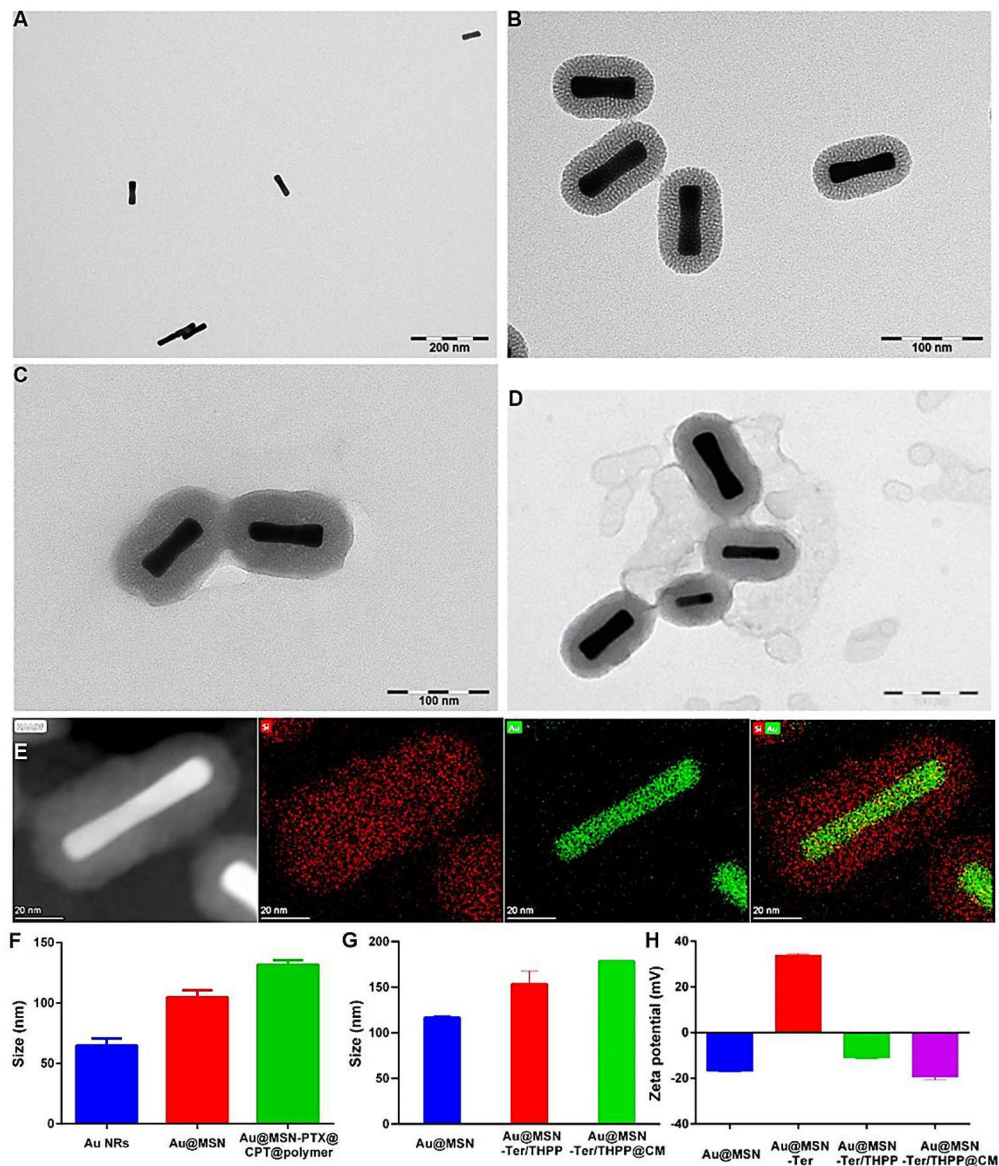


Figure 15. Morphology, size and zeta-potential of Au-MSN NPs. Representative TEM images depicting Au NRs (A), Au@MSN (B), Au@MSN-PTX@CPT@polymer (C) and Au@MSN-Ter/THPP@CM (D) NPs; E. Representative HAADF images of Au@MSN NPs; (F and G). Nanoparticle size of Au NRs, Au@MSN, Au@MSN-PTX@CPT@polymer and Au@MSN-Ter/THPP@CM NPs; H. Zeta-potential of Au@MSN, Au@MSN-Ter, Au@MSN-Ter/THPP, and Au@MSN-Ter/THPP@CM NPs. Scale bars are as follows: 200 nm in A, 100 nm in B-D, and 20 nm in E. Data in F-I are presented as mean \pm SD from three independent experiments. A, B, C and F are figures from paper I; D, E, G and H are from paper II.

silica, the NPs display a distinct sponge-like outer layer with pores, increasing their diameter significantly to 101 nm and carrying a negative charge (Figure 15 B, F, G and H). The STEM elemental analysis (Figure 15 E) also reveals a clear enrichment of gold and silicon elements on the surface. Further modifications with drug loading and the addition of a thermally responsive polymer poly(N-isopropylacrylamide-co-methacrylic acid) (p(NIPAM-co-MAAc)) or tumor cell-targeting cell membranes resulted in a less visible porous structure of the mesoporous silica layer, with a notable membrane-like structure on the nanoparticle surface (Figure 15 C and D). Concurrently, the diameter of the NPs increased significantly, reaching 130-180 nm (Figure 15 F and G). Notably, the negative charge of the gold rod NPs in deionized water is primarily due to the dissociation of H ions from the -OH groups on the mesoporous silica surface. However, due to the inert nature of -OH groups, we chemically modified the surface -OH groups to more reactive -NH₂ groups. The prodrug PTX-SS-COOH and the endoplasmic reticulum-targeting ligand Tosyl Ethylenediamine (Ter) were then covalently attached through the condensation of -NH₂ and -COOH groups, facilitating the surface loading of PTX and Ter. This modification enabled controlled and responsive co-loading of multiple drugs in the Au@MSNs.

5.3.1.2. Drug loading and stimuli-responsive release

Next, the photothermal responsiveness and controlled drug release capabilities of the drug-loaded Au@MSNs were thoroughly validated. As illustrated in Figure 16 C-E, under 980 nm laser irradiation, both types of the prepared Au@MSNs, i.e., Au@MSN-PTX@CPT@polymer and Au@MSN-Ter/THPP@CM, demonstrated superb photothermal conversion capabilities. This conversion was proportionally related to the laser intensity, nanoparticle concentration, and irradiation time. Notably, by irradiating with 1W/cm² with a 980 nm laser for 300 seconds, both NPs at 1mg/ml generated temperatures up to 60°C, which is sufficient to effectively kill cells, with good repeatability.

The thermosensitive polymer p(NIPAM-co-MAAc) was used to encapsulate Au@MSN-PTX@CPT@polymer NPs, enabling photothermally controlled release of the chemotherapeutic drug CPT. The results, as shown in Figure 16 I, demonstrated a significant increase in drug release efficiency from the mesoporous silica channels of these NPs under 980 nm laser irradiation. Similarly, the release of the photosensitizer THPP from the mesoporous silica channels of Au@MSN-Ter/THPP@CM NPs was significantly increased in laser exposure group (Figure 16 H). This can be attributed to photothermal damage to the cell membrane coating on the nanoparticle surface.

Furthermore, the Au@MSN-PTX@CPT@polymer NPs initially contained the chemotherapeutic drug PTX in the prodrug form of PTX-SS-COOH, as shown in Figures 16 A and B. This prodrug was loaded onto the NPs through a reaction that involved the activated -NH₂ groups present on the surface of the Au@MSNs. The disulfide bond -SS- in this compound can respond to the specific redox microenvironment in tumor cells, like high GSH (Glutathione) concentrations, which can break the -SS- bond and release PTX. Therefore, DTT (Dithiothreitol) was used to simulate the tumor cell microenvironment for stimulating PTX

release. As indicated in Figure 16 G, the presence of 10 mM DTT notably increased the release efficiency of PTX post 980 nm laser irradiation.

In conclusion, the drug-loaded Au@MSNs, Au@MSN-PTX@CPT@polymer, and Au@MSN-Ter/THPP@CM NPs exhibit effective photothermal response capabilities, as well as the ability to release drugs in a controlled manner responsive to both photothermal and tumor cell microenvironment-specific conditions.

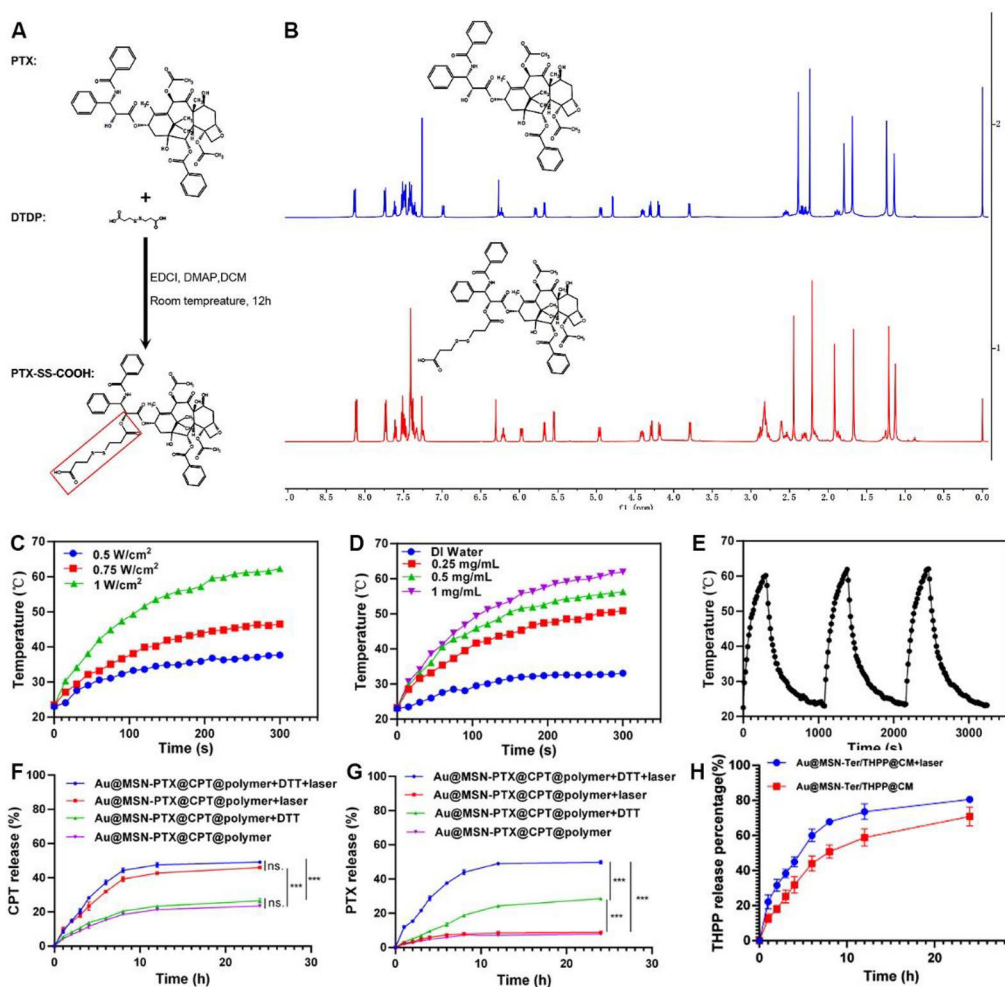
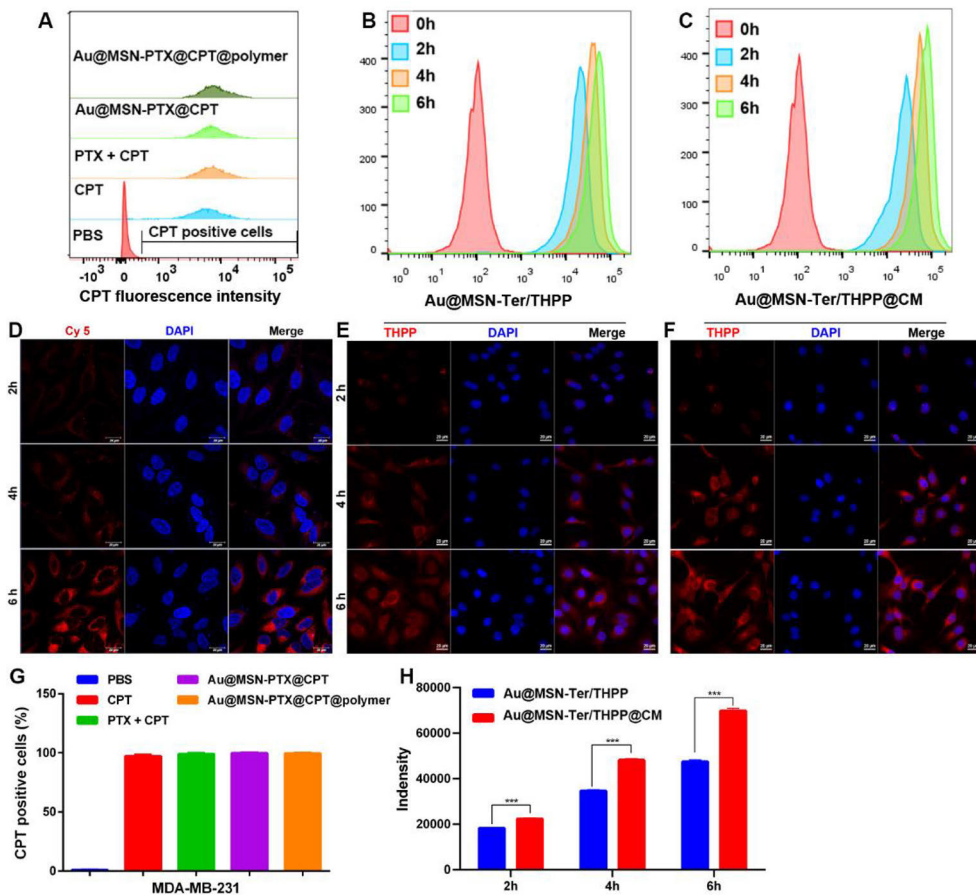


Figure 16. Drug loading and physical properties of Au@MSN NPs. Schematic of PTX prodrug synthesis (A) and the results of ^1H NMR spectra analysis (B); Photothermal response curves of Au@MSN - PTX@CPT@polymer NPs (C-E) under 980nm laser irradiation at different concentrations and different laser conditions; The release profiles of CPT (F) and PTX (G) from Au@MSN-PTX@CPT@polymer NPs under DTT and laser conditions; H. The release profiles of THPP from Au@MSN-Ter/THPP@CM NPs under laser condition. Data in F-H are presented as mean \pm SD from three independent experiments. A-G are figures from paper I; H is from paper II.

5.3.2. Cellular interactions

The dynamic interactions between cells and NPs are crucial in determining the success of these nanocarriers for drug delivery. These interactions encompass cellular uptake of NPs, their intracellular localization, metabolism, and the toxicity they may impart on cells. Comprehensive evaluations were conducted to thoroughly assess the interaction between tumor cells and the two types of Au@MSNs that were developed. Confocal microscopy and flow cytometry were used to investigate the efficiency of cellular nanoparticle engulfment, lysosomal escape within cells, and the impact of NPs on cell toxicity and inhibitory effects on cell survival.

5.3.2.1. Cell uptake



Cellular uptake of NPs is a critical factor in intracellular drug delivery, influenced by aspects such as nanoparticle size and surface charge. Flow cytometry and confocal microscopy were used to observe and analyze cell uptake after incubating MDA-MB-231 breast cancer cells and SKOV3 ovarian cancer cells with drug-loaded Au@MSNs for 0-6 hours. The results showed that 100% of the cells were CPT positive after 2 hours of co-incubation of Au@MSN-PTX@CPT@polymer NPs with MDA-MB-231 cells (Figures 17 A and G), which was consistent with confocal microscopy observations (Figure 17 D). These findings indicate that Au@MSN-PTX@CPT@polymer NPs can be rapidly uptaken by MDA-MB-231 cells with high efficiency. Simultaneously, Au@MSN-Ter/THPP NPs demonstrated efficient uptake by SKOV3 cells, with a significant increase in THPP-positive cells over time (Figures 17 B, E, and H). Notably, Au@MSN-Ter/THPP@CM NPs, which were coated with the SKOV3 cell-derived membrane, exhibited a significantly higher intracellular THPP nanoparticle content under identical incubation conditions (Figures 17 C, F, and H). This observation indicates that the tumor cell membrane coating can potentiate the cellular uptake of Au@MSN NPs.

5.3.2.2. Lysosomal escape

The capability of NPs to escape from lysosomes is a critical determinant for the successful delivery of drugs by nanocarriers, and is closely linked to surface modifications, nanoparticle composition, and loaded drugs. The ability of two drug-loaded Au@MSNs to escape from lysosomes were further evaluated by using confocal microscopy. NPs were incubated with tumor cells for 2-6 hours, followed by treatment with a 980 nm laser for 10 minutes before staining with green LysoTracker and blue DAPI. Confocal microscopy images revealed that while laser irradiation decreased the colocalization of Cy5-labeled Au@MSN-PTX@CPT@polymer NPs with LysoTracker, this effect was not substantial with extended incubation durations (Figure 18A). This observation implies that laser irradiation plays a crucial role in facilitating the lysosomal escape of the Au@MSN-PTX@CPT@polymer NPs.

When Cy5.5-labeled Au@MSN-Ter@CM NPs were co-incubated with OVCAR3 and SKOV3 cells for 3-6 hours (Figure 18 B), a strong red fluorescence signal (representing Au@MSN-Ter/Cy5.5@CM NPs) was observed in both cell types at both time points. Additionally, a significant overlap was noticed between the red fluorescence and the green fluorescence signal, which represented lysosomes. However, in laser-treated groups, the overlap of red and green fluorescence signals was significantly reduced. This indicated enhanced lysosomal escape of Au@MSNs in cells, likely due to photothermal conversion effects generated by Au@MSNs under 980 nm laser irradiation.

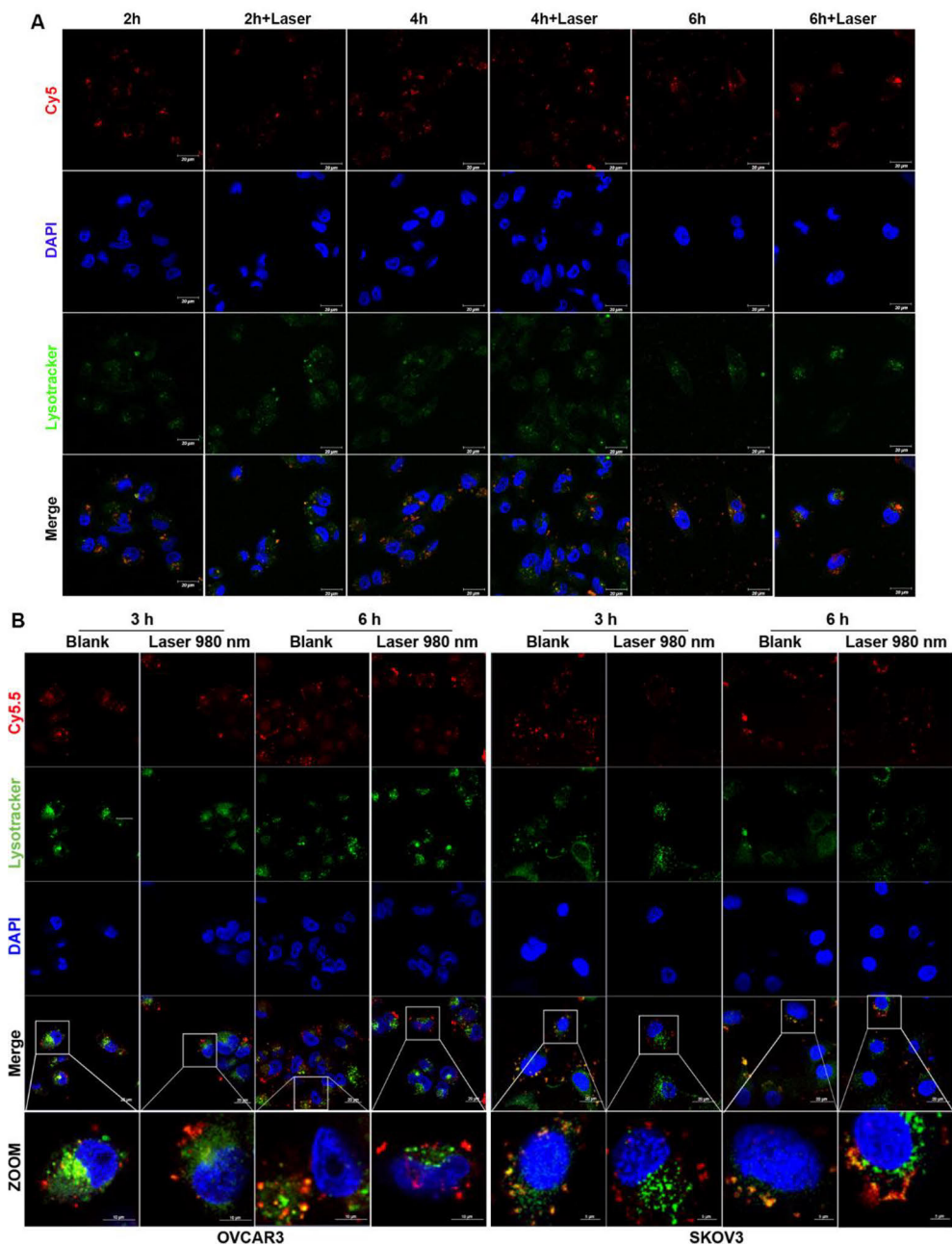


Figure 18. Lysosomal escape of Au@MSN NPs. A. Representative confocal microscopy images depicting cells incubated with Cy 5-labeled Au@MSN-PTX@CPT@ NPs for 2-6 hours with or without laser irradiation conditions; B. Representative confocal microscopy images of SKOV3 and OVCAR3 cells following incubation with Cy5.5 labeled Au@MSN-Ter@CM NPs for 2-6 hours with or without laser conditions. Scale bars are as follows: 200 μm in A and B, 10 μm in ZOOM images of B. A is from paper I; B is figure from paper II.

5.3.3. Preparation and characterization of GelMA microhydrogels

Au@MSN-Ter/THPP@CM NPs and Catalase (CAT) were excapsulated within GelMA microspheres using microfluidic technology. This to effectively reduce the systemic toxicity potentially caused by intravenous injection of Au@MSNs, and to endow the nano-delivery system with multifunctional capabilities for synergistic anti-tumor effects using the same nanocarrier. Au@MSN-Ter/THPP@CM@GelMA/CAT microspheres ranging from 50 to 500 micrometers in size were successfully prepared by controlling the internal and external flow rates in the microfluidic system (Figures 19 A and B). CAT catalyzes the conversion of tumor-specific high concentrations of hydrogen peroxide into oxygen, which then serves as a substrate for the photodynamic reaction of the photosensitizer THPP within the NPs, thus achieving a cascading photodynamic tumor treatment effect. To evaluate the stability of the prepared Au@MSN-Ter/THPP@CM@GelMA/CAT microspheres and further to apply them in anti-

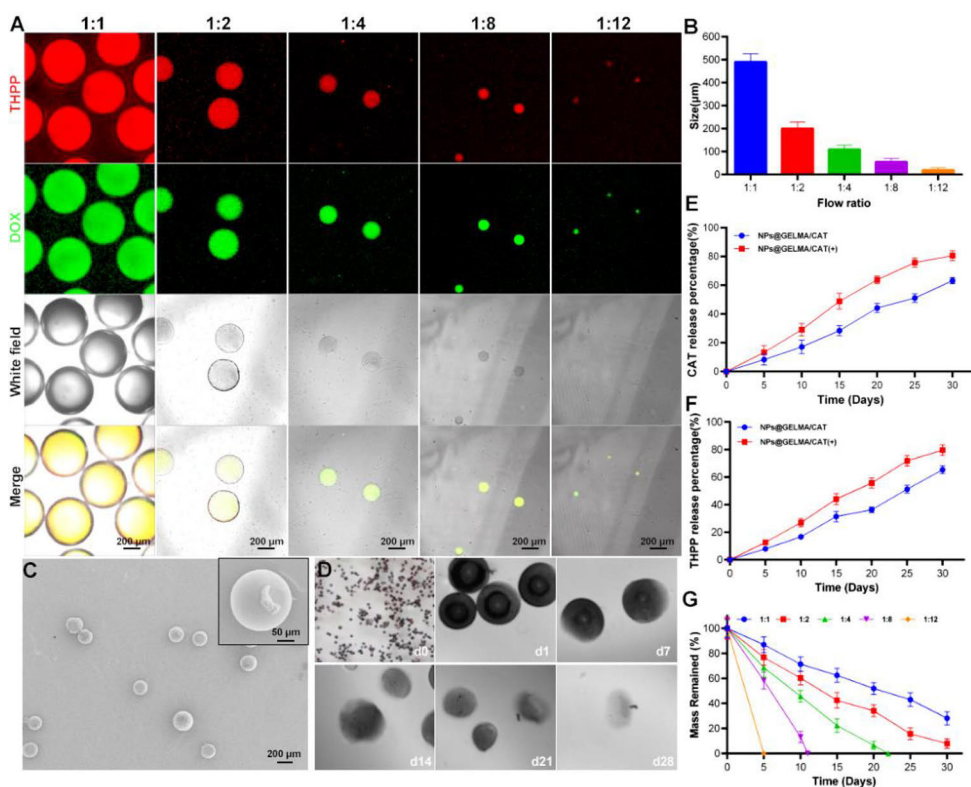


Figure 19. Morphology and release dynamics of Au@MSN-Ter/THPP@CM@GelMA/CAT Microspheres. A, B. Representative confocal microscopy images and particle size of Au@MSN-Ter/THPP@CM@GelMA/CAT microspheres, synthesized using varying external (5% Span 80 in mineral oil) and internal (mix of NPs, DOX, and GELMA) flow rates; C. Representative SEM images of the microspheres formed at an external to internal flow rate ratio of 2:1; D. Time-lapse microscopy images showcasing the structural evolution of the microspheres; E, F. Release profiles of CAT and THPP from the microspheres in PBS buffer, with and without laser irradiation (980nm, 1 W/cm², 10 min); G. Degradation curves comparing microspheres formed at different flow rate ratios. Data are presented as mean ± SD from three independent experiments.

tumor therapy tests, a 1:2 flow rate ratio was selected to prepare the optimal biomimetic nano@microgel (200 micrometers in diameter, Figure 19C) for biodegradation and drug release testing. As depicted in Figure 19D, damage to the nano@microgel surface was observed after 7 days, with continuous decomposition after 14 and up to 28 days. Moreover, the Au@MSN-Ter/THPP@CM@GelMA/CAT microspheres exhibited extended release of CAT and Au@MSN-Ter/THPP@CM NPs over 30 days and showed a significant dependency on 980 nm laser irradiation (Figures 19 E and F). *In vitro* and *in vivo* experiments also confirmed that a single *in situ* injection of Au@MSN-Ter/THPP@CM@GelMA/CAT microspheres resulted in effective anti-tumor action and significantly improved the distribution of Au@MSN-Ter/THPP@CM NPs within the body (Figures 20-23).

5.3.4. *In vitro* anti-tumor activity

5.3.4.1. Cell growth inhibition

To evaluate the anti-tumor effects of our synthesized Au@MSNs, the impact of two types of Au@MSNs on tumor cell survival at the cellular level were firstly evaluated. As depicted in Figure 20, the Annexin V/PI dual-staining apoptosis analysis assay and WST-1 cell viability assay (Figures 20 A, B, and C) revealed that Au@MSN-PTX@CPT@polymer NPs exhibited no significant cytotoxicity to normal breast tissue-derived MCF-10A cells. In contrast, the cell viability of MDA-MB-231 cells treated with Au@MSN-PTX@CPT@polymer + Laser 980 significantly decreased to 28.3% compared to the groups treated with Au@MSN + Laser 980 and Au@MSN-PTX@CPT@polymer NPs. The flow cytometry apoptosis analysis showed a marked increase in Annexin V positive apoptotic cells after 48 hours of co-incubation cells with Au@MSN + Laser 980 and Au@MSN-PTX@CPT@polymer + Laser 980. However, the increase in apoptosis was not significant in the group treated only with Au@MSN-PTX@CPT@polymer NPs. Furthermore, the highest proportion of Annexin V positive cells, reaching 78.5%, was observed in the Au@MSN-PTX@CPT@polymer + Laser 980 treatment group. These findings suggest that Au@MSN-PTX@CPT@polymer + Laser 980 is the most effective treatment modality for inhibiting MDA-MB-231 cell growth.

Correspondingly, a co-incubation for 24 hours and selective exposure to 980 nm (1 W/cm^2 , 10 minutes) and 650 nm (0.4 W/cm^2 , 5 minutes) laser irradiation were performed with OVCAR3 and SKOV3 cells, and different Au@MSN-Ter/THPP@CM NPs. The WST-1 and flow cytometry apoptosis analysis demonstrated that the cell viabilities of OVCAR3 and SKOV3 cells within the Au@MSNs treated groups significantly decreased post 980 nm laser treatment primarily due to cell death induced by photothermal effect, especially in the highest NP concentration groups (Figures 20 D and E). When combined with 650 nm laser irradiation, the $5 \mu\text{g/mL}$ Au@MSN-Ter/THPP@CM NPs significantly reduced the viability of both OVCAR3 and SKOV3 cells. These findings suggest that the Au@MSN-Ter/THPP@CM NPs can trigger fatal photodynamic reactions under 650 nm laser light, primarily due to the THPP photosensitizer encapsulated within the NPs. Therefore, these NPs demonstrate considerable promise for enhancing the efficacy of Photodynamic Therapy (PDT).

Furthermore, the viability of OVCAR3 and SKOV3 cells treated with Au@MSN-Ter/THPP@CM NPs in combination with both 980 nm and 650 nm laser irradiations decreased more significantly compared to treatment with a single laser irradiation, reaching $7.7 \pm 0.5\%$ and $14.8 \pm 6.4\%$, respectively. Meanwhile, in normal human dermal fibroblasts (NHDF), the cell viability after treatment with $5 \mu\text{g/ml}$ Au@MSN-Ter/THPP@CM NPs and both lasers was $41.5 \pm 2.8\%$, suggesting a certain level of selectivity towards tumor cells exhibited by the Au@MSN-Ter/THPP@CM NPs. This phenomenon is primarily attributed to the tumor cell membrane wrapping induced by the NPs, resulting in selective cellular uptake.

To improve the targeting of tumor sites by Au@MSN-Ter/THPP@CM NPs and to achieve enzyme-catalyzed photodynamic tumor destruction, we encapsulated these NPs within GelMA microspheres using microfluidic technology. UV crosslinking then made these microhydrogels suitable for direct injection into tumors (Figure 19). To test their antitumor effects on SKOV3 and OVCAR3 cells, we used live-dead and Annexin V/PI staining assays. Results showed that after 48 hours, both Au@MSN-Ter/THPP@CM@GelMA and Au@MSN-Ter/THPP@CM@GelMA/CAT treatments increased Annexin V-positive cells, indicating apoptosis. This effect was stronger with dual laser irradiation (650 nm and 980 nm) compared to single laser treatment, especially for the CAT-containing microgel. Since Annexin V binds to damaged cell membranes, its fluorescence signals marked apoptotic cells. Thus, our findings suggest that these microgels effectively induce apoptosis in tumor cells, and dual laser irradiation further enhances this effect.

The red fluorescent dye PI stains dead cells with damaged membranes, while Calcein-AM glows green in living cells. Using both dyes helps us distinguish between live and dead cells. In our experiments (Figure 20 H), SKOV3 and OVCAR3 cells treated with Au@MSN-Ter/THPP@CM@GelMA or Au@MSN-Ter/THPP@CM@GelMA/CAT showed more red PI fluorescence and less green Calcein-AM fluorescence, indicating cell death. Laser treatments (650 nm and/or 980 nm) intensified this effect, especially when both lasers were used together. Cells treated with Au@MSN-Ter/THPP@CM@GelMA/CAT and double lasers showed the most significant increase in cell death. These results suggest that our formulations, especially when combined with laser treatments, effectively induce apoptosis in OVCAR3 and SKOV3 cells. Moreover, Au@MSN-Ter/THPP@CM@GelMA/CAT is more potent in causing cell death than Au@MSN-Ter/THPP@CM@GelMA alone.

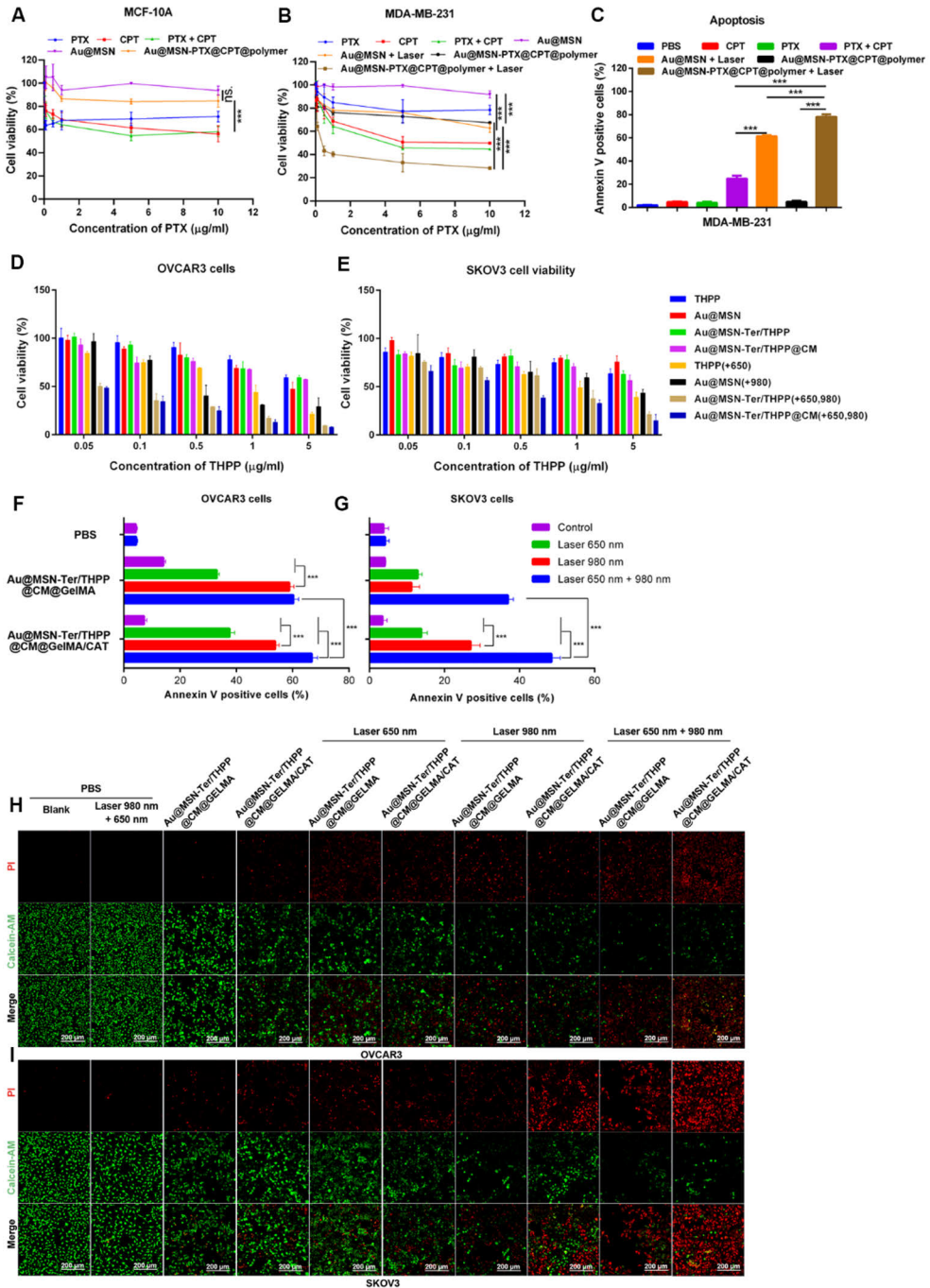


Figure 20. Cell growth inhibition by drug loaded Au@MSNs or their formed GELMA microspheres. Cell viabilities (A-B, and D-E), and cell apoptosis analysis (C) after 48 hours incubation with different drug combinations or different Au@MSN-PTX@CPT@polymer NPs with/without laser conditions; Cell apoptosis analysis (F and G) and representative confocal images (H and I) after 48 hours incubation with different Au@MSNs GELMA microspheres with/without laser conditions. Data in A-G are presented as mean \pm SD from three independent experiments; Scale bar=200 nm in H and I.

5.3.4.2. Immunogenic cell death (ICD) pathway activation

To validate the enhanced photodynamic reactions of Au@MSN-Ter/THPP@CM@GelMA/CAT, we monitored reactive oxygen species (ROS) levels in SKOV3 cells using the DCFH-DA indicator. This non-fluorescent molecule turns fluorescent upon oxidation, allowing us to analyze cellular ROS. After 48 hours, a faint green signal was observed in cells treated with Au@MSN-Ter/THPP@CM@GelMA/CAT (Figure 21 A and B). However, a significant increase in fluorescence occurred in both treated cell groups, especially with Au@MSN-Ter/THPP@CM@GelMA/CAT, upon additional 650 nm laser treatment.

Photodynamic therapy-induced cell-lethal ROS triggers the ICD signaling pathway. We further assessed ICD levels by analyzing Calreticulin (CRT) and High Mobility Group Box 1 (HMGB1). CRT, typically in the endoplasmic reticulum, relocates to the cell membrane under stress, signaling the immune system. HMGB1, an immune activator, is released from the nucleus under stress. As shown in Figure 21 C-D, while treatments with 5 mg/ml CAT and 10 μ g/ml Au@MSN-Ter/THPP@CM NPs alone didn't significantly affect SKOV3 cell viability, combinations with 650 nm laser irradiation increased CRT and HMGB1 signals, indicating ICD activation. Similar results were observed with Au@MSN-Ter/THPP@CM@GelMA/CAT samples, confirming enhanced ICD activation with this treatment.

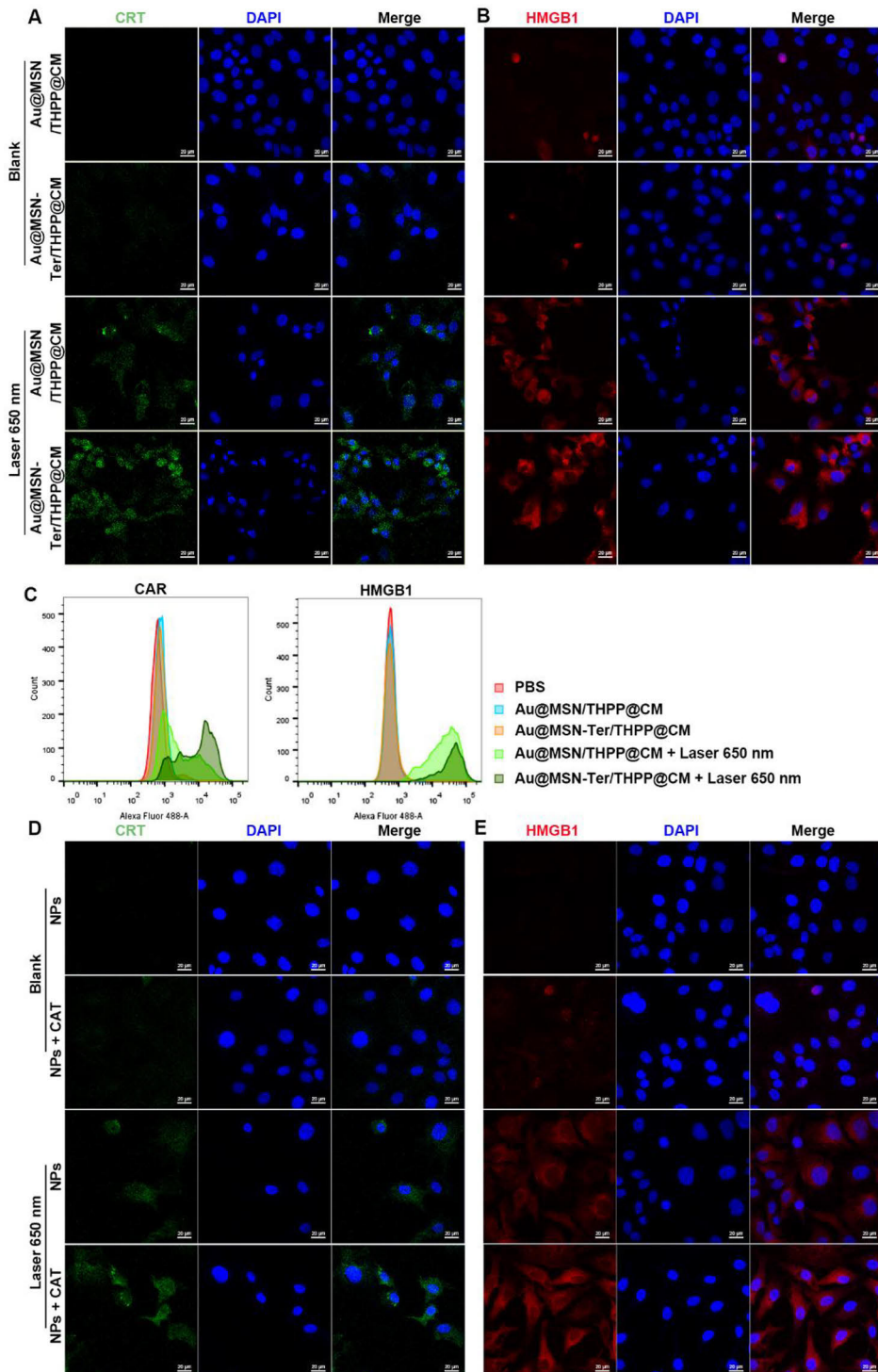


Figure 21. Drug loaded Au@MSNs activate ICD signal in SKOV3 cells. Representative confocal microscope images (A, B, D and E) and flow cytometry analysis results (C) of CRT and HMGB1 stained SKOV3 cells after 24 hours of treatment of different Au@MSNs with or without laser irradiation. Scale bar = 20 μ m.

5.3.5. Biodistribution and *in vivo* anti-tumor activity

5.3.5.1. *In vivo* biodistribution

The biodistribution of nanocarriers in the body, especially their accumulation in tumors, is key to the success of nanoparticle-based tumor therapies and minimizing organ toxicity. To assess this, we used xenograft mouse models derived from TNBC 4T1 and SKOV3 cells to study the biodistribution of Au@MSN-PTX@CPT@polymer NPs, Au@MSN-Ter/THPP@CM NPs, and a hydrogel formulation (Au@MSN-Ter/THPP@CM@GelMA/CAT).

After injecting Au@MSN-PTX@CPT@polymer NPs into the tail vein, we observed rapid accumulation in tumor tissues within an hour, which continued to increase over 24 hours (Figure 22 A and B). Notably, their presence in critical organs like the liver, kidneys, and heart remained low. This may be due to the enhanced permeability and retention (EPR) effect and the coated p(NIPAM-co-MAAc) polymer, but further studies are needed.

Intratumoral injection of Au@MSN-Ter/THPP@CM@GelMA/CAT resulted in predominant NP accumulation in the tumor, with minimal detection in the liver. However, tail vein injection of Au@MSN-Ter/THPP NPs followed by dual laser treatment led to NP accumulation in the liver, tumor, lungs, and kidneys at 24 and 48 hours (Figure 22 C).

These results suggest that the *in vivo* distribution of Au@MSNs is influenced by the loaded drug and surface modifications. *In situ* injection formulations may be optimal for enhancing tumor-specific accumulation.

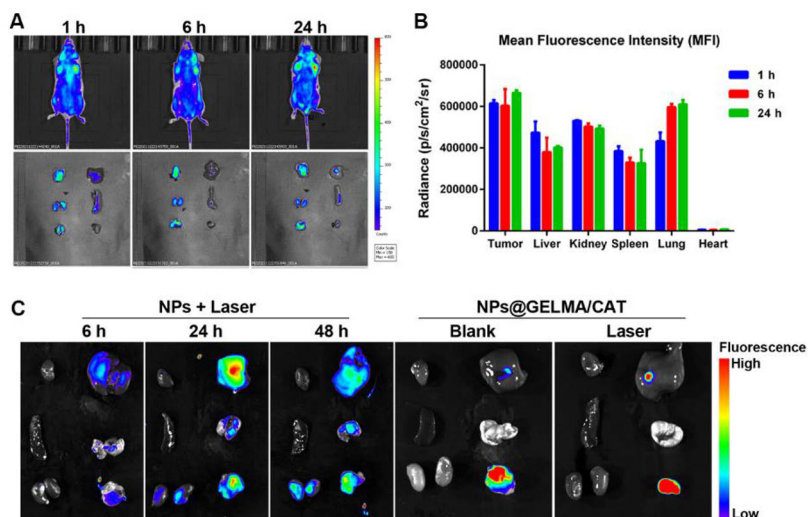


Figure 22. *In vivo* biodistribution of different Au@MSNs and Au@MSNs formed GELMA microspheres. A, B. Representative IVIS images and corresponding quantitative data of mice and main organs at 1-24 hours post tail vein injection of Cy 5 labeled Au@MSN-PTX@CPT@polymer NPs (Organs in A: from left to right and up to down panels are tumor, liver, kidney, spleen, lung and heart); C. Representative IVIS images of mouse main organs post tail vein injection of Au@MSN-Ter/THPP@CM NPs or intratumoral injection of Au@MSN-Ter/THPP@CM@GELMA/CAT microspheres (Organs in C: from left to right and up to down panels are heart, liver, spleen, lung, kidney and tumor). Data in B are presented as mean \pm SD from three independent experiments.

5.3.5.2. Anti-tumor activity in animal models

Next, we conducted anti-tumor tests on Au@MSN-PTX@CPT@polymer NPs, Au@MSN-Ter/THPP@CM NPs, and the Au@MSN-Ter/THPP@CM@GelMA/CAT hydrogel in mouse tumor models. In the 4T1 model, both Au@MSN-PTX@CPT@polymer NPs and the same NPs with laser treatment significantly inhibited tumor growth, with the latter being more effective. Body weight remained stable during treatment, and HE staining showed increased tumor apoptosis in both treated groups (Figure 23 A-C and G-H).

In the ovarian tumor model developed from SKOV3 cells, both tail vein-injected Au@MSN-Ter/THPP@CM NPs and in situ-injected Au@MSN-Ter/THPP@CM@GelMA/CAT reduced tumor weight under dual laser treatment. Tumors treated with Au@MSN-Ter/THPP NPs or Au@MSN-Ter/THPP@CM@GelMA/CAT plus dual laser were significantly lighter than those treated only with the hydrogel. Histological analysis confirmed increased tumor cell death in all treated groups, particularly with the hydrogel plus laser. Ki 67 and TUNEL staining mirrored these results, indicating reduced proliferation and increased apoptosis (Figure 23 D-F and I-N). In conclusion, both formulations and treatment methods effectively inhibited tumor growth, with in situ injection of Au@MSN-Ter/THPP@CM@GelMA/CAT plus laser treatment being the most effective cancer therapy strategy.

In summary, the Au@MSNs drug-loaded NPs and their hydrogel microspheres prepared in this work exhibited remarkable anti-tumor effects, particularly when used in conjunction with specific lasers, i.e., 980nm laser required for gold rod photothermal response and 650nm laser needed for THPP photodynamic reaction, thus achieving a synergistic effect of multiple anti-tumor actions.

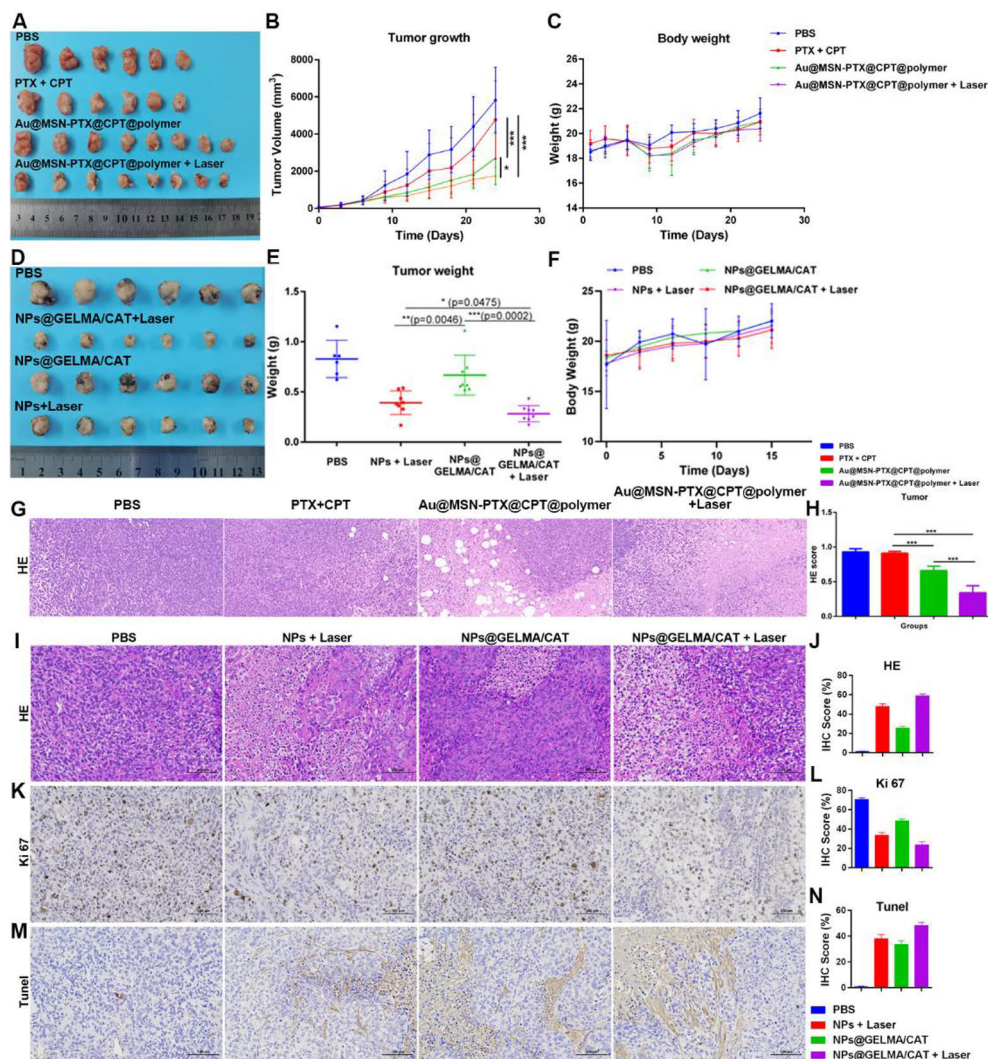


Figure 23. Antitumor efficacy of different drug loaded Au@MSN formulations. A-C. Representative tumour tissues, tumor growth curves, and body weight changes under different drug combinations and Au@MSN-PTX@CPT@polymer NPs, with/without laser treatment; **D-F.** Representative tumour tissues, tumor growth curves, and body weight changes under Au@MSN-Ter/THPP@CM NPs and Au@MSN-Ter/THPP@CM@GELMA/CAT microspheres, with/without laser treatment; **G-N.** Representative HE, Ki67, and TUNEL staining of tumor tissues, along with their corresponding quantitative scores. Data are presented as mean \pm SD from three independent experiments; Scale bar=200 μ m in G-M; * $P < 0.05$, ** $P < 0.01$, *** $P < 0.001$.

5.3.5.3. Safety assessment and biocompatibility

Finally, the main organs (including the heart, liver, spleen, lungs, and kidneys) of mice treated for 24 days with Au@MSN-PTX@CPT@polymer NPs and for 15 days with either Au@MSN-Ter/THPP@CM NPs or the Au@MSN-Ter/THPP@CM@GelMA/CAT hydrogel were examined. Histological analysis of these organs, conducted through Hematoxylin and Eosin (HE) staining of tissue

sections revealed no significant tissue damage (Figures 24 A and B). These findings indicate that over the duration of treatment, both the Au@MSNs formulations and hydrogel microspheres did not exhibit significant organ toxicity.

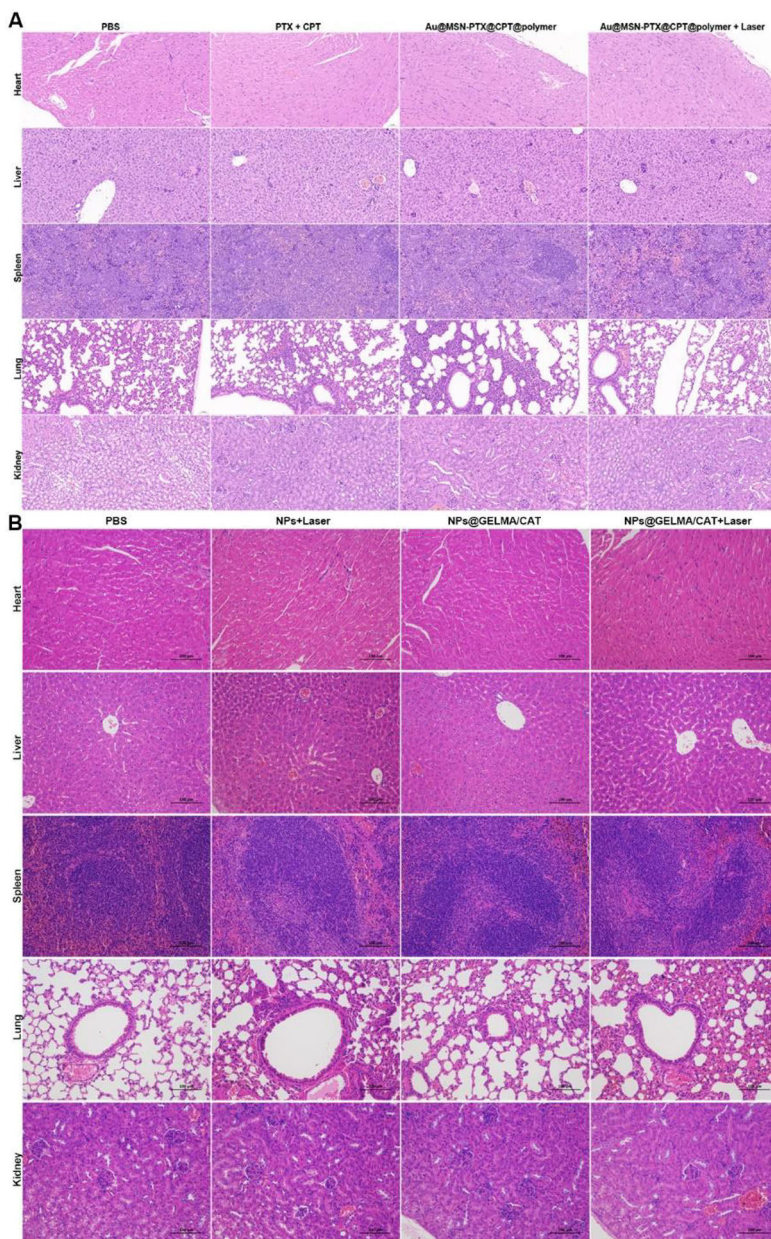


Figure 24. Representative HE staining images of mouse main organs after treatment of different drug loaded Au@MSNs formulations. Scale bar=200 μm.

5.4. MOFs for precision cancer therapy (papers III, IV & V)

This section mainly centers around the application of MOFs in the precise treatment of tumors. It showcases the preparation, characterization, and the anti-tumor efficacy at both cellular and animal levels of ZIF-8 and ZrTCP NP-based drug delivery carriers.

5.4.1. Preparation and characterization of multifunctional MOFs (paper III, IV & V)

5.4.1.1. Morphology and physicochemical properties of MOFs

In this work, self-assembly techniques were employed to fabricate ZIF-8 NPs by using zinc ions and 2-methylimidazole (2-MIM) as a ligand, and ZrTCP NPs by using metal zirconium ions and the photosensitizer TCPP as a ligand. The aim was to demonstrate their use for the delivery of mRNA, siRNA, and natural active small molecule drugs for tumor therapy. As illustrated in Figure 25, the synthesized ZIF-8 NPs are regular polyhedral particles measuring 120-130 nm in size and carry a positive charge in water solutions (Figures 25A, D, J, and I). Following the loading of EGFP mRNA or the natural compound AE, the mEGFP@ZIF-8 NPs exhibited significant alterations in dispersibility and morphology in deionized water, and the size of the AE@ZIF-8 NPs increased to

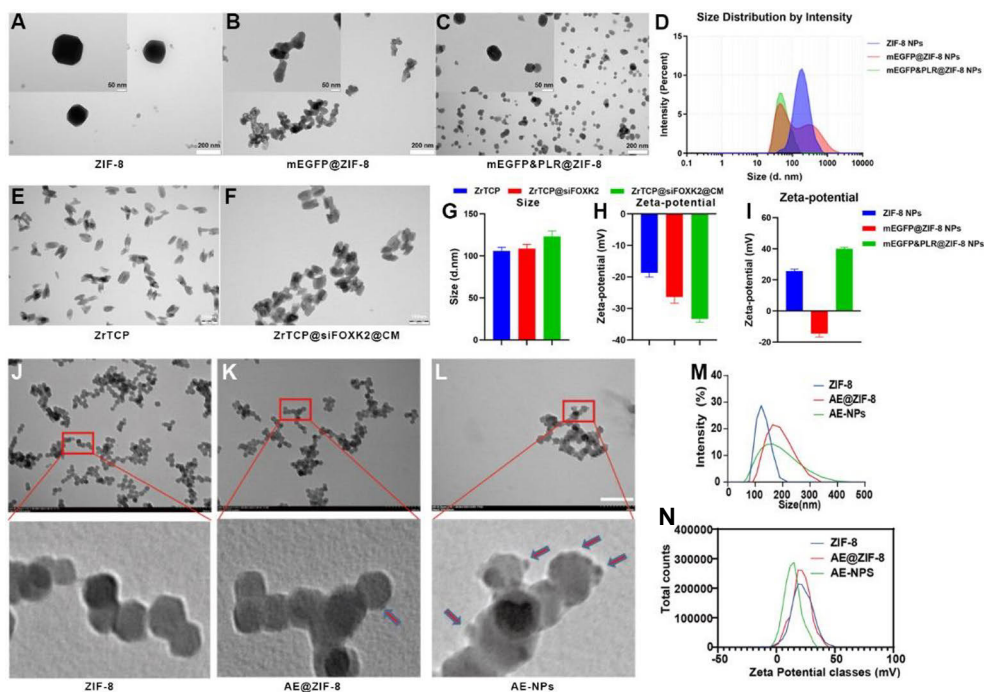


Figure 25. Morphology, size and zeta-potential of ZIF-8 and ZrTCP NPs. Representative TEM images of ZIF-8 and EGFP mRNA loaded ZIF-8 NPs (A-C), ZrTCP and FOXK2 siRNA loaded NPs (E and F), ZIF-8 and AE loaded NPs (J-L); Nanoparticle size and Zeta-potential of mEGFP@ZIF-8 NPs (D and I), ZrTCP@siFOXK2@CM NPs (G and H), and AE@ZIF-8 NPs (M and N). Scale bars are as follows: 200 nm in A-C and J-L; 100 nm in E and F; . Data in D, G-I, and M-N are presented as mean \pm SD from three independent experiments.

155 nm (Figures 25B, D, K, and M). To optimize the dispersibility and surface charge of mEGFP@ZIF-8 NPs for enhanced mRNA delivery, Poly-L-arginine hydrochloride (PLR) polymer (positively charged, facilitating electrostatic adsorption of mEGFP molecules and modulating the nanoparticle surface charge) was introduced during their synthesis. Meanwhile, to enhance the blood circulation time and blood-brain barrier penetration of AE@ZIF-8 NPs, the NPs were further coated with transferrin-modified PLGA polymer Tf-PEG-PLGA, which targets transferrin receptors (TfR) on vascular endothelial cells and glioblastoma cells in the brain. As shown in Figures 25C, D, and I, the introduction of PLR significantly improved the dispersibility of mEGFP&PLR@ZIF-8 NPs and adjusted their size to 80 nm simultaneously rendering the NPs with a positive charge (facilitating interaction with negatively charged cell membranes). Furthermore, after coating with Tf-PEG-PLGA polymer, the surface of the AE-NPs exhibited noticeable cloudy structural changes (Figures 25 L-N). Correspondingly, the ZrTCP NPs, synthesized using the photosensitizer TCPP as a ligand in a reaction with zirconium ions, were regularly spindle-shaped, about 104 nm in diameter, and negatively charged (Figures 25E and G). After adsorption loading with FOXK2 siRNA and coating with cell membranes derived from SKOV3 cells, the ZrTCP@siFOXK2@CM particles maintained an elliptical shape, and displayed a clear membrane structure on their surface (Figure 25F). Notably, the particle size of these cell membrane-coated NPs increased to 125.3 nm, and their surface charge was further reduced to -34.6 mV (Figures 25G and H).

5.4.1.2. Drug loading and stimuli-responsive release

Compared to traditional small molecule chemotherapy drugs, nucleic acid-based drugs face more challenges in *in vivo* delivery. This is mainly due to the instability and sequence specificity of nucleic acid molecules. To better validate the feasibility of MOFs as carriers for nucleic acid-based drugs, mEGFP&PLR@ZIF-8 NPs were used as a template. This work demonstrates the encapsulation efficiency and protective ability of ZIF-8 NPs for mEGFP RNA. As shown in Figure 26, by mixing mEGFP RNA with PLR to aggregate the RNA molecules, and then by using different mass ratios of the ligand 2-methylimidazole (2-MIM) and mRNA enabled the preparation of mEGFP&PLR@ZIF-8 NPs. After quantitatively analyzing the free RNA in the post-reaction supernatant, it was found that the highest loading efficiency of mEGFP was 15% at a 1:400 mass ratio of 2-MIM to RNA, with an encapsulation efficiency of 100% (Figure 26 A). When mEGFP&PLR@ZIF-8 was incubated with culture medium containing 20% FBS at 37 °C for 0-4 hours, agarose gel electrophoresis showed only minor degradation of mEGFP RNA within the NPs (Figure 26 A).

ZIF-8 NPs have garnered attention in the field of drug delivery due to their excellent pH responsiveness. To verify the pH-responsive degradation and drug release of our ZIF-8 NPs, the AE-NPs encapsulated with AE drug and coated with Tf-PEG-PLGA (Figure 26 C and D) were exposed to solutions of pH 5.5 and pH 7.4. TEM images showed that an exposure of 48 hours to the pH 5.5 environment led to structural changes in the AE-NPs, and that the AE-NPs had almost

completely disintegrated after 96 hours (Figure 26 E). Meanwhile, AE was gradually released from the AE-NPs, with almost complete release after 120 hours. In contrast, only a small amount of AE was released from the AE-NPs in the pH 7.4 solution after 120 hours (Figure 26 F). These results indicate that ZIF-8 NPs possess excellent capabilities for loading and protecting RNA and small molecule drugs, while also possessing pH responsiveness.

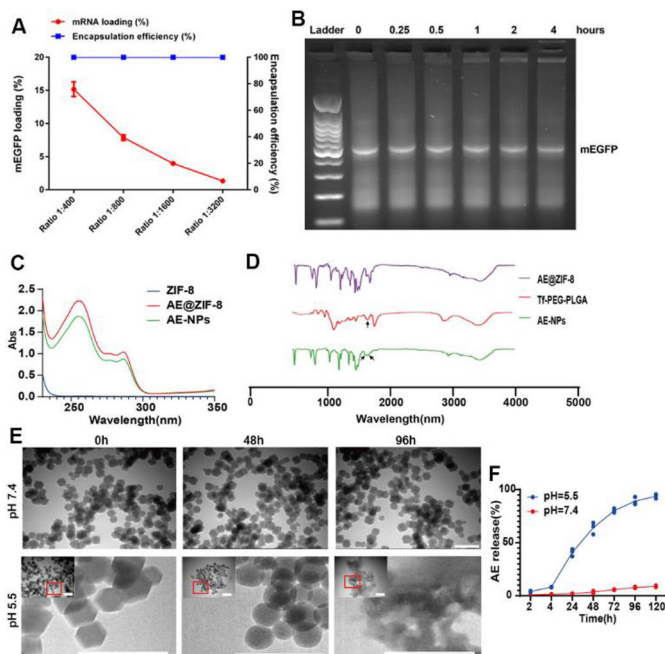


Figure 26. Drug loading and physical properties of ZIF-8 NPs. **A.** Encapsulation efficiency of EGFP mRNA by ZIF-8 NPs at different mRNA to ZIF-NPs mass ratio (ZIF-8 NPs are calculated by the weight of 2-MIM used for ZIF-8 synthesis); **B.** Agarose-gel electrophoresis of mEGFP&PLR@ZIF-8 NPs after 0-4 hours of incubation with 20%FBS at 37 °C; UV absorption spectrum (**C**) and FTIR spectra analysis (**D**) of AE@ZIF8 NPs; Representative TEM images (**E**) and drug release profiles (**F**) AE@ZIF-8 NPs under different pH conditions. Scale bar in **E** is 200nm. Data in **A**, **C**, **D** and **F** are presented as mean \pm SD from three independent experiments.

5.4.2. Cellular interactions

5.4.2.1. Cell uptake

Next, the cellular uptake capabilities were investigated of ZrTCP NPs labeled with the fluorescent dye Cy5.5, and ZIF-8 NPs labeled with the fluorescent dye ICG by using fluorescence confocal microscopy and flow cytometry. The results, as illustrated in Figure 27, showed that the intracellular fluorescence intensity of ZrTCP@siCtrl-Cy5.5 NPs, marked with red fluorescence did significantly increase in a time-dependent manner after 2-6 hours co-incubation of the NPs with SKOV3 cells. Moreover, compared to NPs without cell membrane wrapping, the ZrTCP@siCtrl-Cy5.5@CM NPs enveloped by SKOV3 cell membranes exhibited a significant increase in intracellular NP fluorescence intensity after the same duration of incubation with SKOV3 cells (Figures 27A, B, and D). In contrast to free

ICG fluorescent dye, the ICG@ZIF-8 NPs showed less intracellular ICG fluorescence intensity after 6 hours of co-incubation with glioblastoma U87MG cells. However, ICG-NPs coated with Tf-PEG-PLGA demonstrated a significant enhancement in intracellular ICG fluorescence intensity after 6 hours of co-incubation with U87MG cells (Figures 27C and E). These results indicate that MOFs represented by ZrTCP and ZIF-8 exhibit efficient cellular phagocytosis, and modifications such as cell membrane or polymer coatings can enhance the cellular uptake of these types of NPs.

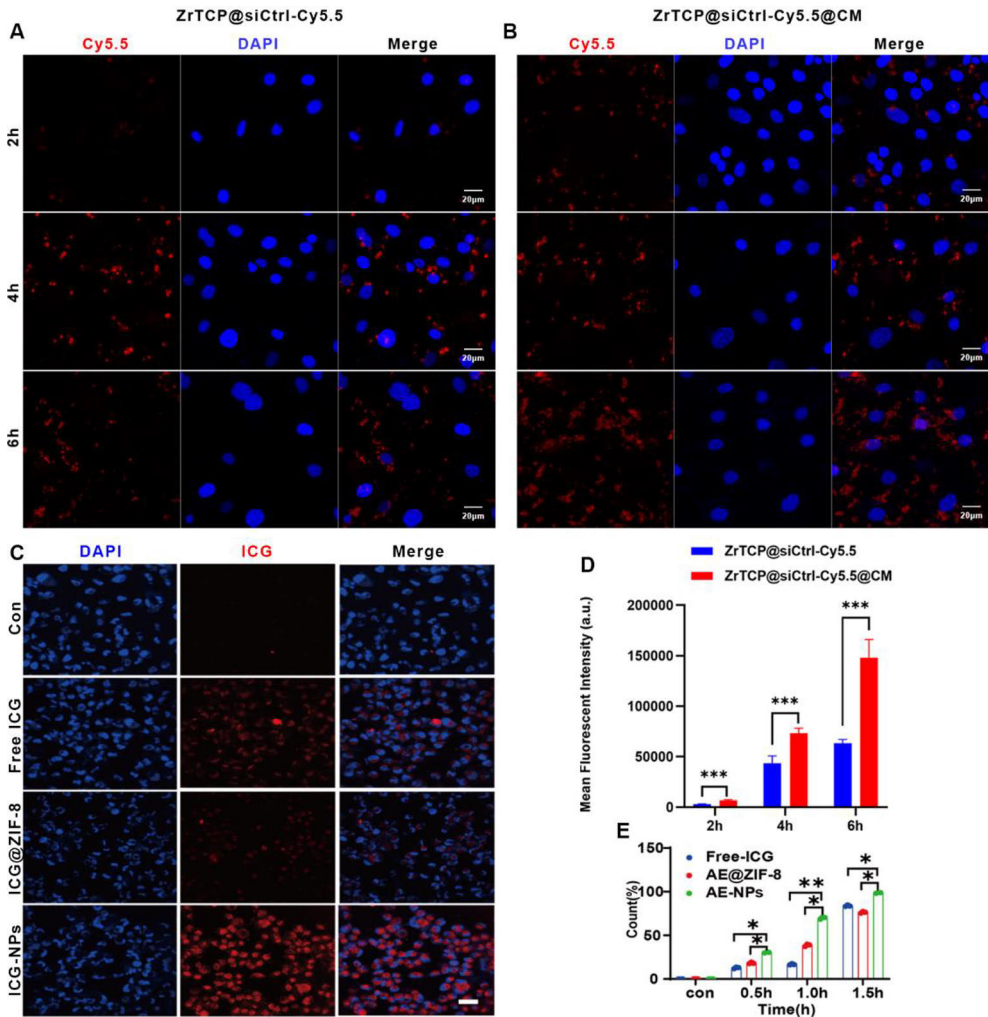


Figure 27. Cell uptake of ZrTCP and ZIF-8 NPs. Representative confocal images (A and B) and quantitative data (D) of Cy5.5 positive SKOV3 cells after 24 hours incubation with siCtrl-Cy5.5 loaded ZrTCP NPs; Representative confocal images (C) and flow cytometry analysis results (E) of ICG positive cells after incubation with free ICG or ICG labeled ZIF-8 NPs. Scale bars are as follows: 20 μ m in A and B; 200 μ m in C. Data in D and E are presented as mean \pm SD from three independent experiments; * $P < 0.05$, ** $P < 0.01$, *** $P < 0.001$.

5.4.2.2. Lysosomal escape

Subsequently, the assessment of the capability of MOFs to escape from lysosomes was evaluated by using ZrTCP NPs as an example. Observations from fluorescence confocal microscopy revealed that after co-incubation with SKOV3 cells, the ZrTCP@siCtrl-Cy5.5@CM NPs primarily distributed within the cytoplasm. However, the green fluorescence signal of the lysosomal probe LysoTracker did not overlap with the red fluorescence signal of the NPs. This was also independent of the duration of incubation (Figures 28A and B). These results suggest that ZrTCP@siCtrl-Cy5.5@CM NPs possess a strong ability to escape from lysosomes. Alternatively, the pathway for ZrTCP@siCtrl-Cy5.5@CM NPs entering the cells might not rely on the conventional endocytic pathways. However, further research is needed to confirm these findings.

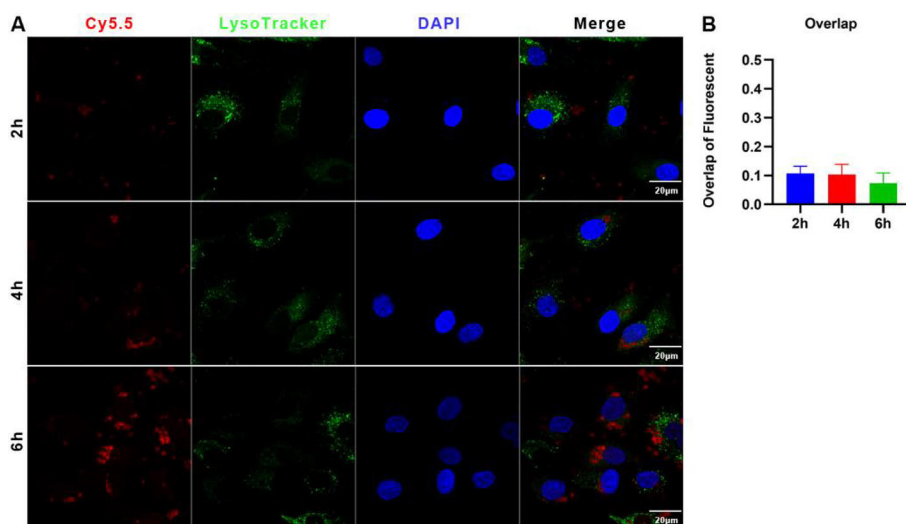


Figure 28. Lysosomal escape of ZrTCP NPs in SKOV3 cells. A. Representative confocal images of SKOV3 cells after incubation with ZrTCP@siCtrl-Cy5.5@CM NPs; B. Overlap analysis of the red Cy5.5 and green LysoTracker fluorescence signals in A. Scale bar in A are 20 μ m. Data in B are presented as mean \pm SD from three independent experiments.

5.4.3. GelMA microhydrogel preparation and characterization

The strategy of encapsulating NPs in GelMA hydrogel microspheres for *in situ* injection was also applied in the precise treatment of cancer using ZrTCP NPs. In this work, ZrTCP@siFOXK2@CM NPs were co-encapsulated with the diabetes medicine Metformin within GelMA microspheres. When the GelMA microspheres gradually released Metformin and ZrTCP@siFOXK2@CM NPs into cells, the Metformin and FOXK2 siRNA within the NPs synergistically targeted the metabolic pathways of the tumor cells. As shown in Figure 29, after 48 hours of combined treatment with Metformin and ZrTCP@siFOXK2@CM the cell viabilities of SKOV3 and OVCAR3 cells were significantly decreased (Figures 29 A and B). ZrTCP@siFOXK2/Met@CM@GelMA microspheres of various sizes were successfully fabricated by using microfluidic technology (Figures 29 C-E).

These GelMA microspheres demonstrated effective drug release with time-dependent degradation (Figures 29 F and G). Furthermore, the ZrTCP@siFOXK2/Met@CM@GelMA microspheres exhibited potent anti-tumor effects both in cells and in mice under the influence of 650 nm laser treatment (Figures 30 and 33).

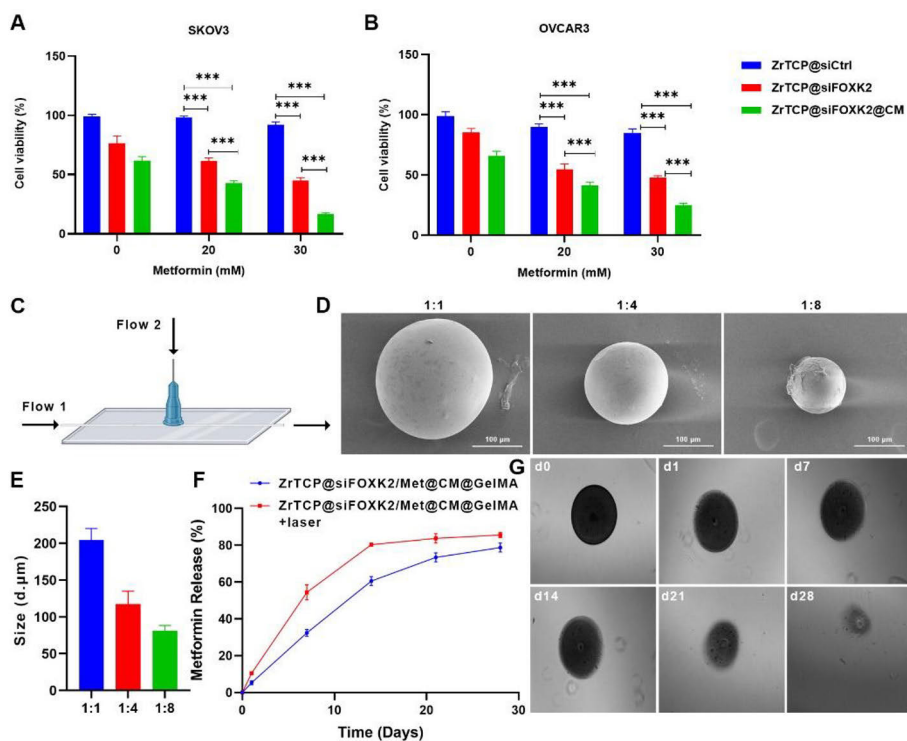


Figure 29. Synthesis and release dynamics of ZrTCP@siFOXK2/Met@CM@GelMA. A, B. Cell viabilities after 48 hours treatment with different ZrTCP NPs; C-E. Schematic of microfluidic chip for the preparation, representative SEM images and particle size of ZrTCP@siFOXK2/Met@CM@GelMA microspheres synthesized using varying external (flow2: 5% Span 80 in mineral oil) and internal (flow1: mix of NPs, metformin, and GELMA) flow rates; F. Release profiles of metformin from the microspheres in PBS buffer, with/without 980 nm laser irradiation (1 W/cm^2 , 10 min); G. Representative microscope images of ZrTCP@siFOXK2/Met@CM@GelMA microspheres in 28 days. Scale bar in D is 100 μm . Data in A, B, E and F are presented as mean \pm SD from three independent experiments; * $P < 0.05$, ** $P < 0.01$, *** $P < 0.001$.

5.4.4. In vitro anti-tumor activity

5.4.4.1. Cell growth inhibition

The findings in this work demonstrate that tumor cells exhibit a high phagocytic efficiency towards MOFs, and these MOFs also exhibit excellent lysosomal escape capabilities within cells. The cytotoxicity of MOFs and their drug-loaded counterparts in combating tumor cells at the cellular level were further assessed.

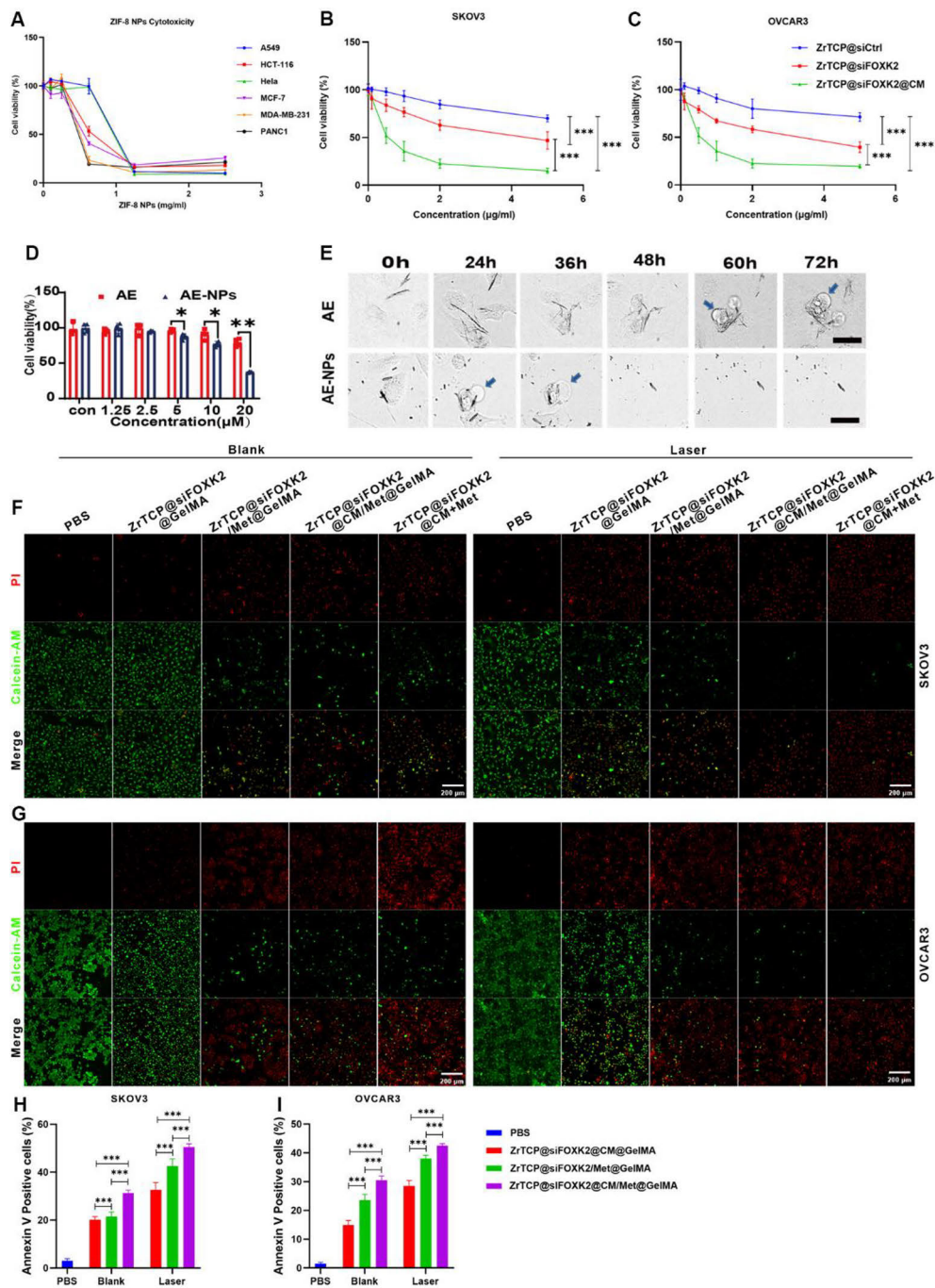


Figure 30. Cell survival inhibition by drug loaded ZIF-8 and ZrTCP NPs. Cell viabilities (A-D), and representative microscope images (E) of cells after incubation with different ZIF-8 and ZrTCP NPs; Representative confocal microscope images of Calcein-AM/PI stained cells (F and G) and cell apoptosis analysis (H and I) of cells after incubation with ZrTCP NPs based GelMA microspheres with/without laser irradiation. Scale bar=200 μm in E, F and G. Data in A-D and H-I are presented as mean ± SD from three independent experiments.

Initially, the cytotoxicity of empty ZIF-8 NPs was tested to determine the safe concentration for their use. As shown in Figure 30A, after co-incubation with various tumor cells for 48 hours, the ZIF-8 NPs at a concentration of 0.625 mg/ml significantly decreased the cell viabilities of HCT-116 colon cancer cells, MCF-7 breast cancer cells, MDA-MB-231 cells, and PANC1 pancreatic cancer cells. Additionally, the cell viabilities of A549 lung cancer cells and HeLa cervical cancer cells were significantly suppressed at a concentration of 1.25 mg/ml of ZIF-8 NPs. These results indicate that empty ZIF-8 NPs at low concentrations (less than 0.625 mg/ml) do not exhibit significant cytotoxicity to tumor cells. Subsequently, the cytotoxicity of ZrTCP NPs loaded with siFOXK2 RNA and ZIF-8 NPs loaded with AE, as well as their anti-tumor effectiveness at the cellular level were examined. As depicted in Figure 29, the ZrTCP@siFOXK2 NPs carrying RNA for silencing the FOXK2 tumor gene did significantly inhibit the survival of SKOV3 and OVCAR3 cells. Moreover, when encapsulated with the cell membrane of SKOV3 cells, the ZrTCP@siFOXK2@CM NPs showed a notably enhanced inhibitory effect on cell survival (Figures 30 B and C). Additionally, co-incubation of U87MG cells with 5 μ M AE-NPs for 24 hours caused a significant reduction in cell survival and noticeable pyroptotic-like changes in cell morphology (Figures 30 D and E). These results suggest that both ZrTCP NPs carrying therapeutic RNA and ZIF-8 NPs loaded with AE significantly suppress the survival of specific tumor cells.

Furthermore, to enhance the anti-tumor efficacy of ZrTCP@siFOXK2 NPs, the same strategy used for Au@MSN-Ter/THPP@CM@GelMA/CAT microspheres was adopted. This involved encapsulating ZrTCP@siFOXK2 NPs within GelMA microspheres which also contained the FDA-approved diabetes medicine Metformin to synergistically target tumor cell metabolic pathways for cancer treatment (Figure 30). The anti-tumor efficacy of the prepared ZrTCP@siFOXK2/Met@GelMA microspheres was then assessed at the cellular level by using Calcein-AM/PI dual staining and flow cytometric apoptosis assays. As shown in Figures 30F-I, the ZrTCP@siFOXK2/Met@GelMA microspheres significantly enhanced apoptosis in SKOV3 and OVCAR3 cells. The combined use of 650 nm laser irradiation further augmented their apoptosis-inducing effect. This study essentially confirms the synergistic anti-tumor actions of siFOXK2 and Metformin, as well as the photodynamic anti-tumor effect produced by the photosensitizer TCPP within the ZrTCP NPs, which can be activated by 650 nm laser light.

5.4.4.2. Induced gene therapy

The concept of using MOFs for gene therapy for precision cancer therapy was further explored in this work. As depicted in Figure 31, EGFP mRNA was loaded into ZIF-8 NPs and FOXK2 siRNA into ZrTCP NPs. These Nps were then co-incubated with cells. After 48 hours, the HeLa cells co-incubated with mEGFP&PLR@ZIF-8 NPs exhibited substantial expression of green fluorescent protein (Figure 31A). Meanwhile, the cell viability of SKOV3 and OVCAR3 cells significantly decreased after 48 hours of co-incubation with ZrTCP@siFOXK2 NPs and Metformin (Figures 29 A and B). At the cellular level, the combined treatment with siFOXK2 and Met led to a noticeable downregulation of FOXK2 gene expression and a significant reduction in cell viability (Figures 31B-D).

These results indicates that the MOFs successfully delivered mRNA and siRNA into the cells, thus achieving RNA-based gene expression and gene silencing.

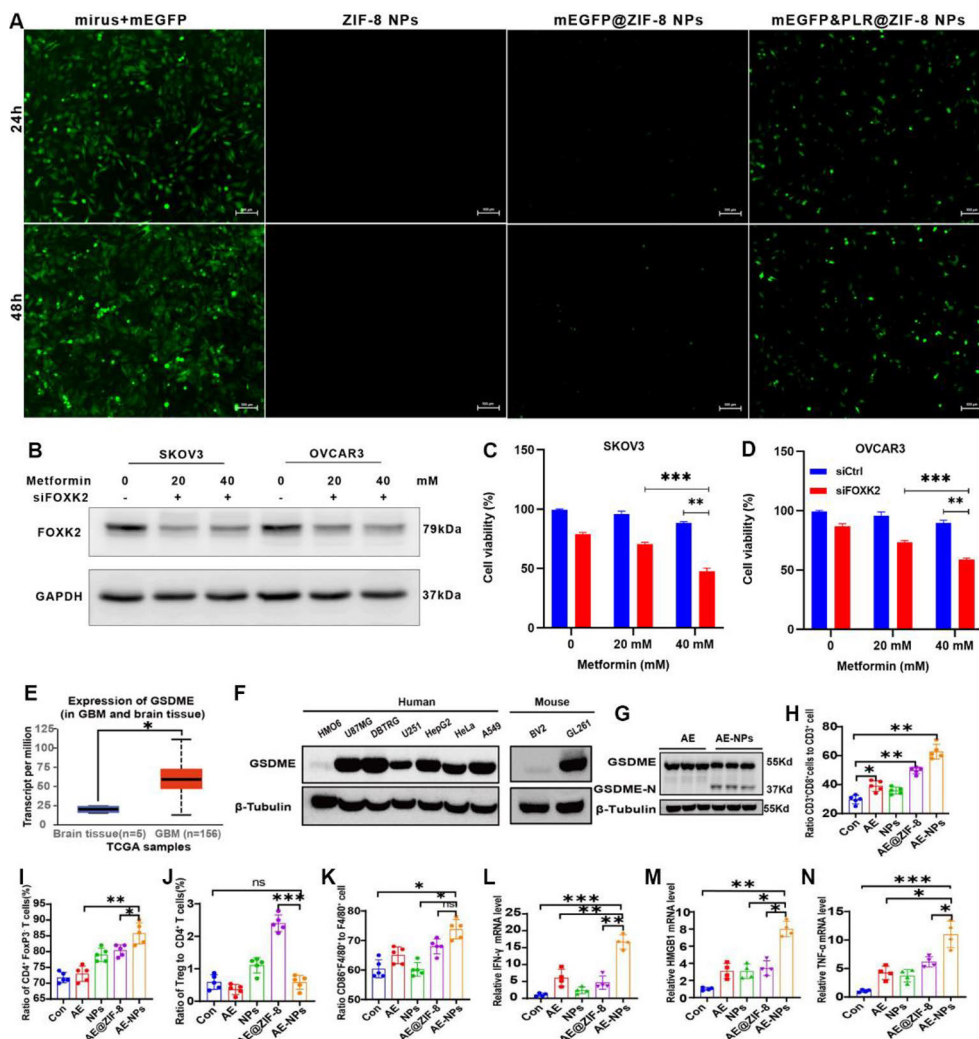


Figure 31. ZIF-8 and ZrTCP NPs for RNA and targeted molecular intracellular delivery. A. Representative fluorescence microscope images of HeLa cells after incubation with EGFP mRNA loaded ZIF-8 NPs; FOXK2 expression analysis (B) and cell viabilities (C and D) following a 48-hours treatment with metformin and FOXK2 siRNA; E, F. GSDME expression in GBM cancer and cancer cells; G. GSDME expression in U87MG cells after treatment with AE or AE loaded ZIF-8 NPs; Flow cytometry analysis of T cells (H-K) and q-PCR analysis of immune-related biomarker (L-N) changes in tumor tissues; Scale bar in A is 100 μ m. Data in C-E and H-N are presented as mean \pm SD from three independent experiments; * $P < 0.05$, ** $P < 0.01$, *** $P < 0.001$.

5.4.4.3. Activation of the cell pyroptosis pathway

Previously when utilizing ZIF-8 NPs to deliver AE for the treatment of glioblastoma, they were initially encapsulated with Tf-PEG-PLGA polymer. This successfully achieved targeted delivery to glioblastoma cells (Figures 27 and

32). The reason for loading AE into ZIF-8 NPs was primarily due to the ability of AE to activate the pyroptotic pathways in glioblastoma cells, thereby promoting cell pyroptosis (Figure 31E). As shown in Figure 31, the AE-induced pyroptosis was mainly dependent on the activation of the GSDME pyroptotic signaling pathway (Figures 31E-G). The use of ZIF-8 NPs for the delivery of AE also successfully induced pyroptosis in glioblastoma cells at the animal level (Figures 31H-L). Moreover, AE-NPs also activated the immune status within the glioblastoma tumor microenvironment, thereby showing high potential to be used in immunotherapy for glioblastoma (Figures 31H-N).

5.4.5. Biodistribution and *in vivo* anti-tumor activity

5.4.5.1. *In vivo* biodistribution

So far, this work has confirmed the anti-tumor activity of drug-loaded ZrTCP and ZIF-8 NPs at the cellular level. To validate their anti-tumor efficacy *in vivo* requires an examination of their distribution in the body following intravenous tail injection or *in situ* injection.

As illustrated in Figures 32A and B where a mouse tumor model developed from subcutaneous implantation of SKOV3 cells were used, a high concentration of ZrTCP@siFOXK2@CM NPs was detected in mouse tumor tissues just 24 hours after intravenous tail injection or *in situ* injection of ZrTCP@siFOXK2@CM/Met@GelMA. However, a significant accumulation of intravenously injected ZrTCP@siFOXK2@CM NPs was also observed in the liver and kidney tissues of mice. In contrast, *in situ* injected ZrTCP@siFOXK2@CM/Met@GelMA NPs resulted only in partial accumulation in the kidneys, and these NPs persisted in the tumor tissue for up to 15 days after a single tumor injection.

The distribution of ICG-labeled ZIF-8 NPs in a mouse model of glioma following intravenous tail injection was simultaneously tested. Analysis of the mouse brain tissue and major organs (heart, liver, spleen, lung, kidney) through *in vivo* imaging (Figures 32C-E) showed that the free ICG dye, ICG@ZIF-8 NPs, and ICG-NPs accumulated in large amounts in the brain tissue within 15 minutes post-injection. Notably, ICG-NPs persisted in significant amounts for at least 24 hours, while ICG@ZIF-8 NPs remained in the brain tissue for 12 hours, which was longer than the 6 hours for the free ICG dye. Moreover, the accumulation of ICG-NPs in the brain tissue was markedly higher than that of ICG@ZIF-8 NPs. However, all three materials extensively accumulated in the liver, lungs, and kidneys post-injection. Further brain tissue slice analysis (Figure 32F) revealed that ICG was widely distributed in both brain and tumor tissues in the free ICG injection group. In contrast, the ICG fluorescence signals in the ICG@ZIF-8 and ICG-NP groups were primarily concentrated in the tumor tissue areas, with the ICG-NPs group showing a more pronounced distribution in tumor tissues.

These results indicate that MOFs injected intravenously can rapidly accumulate in tumor tissues, but also extensively in the liver and kidneys, which is a major metabolic pathway for most intravenously injected NPs in the body. However, it was also found that *in situ* injection of GelMA microspheres significantly enhanced the retention and persistence of ZrTCP NPs in tumor

tissues. Furthermore, Tf-PEG-PLGA-coated ZIF-8 NPs (ICG-NPs) demonstrated significantly enhanced accumulation and persistence in brain tissues. This suggests that Tf-PEG-PLGA coating effectively enhances their ability to breach the blood-brain barrier and target glioma cells.

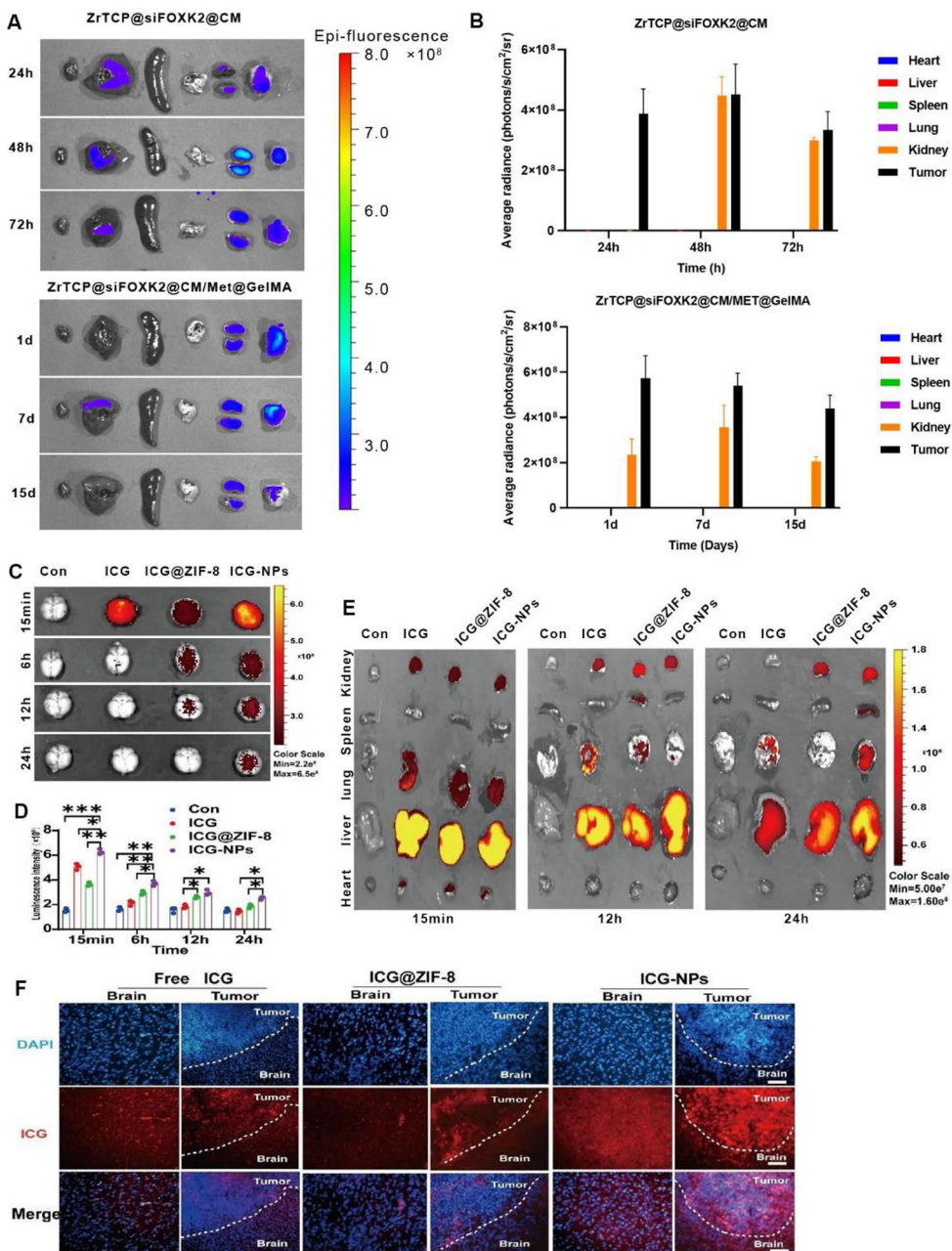


Figure 32. In vivo biodistribution of different ZrTCP NPs and ZIF-8 NPs. A, B. Representative IVIS images and corresponding quantitative data of mice main organs at indicated time points by tail vein injection of ZrTCP@siFOXK2@CM and post-intratumoral injection of ZrTCP@siFOXK2@CM/Met@GelMA; C-E. Representative IVIS images and corresponding quantitative data of mice brain and main organs at indicated time point by tail vein injection of different ZIF-8 formulations; F. Representative confocal microscope images of brain slices after 6 hours of tail vein injection of different ZIF-8 formulations. Scale bar in F is 200 μ m. Data in B and D are presented as mean \pm SD from three independent experiments.

5.4.5.2. Anti-tumor activity in animal models

Next, the *in vivo* anti-tumor efficacy of various MOF formulations in mice were evaluated. The anti-tumor effects of ZrTCP NPs were initially tested in a subcutaneous tumor model in mice using SKOV3 cells. As depicted in Figure 31, significant tumor growth inhibition was observed following *in situ* injection of ZrTCP@siFOXK2/Met@CM@GelMA or equivalent doses of ZrTCP@siFOXK2@CM and Met via tail vein injection, coupled with selective 650 nm laser irradiation in the tumor area of mice every three days for 18 consecutive days. Treatments with ZrTCP@siFOXK2/Met@CM@GelMA, ZrTCP@siFOXK2/Met@CM+laser, ZrTCP@siFOXK2/Met@GelMA+laser, and ZrTCP@siFOXK2/Met@CM@GelMA+laser all significantly curbed tumor growth, with the latter three demonstrating a more pronounced effect compared to the ZrTCP@siFOXK2/Met@CM@GelMA group alone (Figures 33A and B). Analysis of tumor tissues through FOXK2 immunohistochemistry, H&E, Ki67, and TUNEL staining revealed extensive damage and necrosis in tumors treated with these formulations, particularly notable in the ZrTCP@siFOXK2/Met@GelMA+laser and ZrTCP@siFOXK2/Met@CM@GelMA+laser groups. Furthermore, a significant reduction in FOXK2 gene expression was observed in tumor tissues across all treatment groups, with the lowest levels in the ZrTCP@siFOXK2/Met@CM@GelMA and ZrTCP@siFOXK2/Met@CM@GelMA+laser groups (Figures 33C-G). These results indicate that ZrTCP NPs successfully delivered the FOXK2 gene to tumor cells, producing a significant combined anti-tumor effect under the influence of 650 nm laser irradiation.

Subsequently, *in vivo* experiments on a GL261 cell orthotopic glioma mouse model (TU 33H-L) demonstrated that both free AE and AE-NPs significantly inhibited tumor growth. However, the tumor growth inhibition caused by AE was likely primarily through inducing tumor tissue necrosis. Additionally, a significant increase in survival rates in mice treated with free AE, AE@ZIF-8, and AE-NPs was observed. This indicates that drug-loaded ZIF-8 NPs not only suppress the growth of gliomas, but also significantly improve the survival status of mice.

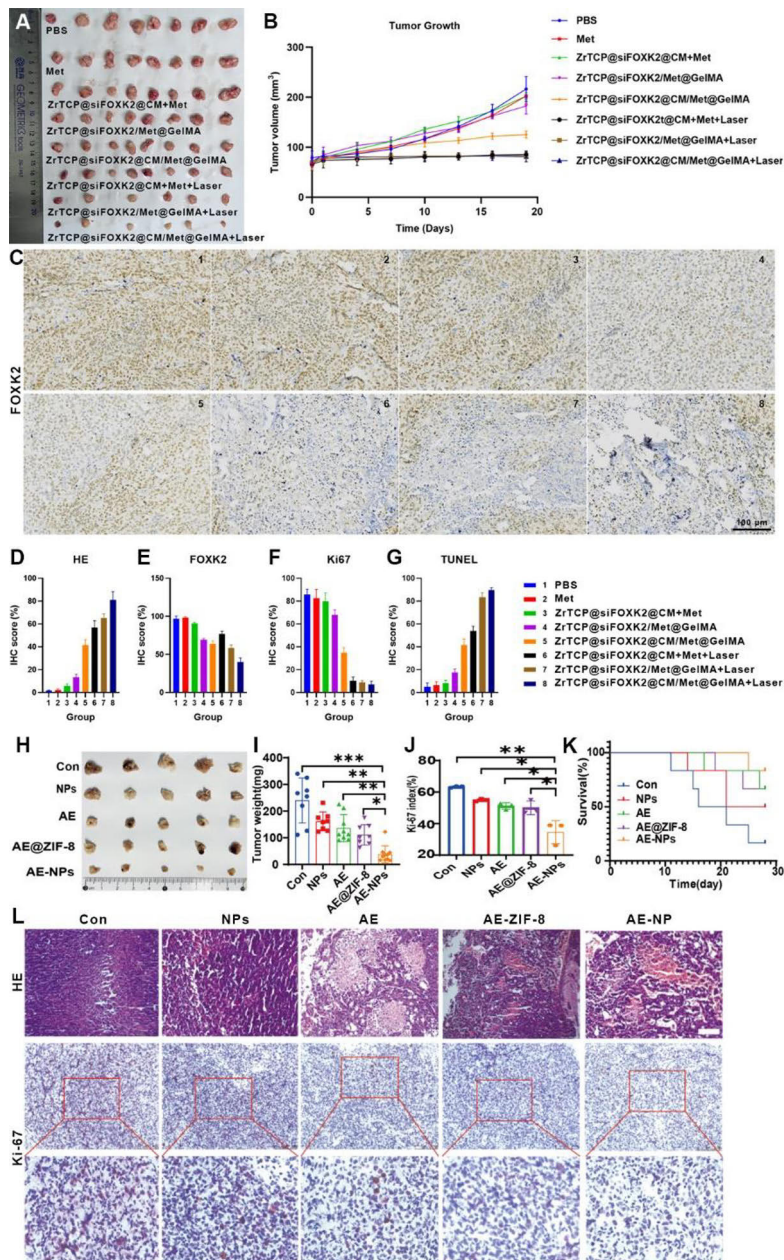


Figure 33. Antitumor efficacy of different drug loaded ZrTCP and ZIF-8 NPs formulations. Representative tumour tissues (A), tumor growth curves (B), representative FOXX2 stain images (C), HE stain score (D), FOXX2 stain score (E), Ki67 stain score (F) and TUNEL stain score (G) of tumor tissues after treatment with different ZrTCP NP formulations; Representative tumour tissues (H), tumor weight (I), Ki67 index (J), mice survival curve (K), and representative images of tumor slices with HE and Ki67 (L) staining after treatment with different ZIF-8 NP formulations. Scale bars are as follow: 100 μ m in C; 200 μ m in L. Data are presented as mean \pm SD from three independent experiments; * $P < 0.05$, ** $P < 0.01$, *** $P < 0.001$.

5.4.5.3. Safety assessment and biocompatibility

Finally, examination of the major organs and blood biochemical markers of the test mice were conducted to better assess the potential *in vivo* toxicity of MOFs. The results, as shown in Figures 34A and B, indicated that neither *in situ* injection of ZrTCP@siFOXK2/Met@CM@GelMA microspheres nor intravenous injection of ZrTCP@siFOXK2@CM and various ZIF-8 NPs caused any noticeable damage to the major organs of the mice. However, intravenous injection of free AE did result in a certain degree of liver damage. Changes in the key markers for liver and kidney damage, such as ALT, AST, γ -GT, BUN, and CRE, suggest that intravenous injection of free AE and AE@ZIF-8 NPs caused varying levels of damage to liver and kidney functions. In contrast, AE-NPs effectively avoided causing damage to the liver and kidney functions.

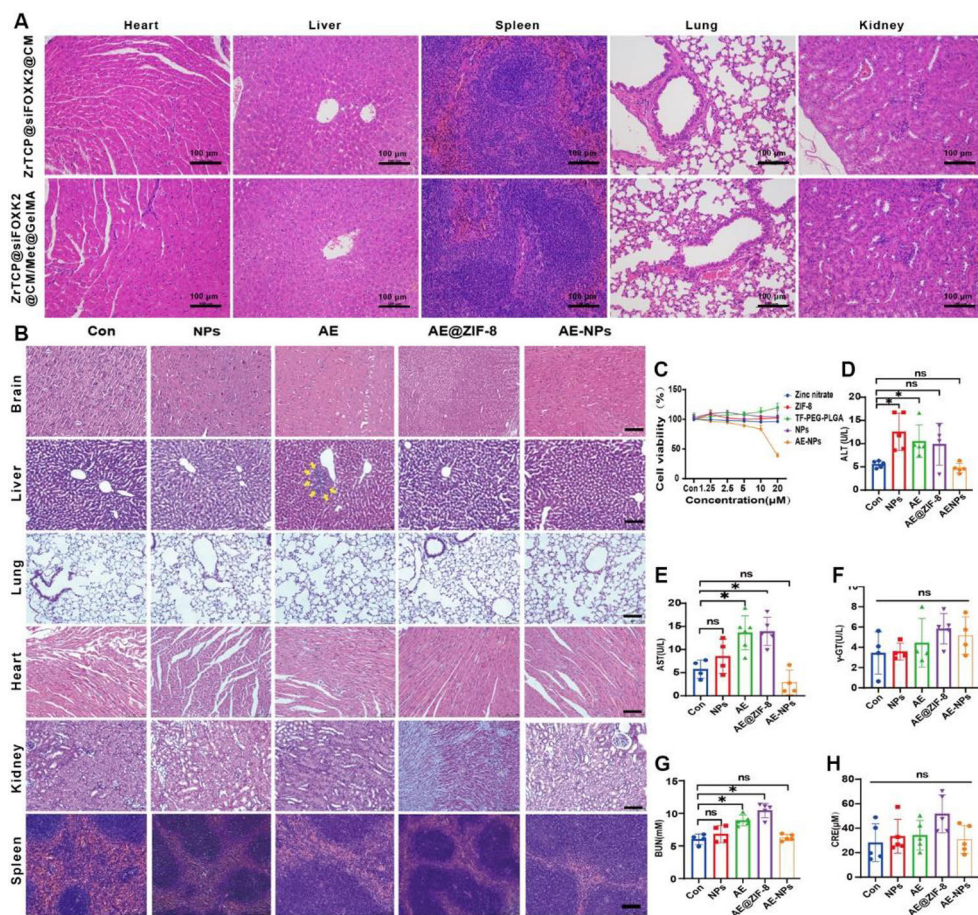


Figure 34. *In vivo* cytotoxicity of different ZrTCP and ZIF-8 NP formulations. Representative HE stain images of main organs after treatment with different ZrTCP (A) or ZIF-8 (B) NPs formulations; Cell viability of U87MG cells (C) and mouse serum main biomarker changes (D-H) after treatment with different ZIF-8 nanoformulations. Scale bar in A and B are 100 μ m. Data in C-H are presented as mean \pm SD from three independent experiments; * $P < 0.05$, ** $P < 0.01$, *** $P < 0.001$.

6. Conclusion and future perspectives

6.1. Summary of key findings

This thesis is a comprehensive study that demonstrates the utilization of MSNs and MOFs to synthesize and fabricate various multifunctional, combined drug delivery carriers targeting tumor cells through intelligent structural designs. These carriers not only achieve multi-modal tumor treatment combining PDT, PTT, chemotherapy, and gene therapy, but also enable controlled drug release, and synergistic tumor treatment through meticulous structural design. The main aspects in this thesis are summarized as follows.

One of the key achievements of the research in this thesis is the development of a multifunctional nanocarrier, capable of enhancing drug loading, targeting specificity, and reducing systemic toxicity. Specifically, the development of the photothermal/temperature-responsive nanoplatfrom for the treatment of TNBC, effectively integrating photothermal therapy with combined chemotherapy treatment strategies. Additionally, the biomimetic nano@microgel systems developed for the treatment of ovarian cancer enhanced the photodynamic responses and photothermal conversion, resulting in significant anti-tumor effects.

Another notable achievement is the smart designs of various drug delivery systems. In particular, the ZrTCP@siFOXK2@CM/Met@GelMA hydrogel microspheres that were developed and demonstrated in use for ovarian cancer treatment. This novel strategy facilitated dual delivery of Metformin and FOXK2 siRNA, and targeting the metabolic pathways of cancer cells which significantly inhibited tumor growth. This thesis also explores the use of aloe-emodin (AE) to induce cell death in GBM cells and the enhancement of blood-brain barrier penetration through AE@ZIF-8/Tf-PEG-PLGA NPs, thus demonstrating the multifunctionality and efficacy of these nanocarriers. Moreover, the potential application of ZIF-8 NPs as intracellular messengers for RNA delivery was studied and discussed.

Overall, this thesis comprehensively analyzes the potential of porous nanomaterials in cancer therapy. In-depth investigations were conducted in the synthesis, characterization, and application of these NPs as drug delivery vehicles, highlighting their efficiency in co-delivering drugs, their capability of controlled drug release, and responsiveness to specific tumor conditions. These findings paves a new path for the use of nanomaterials in cancer treatment and offers fresh opportunities and possible solutions for precision oncology.

6.2. Future directions and recommendations

With the continuous advancement of medical nanomaterials technology, its potential in the field of precise cancer treatment is increasingly apparent. Especially in the aspect of drug delivery, the development of nanomaterials is constantly promoting the research and application of nanomedicine for precise

cancer treatment. Porous nanomaterials, as a special type of nanomaterials, are expected to play a significant role in precise cancer treatment.

Firstly, porous nanomaterials have broad applications in the *in vivo* delivery of nucleic acid drugs. Small molecules of nucleic acid drugs, with their remarkable specificity and effectiveness, have become an ideal choice for personalized cancer treatment. However, their clinical application is limited by factors such as instability and biological membrane barriers. Porous nanomaterials, with their high specific surface area and good biocompatibility, provide an effective carrier for the delivery of nucleic acid drugs. Nevertheless, it should be noted that the current loading methods may lead to the exposure and degradation of drug fragments. Therefore, optimizing the performance of porous nanomaterials through structural design and surface modification will be the key to promoting their application in nucleic acid drug delivery.

Secondly, porous nanomaterials are expected to provide effective transport carriers for specific drug delivery to brain tumors. The special physiological structure of the blood-brain barrier has always been a challenge in drug treatment for brain tumors. The customizable preparation characteristics and abundant surface-active groups of porous nanomaterials enable them to be specifically modified (such as with tumor-specific antibodies or blood-brain barrier-specific receptors) and tailored to specific sizes for targeted drug delivery to brain tumor tissues. This opens up new possibilities for the treatment of brain tumors.

Thirdly, porous nanomaterials also show great potential in the treatment of solid tumor tissues. The density of solid tumors and the encapsulation of external collagen make it difficult for drugs or conventional nanocarriers to penetrate. However, porous nanomaterials, with their strong drug-loading capacity and modifiable surface, can be designed as targeted delivery carriers for solid tumors. Through approaches like cascade reactions, they can first disrupt the dense outer structure of tumor tissues and then release the drugs to exert their therapeutic effects.

Acknowledgements

The research work presented in this doctoral thesis was mainly undertaken at the Pharmaceutical Sciences Laboratory (PSL) of Åbo Academic University and the Turku Bioscience Center between October 2019 and January 2024. I am immensely grateful to the funding provided by Shanghai Fengxian District Central Hospital, China Scholarship Council, and Åbo Academic University, which has been pivotal in supporting my research works.

First and foremost, I would like to extend my heartfelt gratitude to my supervisor, Professor Hongbo Zhang. Thank you for your gentle and patient mentorship and your tireless teaching. Your scholarly demeanor has been a guiding light throughout my scientific journey, inspiring me to advance relentlessly and strive for excellence. I am also immensely grateful for the substantial support you have provided in my everyday life, allowing me to dedicate myself fully to my studies and work, while enjoying a fulfilling life experience in Finland.

Secondly, I am profoundly grateful for the exceptional guidance and support provided by my co-supervisors, Professor Jing Feng and Professor Tapani Viitala. Professor Feng, your steadfast support and selfless commitment to both my academic and personal development have been transformative. I am eternally grateful for your guidance and encouragement. Professor Viitala, your significant contributions to my research at Åbo Akademi University have crucially shaped the outcomes of this dissertation. Your patience, expertise, and insightful guidance throughout my research project and academic planning have been invaluable.

Furthermore, my heartfelt appreciation goes to Professor Jessica M. Rosenholm for your consistent support, patient mentorship, and critical contributions to my daily academic endeavors and the successful completion of this doctoral dissertation. Your ongoing guidance and generous assistance have been pivotal to my academic journey and have profoundly influenced my professional development.

Additionally, I am thankful for the opportunity to have collaborated with extraordinary individuals whose input has been critical to my research. I extend my sincerest thanks to Chang, Xiaoyu, Xiaodong, and Jixiang for their invaluable support, guidance, and collaborative spirit. Your expertise and assistance have been vital in achieving the research outcomes detailed in this dissertation, and I deeply value our partnership.

I also want to express my profound gratitude to the remarkable team at the PSL group, including D.K., Wali, Oliver, Ezgi, Rawand, Fadak, Rathna, Alaa, Sofia, Yonghui, Jiaqi, Meixin, Yunru, Chengcheng, Wu Yang, Shengyi, Fanny, Jessica, Joni, Qingbo, Shujun, Yu Chen, Yu Zhang, and Pengzhen. Your camaraderie, support, and collaborative efforts have created an outstanding work environment that has been fundamental to my research success. I am thankful for your contributions and fervently wish for the PSL group's continued success and prosperity. I am also deeply thankful to my friends in Finland, especially Li Chen,

Hao Lu, Han Jin and Qin Shang, whose warmth and kindness have made my experience of life here truly wonderful.

Lastly, I extend my deepest and most heartfelt thanks to my parents for their constant love, support, and encouragement throughout my academic journey. Special recognition is due to my wife, Shuqin, for your steadfast support, understanding, and companionship. To our beloved child, Zhaoyang, you are the brightest light in our lives and the source of immense joy. I love you all deeply and am endlessly grateful for your presence in my life.

Turku, 2024

Wenhui Zhou

References

- Aghebati-Maleki, A., Dolati S., Ahmadi M., Baghbanzhadeh A., Asadi M., Fotouhi A., Yousefi M., Aghebati-Maleki L., 2020. Nanoparticles and cancer therapy: Perspectives for application of nanoparticles in the treatment of cancers. *J Cell Physiol.* 235, 1962-1972. <https://doi.org/10.1002/jcp.29126>
- Alvarez, P., Marchal J. A., Boulaiz H., Carrillo E., Velez C., Rodriguez-Serrano F., Melguizo C., Prados J., Madeddu R., Aranega A., 2012. 5-Fluorouracil derivatives: a patent review. *Expert Opin Ther Pat.* 22, 107-123. <https://doi.org/10.1517/13543776.2012.661413>
- Anand, U., Dey A., Chandel A. K. S., Sanyal R., Mishra A., Pandey D. K., De Falco V., Upadhyay A., Kandimalla R., Chaudhary A., Dhanjal J. K., Dewanjee S., Vallamkondu J., Perez de la Lastra J. M., 2023. Cancer chemotherapy and beyond: Current status, drug candidates, associated risks and progress in targeted therapeutics. *Genes Dis.* 10, 1367-1401. <https://doi.org/10.1016/j.gendis.2022.02.007>
- Baeza, A., Ruiz-Molina D., Vallet-Regi M., 2017. Recent advances in porous nanoparticles for drug delivery in antitumoral applications: inorganic nanoparticles and nanoscale metal-organic frameworks. *Expert Opin Drug Deliv.* 14, 783-796. <https://doi.org/10.1080/17425247.2016.1229298>
- Barkat, A., Beg S., Panda S. K., K.S. A., Rahman M., Ahmed F. J., 2021. Functionalized mesoporous silica nanoparticles in anticancer therapeutics. *Semin Cancer Biol.* 69, 365-375. <https://doi.org/10.1016/j.semcancer.2019.08.022>
- Bender, E., 2018. Regulating the gene-therapy revolution. *Nature.* 564, S20-S22. <https://doi.org/10.1038/d41586-018-07641-1>
- Benová, E., Hornebecq V., Zelenák V., Huntosová V., Almási M., Mácajová M., Bergé-Lefranc D., 2021. pH-responsive mesoporous silica drug delivery system, its biocompatibility and co-adsorption/co-release of 5-Fluorouracil and Naproxen. *Appl Surf Sci.* 561, <https://doi.org/ARTN150011> 10.1016/j.apsusc.2021.150011
- Cesur-Ergun, B., Demir-Dora D., 2023. Gene therapy in cancer. *J Gene Med.* 25, e3550. <https://doi.org/10.1002/jgm.3550>
- Chen, M., Mao A., Xu M., Weng Q., Mao J., Ji J., 2019. CRISPR-Cas9 for cancer therapy: Opportunities and challenges. *Cancer letters.* 447, 48-55. <https://doi.org/10.1016/j.canlet.2019.01.017>
- Chen, X., Liu Z., 2016. Dual responsive mesoporous silica nanoparticles for targeted co-delivery of hydrophobic and hydrophilic anticancer drugs to tumor cells. *J Mater Chem B.* 4, 4382-4388. <https://doi.org/10.1039/c6tb00694a>
- Cheng, R., Meng F., Deng C., Klok H. A., Zhong Z., 2013. Dual and multi-stimuli responsive polymeric nanoparticles for programmed site-specific drug delivery. *Biomaterials.* 34, 3647-3657. <https://doi.org/10.1016/j.biomaterials.2013.01.084>
- Cheng, Z., Li M., Dey R., Chen Y., 2021. Nanomaterials for cancer therapy: current progress and perspectives. *J Hematol Oncol.* 14, 85. <https://doi.org/10.1186/s13045-021-01096-0>
- Chiappetta, M., Sessorossi C., Cusumano G., 2023. Surgery for Non-Small Cell Lung Cancer in the Personalized Therapy Era. *Curr Oncol.* 30, 7773-7776. <https://doi.org/10.3390/curroncol30080563>
- Collins, F. S., Gottlieb S., 2019. The Next Phase of Human Gene-Therapy Oversight. *N Engl J Med.* 380, 402. <https://doi.org/10.1056/NEJMc1815776>
- Das, S. K., Menezes M. E., Bhatia S., Wang X. Y., Emdad L., Sarkar D., Fisher P. B., 2015. Gene Therapies for Cancer: Strategies, Challenges and Successes. *J Cell Physiol.* 230, 259-271. <https://doi.org/10.1002/jcp.24791>
- Dasari, S., Tchounwou P. B., 2014. Cisplatin in cancer therapy: molecular mechanisms of action. *Eur. J. Pharmacol.* 740, 364-378.

- <https://doi.org/10.1016/j.ejphar.2014.07.025>
- Debnath, S. K., Srivastava R., 2021. Drug Delivery With Carbon-Based Nanomaterials as Versatile Nanocarriers: Progress and Prospects. *Front Nanotechnol.* 3, <https://doi.org/ARTN10.3389/fnano.2021.644564>
- Demir Duman, F., Forgan R. S., 2021. Applications of nanoscale metal-organic frameworks as imaging agents in biology and medicine. *J Mater Chem B.* 9, 3423-3449. <https://doi.org/10.1039/d1tb00358e>
- Derdeyn, C. P., Chimowitz M. I., Lynn M. J., Fiorella D., Turan T. N., Janis L. S., Montgomery J., Nizam A., Lane B. F., Lutsep H. L., Barnwell S. L., Waters M. F., Hoh B. L., Hourihane J. M., Levy E. I., Alexandrov A. V., Harrigan M. R., Chiu D., Klucznik R. P., Clark J. M., McDougall C. G., Johnson M. D., Pride G. L., Jr., Lynch J. R., Zaidat O. O., Rumboldt Z., Cloft H. J., Stenting, Aggressive Medical Management for Preventing Recurrent Stroke in Intracranial Stenosis Trial I, 2014. Aggressive medical treatment with or without stenting in high-risk patients with intracranial artery stenosis (SAMMPRIS): the final results of a randomised trial. *Lancet.* 383, 333-341. [https://doi.org/10.1016/S0140-6736\(13\)62038-3](https://doi.org/10.1016/S0140-6736(13)62038-3)
- Ding, H., Tan P., Fu S., Tian X., Zhang H., Ma X., Gu Z., Luo K., 2022. Preparation and application of pH-responsive drug delivery systems. *Journal of controlled release : official journal of the Controlled Release Society.* 348, 206-238. <https://doi.org/10.1016/j.jconrel.2022.05.056>
- Du, B., Han S., Li H., Zhao F., Su X., Cao X., Zhang Z., 2015. Multi-functional liposomes showing radiofrequency-triggered release and magnetic resonance imaging for tumor multi-mechanism therapy. *Nanoscale.* 7, 5411-5426. <https://doi.org/10.1039/c4nr04257c>
- Dunbar, C. E., High K. A., Joung J. K., Kohn D. B., Ozawa K., Sadelain M., 2018. Gene therapy comes of age. *Science.* 359, <https://doi.org/10.1126/science.aan4672>
- El-Sayed, I. H., Huang X., El-Sayed M. A., 2006. Selective laser photo-thermal therapy of epithelial carcinoma using anti-EGFR antibody conjugated gold nanoparticles. *Cancer letters.* 239, 129-135. <https://doi.org/10.1016/j.canlet.2005.07.035>
- Farokhzad, O. C., Jon S., Khademhosseini A., Tran T. N., Lavan D. A., Langer R., 2004. Nanoparticle-aptamer bioconjugates: a new approach for targeting prostate cancer cells. *Cancer Res.* 64, 7668-7672. <https://doi.org/10.1158/0008-5472.CAN-04-2550>
- Feldman, S. A., Assadipour Y., Kriley I., Goff S. L., Rosenberg S. A., 2015. Adoptive Cell Therapy--Tumor-Infiltrating Lymphocytes, T-Cell Receptors, and Chimeric Antigen Receptors. *Semin. Oncol.* 42, 626-639. <https://doi.org/10.1053/j.seminoncol.2015.05.005>
- Fernandez-Rozadilla, C., Simoes A. R., Leonart M. E., Carnero A., Carracedo A., 2021. Tumor Profiling at the Service of Cancer Therapy. *Frontiers in Oncology.* 10, <https://doi.org/ARTN10.3389/fonc.2020.595613>
- Fisusi, F. A., Akala E. O., 2019. Drug Combinations in Breast Cancer Therapy. *Pharm Nanotechnol.* 7, 3-23. <https://doi.org/10.2174/2211738507666190122111224>
- Fong, P. C., Boss D. S., Yap T. A., Tutt A., Wu P., Mergui-Roelvink M., Mortimer P., Swaisland H., Lau A., O'Connor M. J., Ashworth A., Carmichael J., Kaye S. B., Schellens J. H., de Bono J. S., 2009. Inhibition of poly(ADP-ribose) polymerase in tumors from BRCA mutation carriers. *N Engl J Med.* 361, 123-134. <https://doi.org/10.1056/NEJMoa0900212>
- Fukui, T., Otani S., Hataishi R., Jiang S. X., Nishii Y., Igawa S., Mitsufuji H., Kubota M., Katagiri M., Masuda N., 2010. Successful rechallenge with erlotinib in a patient with EGFR-mutant lung adenocarcinoma who developed gefitinib-related interstitial lung disease. *Cancer Chemother Pharmacol.* 65, 803-806. <https://doi.org/10.1007/s00280-009-1212-5>

- Gao, P., Chen Y., Pan W., Li N., Liu Z., Tang B., 2021. Antitumor Agents Based on Metal-Organic Frameworks. *Angewandte Chemie*. 60, 16763-16776. <https://doi.org/10.1002/anie.202102574>
- Gavas, S., Quazi S., Karpinski T. M., 2021. Nanoparticles for Cancer Therapy: Current Progress and Challenges. *Nanoscale research letters*. 16, 173. <https://doi.org/10.1186/s11671-021-03628-6>
- Geukes Foppen, M. H., Donia M., Svane I. M., Haanen J. B., 2015. Tumor-infiltrating lymphocytes for the treatment of metastatic cancer. *Mol Oncol*. 9, 1918-1935. <https://doi.org/10.1016/j.molonc.2015.10.018>
- GlobalSurg, C., Surgery N. G. H. R. U. o. G., 2022. Effects of hospital facilities on patient outcomes after cancer surgery: an international, prospective, observational study. *Lancet Glob Health*. 10, e1003-e1011. [https://doi.org/10.1016/S2214-109X\(22\)00168-1](https://doi.org/10.1016/S2214-109X(22)00168-1)
- Goldstein, M. R., Mascitelli L., 2011. Surgery and cancer promotion: are we trading beauty for cancer? *QJM*. 104, 811-815. <https://doi.org/10.1093/qjmed/hcr039>
- Guan, Y. S., Liu Y., Zou Q., He Q., La Z., Yang L., Hu Y., 2009. Adenovirus-mediated wild-type p53 gene transfer in combination with bronchial arterial infusion for treatment of advanced non-small-cell lung cancer, one year follow-up. *J Zhejiang Univ Sci B*. 10, 331-340. <https://doi.org/10.1631/jzus.B0820248>
- Gupta, J., Quadros M., Momin M., 2023. Mesoporous silica nanoparticles: Synthesis and multifaceted functionalization for controlled drug delivery. *J. Drug Deliv. Sci. Technol*. 81, 104305. <https://doi.org/10.1016/j.jddst.2023.104305>
- Hainaut, P., Plymoth A., 2013. Targeting the hallmarks of cancer: towards a rational approach to next-generation cancer therapy. *Curr Opin Oncol*. 25, 50-51. <https://doi.org/10.1097/CCO.0b013e32835b651e>
- Hanahan, D., Weinberg R. A., 2011. Hallmarks of cancer: the next generation. *Cell*. 144, 646-674. <https://doi.org/10.1016/j.cell.2011.02.013>
- He, J., Huang Z., Han L., Gong Y., Xie C., 2021. Mechanisms and management of 3rd-generation EGFR-TKI resistance in advanced non-small cell lung cancer (Review). *Int. J. Oncol*. 59, 5270. <https://doi.org/10.3892/ijo.2021.5270>
- He, Q., Zhang Z., Gao F., Li Y., Shi J., 2011. In vivo biodistribution and urinary excretion of mesoporous silica nanoparticles: effects of particle size and PEGylation. *Small*. 7, 271-280. <https://doi.org/10.1002/sml.201001459>
- Hong, B., van den Heuvel A. P., Prabhu V. V., Zhang S., El-Deiry W. S., 2014. Targeting tumor suppressor p53 for cancer therapy: strategies, challenges and opportunities. *Curr. Drug Targets*. 15, 80-89. <https://doi.org/10.2174/1389450114666140106101412>
- Horcajada, P., Chalati T., Serre C., Gillet B., Sebrie C., Baati T., Eubank J. F., Heurtaux D., Clayette P., Kreuz C., Chang J. S., Hwang Y. K., Marsaud V., Bories P. N., Cynober L., Gil S., Ferey G., Couvreur P., Gref R., 2010. Porous metal-organic-framework nanoscale carriers as a potential platform for drug delivery and imaging. *Nat Mater*. 9, 172-178. <https://doi.org/10.1038/nmat2608>
- Hsu, H. J., Bugno J., Lee S. R., Hong S., 2017. Dendrimer-based nanocarriers: a versatile platform for drug delivery. *Wiley Interdiscip Rev Nanomed Nanobiotechnol*. 9, 1409. <https://doi.org/10.1002/wnan.1409>
- Huang, Y. Y., Lee Z. H., Chang K. C., Wu Z. Y., Lee C. C., Tsou M. H., Lin H. M., 2023. Mesoporous silica nanoparticles with dual-targeting agricultural sources for enhanced cancer treatment via tritherapy. *RSC Adv*. 13, 19079-19090. <https://doi.org/10.1039/d3ra02068a>
- Hughes, J. P., Alusi G., Wang Y., 2015. Viral gene therapy for head and neck cancer. *J Laryngol Otol*. 129, 314-320. <https://doi.org/10.1017/S0022215114003247>
- Hurwitz, H., Fehrenbacher L., Novotny W., Cartwright T., Hainsworth J., Heim W., Berlin J., Baron A., Griffing S., Holmgren E., Ferrara N., Fyfe G., Rogers B., Ross R., Kabbinavar F., 2004. Bevacizumab plus

- irinotecan, fluorouracil, and leucovorin for metastatic colorectal cancer. *N Engl J Med.* 350, 2335-2342. <https://doi.org/10.1056/NEJMoa032691>
- Hussein, A. A., Mohsin R., Qureshi H., Leghari R., Jing Z., Ramahi Y. O., Rizvi I., Guru K. A., Rizvi A., 2023. Transition from da Vinci to Versius robotic surgical system: initial experience and outcomes of over 100 consecutive procedures. *J Robot Surg.* 17, 419-426. <https://doi.org/10.1007/s11701-022-01422-9>
- Hutter, E., Maysinger D., 2011. Gold nanoparticles and quantum dots for bioimaging. *Microsc. Res. Tech.* 74, 592-604. <https://doi.org/10.1002/jemt.20928>
- Janjua, T. I., Cao Y., Kleitz F., Linden M., Yu C., Popat A., 2023. Silica nanoparticles: A review of their safety and current strategies to overcome biological barriers. *Advanced drug delivery reviews.* 115115. <https://doi.org/10.1016/j.addr.2023.115115>
- Jayne, D., Pigazzi A., Marshall H., Croft J., Corrigan N., Copeland J., Quirke P., West N., Edlin R., Hulme C., Brown J., in *Robotic-assisted surgery compared with laparoscopic resection surgery for rectal cancer: the ROLARR RCT.* (Southampton (UK), 2019).
- Jiang, Y., Chen M., Nie H., Yuan Y., 2019. PD-1 and PD-L1 in cancer immunotherapy: clinical implications and future considerations. *Hum Vaccin Immunother.* 15, 1111-1122. <https://doi.org/10.1080/21645515.2019.1571892>
- Jin, H., Wang L., Bernards R., 2023. Rational combinations of targeted cancer therapies: background, advances and challenges. *Nat Rev Drug Discov.* 22, 213-234. <https://doi.org/10.1038/s41573-022-00615-z>
- Jones, P. A., Baylin S. B., 2007. The epigenomics of cancer. *Cell.* 128, 683-692. <https://doi.org/10.1016/j.cell.2007.01.029>
- Kampouraki, Z. C., Giannakoudakis D. A., Nair V., Hosseini-Bandegharaei A., Colmenares J. C., Deliyanni E. A., 2019. Metal Organic Frameworks as Desulfurization Adsorbents of DBT and 4,6-DMDBT from Fuels. *Molecules.* 24, 4525. <https://doi.org/ARTN> 4525 10.3390/molecules24244525
- Kanasty, R., Dorkin J. R., Vegas A., Anderson D., 2013. Delivery materials for siRNA therapeutics. *Nat Mater.* 12, 967-977. <https://doi.org/10.1038/nmat3765>
- Karapetis, C. S., Khambata-Ford S., Jonker D. J., O'Callaghan C. J., Tu D., Tebbutt N. C., Simes R. J., Chalchal H., Shapiro J. D., Robitaille S., Price T. J., Shepherd L., Au H. J., Langer C., Moore M. J., Zalcberg J. R., 2008. K-ras mutations and benefit from cetuximab in advanced colorectal cancer. *N Engl J Med.* 359, 1757-1765. <https://doi.org/10.1056/NEJMoa0804385>
- Kaur, R., Bhardwaj A., Gupta S., 2023. Cancer treatment therapies: traditional to modern approaches to combat cancers. *Mol Biol Rep.* 50, 9663-9676. <https://doi.org/10.1007/s11033-023-08809-3>
- Kaushik, N., Borkar S. B., Nandanwar S. K., Panda P. K., Choi E. H., Kaushik N. K., 2022. Nanocarrier cancer therapeutics with functional stimuli-responsive mechanisms. *J Nanobiotechnology.* 20, 152. <https://doi.org/10.1186/s12951-022-01364-2>
- Keller, D. S., Berho M., Perez R. O., Wexner S. D., Chand M., 2020. The multidisciplinary management of rectal cancer. *Nat Rev Gastroenterol Hepatol.* 17, 414-429. <https://doi.org/10.1038/s41575-020-0275-y>
- Kesse, S., Boakye-Yiadom K. O., Ochete B. O., Opoku-Damoah Y., Akhtar F., Filli M. S., Asim Farooq M., Aquib M., Maviah Mily B. J., Murtaza G., Wang B., 2019. Mesoporous Silica Nanomaterials: Versatile Nanocarriers for Cancer Theranostics and Drug and Gene Delivery. *Pharmaceutics.* 11, <https://doi.org/10.3390/pharmaceutics11020077>
- Koller, U., Bauer J. W., 2021. Gene Replacement Therapies for Genodermatoses: A Status Quo. *Front Genet.* 12, 658295. <https://doi.org/10.3389/fgene.2021.658295>

- Lammers, T., Rizzo L. Y., Storm G., Kiessling F., 2012. Personalized nanomedicine. *Clinical cancer research : an official journal of the American Association for Cancer Research*. 18, 4889-4894. <https://doi.org/10.1158/1078-0432.CCR-12-1414>
- Lawson, H. D., Walton S. P., Chan C., 2021. Metal-Organic Frameworks for Drug Delivery: A Design Perspective. *ACS applied materials & interfaces*. 13, 7004-7020. <https://doi.org/10.1021/acsami.1c01089>
- Le, B. Q. G., Doan T. L. H., 2023. Trend in biodegradable porous nanomaterials for anticancer drug delivery. *Wiley Interdiscip Rev Nanomed Nanobiotechnol*. 15, e1874. <https://doi.org/10.1002/wnan.1874>
- Lerida-Viso, A., Estepa-Fernandez A., Garcia-Fernandez A., Marti-Centelles V., Martinez-Manez R., 2023. Biosafety of mesoporous silica nanoparticles; towards clinical translation. *Advanced drug delivery reviews*. 201, 115049. <https://doi.org/10.1016/j.addr.2023.115049>
- Li, F., Wang Y., Chen W. L., Wang D. D., Zhou Y. J., You B. G., Liu Y., Qu C. X., Yang S. D., Chen M. T., Zhang X. N., 2019. Co-delivery of VEGF siRNA and Etoposide for Enhanced Anti-angiogenesis and Anti-proliferation Effect via Multi-functional Nanoparticles for Orthotopic Non-Small Cell Lung Cancer Treatment. *Theranostics*. 9, 5886-5898. <https://doi.org/10.7150/thno.32416>
- Li, M., Zhang Y., Zhang X., Liu Z., Tang J., Feng M., Chen B., Wu D., Liu J., 2022. Degradable Multifunctional Porphyrin-Based Porous Organic Polymer Nanosonosensitizer for Tumor-Specific Sonodynamic, Chemo- and Immunotherapy. *ACS applied materials & interfaces*. 14, 48489-48501. <https://doi.org/10.1021/acsami.2c14776>
- Li, S. R., Huo F. Y., Wang H. Q., Wang J., Xu C., Liu B., Bu L. L., 2022. Recent advances in porous nanomaterials-based drug delivery systems for cancer immunotherapy. *J Nanobiotechnology*. 20, 277. <https://doi.org/10.1186/s12951-022-01489-4>
- Li, T., Kang G., Wang T., Huang H., 2018. Tumor angiogenesis and anti-angiogenic gene therapy for cancer. *Oncology letters*. 16, 687-702. <https://doi.org/10.3892/ol.2018.8733>
- Li, T., Shen X., Geng Y., Chen Z., Li L., Li S., Yang H., Wu C., Zeng H., Liu Y., 2016. Folate-Functionalized Magnetic-Mesoporous Silica Nanoparticles for Drug/Gene Codelivery To Potentiate the Antitumor Efficacy. *ACS applied materials & interfaces*. 8, 13748-13758. <https://doi.org/10.1021/acsami.6b02963>
- Liu, C., Yan P., Xu X., Zhou W., Prakash D. R., Wang S., Zhou J., Wang R., Huang H., Chen J., Zhang H., Shen J., 2022. In Vivo Kidney Allograft Endothelial Specific Scavengers for On-Site Inflammation Reduction under Antibody-Mediated Rejection. *Small*. 18, e2106746. <https://doi.org/10.1002/sml.202106746>
- Liu, J., Huang J., Zhang L., Lei J., 2021. Multifunctional metal-organic framework heterostructures for enhanced cancer therapy. *Chem Soc Rev*. 50, 1188-1218. <https://doi.org/10.1039/d0cs00178c>
- Lockman, P. R., Mumper R. J., Khan M. A., Allen D. D., 2002. Nanoparticle technology for drug delivery across the blood-brain barrier. *Drug Dev. Ind. Pharm*. 28, 1-13. <https://doi.org/10.1081/ddc-120001481>
- Luo, Y., Yang H., Zhou Y. F., Hu B., 2020. Dual and multi-targeted nanoparticles for site-specific brain drug delivery. *Journal of controlled release : official journal of the Controlled Release Society*. 317, 195-215. <https://doi.org/10.1016/j.jconrel.2019.11.037>
- Luque-Michel, E., Imbuluzqueta E., Sebastian V., Blanco-Prieto M. J., 2017. Clinical advances of nanocarrier-based cancer therapy and diagnostics. *Expert Opin Drug Deliv*. 14, 75-92. <https://doi.org/10.1080/17425247.2016.1205585>
- Mahor, A., Singh P. P., Bharadwaj P., Sharma N., Yadav S., Rosenholm J. M., Bansal K. K., 2021. Carbon-Based Nanomaterials for Delivery of Biologicals and Therapeutics:

- A Cutting-Edge Technology. *C-J Carbon Res.* 7, [https://doi.org/ARTN 19 10.3390/c7010019](https://doi.org/ARTN%2010.3390/c7010019)
- Mayer, L. D., Janoff A. S., 2007. Optimizing combination chemotherapy by controlling drug ratios. *Mol Interv.* 7, 216-223. <https://doi.org/10.1124/mi.7.4.8>
- McKeown, M. R., Bradner J. E., 2014. Therapeutic strategies to inhibit MYC. *Cold Spring Harb Perspect Med.* 4, <https://doi.org/10.1101/cshperspect.a014266>
- McNeel, D. G., Dunphy E. J., Davies J. G., Frye T. P., Johnson L. E., Staab M. J., Horvath D. L., Straus J., Alberti D., Marnocha R., Liu G., Eickhoff J. C., Wilding G., 2009. Safety and immunological efficacy of a DNA vaccine encoding prostatic acid phosphatase in patients with stage D0 prostate cancer. *J Clin Oncol.* 27, 4047-4054. <https://doi.org/10.1200/JCO.2008.19.9968>
- McNeel, D. G., Eickhoff J. C., Johnson L. E., Roth A. R., Perk T. G., Fong L., Antonarakis E. S., Wargowski E., Jeraj R., Liu G., 2019. Phase II Trial of a DNA Vaccine Encoding Prostatic Acid Phosphatase (pTVG-HP [MVI-816]) in Patients With Progressive, Nonmetastatic, Castration-Sensitive Prostate Cancer. *J Clin Oncol.* 37, 3507-3517. <https://doi.org/10.1200/JCO.19.01701>
- Mitchell, M. J., Billingsley M. M., Haley R. M., Wechsler M. E., Peppas N. A., Langer R., 2021. Engineering precision nanoparticles for drug delivery. *Nat Rev Drug Discov.* 20, 101-124. <https://doi.org/10.1038/s41573-020-0090-8>
- Moo, T. A., Sanford R., Dang C., Morrow M., 2018. Overview of Breast Cancer Therapy. *PET Clin.* 13, 339-354. <https://doi.org/10.1016/j.cpet.2018.02.006>
- Muller, R. H., Mader K., Gohla S., 2000. Solid lipid nanoparticles (SLN) for controlled drug delivery - a review of the state of the art. *European journal of pharmaceutics and biopharmaceutics : official journal of Arbeitsgemeinschaft fur Pharmazeutische Verfahrenstechnik e.V.* 50, 161-177. [https://doi.org/10.1016/s0939-6411\(00\)00087-4](https://doi.org/10.1016/s0939-6411(00)00087-4)
- Nair, M., 2020. Personalized NanoMedicine: Novel Theranostic Approach. *Crit. Rev. Biomed. Eng.* 48, 133-135. <https://doi.org/10.1615/CritRevBiomedEng.2020032948>
- Neelapu, S. S., Tummala S., Kebriaei P., Wierda W., Gutierrez C., Locke F. L., Komanduri K. V., Lin Y., Jain N., Daver N., Westin J., Gulbis A. M., Loghini M. E., de Groot J. F., Adkins S., Davis S. E., Rezvani K., Hwu P., Shpall E. J., 2018. Chimeric antigen receptor T-cell therapy - assessment and management of toxicities. *Nature reviews. Clinical oncology.* 15, 47-62. <https://doi.org/10.1038/nrclinonc.2017.148>
- Nemunaitis, J., Swisher S. G., Timmons T., Connors D., Mack M., Doerksen L., Weill D., Wait J., Lawrence D. D., Kemp B. L., Fossella F., Glisson B. S., Hong W. K., Khuri F. R., Kurie J. M., Lee J. J., Lee J. S., Nguyen D. M., Nesbitt J. C., Perez-Soler R., Pisters K. M., Putnam J. B., Richli W. R., Shin D. M., Walsh G. L., Merritt J., Roth J., 2000. Adenovirus-mediated p53 gene transfer in sequence with cisplatin to tumors of patients with non-small-cell lung cancer. *J Clin Oncol.* 18, 609-622. <https://doi.org/10.1200/JCO.2000.18.3609>
- Nicolini, C., Bragazzi N., Pechkova E., 2012. Nanoproteomics enabling personalized nanomedicine. *Advanced drug delivery reviews.* 64, 1522-1531. <https://doi.org/10.1016/j.addr.2012.06.015>
- Nowag, S., Haag R., 2014. pH-responsive micro- and nanocarrier systems. *Angewandte Chemie.* 53, 49-51. <https://doi.org/10.1002/anie.201308619>
- O'Brien, M. E., Wigler N., Inbar M., Rosso R., Grischke E., Santoro A., Catane R., Kieback D. G., Tomczak P., Ackland S. P., Orlandi F., Mellars L., Alland L., Tendler C., Group C. B. C. S., 2004. Reduced cardiotoxicity and comparable efficacy in a phase III trial of pegylated liposomal doxorubicin HCl (CAELYX/Doxil) versus conventional doxorubicin for first-line treatment of metastatic breast cancer. *Ann Oncol.* 15, 440-449.

- <https://doi.org/10.1093/annonc/mdh097>
- Ou, Y. C., Wen X., Bardhan R., 2020. Cancer Immunoimaging with Smart Nanoparticles. *Trends Biotechnol.* 38, 388-403. <https://doi.org/10.1016/j.tibtech.2019.11.001>
- Paleari, L., 2022. Cancer Prevention with Molecular Targeted Therapies. *International journal of molecular sciences.* 23, <https://doi.org/10.3390/ijms23158429>
- Pantwalawalkar, J., Mhettar P., Nangare S., Mali R., Ghule A., Patil P., Mohite S., More H., Jadhav N., 2023. Stimuli-Responsive Design of Metal-Organic Frameworks for Cancer Theranostics: Current Challenges and Future Perspective. *ACS Biomater Sci Eng.* 9, 4497-4526. <https://doi.org/10.1021/acsbiomaterials.3c00507>
- Parker, R. J., Dabholkar M. D., Lee K. B., Bostick-Bruton F., Reed E., 1993. Taxol effect on cisplatin sensitivity and cisplatin cellular accumulation in human ovarian cancer cells. *J Natl Cancer Inst Monogr.* 83-88. <https://www.ncbi.nlm.nih.gov/pubmed/7912534>)
- Paunovska, K., Loughrey D., Dahlman J. E., 2022. Drug delivery systems for RNA therapeutics. *Nature reviews. Genetics.* 23, 265-280. <https://doi.org/10.1038/s41576-021-00439-4>
- Pecot, C. V., Wu S. Y., Bellister S., Filant J., Rupaimoole R., Hisamatsu T., Bhattacharya R., Maharaj A., Azam S., Rodriguez-Aguayo C., Nagaraja A. S., Morelli M. P., Gharpure K. M., Waugh T. A., Gonzalez-Villasana V., Zand B., Dalton H. J., Kopetz S., Lopez-Berestein G., Ellis L. M., Sood A. K., 2014. Therapeutic silencing of KRAS using systemically delivered siRNAs. *Mol Cancer Ther.* 13, 2876-2885. <https://doi.org/10.1158/1535-7163.MCT-14-0074>
- Peer, D., Karp J. M., Hong S., Farokhzad O. C., Margalit R., Langer R., 2007. Nanocarriers as an emerging platform for cancer therapy. *Nature nanotechnology.* 2, 751-760. <https://doi.org/10.1038/nnano.2007.387>
- Pomeroy, A. E., Schmidt E. V., Sorger P. K., Palmer A. C., 2022. Drug independence and the curability of cancer by combination chemotherapy. *Trends Cancer.* 8, 915-929. <https://doi.org/10.1016/j.trecan.2022.06.009>
- Qin, X., Li Y., 2020. Strategies To Design and Synthesize Polymer-Based Stimuli-Responsive Drug-Delivery Nanosystems. *Chembiochem : a European journal of chemical biology.* 21, 1236-1253. <https://doi.org/10.1002/cbic.201900550>
- Raj, S., Khurana S., Choudhari R., Kesari K. K., Kamal M. A., Garg N., Ruokolainen J., Das B. C., Kumar D., 2021. Specific targeting cancer cells with nanoparticles and drug delivery in cancer therapy. *Semin Cancer Biol.* 69, 166-177. <https://doi.org/10.1016/j.semcancer.2019.11.002>
- Rezaee, T., Fazel-Zarandi R., Karimi A., Ensafi A. A., 2022. Metal-organic frameworks for pharmaceutical and biomedical applications. *Journal of pharmaceutical and biomedical analysis.* 221, 115026. <https://doi.org/10.1016/j.jpba.2022.11.5026>
- Rosenberg, S. A., Yang J. C., Sherry R. M., Kammula U. S., Hughes M. S., Phan G. Q., Citrin D. E., Restifo N. P., Robbins P. F., Wunderlich J. R., Morton K. E., Laurencot C. M., Steinberg S. M., White D. E., Dudley M. E., 2011. Durable complete responses in heavily pretreated patients with metastatic melanoma using T-cell transfer immunotherapy. *Clinical cancer research : an official journal of the American Association for Cancer Research.* 17, 4550-4557. <https://doi.org/10.1158/1078-0432.CCR-11-0116>
- Sajjadi, M., Nasrollahzadeh M., Jaleh B., Soufi G. J., Irvani S., 2021. Carbon-based nanomaterials for targeted cancer nanotherapy: recent trends and future prospects. *J Drug Target.* 29, 716-741. <https://doi.org/10.1080/1061186X.2021.1886301>
- Sawdon, A. J., Zhang J., Peng S., Alyami E. M., Peng C. A., 2021. Polymeric Nanovectors Incorporated with Ganciclovir and HSV-tk Encoding Plasmid for Gene-Directed Enzyme Prodrug Therapy. *Molecules.* 26,

- <https://doi.org/10.3390/molecules26061759>
- Scappaticci, F. A., Smith R., Pathak A., Schloss D., Lum B., Cao Y., Johnson F., Engleman E. G., Nolan G. P., 2001. Combination angiostatin and endostatin gene transfer induces synergistic antiangiogenic activity in vitro and antitumor efficacy in leukemia and solid tumors in mice. *Mol Ther.* 3, 186-196. <https://doi.org/10.1006/mthe.2000.0243>
- Sharma, G., Sharma A. R., Bhattacharya M., Lee S. S., Chakraborty C., 2021. CRISPR-Cas9: A Preclinical and Clinical Perspective for the Treatment of Human Diseases. *Mol Ther.* 29, 571-586. <https://doi.org/10.1016/j.ymthe.2020.09.028>
- Singh, C., Mukhopadhyay S., Hod I., 2021. Metal-organic framework derived nanomaterials for electrocatalysis: recent developments for CO(2) and N(2) reduction. *Nano Converg.* 8, 1. <https://doi.org/10.1186/s40580-020-00251-6>
- Singhal, S., 2016. The Future of Surgical Oncology: Image-Guided Cancer Surgery. *JAMA Surg.* 151, 184-185. <https://doi.org/10.1001/jamasurg.2015.3604>
- Sk, U. H., Kojima C., 2015. Dendrimers for theranostic applications. *Biomol Concepts.* 6, 205-217. <https://doi.org/10.1515/bmc-2015-0012>
- Slamon, D. J., Leyland-Jones B., Shak S., Fuchs H., Paton V., Bajamonde A., Fleming T., Eiermann W., Wolter J., Pegram M., Baselga J., Norton L., 2001. Use of chemotherapy plus a monoclonal antibody against HER2 for metastatic breast cancer that overexpresses HER2. *N Engl J Med.* 344, 783-792. <https://doi.org/10.1056/NEJM200103153441101>
- Slowing, II, Vivero-Escoto J. L., Wu C. W., Lin V. S., 2008. Mesoporous silica nanoparticles as controlled release drug delivery and gene transfection carriers. *Advanced drug delivery reviews.* 60, 1278-1288. <https://doi.org/10.1016/j.addr.2008.03.012>
- Sousa de Almeida, M., Susnik E., Drasler B., Taladriz-Blanco P., Petri-Fink A., Rothen-Rutishauser B., 2021. Understanding nanoparticle endocytosis to improve targeting strategies in nanomedicine. *Chem Soc Rev.* 50, 5397-5434. <https://doi.org/10.1039/d0cs01127d>
- Sterner, R. C., Sterner R. M., 2021. CAR-T cell therapy: current limitations and potential strategies. *Blood Cancer J.* 11, 69. <https://doi.org/10.1038/s41408-021-00459-7>
- Sun, J., Meng H., Yao L., Lv M., Bai J., Zhang J., Wang L., Ouyang T., Li J., Wang T., Fan Z., Fan T., Lin B., Xie Y., 2017. Germline Mutations in Cancer Susceptibility Genes in a Large Series of Unselected Breast Cancer Patients. *Clinical cancer research : an official journal of the American Association for Cancer Research.* 23, 6113-6119. <https://doi.org/10.1158/1078-0432.CCR-16-3227>
- Swain, S. M., Shastry M., Hamilton E., 2023. Targeting HER2-positive breast cancer: advances and future directions. *Nat Rev Drug Discov.* 22, 101-126. <https://doi.org/10.1038/s41573-022-00579-0>
- Tang, F., Li L., Chen D., 2012. Mesoporous silica nanoparticles: synthesis, biocompatibility and drug delivery. *Advanced materials.* 24, 1504-1534. <https://doi.org/10.1002/adma.201104763>
- Tarn, D., Ashley C. E., Xue M., Carnes E. C., Zink J. I., Brinker C. J., 2013. Mesoporous silica nanoparticle nanocarriers: biofunctionality and biocompatibility. *Acc Chem Res.* 46, 792-801. <https://doi.org/10.1021/ar3000986>
- Tekedereli, I., Alpay S. N., Akar U., Yuca E., Ayugo-Rodriguez C., Han H. D., Sood A. K., Lopez-Berestein G., Ozpolat B., 2013. Therapeutic Silencing of Bcl-2 by Systemically Administered siRNA Nanotherapeutics Inhibits Tumor Growth by Autophagy and Apoptosis and Enhances the Efficacy of Chemotherapy in Orthotopic Xenograft Models of ER (-) and ER (+) Breast Cancer. *Mol Ther Nucleic Acids.* 2, e121. <https://doi.org/10.1038/mtna.2013.45>
- Tian, Z., Liang G., Cui K., Liang Y., Wang Q., Lv S., Cheng X., Zhang L., 2021. Insight Into the Prospects for RNAi Therapy of Cancer. *Frontiers in pharmacology.* 12,

644718.
<https://doi.org/10.3389/fphar.2021.644718>
- Tieu, T., Dhawan S., Haridas V., Butler L. M., Thissen H., Cifuentes-Rius A., Voelcker N. H., 2019. Maximizing RNA Loading for Gene Silencing Using Porous Silicon Nanoparticles. *ACS applied materials & interfaces*. 11, 22993-23005. <https://doi.org/10.1021/acsami.9b05577>
- Topaly, J., Zeller W. J., Fruehauf S., 2001. Synergistic activity of the new ABL-specific tyrosine kinase inhibitor STI571 and chemotherapeutic drugs on BCR-ABL-positive chronic myelogenous leukemia cells. *Leukemia*. 15, 342-347. <https://doi.org/10.1038/sj.leu.2402041>
- Trueman, P., 2009. Prophylactic G-CSF in patients with early-stage breast cancer: a health economic review. *Br J Cancer*. 101 Suppl 1, S15-17. <https://doi.org/10.1038/sj.bjc.6605271>
- Vallet-Regi, M., Colilla M., Izquierdo-Barba I., Manzano M., 2017. Mesoporous Silica Nanoparticles for Drug Delivery: Current Insights. *Molecules*. 23, <https://doi.org/10.3390/molecules23010047>
- Vallet-Regi, M., Rámila A., del Real R. P., Pérez-Pariante J., 2001. A new property of MCM-41:: Drug delivery system. *Chem Mater*. 13, 308-311. <https://doi.org/DOI.10.1021/cm0011559>
- Wang, C., Shen Y., Ma Y., 2023. Bifidobacterium infantis-Mediated Herpes Simplex Virus-TK/Ganciclovir Treatment Inhibits Cancer Metastasis in Mouse Model. *International journal of molecular sciences*. 24, <https://doi.org/10.3390/ijms241411721>
- Wang, Y., Yan J., Wen N., Xiong H., Cai S., He Q., Hu Y., Peng D., Liu Z., Liu Y., 2020. Metal-organic frameworks for stimuli-responsive drug delivery. *Biomaterials*. 230, 119619. <https://doi.org/10.1016/j.biomaterials.2019.119619>
- Wei, G., Wang Y., Yang G., Wang Y., Ju R., 2021. Recent progress in nanomedicine for enhanced cancer chemotherapy. *Theranostics*. 11, 6370-6392. <https://doi.org/10.7150/thno.57828>
- Weng, Y., Guan S., Wang L., Lu H., Meng X., Waterhouse G. I. N., Zhou S., 2020. Defective Porous Carbon Polyhedra Decorated with Copper Nanoparticles for Enhanced NIR-Driven Photothermal Cancer Therapy. *Small*. 16, e1905184. <https://doi.org/10.1002/sml.201905184>
- Wu, G., Wilson G., George J., Liddle C., Hebbard L., Qiao L., 2017. Overcoming treatment resistance in cancer: Current understanding and tactics. *Cancer letters*. 387, 69-76. <https://doi.org/10.1016/j.canlet.2016.04.018>
- Wu, H., Zhang T., Li N., Gao J., 2023. Cell membrane-based biomimetic vehicles for effective central nervous system target delivery: Insights and challenges. *Journal of controlled release : official journal of the Controlled Release Society*. 360, 169-184. <https://doi.org/10.1016/j.jconrel.2023.06.023>
- Wu, L., Leng D., Cun D., Foged C., Yang M., 2017. Advances in combination therapy of lung cancer: Rationales, delivery technologies and dosage regimens. *Journal of controlled release : official journal of the Controlled Release Society*. 260, 78-91. <https://doi.org/10.1016/j.jconrel.2017.05.023>
- Wu, M. X., Yang Y. W., 2017. Metal-Organic Framework (MOF)-Based Drug/Cargo Delivery and Cancer Therapy. *Advanced materials*. 29, <https://doi.org/10.1002/adma.201606134>
- Wu, Q., Yang Z., Nie Y., Shi Y., Fan D., 2014. Multi-drug resistance in cancer chemotherapeutics: mechanisms and lab approaches. *Cancer letters*. 347, 159-166. <https://doi.org/10.1016/j.canlet.2014.03.013>
- Wyld, L., Audisio R. A., Poston G. J., 2015. The evolution of cancer surgery and future perspectives. *Nature reviews. Clinical oncology*. 12, 115-124. <https://doi.org/10.1038/nrclinonc.2014.191>
- Xu, B., Li S., Shi R., Liu H., 2023. Multifunctional mesoporous silica nanoparticles for biomedical applications. *Signal Transduct Target*

- Ther.* 8, 435.
<https://doi.org/10.1038/s41392-023-01654-7>
- Xu, R., Saw P. E., Xu L., 2022. Long-Circulating Theranostic 2D Metal-Organic Frameworks with Concurrent O(2) Self-Supplying and GSH Depletion Characteristic for Enhanced Cancer Chemodynamic Therapy. *Small Methods*. 6, e2200178.
<https://doi.org/10.1002/smtd.202200178>
- Yang, J., Yang Y. W., 2020. Metal-Organic Frameworks for Biomedical Applications. *Small*. 16, e1906846.
<https://doi.org/10.1002/sml.201906846>
- Zhang, C., Xie H., Zhang Z., Wen B., Cao H., Bai Y., Che Q., Guo J., Su Z., 2022. Applications and Biocompatibility of Mesoporous Silica Nanocarriers in the Field of Medicine. *Frontiers in pharmacology*. 13, 829796.
<https://doi.org/10.3389/fphar.2022.829796>
- Zhang, L. R., Ma X. D., Zhou W. H., Wu Q. W., Yan J. Q., Xu X. Y., Ghimire B., Rosenholm J. M., Feng J., Wang D. Q., Zhang H. B., 2022. Combination of photothermal, prodrug and tumor cell camouflage technologies for triple-negative breast cancer treatment. *Mater Today Adv.* 13, 100199.
<https://doi.org/ARTN100199>
- Zhang, M., Cheng S., Jin Y., Zhang N., Wang Y., 2021. Membrane engineering of cell membrane biomimetic nanoparticles for nanoscale therapeutics. *Clin Transl Med.* 11, e292.
<https://doi.org/10.1002/ctm2.292>
- Zhou, Y., Peng Z., Seven E. S., Leblanc R. M., 2018. Crossing the blood-brain barrier with nanoparticles. *Journal of controlled release : official journal of the Controlled Release Society.* 270, 290-303.
<https://doi.org/10.1016/j.jconrel.2017.12.015>
- Zu, H., Gao D., 2021. Non-viral Vectors in Gene Therapy: Recent Development, Challenges, and Prospects. *The AAPS journal.* 23, 78.
<https://doi.org/10.1208/s12248-021-00608-7>


Original publications

Co-delivery CPT and PTX prodrug with a photo/thermo-responsive nanoplatform for triple-negative breast cancer therapy

Wenhui Zhou, Xiaodong Ma, Jie Wang, Xiaoyu Xu, Oliver Koivisto, Jing Feng, Tapani Viitala, Hongbo Zhang*. *Smart Medicine* **2022**;1:e20220036

RESEARCH ARTICLE

Co-delivery CPT and PTX prodrug with a photo/thermo-responsive nanoplatform for triple-negative breast cancer therapy

Wenhui Zhou^{1,2,3} | Xiaodong Ma^{1,2} | Jie Wang³ | Xiaoyu Xu^{1,2} |
Oliver Koivisto^{1,2} | Jing Feng^{3,4} | Tapani Viitala^{1,2} | Hongbo Zhang^{1,2} 

¹Pharmaceutical Sciences Laboratory, Åbo Akademi University, Turku, Finland

²Turku Bioscience Centre, University of Turku and Åbo Akademi University, Turku, Finland

³Southern Medical University Affiliated Fengxian Hospital, Shanghai, China

⁴Longgang District People's Hospital of Shenzhen, Shenzhen, China

Correspondence

Hongbo Zhang, Pharmaceutical Sciences Laboratory, Åbo Akademi University, Turku 20520, Finland.

Email: hongbo.zhang@abo.fi

Funding information

Suomen Akatemia, Grant/Award Numbers: 328933, 347897, 336355, 337531; Sigrid Juséliuksen Säätiö; National Natural Science Foundation of China, Grant/Award Number: 81871472; China Postdoctoral Science Foundation, Grant/Award Number: 2021M700830; the Finnish Ministry of Education and Culture funded international pilot project "Finland-China Food and Health Network"

Abstract

Triple-negative breast cancer (TNBC) is still the most aggressive cancer in women. Combination chemotherapy holds great potential for cancer therapy; however, the off-target and side effects of free chemotherapy administration remain a major challenge. In this study, we developed a photo/thermo-responsive nanoplatform that can be used for TNBC treatment via photothermal therapy in combination with multidrug therapy. By conjugating the chemotherapy drug PTX prodrug on the surface of mesoporous silica-coated gold nanorod nanoparticles and then loading another chemotherapy drug, CPT, the Au@MSN-PTX@CPT nanoparticles exhibited great photothermal response, redox response drug release and cancer cell inhibition abilities. Otherwise, we further coated the Au@MSN-PTX@CPT nanoparticle with a temperature-sensitive polymer poly(N-isopropylacrylamide-co-methacrylic acid) (p(NIPAM-co-MAAc)), and the polymer-coated Au@MSN-PTX@TPT@polymer nanoparticles showed perfect near-infrared (NIR) light controlled drug release. Finally, the Au@MSN-PTX@CPT@polymer nanoparticles were injected into the 4T1 breast cancer mouse model. The Au@MSN-PTX@CPT@polymer nanoparticles preferably accumulated at the tumor site and had reduced chemotherapy injuries and great antitumor activity when combined with 650 nm laser treatment. In summary, our developed Au@MSN-PTX@CPT@polymer nanoparticles served as a good method for controlled chemodrug delivery and provided a good choice for TNBC combination therapy.

KEYWORDS

combination chemotherapy, MSN, photothermal therapy, prodrug, TNBC

This is an open access article under the terms of the Creative Commons Attribution License, which permits use, distribution and reproduction in any medium, provided the original work is properly cited.

© 2022 The Authors. *Smart Medicine* published by Wiley-VCH GmbH on behalf of Wenzhou Institute, University of Chinese Academy of Sciences.

1 | INTRODUCTION

Triple-negative breast cancer (TNBC) is one of the most aggressive breast cancer subtypes and has high rates of recurrence and metastasis and a poor prognosis.¹ The main methods for breast cancer treatment include surgery, chemotherapy, hormonal therapy, and targeted drug therapy.^{1b} However, due to the lack expression of progesterone receptor (PR), estrogen receptor (ER) and human epidermal growth factor receptor 2 (HER2), TNBC does not respond to most developed breast cancer target drugs^{1a,2}; thus, chemotherapy is still the only option for TNBC patients.³ However, the treatment is unsatisfactory because of frequently occurring drug resistance, and the overall survival is only 10–13 months. Therefore, the development of new therapies for the treatment of TNBC is still in high demand.

Combination chemotherapy, the use of two or more chemotherapy drugs for cancer treatment, has emerged as a widely used method for cancer treatment in the clinic because of reduced chemotherapy drug administration and the potential synergistic antitumor activity of chemotherapy drugs.⁴ It was reported that the combined use of multiple chemotherapy drugs reduced drug resistance owing to its multiple antitumor activities. Targeting different cell pathways by the combination of several different chemotherapy drugs enhanced the antitumor effect.⁵ In addition, the cytotoxicity of chemotherapy drugs can be reduced via the selection using of certain chemotherapy drugs. For example, the toxicity of alkylating agents can be reduced by using euclidean compounds. Combination chemotherapy is also used for the treatment of breast cancer, for example, the commonly used regimens TAC (the combination of paclitaxel [PTX], doxorubicin [DOX] and cyclophosphamide [CTX]) and AT (the combination of DOX and PTX).⁶ Therefore, the combination therapy holds great potential for TNBC treatment.⁷ However, despite the big advantages of combination therapy, unexpected drug interactions and the special drug duration of action may also cause some irreversible side effects for the hosts. Therefore, the ratio of each combined chemotherapy drug needs to be controlled precisely. Otherwise, the order for chemotherapy drug administration should also be considered.⁸

Prodrugs are compounds that can be catalyzed into pharmacological molecules once they enter the human body.⁹ According to the modification methods, prodrugs can be divided into carrier-linked prodrugs and bioprecursor prodrugs. Both of these prodrug forms can be regarded as good strategies for improving bioavailability and stability, reducing side effects, and prolonging the

Key points

- PTX prodrug is synthesized for combination chemotherapy.
- A photo/thermos responsive nanoplatform for TNBC combination therapy is developed.
- Near-infrared (NIR) light-controlled drug release is realized.
- The nanoplatform exhibits redox responsive drug release and preferred tumor tissue accumulation.
- It provides a good choice for TNBC treatment via photothermal therapy in combination with multidrug therapy.

release of certain drugs.¹⁰ For example, by introducing a trisulfide bond to DOX, a redox-sensitive nanoparticulate drug delivery system for cancer therapy was developed.¹¹ Moreover, by using heterotelechelic polymer prodrugs, the loading of both different chemotherapy drug combinations and different chemotherapy drug ratios in the same nanocarrier was realized.¹² Therefore, prodrug technology is an ideal choice for promoting combination chemotherapy.

In this study, to provide a good solution for combination chemotherapy-based TNBC treatment, we first conjugated a PTX prodrug on the surface of mesoporous silicon-coated gold nanorods (Au NRs) via disulfide bonds to form Au@MSN-PTX nanoparticles (NPs). The redox-sensitive disulfide bond can be catalyzed by the redox microenvironment of tumor tissue; therefore, PTX will be released to kill cancer cells. Meanwhile, the Au NRs in the core of Au@MSN-PTX NPs will also be able to generate a photothermal response under 980 nm laser irradiation. Thus, combination chemotherapy and photothermal therapy (PTT) are realized. Furthermore, another chemotherapy drug, camptothecin (CPT), was loaded into the MSN pore structures at the best PTX and CPT mass ratio prior to a temperature-sensitive polymer poly(N-isopropylacrylamide-co-methacrylic acid) (p(NIPAM-co-MAAc)) coating. Finally, the formed Au@MSN-PTX@CPT@polymer NPs exhibited a perfect photothermal response, redox-controlled PTX release and enhanced antitumor activity both *in vitro* and *in vivo*. In general, our developed Au@MSN-PTX@CPT@polymer NPs provided a good solution for combination chemotherapy and PTT-based cancer treatment and offered an ideal nanocarrier for controlled release of chemotherapy drugs.

2 | RESULTS AND DISCUSSION

2.1 | PTX-SS-COOH synthesis and characterization

According to our previous protocol,¹³ the disulfide bond was first introduced to PTX for the prodrug form PTX-SS-COOH via a one-step reaction under a DTDP environment (Figure 1A). As shown in Figure 1B, the ¹H NMR spectra analysis result showed new peaks occurred in the range of 2.5–3.0 ppm, which indicated that the redox-sensitive linker DTDP was successfully linked to the PTX molecule.

2.2 | Au nanorod and Au@MSN-PTX@CPT@polymer NPs preparation and characterization

Next, the Au NRs were first prepared by a seed-mediated growth method in a cetyltrimethylammonium bromide

(CTAB) environment as described previously.¹⁴ After that, the harvested Au NRs were kept in another CTAB environment to generate the MSN layer growth. Subsequently, the PTX-SS-COOH and Au@MSN-NH₂ NPs were conjugated via activated –COOH and –NH₂ groups.¹⁵ Then, the collected Au@MSN-PTX NPs were coincubated with CPT in DMSO overnight for CPT loading. Finally, the p(NIPAM-co-MAAc) polymer was further coated onto the Au@MSN-PTX@CPT NPs in the water solution to block the release of both PTX and CPT.

As the result shown in Figures 1C–E, 2A and S1, the particle size of the synthesized Au NRs was 65.7 ± 10.3 nm with a corresponding zeta potential of 9.7 ± 0.7 mV. While after MSN layer growth, a pore structure layer appeared on the surface of the Au NRs, and the particle size increased up to 101.2 ± 15.8 nm. And the zeta potential was increased to 29.5 ± 0.7 mV, which was attributed to the ionizable –NH₂ groups on the surface of MSN. After that, PTX and CPT loading, as well as the p(NIPAM-co-MAAc) polymer coating, made the

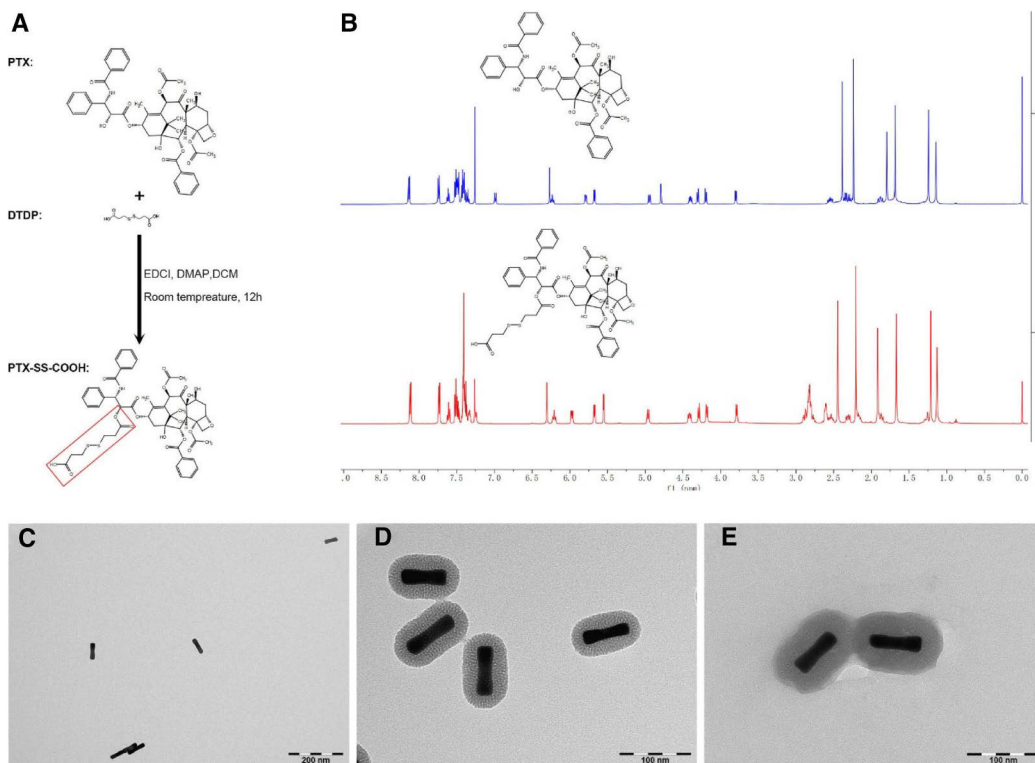


FIGURE 1 PTX-SS-COOH prodrug synthesis and characterization and the morphologies of Au@MSN-PTX@CPT@polymer NPs. (A) Schematic of PTX-SS-COOH synthesis; (B) ¹H NMR spectra analysis results; TEM images of Au NRs (C), Au@MSN NPs (D) and Au@MSN-PTX@CPT@polymer NPs (E).

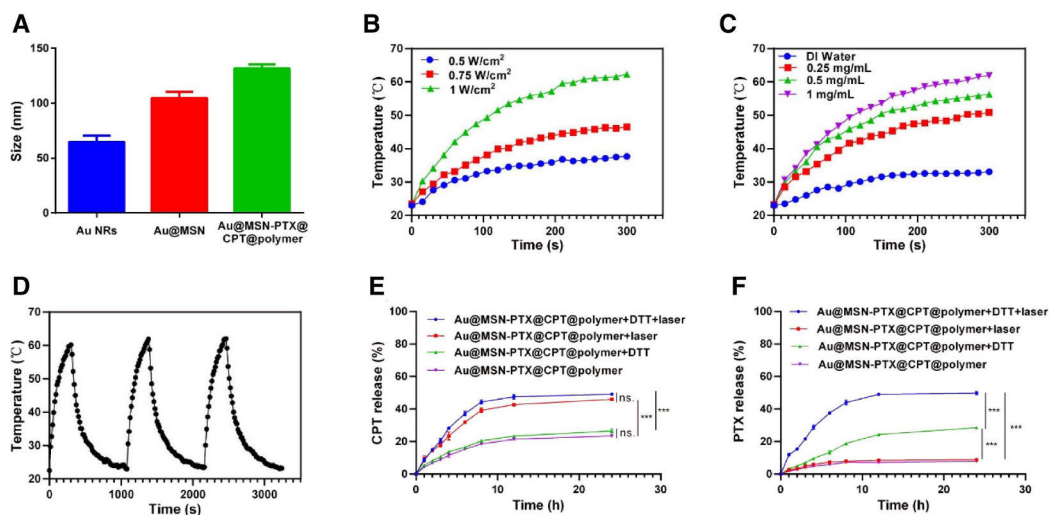


FIGURE 2 Particle size, photothermal response and drug release of Au@MSN-PTX@CPT@polymer NPs. (A) Particle size of Au NRs, Au@MSN and Au@MSN-PTX@CPT@polymer NPs; Photothermal cure of different powers of 980 nm laser treatment (B) and different concentrations of Au@MSN-PTX@CPT@polymer NPs (C); (D) Photothermal cure of three cycles of NIR on-off irradiation (1.0 W/cm², 980 nm); CPT (E) and PTX (F) release profiles under DTT (10 mM) and 980 nm laser conditions.

pore MSN structure of Au@MSN-PTX@CPT@polymer NPs more compact, but the particle size only increased up to 130.2 ± 25.3 nm. Interestingly, the zeta potential of Au@MSN-PTX@CPT@polymer NPs was decreased to 14.1 ± 0.7 mV. We believe that this is mainly because PTX-SS-COOH interacted with the $-NH_2$ groups.

As we hypothesized, the Au NRs can generate a photothermal response, which can be used to combine chemotherapy and PTT, and can also control CPT and PTX release. Therefore, we next performed NIR excitation assays to evaluate the photothermal performance of Au@MSN-PTX@CPT@polymer NPs. As the result shown in Figure 2B–D, the photothermal conversion by Au@MSN-PTX@CPT@polymer NPs occurred in a laser power- and concentration-dependent manner. The highest temperature of 64°C was produced by a 1 W/cm² laser and 1 mg/ml Au@MSN-PTX@CPT@polymer NPs at 300 s. Moreover, a three NIR on-off irradiation cycle assay also showed that the photothermal conversion ability of Au@MSN-PTX@CPT@polymer NPs was repeatable and without attenuation. All of these results indicated that the Au@MSN-PTX@CPT@polymer NPs had perfect photothermal performance. Subsequently, we tested the temperature-sensitive polymer p(NIPAM-co-MAAc) and redox environment controlled drug release. As shown in Figure 2E,F, the CPT release was significantly increased by laser irradiation but not dithiothreitol (DTT). Meanwhile, the PTX release was significantly

increased by DTT, while laser irradiation promoted PTX release only under DTT conditions. Since the existence of DTT can best mimic the redox environment, the PTX release only under DTT conditions can be attributed to the disulfide bond breakage under redox catalysis. Overall, these results demonstrated that the Au@MSN-PTX@CPT@polymer NPs had temperature- and redox-controlled drug releases.

2.3 | Cell uptake and lysosomal escape of Au@MSN-PTX@CPT@polymer NPs

Previously, we showed that the Au@MSN-PTX@CPT@polymer NPs had perfect photothermal performance and controlled drug release. To further investigate whether Au@MSN-PTX@CPT@polymer NPs can be used for cancer treatment, we further performed cell uptake and lysosomal escape assays to distinguish the interactions between cancer cells and Au@MSN-PTX@CPT@polymer NPs. Considering that CPT can be excited by 365 nm UV-light and can emit blue fluorescence at 430 nm, therefore, MDA-MB-231 cells after treated with PBS, 10 μg/ml CPT, 10 μg/ml PTX + CPT (mass ratio 1:1), Au@MSN-PTX@CPT (equal to 10 μg/ml CPT) and Au@MSN-PTX@CPT@polymer NPs (equal to 10 μg/ml CPT) for 24 h were collected to count the CPT-positive cells by a flow cytometer. As the result shown in Figure 3A,B, the

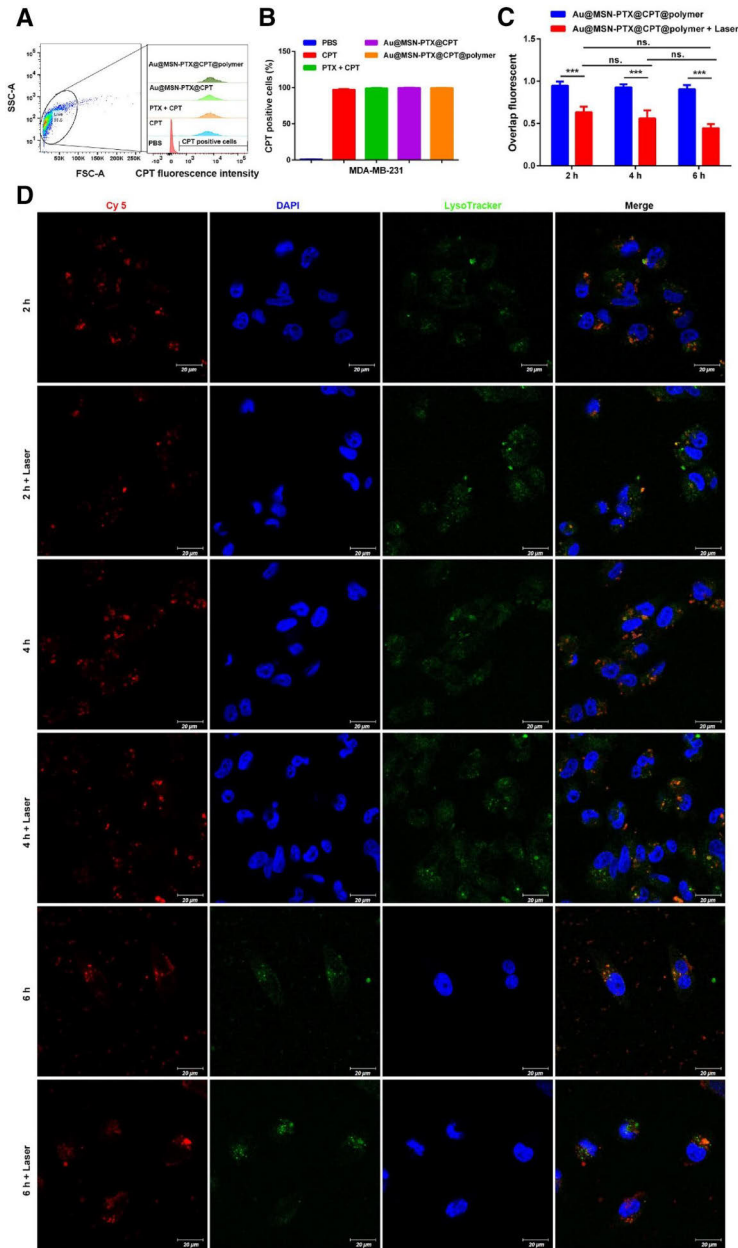


FIGURE 3 Cell uptake and lysosomal escape of Au@MSN-PTX@CPT@polymer NPs. Flow cytometry analysis (A) and quantitative results (B) of CPT-positive cells; Overlap fluorescence (C) and confocal microscopy images (D) of MDA-MB-231 cells after incubation with Cy 5-loaded Au@MSN-PTX@CPT@polymer NPs for 1–6 h with/without laser irradiation (red: Cy 5; green: LysoTracker; blue: DAPI; scale bar: 20 μm).

CPT-positive cells were all approximately 100% in all of the treated groups compared to PBS groups. The results indicated that Au@MSN-PTX@CPT and Au@MSN-PTX@CPT@polymer NPs can freely enter cells as free CPT after 24 h of co-incubation.

However, the lysosomal escape results showed that (Figure 3C,D) the overlap of Cy 5-labeled Au@MSN-PTX@CPT@polymer NPs and LysoTracker was decreased by laser irradiation at all time points, but the overlap decrease followed by incubation time was not significant. The results indicated that laser irradiation is a key promoter of Au@MSN-PTX@CPT@polymer NPs lysosomal escape.

2.4 | Antitumor activity of Au@MSN-PTX@CPT@polymer NPs at the cellular level

To determine whether there are synergistic antitumor effects of CPT and PTX, we treated MDA-MB-231 cells in a logarithmic growth phase with a total of 10 $\mu\text{g/ml}$ PTX + CPT (containing 0%–100% PTX). As shown in

Figure S4, only 70.07% of MDA-MB-231 cells survived after treatment with PTX + CPT (containing 50% PTX) for 48 h, which is the most significant group leading to MDA-MB-231 cell growth inhibition. Compared to 94.8% and 72.3% survival rates in the 10 $\mu\text{g/ml}$ CPT- and 10 $\mu\text{g/ml}$ PTX + CPT (containing 50% PTX) obviously enhanced MDA-MB-231 inhibition. Therefore, we controlled the loading of CPT into Au@MSN-PTX@CPT@polymer NPs at a CPT and PTX mass ratio of 1:1 for the final nanoformulation to realize the best antitumor effect.

Next, we evaluated the antitumor effect on TNBC tissue-derived MDA-MB-231 and normal breast tissue-derived MCF-10 cells by WST-1 cell proliferation assay and Annexin V and PI double staining apoptosis assay. The results in Figure 4A,B show that there was no obvious cytotoxicity of Au@MSN-PTX@CPT@polymer NPs in MCF-10A cells. While compared with Au@MSN + Laser and Au@MSN-PTX@CPT@polymer NPs-treated groups, the cell viability of Au@MSN-PTX@CPT@polymer + Laser-treated MDA-MB-231 cells was significantly decreased to 28.3%. And the apoptosis analysis results in Figure 4C,D show that Annexin

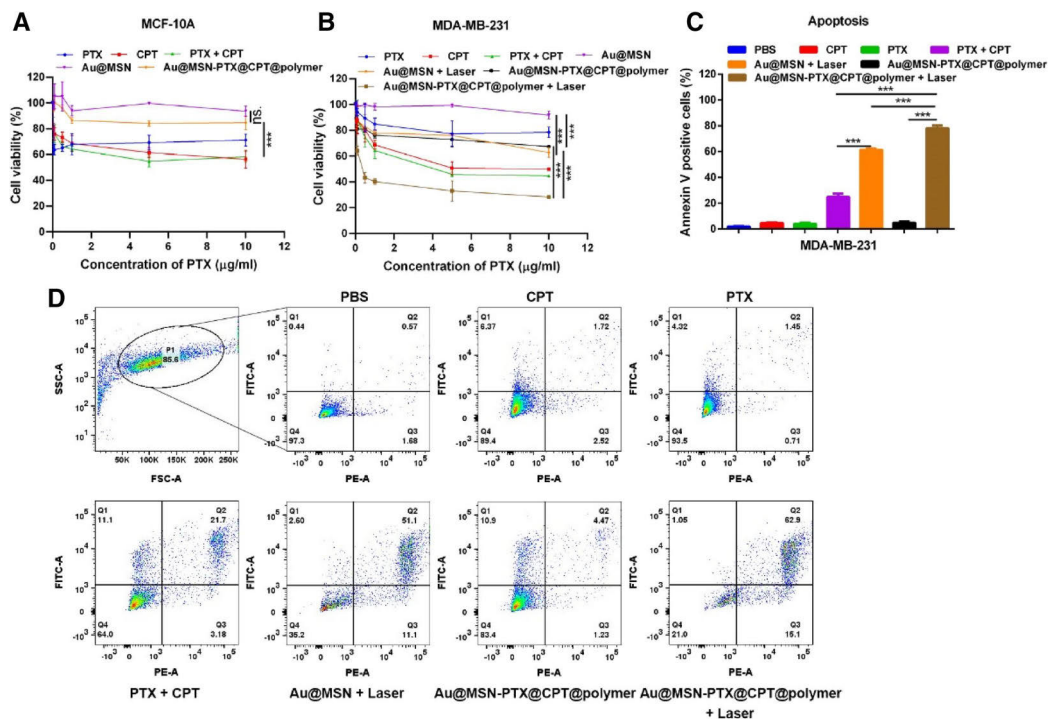


FIGURE 4 Antitumor activity of Au@MSN-PTX@CPT@polymer NPs at the cellular level. Cell viability (A, B) and apoptosis analysis (C, D) after treatment with each formulation for 48 h.

V-positive cells were significantly increased in Au@MSN + Laser and Au@MSN-PTX@CPT@polymer + Laser-treated groups after 48 h of co-incubation. However, the increase was not significant in the Au@MSN-PTX@CPT@polymer NPs-only treated group. Moreover, the Annexin V-positive cells in the Au@MSN-PTX@CPT@polymer + Laser-treated group was the highest at 78.5%. These results indicated that Au@MSN-PTX@CPT@polymer + Laser was the most efficient treatment for MDA-MB-231 cell inhibition.

2.5 | In vivo distribution of Au@MSN-PTX@CPT@polymer NPs

In order to further evaluate the antitumor activity of Au@MSN-PTX@CPT@polymer NPs in vivo, we first measured the biodistribution in a mouse TNBC tissue-derived 4T1 cell-formed xenograft mouse model. After injection with 5 mg/kg Au@MSN-PTX@CPT@polymer NPs (equal to 5 mg/kg CPT) through the tail vein for interval times, the mice were first anaesthetized for CPT fluorescence signal analysis with an in vivo imaging system (IVIS). After that, the mice were sacrificed for the main organs and tumor tissue imaging. The results in Figure 5A,B show that the Au@MSN-PTX@CPT@polymer NPs were highly accumulated in tumor tissues only after 1 h of tail vein administration. And the accumulation of Au@MSN-PTX@CPT@polymer NPs in tumor tissues was gradually increased within 24 h. Interestingly, the amount of Au@MSN-PTX@CPT@polymer NPs in the liver, kidney and heart was kept at a low level within 24 h. Except for the enhanced permeability and retention (EPR) effect of NPs, this might also be caused by the

coated p(NIPAM-co-MAAc) polymer, but this still needs to be further verified.

2.6 | In vivo antitumor activity and cytotoxicity of Au@MSN-PTX@CPT@polymer NPs

Finally, we evaluated the antitumor activity of Au@MSN-PTX@CPT@polymer NPs in a 4T1 cell-formed xenograft mouse model. The treatment was performed by tail vein injection of 5 mg/ml CPT + PTX or Au@MSN-PTX@CPT@polymer NPs every 3 days, and the next day, the tumor tissue was selectively irradiated by a 1 W/cm² 980 nm laser for 10 min. Tumor volume and mouse body weight were recorded. Once the largest tumor reached to 2 cm in size, the mice were sacrificed to harvest the tumor tissue and main organs. Finally, hematoxylin and eosin (HE) staining was performed to evaluate the cytotoxicity of Au@MSN-PTX@CPT@polymer NPs in vivo.

As the results shown in Figure 6A-C, the tumor growth of the 4T1 mouse model was significantly inhibited by Au@MSN-PTX@CPT@polymer and Au@MSN-PTX@CPT@polymer + Laser treatment, and the treatment of Au@MSN-PTX@CPT@polymer + Laser was the most efficient. Moreover, there was no significant body weight change observed during the treatment, and the tumor/body weight ratio results exhibited significantly decreased values in both Au@MSN-PTX@CPT@polymer and Au@MSN-PTX@CPT@polymer + Laser-treated groups (Figure 6D). Furthermore, the HE staining results (Figure 6E,F) showed increased tumor tissue apoptosis in Au@MSN-PTX@CPT@polymer and Au@MSN-PTX@CPT@polymer + Laser-treated groups. Meanwhile, no

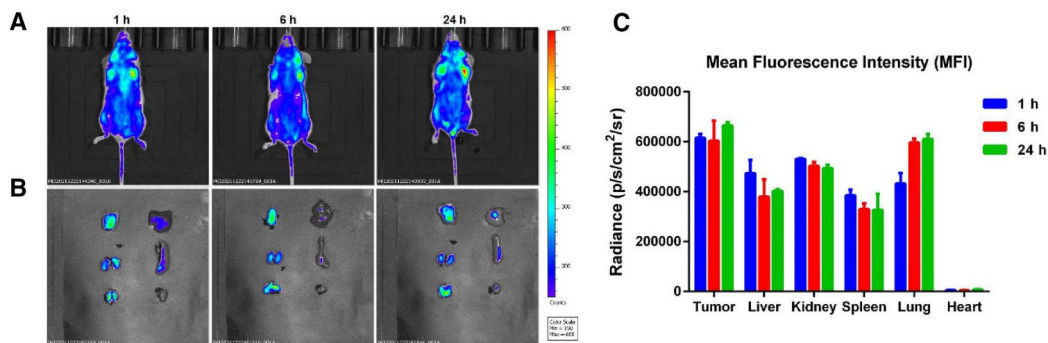


FIGURE 5 In vivo distribution of Au@MSN-PTX@CPT@polymer NPs after tail vein injection. Representative fluorescence images of tumor-bearing mice (A) and major organs (B) after injection with Au@MSN-PTX@CPT@polymer NPs for 1–24 h from the tail vein (the indicated order of organs in B is tumor, liver, kidney, spleen, lung and heart [from left to right, up to down]); (C) Mean fluorescence intensity of the main organs from each group.

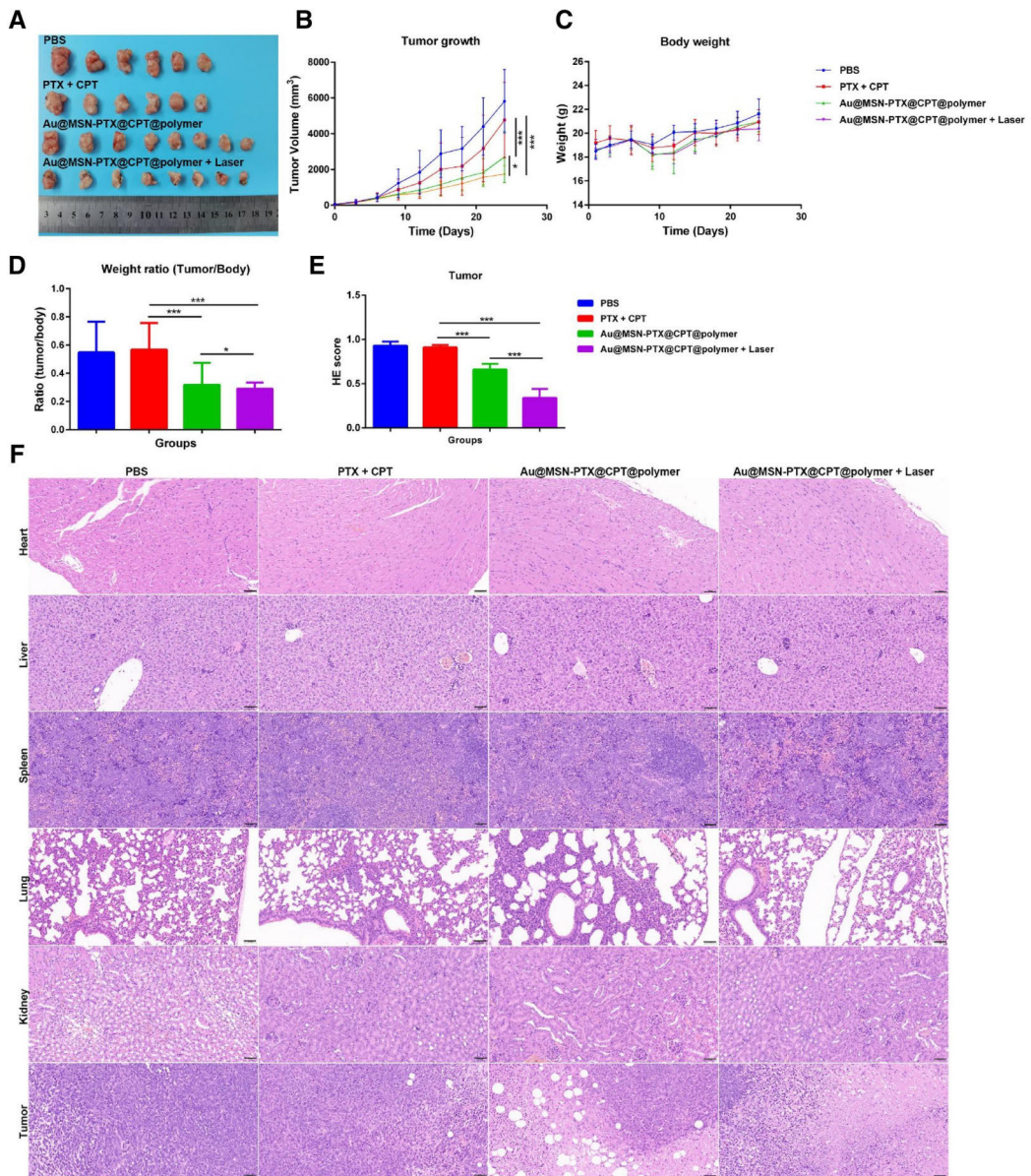


FIGURE 6 Antitumor activity and cytotoxicity of Au@MSN-PTX@CPT@polymer NPs in vivo. Tumor tissue (A), tumor growth (B), body weight (C) of mice and tumor/body weight ratio (D) of each formulation treated xenograft mouse model; HE score (E) of tumor tissues and main organs HE staining (F). (Scale bar: 50 μ m).

obvious organ damage occurred in any of the treated groups. All of these results demonstrated that Au@MSN-PTX@CPT@polymer NPs have good antitumor activity

and biocompatibility in vivo, and enhanced antitumor effects can be achieved when combined with 980 nm laser irradiation.

3 | CONCLUSIONS

In summary, we have developed a redox-responsive and photothermic controlled CPT and PTX codelivery nanoplatform. The nanoplatform Au@MSN-PTX@CPT@polymer showed perfect photothermal conversion ability and exhibited great antitumor activity both in vitro and in vivo. Moreover, combination chemotherapy and PTT were realized, and the enhanced antitumor activity was achieved. In general, our developed Au@MSN-PTX@CPT@polymer NPs provide a controlled chemotherapy drug intracellular delivery nanoplatform and give a good solution for TNBC combination therapy.

4 | EXPERIMENTAL METHODS

4.1 | PTX-SS-COOH prodrug synthesis

The synthesis of PTX-SS-COOH prodrug was generated by an esterification reaction between PTX and 3,3'-dithiodipropionic acid (DTDP). Briefly, 1.0 g PTX, 295.47 mg DTDP, 171.68 mg 4-dimethylaminopyridine (DMAP) and 268.51 mg 1-ethyl-3-(3-dimethylaminopropyl) carbodiimide (EDCI) were robustly dissolved in 20 ml DCM and stirred at room temperature for 12 h. After that, the reaction was stopped, and PTX-SS-COOH prodrug was purified by a silica gel column. And the ¹H NMR spectra of PTX-SS-COOH prodrug was detected.

4.2 | Au@MSN-PTX@CPT@polymer NPs preparation and characterization

The Au NRs and Au@MSN-NH₂ NPs were prepared by the seed-mediated growth method as described previously.¹³ After that, Au@MSN-NH₂ NPs, PTX-SS-COOH prodrug, EDCI and DMAP were dissolved in deionized water and stirred at room temperature for 12 h. Then, the Au@MSN-PTX NPs were collected and washed three times with deionized water. Next, Au@MSN-PTX NPs were first stirred with CPT in DMSO for one night and then stirred with p(NIPAM-co-MAAc) in deionized water for another night. Finally, the Au@MSN-PTX@CPT@polymer NPs were collected and characterized by DLS and TEM microscopy.

4.3 | Drug release assay

Drug release assays were performed with a 10 mM DTT solution. Briefly, 5 mg Au@MSN-PTX@CPT@polymer NPs were first dissolved in 1 ml of 10 mM DTT solution

and then equally divided into 10 1.5 ml EP tubes. At the indicated time points of 1, 2, 3, 4, 6, 8, 12 and 24 h, the Au@MSN-PTX@CPT@polymer NP dispersed solution was centrifuged at 13,000 rpm for 20 min after irradiation with a 1 W/cm² 980 nm laser for 10 min. Subsequently, 10 μl of supernatant was taken for CPT and PTX measurement by a Nanodrop 2000 (Thermo).

4.4 | Cell culture

MCF-10A and MDA-MB-231 cells were purchased from American Type Culture Collection (ATCC). MCF-10A cells were cultured with an MEBM cell culture medium kit. MDA-MB-231 cells were cultured in DMEM and supplemented with 10% FBS and 1% PS. And all cells were maintained in an atmosphere of 5% CO₂ and 37°C.

4.5 | Cell viability assay

The cell viability was measured with a WST-1 kit. Briefly, cells were first seeded in to a 96-well plate at the density of 5000 per well. And next, different amounts of NPs dispersed in the Opti-MEM medium were added to the cultured cells the next day. Twenty-four hours later, cells were selectively treated with 1 W/cm² 980 nm laser for 10 min. And 10 μl per well of WST-1 solution was added to the cultured cells the next day. And after 2 h of further incubation at 37°C, the absorbance (Ab) of each well at 450 nm was measured with a scanning multiwell spectrophotometer. The cell viability was calculated by Cell viability (%) = $\frac{Ab \text{ value (experimet group)}}{Ab \text{ value (control group)}} \times 100\%$. All the experiments were performed in three independent assays, and $p < 0.05$ was considered as significant.

4.6 | Flow cytometry assay

First, MDA-MB-231 cells were seeded in 12-well plates at a density of 1.5×10^5 per well. The next day, different NP formulations were added to the cells (equal to 10 μg/ml CPT) and incubated for 2–6 h. After that, the cells were washed with PBS and harvested for analysis. And DAPI channel was used for the analysis.

4.7 | Lysosomal escape assay

Briefly, MDA-MB-231 cells were first seeded in 3 cm glass dishes at a density of 3.0×10^5 per dish for 24 h. Next, Au@MSN-PTX@CPT@polymer NPs labeled with Cy 5 during the synthesis were added to the cells (equal to

10 µg/ml CPT) and incubated for 2–6 h. After that, cells were washed with PBS, and the cell culture medium was replaced with a fresh medium containing 10 mM Lyso-Tracker green dye (Thermo, L7526). Three hours later, the cells were fixed by 4% PFA and stained with 5 µg/ml DAPI. Finally, the cells were imaged by ZEISS LSM880 confocal microscopy.

4.8 | Animal experiment

All of the animal experiments and operations were conducted by following the guidelines and were approved by the Animal Research Committee of Shanghai Jiao Tong University School of Medicine, China (SHZY-202110262). The animal study was performed with 4T1 xenograft mouse models. Briefly, 1×10^6 4T1 cells in PBS were first injected into the axillary fat pad of 5-week-old female nude mice. Once the tumor volume reached to 80 mm³, the mice were randomly divided into five groups (six in each group). Among them, one group of the mice was injected with 10 mg/kg Au@MSN-PTX@CPT@polymer NPs (equal to 10 mg/ml CPT) through the tail vein, and the in vivo distribution of Au@MSN-PTX@polymer NPs at 1, 6 and 24 h was detected by an IVIS Lumina imaging system (Capiler). Two another groups were administrated with PBS and 5 mg/kg CPT + PTX (ratio of 1:1), and the two remaining groups were all administrated with 5 mg/kg Au@MSN-PTX@CPT@polymer NPs (equal to 5 mg/ml CPT) through the tail vein every 3 days. The next day, the tumors from one Au@MSN-PTX@CPT@polymer NPs-administrated group were treated with a 1 W/cm² 980 nm laser for 10 min. The body weight and tumor growth were recorded. And the mice were sacrificed once the largest tumor diameter reached 2 cm. Finally, tumor tissues and main organs were obtained, and an HE staining assay was performed.

4.9 | Statistical analysis

Both quantified data and nonquantified data were collected from triplicate independent experiments. The confocal images were quantified using Image J software. The data analysis and graphical work were performed with GraphPad and SPSS 20.0 software. $p < 0.05$ was considered as significant (* represent $p < 0.05$; ** represent $p < 0.01$; *** represent $p < 0.001$).

AUTHOR CONTRIBUTIONS

Wenhui Zhou: Experiment design, Cell experiment, data analysis, illustration drawing, original draft preparation

and manuscript revision. Xiaodong Ma: Materials synthesis, experiment design, Cell experiment, data analysis, manuscript revision. Jie Wang: Animal experiment. Xiaoyu Xu: Experiment design, manuscript revision. Oliver Koivisto: Manuscript revision. Jing Feng: Data analysis, manuscript revision. Tapani Viitala: Manuscript revision. Hongbo Zhang: Experiment design, provided funding for this project, manuscript revision.

ACKNOWLEDGMENT

Imaging/flow cytometry was performed at the Cell Imaging and Cytometry core at Turku Bioscience Centre, which is supported by Biocenter Finland. This work was support by grants from China Postdoctoral Science Foundation (2021M700830), National Natural Science Foundation of China (81871472 to Hongbo Zhang); the research Fellow (Grant No. 328933), research project (347897), solutions for Health Profile (336355), INFLAMES Flagship (337531) grants from Academy of Finland; the Finland China Food and Health International Pilot Project funded by the Finnish Ministry of Education and Culture, as well as Sigrid Jusélius Foundation (Finland).

CONFLICT OF INTEREST

The authors declare no conflict of interest. Hongbo Zhang is a member of the *Smart Medicine* editorial board.

ETHICS STATEMENT

The project of use and care of the animals in this research “Co-delivery CPT and PTX prodrug with a photo/thermo-responsive nanoplatform for breast cancer therapy” which was undertaken by Shanghai Jiao Tong University School of Medicine (project leader: Hongbo Zhang) was reviewed and approved by the Institutional Review Board. Animals using in the research were given to the appropriateness of experimental procedures. All animals were lawfully acquired and their retention and use were in every case in compliance with federal, state and local laws and regulations, and in accordance with the Institutional Animal Care and Use Committee of SHZY(IACUC) Guide for Care and Use of Laboratory Animals.

Animals used in this research were received every consideration for their comfort and properly housed, fed, and their surroundings kept in a sanitary condition.

The use of animals was in accordance with the IACUC Guide for Care and Use of Laboratory Animals. The minimal number of mice during the experiment was used in the experiments. Appropriate anesthetics were used to eliminate sensibility to pain during all surgical procedures.

ORCID

Hongbo Zhang  <https://orcid.org/0000-0002-1071-4416>

REFERENCES

1. a) X. Bai, J. Ni, J. Beretov, P. Graham, Y. Li, *Cancer Lett.* **2021**, *497*, 100; b) A. N. Giaquinto, H. Sung, K. D. Miller, J. L. Kramer, L. A. Newman, A. Minihan, A. Jemal, R. L. Siegel, *CA Cancer J. Clin.* **2022**, *72*, 524.
2. a) G. Bianchini, C. De Angelis, L. Licata, L. Gianni, *Nat. Rev. Clin. Oncol.* **2022**, *19*, 91; b) P. Zagami, L. A. Carey, *NPJ Breast Cancer* **2022**, *8*, 95.
3. S. Y. Hwang, S. Park, Y. Kwon, *Pharmacol. Ther.* **2019**, *199*, 30.
4. a) A. E. Pomeroy, E. V. Schmidt, P. K. Sorger, A. C. Palmer, *Trends Cancer* **2022**, *8*, 915; b) P. Jaaks, E. A. Coker, D. J. Vis, O. Edwards, E. F. Carpenter, S. M. Leto, L. Dwane, F. Sassi, H. Lightfoot, S. Barthorpe, D. van der Meer, W. Yang, A. Beck, T. Mironenko, C. Hall, J. Hall, I. Mali, L. Richardson, C. Tolley, J. Morris, F. Thomas, E. Lleshi, N. Aben, C. H. Benes, A. Bertotti, L. Trusolino, L. Wessels, M. J. Garnett, *Nature* **2022**, *603*, 166; c) M. Arora, J. M. Bogenberger, A. M. Abdelrahman, J. Yonkus, R. Alva-Ruiz, J. L. Leiting, X. Chen, P. L. Serrano Uson Junior, C. R. Dumbauld, A. T. Baker, S. I. Gamb, J. B. Egan, Y. Zhou, B. M. Nagalo, N. Meurice, E. L. Eskelinen, M. A. Salomao, H. E. Kosiorek, E. Braggio, M. T. Barrett, K. H. Buetow, M. B. Sonbol, A. S. Mansfield, L. R. Roberts, T. S. Bekaii-Saab, D. H. Ahn, M. J. Truty, M. J. Borad, *Hepatology* **2022**, *75*, 43.
5. L. Huang, S. Zhao, F. Fang, T. Xu, M. Lan, J. Zhang, *Bio-materials* **2021**, *268*, 120557.
6. F. A. Fisusi, E. O. Akala, *Pharm. Nanotechnol.* **2019**, *7*, 3.
7. a) N. Tray, J. Taff, S. Adams, *Cancer Treat Rev.* **2019**, *79*, 101888; b) T. Wang, R. Narayanaswamy, H. Ren, V. P. Torchilin, *Cancer Biol. Ther.* **2016**, *17*, 698.
8. G. Wei, Y. Wang, G. Yang, Y. Wang, R. Ju, *Theranostics* **2021**, *11*, 6370.
9. a) S. Sheikh, D. Ernst, A. Keating, *Mol. Ther.* **2021**, *29*, 1716; b) B. Sun, C. Luo, W. Cui, J. Sun, Z. He, *J. Control. Release* **2017**, *264*, 145.
10. a) A. Xie, S. Hanif, J. Ouyang, Z. Tang, N. Kong, N. Y. Kim, B. Qi, D. Patel, B. Shi, W. Tao, *EBioMedicine* **2020**, *56*, 102821; b) J. Qian, Z. Xu, C. Meng, Y. Liu, H. Wu, Y. Wang, J. Yang, H. Zheng, F. Ran, G. Liu, Y. Ling, *J. Med. Chem.* **2022**, *65*, 10393; c) L. Chen, W. Zhuang, C. Hu, T. Yu, X. Su, Z. Liang, G. Li, Y. Wang, *J. Mater. Chem. B* **2020**, *8*, 5645; d) C. Hu, W. Zhuang, T. Yu, L. Chen, Z. Liang, G. Li, Y. Wang, *J. Mater. Chem. B* **2020**, *8*, 5267.
11. Y. Yang, B. Sun, S. Zuo, X. Li, S. Zhou, L. Li, C. Luo, H. Liu, M. Cheng, Y. Wang, S. Wang, Z. He, J. Sun, *Sci. Adv.* **2020**, *6*, eabc1725.
12. D. Vinciguerra, M. Jacobs, S. Denis, J. Mougjin, Y. Guillaneuf, G. Lazzari, C. Zhu, S. Mura, P. Couvreur, J. Nicolas, *J. Control. Release* **2019**, *295*, 223.
13. L. Zhang, X. Ma, W. Zhou, Q. Wu, J. Yan, X. Xu, B. Ghimire, J. M. Rosenholm, J. Feng, D. Wang, H. Zhang, *Mater. Today Adv.* **2022**, *13*, 100199.
14. C. J. Murphy, H. Chang, P. Falagan-Lotsch, M. T. Gole, D. M. Hofmann, K. N. L. Hoang, S. M. McClain, S. M. Meyer, J. G. Turner, M. Unnikrishnan, M. Wu, X. Zhang, Y. Zhang, *Acc. Chem. Res.* **2019**, *52*, 2124.
15. J. Yan, X. Xu, J. Zhou, C. Liu, L. Zhang, D. Wang, F. Yang, H. Zhang, *ACS Appl. Bio Mater.* **2020**, *3*, 1216.

SUPPORTING INFORMATION

Additional supporting information can be found online in the Supporting Information section at the end of this article.

How to cite this article: W. Zhou, X. Ma, J. Wang, X. Xu, O. Koivisto, J. Feng, T. Viitala, H. Zhang, *Smart Med.* **2022**, *1*(1), e20220036. <https://doi.org/10.1002/SMMD.20220036>

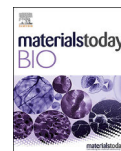
Minimally invasive injection of biomimetic Nano@Microgel for in situ ovarian cancer treatment through enhanced photodynamic reactions and photothermal combined therapy

Xiaodong Ma, **Wenhui Zhou**, Rong Zhang, Cancan Zhang, Jiaqi Yan, Jing Feng, Jessica M. Rosenholm, Tingyan Shi*, Xian Shen*, Hongbo Zhang*. *Materials Today Bio* **2023**; 100663.



Contents lists available at ScienceDirect

Materials Today Bio

journal homepage: www.journals.elsevier.com/materials-today-bio

Minimally invasive injection of biomimetic Nano@Microgel for in situ ovarian cancer treatment through enhanced photodynamic reactions and photothermal combined therapy



Xiaodong Ma^{a,e,f,1}, Wenhui Zhou^{d,e,f,1}, Rong Zhang^{c,d,1}, Cancan Zhang^d, Jiaqi Yan^{e,f}, Jing Feng^{d,g}, Jessica M. Rosenholm^{e,f}, Tingyan Shi^{c,***}, Xian Shen^{b,**}, Hongbo Zhang^{a,e,f,*}

^a Joint Centre of Translational Medicine, The First Affiliated Hospital of Wenzhou Medical University, Wenzhou, 325000, China

^b Department of General Surgery, The First Affiliated Hospital of Wenzhou Medical University, Wenzhou, 325000, China

^c Ovarian Cancer Program, Department of Gynecologic Oncology, Zhongshan Hospital, Fudan University, Shanghai, 200032, China

^d Southern Medical University Affiliated Fengxian Hospital, Shanghai, 201499, China

^e Pharmaceutical Sciences Laboratory, Åbo Akademi University, Turku, 20520, Finland

^f Turku Bioscience Centre, University of Turku and Åbo Akademi University, Turku, 20520, Finland

^g Longgang District People's Hospital of Shenzhen, Shenzhen, 518172, China

ARTICLE INFO

Keywords:

Gelatin methacryloyl
Photodynamic treatment
Photothermal treatment
Immunogenic cell death
Biomimetic Nano@Microgel

ABSTRACT

Photodynamic therapy (PDT) induces immunogenic cell death (ICD) by producing reactive oxygen species (ROS), making it an ideal method for cancer treatment. However, the extremely lower level of oxygen, short half-life of produced ROS, and limited photosensitizers accumulating in the tumor site via intravenous administration are the main reasons that limit the further application of PDT. To address these issues, we loaded the photosensitizer porphine (THPP) into biomimetic gold nanorod-mesoporous silica core-shell nanoparticles (Au-MSN NPs) to prepare Au@MSN/THPP@CM NPs. We then seeded the NPs together with catalase (CAT) into a gelatin methacryloyl (GelMA) microgel matrix to form Au@MSN-Ter/THPP@CM@GelMA/CAT microspheres consisting of biomimetic nano@microgel. The NPs and biomimetic nano@microgel exhibited enhanced photodynamic (PD) reaction and excellent photothermal conversion ability. Moreover, we further conjugated an endoplasmic reticulum (ER) targeting ligand Tosyl Ethylenediamine (Ter) on the surface of Au-MSN NPs. The results showed that both Au@MSN-Ter/THPP@CM NPs and the finally formed Au@MSN-Ter/THPP@CM@GelMA/CAT biomimetic nano@microgel induced precise and prolonged ER stress through photodynamic reactions, which stimulated the exposure of the proapoptotic calreticulin (CRT) on the cell membrane and increased the release of high mobility group box 1 (HMGB1) from the nucleus in SKOV3 cells under near-infrared (NIR) laser irradiation. Additionally, a single dose of the nano@microgel delivered through minimally invasive injection generated a significant anti-tumor effect in the SKOV3 cell line-derived orthotopic ovarian cancer mouse model through a PD and PT combination therapy. This study offers a new strategy for enhanced PDT and provides a PD/PT synergistic treatment method for ovarian cancer.

1. Introduction

Reactive oxygen species (ROS) are metabolic products produced by living cells and are often considered a double-edged sword [1,2]. Under normal conditions, ROS are mainly produced by mitochondria and

endoplasmic reticulum (ER) and are utilized for various cellular activities, such as activating phagocytes [3]. However, high ROS accumulation in cells caused by pathological conditions or external stimuli can trigger irreversible damage and ultimately lead to cell death [4,5]. Prolonged cell stress, such as high levels of ROS accumulation in the ER (ER

* Corresponding author. Joint Centre of Translational Medicine, The First Affiliated Hospital of Wenzhou Medical University, Wenzhou, 325000, China.

** Corresponding author.

*** Corresponding author.

E-mail addresses: shi.tingyan@zs-hospital.sh.cn (T. Shi), shenxian@wmu.edu.cn (X. Shen), hongbo.zhang@abo.fi (H. Zhang).

¹ These authors contributed equally to this work.

<https://doi.org/10.1016/j.mtbio.2023.100663>

Received 19 January 2023; Received in revised form 8 May 2023; Accepted 10 May 2023

Available online 18 May 2023

2590-0064/© 2023 The Authors. Published by Elsevier Ltd. This is an open access article under the CC BY license (<http://creativecommons.org/licenses/by/4.0/>).

stress), can induce immunogenic cell death (ICD) or immunogenic apoptosis, which further activate the anti-tumor immune response [6,7]. This has inspired many researchers to develop ROS-inducing methods for removing unnecessary cells from the body, especially cancer cells. For instance, Zhang has developed ROS-inducing nanoplateforms that can be activated by ultrasound and have demonstrated excellent potential for breast cancer treatment *in vitro* and *in vivo* [8]. Similarly, Gang has developed ROS-inducing nanozymes, showing great potential for breast cancer therapy [9]. Therefore, ROS-inducing has emerged as a promising strategy for cancer therapy.

Photodynamic therapy (PDT) is a promising topical treatment for ROS-based cancer therapy that uses singlet oxygen generated by excited photosensitizers under an appropriate light source to induce cell death [10–12]. However, the oxygen deficiency characteristic of tumors limits the ROS production by traditional photosensitizers administration. To address this issue, strategies have been developed to generate oxygen *in situ* or deliver exogenous oxygen. Generating oxygen *in situ* is a more reliable method for enhancing the PDT effect compared to unstable exogenous oxygen delivery. Recently, a reagent that catalyzes hydrogen peroxide (H_2O_2) to produce oxygen (O_2) has been used to enhance PDT because the concentration of H_2O_2 is much higher than that of superoxide anion (O_2^-) in cancer cells [13]. For instance, a dual nanozyme Au_2Pt -PEG-Ce6 has been shown to have catalase activity, which generates O_2 in cancer cells and has enhanced anti-tumor activity in cervical cancer models when combined with PDT therapy [14]. Encapsulating catalase (CAT) in temperature-dependent nanoformation RGD-BPNS@SMFN has achieved enhanced PDT effect and promising synergistic antitumor effects with photothermal therapy (PTT) [15]. Furthermore, CAT-loaded and HER-2 nanobody-conjugated nanoparticles have shown tremendous potential for ovarian cancer therapy [16]. Therefore, designing materials with catalase or catalase-like activity can be a useful strategy for enhancing the PDT effect.

However, the traditional method for administering photosensitizers is intravenous injection, which can result in uneven distribution throughout the body and increase metabolic stress. Furthermore, only a small amount of photosensitizers penetrating the tumor tissue can lead to limited therapeutic effects [17]. Over the past few decades, nano-delivery systems have become ideal vehicles for delivering functional cargoes, such as DNA, RNA, proteins, and small molecules, targeted to the tumor area due to their flexible structure design, excellent cargo loading capacity, and enhanced permeability and retention effect (EPR). Among these systems, biomimetic-designed nanoparticles, such as those designed to mimic cell surfaces, have attracted widespread interest for targeted intracellular drug delivery due to their excellent biocompatibility and targeting ability [18–20]. For instance, engineered cancer cell membrane-coated CLip-PC@CO-LC NPs have been shown to have great potential for combined RNAi and chemotherapy in the treatment of lung cancer [21]. Similarly, mesenchymal stem cell-derived nanoparticles containing Notch-1 suppressor have demonstrated significant potential for promoting hypoxia and inhibiting angiogenesis *in vitro* and *in vivo* [22]. Furthermore, the extensive homology and homing ability of cell camouflaging nanoparticles make them more easily hidden from the immune system and able to reach their target destination [23–25]. Therefore, cell camouflaging nanoparticles may offer a promising solution to address photosensitizer target loss during intravenous administration.

Inspired by our previous work, we have demonstrated that mesoporous silica-coated gold nanorod nanoparticles (Au@MSN NPs) have a wide range of applications in multi-drug delivery and PTT-based dual anti-tumor therapy [26]. In this study, we utilized Au@MSN NPs as a vehicle for intracellular delivery of a photosensitizer, Tetrakis (4-hydroxyphenyl)-porphine (THPP), to achieve PTT and PDT combined therapy using only one nanocarrier. However, the efficacy of PDT is limited by the short lifetime of ROS, particularly singlet oxygen, generated by the photosensitizer during PDT in biological systems. Additionally, the diffusion distance of ROS is limited to only 0.01–0.02 μm in

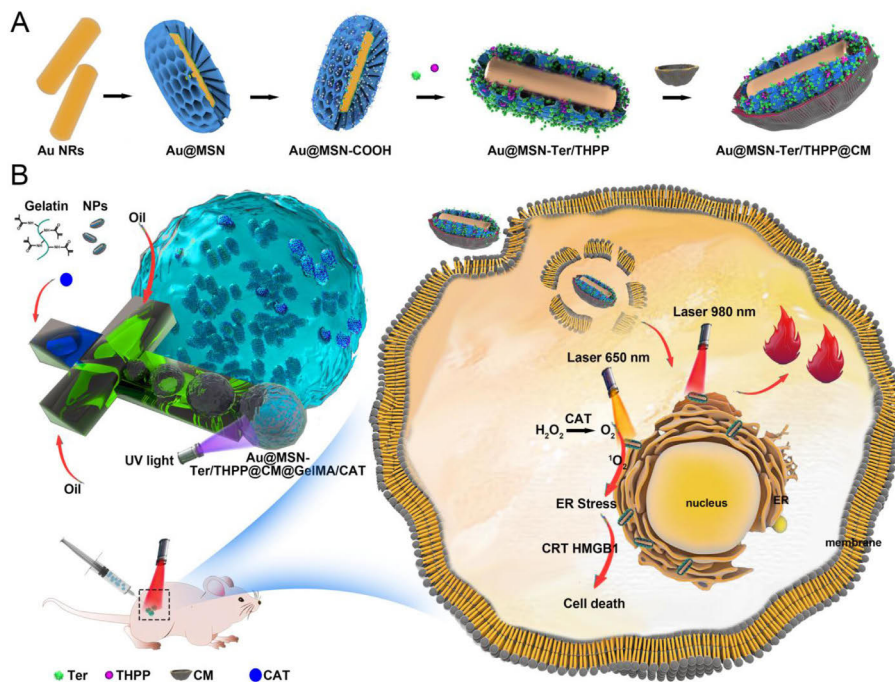
biological systems, which means the location of ROS production affects its therapeutic effect [27]. Therefore, the precise transportation of photosensitizers to important or fragile organelles, such as the endoplasmic reticulum (ER), allows the ROS produced by photosensitizers to accurately attack the "lethal sites" of cancer cells and achieve better therapeutic effects [28]. We conjugated an ER targeting ligand, Tosyl Ethylenediamine (Ter), on the surface of Au@MSN NPs to develop a more precise photosensitizer nano-delivery system for cancer treatment. Once the NPs enter the cancer cells, the Ter ligand can enable the THPP-loaded NPs to precisely move to the ER. Under laser irradiation, the constantly produced ROS will induce irreversible ER stress and activate the ICD. However, photosensitizers' accumulation in the tumor area by nanocarriers is limited due to nanoparticles' excretion in the kidney and preferred accumulation in the liver, requiring multiple intravenous administration of large doses to achieve long-term PDT therapeutic effects. Local administration of photosensitizers is a better method because the photosensitizers can directly reach the tumor site without relying on blood circulation, resulting in reduced side effects and higher efficiency [29]. Gelatin methacryloyl (GelMA) microgel, a gelatin derivative, is an ideal candidate for local administration of photosensitizers due to its good biocompatibility, good retention ability, and ability to cross-link by UV [30]. Therefore, we loaded our developed ER-targeting and PDT-generating biomimetic gold nanorod-mesoporous silica core-shell nanoparticles (Au@MSN-Ter/THPP@CM NPs) with CAT into the GelMA microgel on a microfluidic chip to form Au@MSN-Ter/THPP@CM@GelMA/CAT microspheres consisting of biomimetic nano@microgel. We expect this will enable more efficient administration of photosensitizers and enhanced PD reactions for cancer therapy.

Ovarian cancer remains one of the most malignant cancers affecting women, and effective treatments are needed urgently [31–33]. In order to develop a more effective photodynamic therapy (PDT) method for ovarian cancer, we evaluated the anti-tumor activity of our developed biomimetic nano@microgel systems, including Au@MSN-Ter/THPP@CM NPs and Au@MSN-Ter/THPP@CM@GelMA/CAT nano@microgel, in both *in vitro* and *in vivo* ovarian cancer models (Schematic Figure). The Au@MSN-Ter/THPP@CM NPs showed excellent photothermal conversion ability and were able to be taken up efficiently by ovarian cancer cells. We tested the anti-tumor activity of both Au@MSN-Ter/THPP@CM NPs and Au@MSN-Ter/THPP@CM@GelMA/CAT biomimetic nano@microgel, and found that both exhibited significant cell proliferation inhibition and cell death induction in ovarian cancer cells. Furthermore, we verified the design of CAT for oxygen production and ER-targeted THPP delivery, which led to more precise and enhanced PDT reactions in SKOV3 cells. Finally, in an orthotopic ovarian cancer mouse model, our newly designed Au@MSN-Ter/THPP@CM@GelMA/CAT microgel were able to provoke two ICD markers and demonstrated significant anti-tumor activity through a combination of PDT and photothermal therapy (PTT). Overall, our study suggests that the Au@MSN-Ter/THPP@CM@GelMA/CAT biomimetic nano@microgel may be a promising candidate for enhanced PDT and PTT combined therapy for ovarian cancer.

2. Materials and methods

2.1. Materials

Tetrakis (4-hydroxyphenyl)-porphine (THPP), Tosyl Ethylenediamine (TER), N-(3-dimethylaminopropyl)-N-ethylcarbodiimide hydrochloride (EDC-HCl), N-hydroxysuccinimide (NHS), 2-Hydroxy-4'-(2-hydroxyethoxy)-2-methylpropiophenone and Methacrylic anhydride were purchased from Tansoole (Shanghai, China). Sodium borohydride ($NaBH_4$), tetraethyl orthosilicate (TEOS), silver nitrate ($AgNO_3$), L-ascorbic acid, tetrachloroauric acid ($HAuCl_4$), cetyltrimethyl ammonium bromide (CTAB), succinic anhydride and Mineral oil were purchased from Sigma-Aldrich (Burlington, MA, US). Gelatin was purchased from Aamas (Shanghai, China).



Schematic Figure. The schematic of Au@MSN-Ter/THPP@CM NPs and Au@MSN-Ter/THPP@CM@GelMA/CAT microspheres preparation and working model.

2.2. AuNRs synthesis

The synthesis procedure for AuNRs followed the methodology outlined in our previous work. Initially, a balloon flask was used to mix 7.5 mL of 0.1 M CTAB solution and 0.25 mL of 0.01 M HAuCl₄ solution. The mixture was stirred for 5 min before the addition of 0.6 mL of 0.01 M cold NaBH₄ solution with vigorous stirring. Four hours later, a separate beaker was used to mix 20 mL of 0.01 M HAuCl₄, 4.8 mL of 0.01 M AgNO₃, 400 mL of 0.1 M CTAB, and 7.6 mL of 1 M HCl, which was stirred for 10 min at 30 °C. The resulting mixture was then quickly added to the stirring balloon flask along with 4 mL of 0.1 M ascorbic acid. Subsequently, 0.96 mL of the prepared gold seeds solution was added to the flask and left overnight. Finally, the AuNRs were collected by centrifugation and washed with deionized water.

2.3. Au@MSN-NH₂ and Au@MSN-COOH NPs synthesis

The collected AuNRs were firstly dispersed in deionized water and added to 50 mL of 1 mM CTAB aqueous solution. Next, the pH of the mixture was adjusted to pH 10–11 with 0.1 M NaOH, and then 1.4 mL of 20% (v/v) TEOS ethanol solution was added. After continuous stirring at 30 °C overnight, Au@MSN NPs were collected by centrifugation and washed with 0.6% (w/v) NH₄NO₃ ethanol solution. Finally, Au@MSN NPs were dispersed overnight in APTES containing ethanol solution to get the surface-activated Au@MSN-NH₂ NPs. And Au@MSN-NH₂ NPs were further dispersed in succinic anhydride containing DMF solution overnight under stirring to obtain Au@MSN-COOH NPs.

2.4. Synthesis of Au@MSN-Ter NPs and THPP loading

To prepare Au@MSN-Ter NPs, a mixture of Au@MSN-COOH NPs, Ter, NHS, and EDCI was stirred in DMF at room temperature overnight. The resulting mixture was then collected by centrifugation, and washed with DMF to obtain the Au@MSN-Ter NPs. Subsequently, the Au@MSN-Ter NPs were stirred with a THPP DMF solution overnight to complete the THPP loading process.

2.5. Cell culture

SKOV3 and NHDF cell lines were purchased from ATCC, and SKOV3 was cultured in 10% FBS and 1% PS containing McCoy's 5a Medium. NHDF cells were cultured in 10% FBS and 1% PS containing DMEM Medium. The OVCAR3 cell line was gifted from the laboratory of Research Program in Systems Oncology at the University of Helsinki and cultured in 10% FBS, 1% PS, and 0.01 mg/mL bovine insulin containing RPMI-1640 Medium. All cells were maintained in the incubator of 37 °C and 5% CO₂ atmosphere.

2.6. Cancer cell membrane extraction and NPs coating

SKOV3 cells were collected and washed three times with PBS and then incubated in tris buffer (containing 10 mM tris, 10 mM MgCl₂ and protease inhibitor) for 1 h at 4 °C. After that, the cells were sonicated for 10 min in an ice bath, and cell membrane fragments were obtained by differential centrifugation (500 g for 10 min, 10,000 g for 10 min). Then

the aqueous solution was frozen dried and stored at -20°C for further use. Next, the cancer cell membrane was mixed with different NPs in deionized water at 4°C and stirred overnight. Finally, the cell membrane coated Au@MSN-Ter/THPP@CM and Au@MSN/THPP@CM NPs were obtained by centrifuge.

2.7. GelMA, Au@MSN-Ter/THPP@CM@GelMA and Au@MSN-Ter/THPP@CM@GelMA/CAT microgel preparation

Firstly, 20 g of gelatin was dissolved in 200 mL PBS at 60°C . Next, 16 mL of MA was slowly pumped into the gelatin solution with a micro syringe pump at 0.25 mL/min. Two hours later, 200 mL PBS was added to terminate the reaction for 15 min. After that, the prepared GelMA solution was dialyzed (3500 MWCO dialysis bag) overnight at 38°C . And then, the GelMA solution was centrifuged at 37°C to remove the insoluble and continued dialysis for another 2 days. Finally, the prepared GelMA was frozen dried and stored in -80°C .

The Au@MSN-Ter/THPP@CM@GelMA and Au@MSN-Ter/THPP@CM@GelMA/CAT microgel were prepared in a microfluidic chip, which contains two different channels: internal flow was the mixture of 150 mg/mL GelMA, 10 mg/mL photocrosslinker, 5 mg/mL CAT and 10 mg/mL Au@MSN-Ter/THPP@CM; while the external flow contains of 5% Span 80 in mineral oil. And the Au@MSN-Ter/THPP@CM@GelMA and Au@MSN-Ter/THPP@CM@GelMA/CAT microspheres were produced with the external and internal flow rate of 12–1:1 and cured by UV light. Finally, the Au@MSN-Ter/THPP@CM@GelMA and Au@MSN-Ter/THPP@CM@GelMA/CAT microgel were collected by centrifuge and washed with 75% ethanol.

2.8. Cytotoxicity assay

SKOV3 and OVCAR3 cells were seeded at the density of 5000 per well of 96 well plate. The next day, different NPs formulations were added at indicated concentrations. 12 h later, the cells were selectively irradiated with $1\text{ W}/\text{cm}^2$ of 980 nm laser for 10 min and followed $0.4\text{ W}/\text{cm}^2$ of 650 nm laser for 5 min. And after 24 h, 10 μL of WST-1 reagent per well were added to test the cell viability.

2.9. IF staining assay

The cells were first co-incubated with different NPs formulations for indicated times and selectively treated with $0.4\text{ W}/\text{cm}^2$ of 650 nm laser for 5 min. 6 h later, the cells were washed with PBS and fixed with 4% PFA for 5 min. And then, the cells were washed with PBS three times and incubated with 1:500 diluted anti-CRT (Abcam) or anti-HMGB1 (Abcam) dilutions for 1 h at room temperature in dark. Next, cells were washed with PBS three times and stained with 5 mg/mL DAPI for 5 min. Finally, the images were captured by confocal microscope and analyzed by image J.

2.10. ROS detection

The cells were first co-incubated with Au@MSN-Ter/THPP@CM@GelMA/CAT or Au@MSN-Ter/THPP@CM@GelMA microgel for 48 h. After that, the cells were incubated with the reactive oxygen test dye DCFH-DA (10 μM) for 20 min, and followed irradiate with $0.4\text{ W}/\text{cm}^2$ of 650 nm laser for 5 min. Finally, the cell nuclei were labeled with Hoechst33342 and were observed by confocal microscope.

2.11. Cellular uptake, lysosomal escape and ER targeting assay

Au@MSN-Ter/THPP@CM and Au@MSN/THPP@CM NPs were used for cellular uptake. While fluoresce dye Cy5.5 was first labeled on the surface of Au@MSN-Ter@CM NPs, and then the cancer cells were incubated with Cy5.5 labeled NPs for indicated times. Next, ER-Tracker (1 μM) or lysosomal tracker was added to the culture medium and incubated

for 30–120 min at 37°C according to the protocol. After that, the cells were fixed with 4% PFA, washed and stained with DAPI for 5 min. Finally, the cells were observed by confocal microscope.

2.12. Calcein-AM and PI staining assay

Different formulations of Au@MSN-Ter/THPP@CM@GelMA/CAT and Au@MSN-Ter/THPP@CM@GelMA were firstly incubated with SKOV3 and OVCAR3 cells for 48 h, and then selectively treated with lasers according to the corresponding groups. 6 h later, Calcein-AM (2 μM) and PI (4.5 μM) were added to the culture medium and incubated for 20 min. The cells were observed by confocal microscope.

2.13. Flow cytometry assay

SKOV3 and OVCAR3 cells were firstly incubated with Au@MSN-Ter/THPP@CM@GelMA/CAT or Au@MSN-Ter/THPP@CM@GelMA for 48 h, and then selectively treated with lasers. 6 h later, cells were harvested and stained with Annexin V and PI according to the instructions of the kit, and the cells were analyzed by a flow cytometer.

2.14. Animal study

All animal experiments and operations followed the guideline and approved by the Animal Research Committee of Southern Medical University affiliated Fengxian Hospital, China (SHZY-2021102601). The animal study was performed with ovarian cancer orthotopic xenograft mouse models. Briefly, 2×10^5 SKOV3 cells in PBS were first injected into the axillary fat pad of 6 weeks old female nude mice. The primary SKOV3 tumors were surgically removed and cut into 3–4 mm small cubes under a cryogenic environment once the tumors reached to 2 cm diameter. Next, the small tumor cubes were further surgical placed into the ovarian tissues of 6 weeks old female nude mice.

One week late, the mice were randomly assigned into four groups (each group ≥ 6). Group A: injected with 100 μL of PBS from tail vein; Group B: injected with 100 μL of Au@MSN-Ter/THPP@CM NPs from tail vein; Group C and D: 30 μL of Au@MSN-Ter/THPP@CM@GelMA/CAT microgel were surgical injected into the tumor site once. The amount of Au@MSN-Ter/THPP@CM NPs and Au@MSN-Ter/THPP@CM@GelMA/CAT used for the animal study equals 2.5 mg/kg THPP. On the next day of different formulations injections, mice in Group A, B and C were first treated with $1\text{ W}/\text{cm}^2$ of 980 nm laser irradiation for 10 min, and followed by $0.4\text{ W}/\text{cm}^2$ of 650 nm laser irradiation for another 5 min at the tumor area. The mice continued treated with lasers once each three days, and the mice were sacrificed 15 days late. The main organs (including heart, liver, spleen, lung, and kidney) and tumor tissues were collected for further HE and IHC staining.

2.15. Statistical analysis

Both the quantified and none quantified data were collected from triplicated independent experiments. The confocal images were quantified by using the Image J software. The data analysis and graphical work were performed with GraphPad and SPSS 20.0 software. $P < 0.05$ was considered significant.

3. Results

3.1. Au@MSN and Au@MSN-Ter/THPP@CM NPs preparation and characterization

As we have described before, the Au@MSN NPs were prepared by two steps of seed mediated growth methods [26]. Subsequently, a small molecule Tosyl Ethylenediamine (Ter), which can be used for ER targeting was conjugated on the surface of aminated Au@MSN NPs via a linker, succinic anhydride. After washing, the THPP was further loaded

into the Au@MSN-Ter NPs by overnight incubation in DMF to form the Au@MSN-Ter/THPP NPs. Finally, the cell membrane extracted from Ovarian cancer SKOV3 cells was coated on to the NPs to form the biomimetic NPs Au@MSN-Ter/THPP@CM. As the TEM results shown in Fig. 1 A, the naked gold nanorods were evenly distributed in an aqueous solution with the size of 56.1 ± 5.3 nm. While after mesoporous silica layer growing on the surface of gold nanorods (Fig. 1 B) and both THPP and Ter conjugating, the size of Au@MSN-Ter/THPP NPs and Au@MSN-Ter/THPP@CM NPs (Fig. 1 C) were dramatically increased to 153.5 ± 14.3 nm and 178.6 ± 0.8 nm respectively (Fig. 1 E). The elemental mapping result of Au@MSN NPs in Fig. 1 D and Supplementary Fig. 1 also showed that Si tightly surrounded the Au. And after conjugating of Ter ligand on the surface of Au@MSN NPs, the Fourier transform IR analyzing result (FTIR, Supplementary Fig. 2) showed that the amino group on Ter disappears in Au@MSN-Ter NPs, there came a new

peak at 1631 cm^{-1} , which was caused by new introduced amido link. In addition, Zeta potential of Au@MSN NPs changed from -16.7 ± 0.35 to 33.8 ± 0.6 after Ter modification, and Zeta potential changed to -11.1 ± 0.32 after loading with THPP due to the excess hydroxyl group on THPP. These results demonstrate the success of Au@MSN-Ter synthesis and THPP loading. Moreover, after THPP loading and cell membrane coating, the original outlayer pore structure of Au@MSN NPs was coated with a condensed outlayer, and zeta potential of the corresponding nanoparticles also changed to -19.4 ± 1.2 which illustrate the successful wrapping of cancer cell membranes. (Fig. 1 C, F). Under the protection of cancer cell membrane, Au@MSN-Ter/THPP@CM NPs have good stability. When the nanoparticles were dispersed in the medium, the particle size remained stable within 10 days (Supplementary Fig. 3).

Subsequently, we tested the photothermal activity and singlet oxygen production of the prepared Au@MSN-Ter/THPP@CM NPs. SOSG was

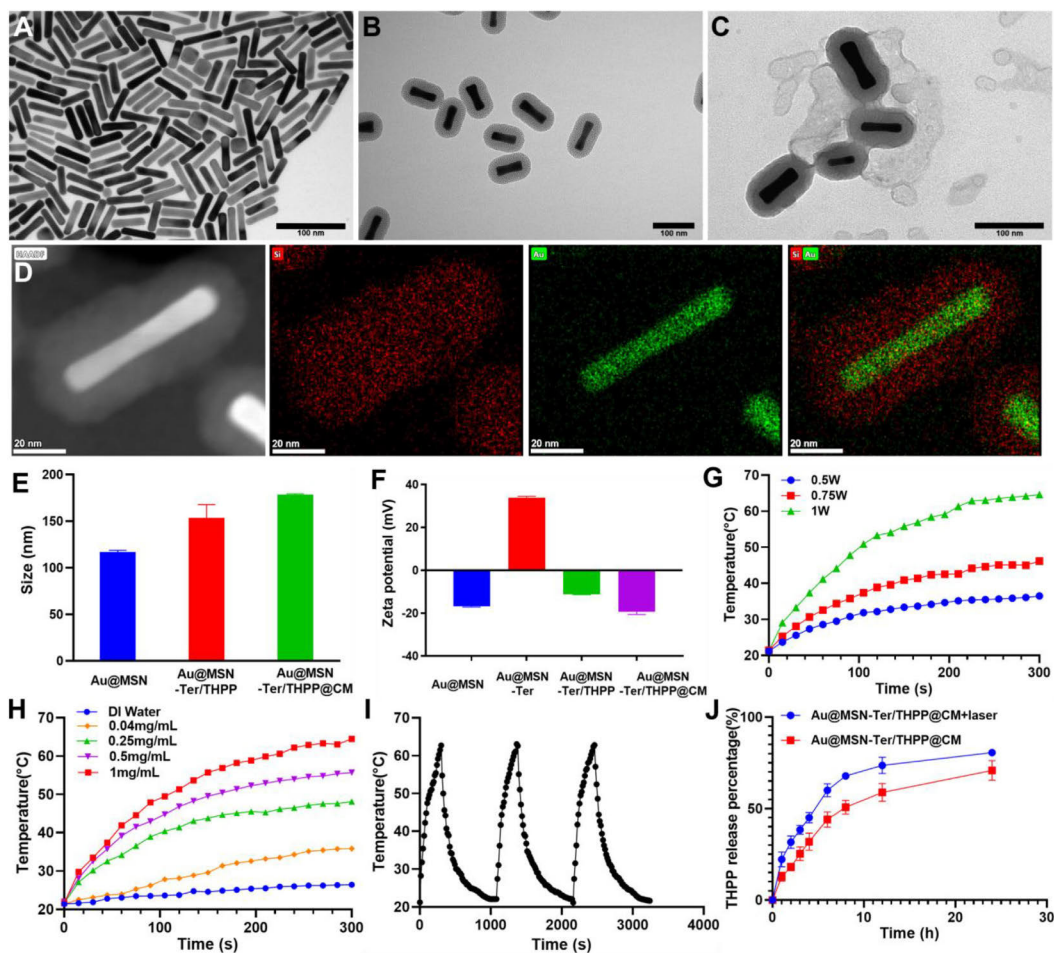


Fig. 1. Morphologies, photothermal effect and drug releasing of different NPs. A-C. TEM images of Au NRs, Au@MSN NPs, Au@MSN-Ter/THPP@CM NPs (Scale bar = 100 nm); D. Image of high-angle annular dark-field and elemental mapping of Au@MSN NPs (Scale bar = 20 nm); Particle size (E), Zeta-potential (F) and photothermal response of Au@MSN-Ter/THPP@CM NPs under 980 nm laser irradiation (G-I) (Total concentration of nanoparticles is used); J. THPP releasing from Au@MSN-Ter/THPP@CM NPs in PBS buffer with or without laser (980 nm, 1 W/cm², 10 min).

used as a probe to detect the generation of singlet oxygen. From Supplementary Fig. 4, under the 650 nm laser irradiation, SOSG fluorescence intensities of THPP group and Au@MSN-Ter/THPP@CM NPs group increased over time, the increase in NPs group is lower than that of THPP group, which might be due to the stacking of THPP in MSN. Photothermal activity of Au@MSN-Ter/THPP@CM NPs shown that, the temperature of 1 mg/mL NPs solution dramatically increased up to 64 °C by 1 W/cm² 980 nm laser irradiation for only 5 min, while only increased up to 36 °C under 0.5 W/cm² 980 nm laser irradiation (Fig. 1 G). And once the concentration of NPs decreased from 1 mg/mL to 0.5 mg/mL and 0.25 mg/mL, the temperature increased to 55 °C and 48 °C respectively by 1 W/cm² 980 nm laser irradiation for 5 min (Fig. 1 H). In addition, the NPs also had excellent photothermal stability, because there was no obvious temperature change happened in three repeated photothermal cycles. These results indicated that the excellent photothermal conversion ability of Au@MSN-Ter/THPP@CM NPs could be activated by 980 nm laser irradiation, and affected by NPs' concentration and irradiation time. Finally, we further evaluated THPP delivery efficiency of Au@MSN-Ter/THPP@CM NPs by the loading and releasing THPP from Au@MSN-Ter/THPP@CM NPs. As the results detected by a UV-Spectrophotometer, the THPP loading capacity and loading efficiency of Au@MSN-Ter/THPP@CM NPs were 11.5% and 73.2%. And as shown in Fig. 1 J, THPP releasing from Au@MSN-Ter/THPP@CM NPs was time-dependent and could reach 50.8 ± 3.8% at 8 h in 0.5% Tween 80 PBS buffer. While the total releasing of THPP was significantly ($p < 0.001$) increased up to 67.9 ± 1.8% under 980 nm laser (1 W/cm²) irradiation at 8 h time point (980 nm laser was treated before each time point). These results indicated that the Au@MSN-Ter/THPP@CM NPs had good THPP loading capability and sustained THPP releasing manner.

3.2. Cytotoxicity and cellular uptake of Au@MSN-Ter/THPP@CM NPs in ovarian cancer cells

We have verified the excellent photothermal conversion ability and sustained THPP release of Au@MSN-Ter/THPP@CM NPs, to further evaluate the inhibitory effect of different preparations on different ovarian cancer cells. We performed WST-1, flow cytometry and confocal microscopy assays to evaluate the cytotoxicity and cellular uptake of Au@MSN-Ter/THPP@CM NPs in Ovarian cancer cell lines OVCAR3 and SKOV3. As shown in Fig. 2 A and B, the cells viability was analyzed by WST1 assays after the cells were co-incubated with different NP formulations for 24 h and selectively treated with 980 nm (1 W/cm², 10 min) and 650 nm (0.4 W/cm², 5 min) lasers irradiation. It was shown that, in Au@MSN NPs groups, the cell viabilities in both OVCAR3 and SKOV3 cells were significantly decreased after 980 nm laser treatment, especially in the highest NPs concentration groups, which is attributed to the photothermal effect induced cell death. And for 5 μg/mL Au@MSN-Ter/THPP@CM NPs, 650 nm laser induced obvious cell viability change in OVCAR3 and SKOV3 cells. These results indicated that the Au@MSN-Ter/THPP@CM NPs can generate lethal level photodynamic reactions under 650 nm laser irradiation, and the Au@MSN-Ter/THPP@CM NPs have great potential for improved PDT. In addition, the cell viabilities of Au@MSN-Ter/THPP@CM NPs treated with both 980 nm and 650 nm lasers, had more significant cell viability change in both OVCAR3 and SKOV3 cells compared to single laser treatment, which were 7.7 ± 0.5% and 14.8 ± 6.4%, respectively. While, in normal human dermal fibroblasts NHDF cells (Supplementary Fig. 5), the cell viabilities of 5 μg/mL Au@MSN-Ter/THPP@CM NPs treated with both 980 nm and 650 nm lasers was 41.5 ± 2.8%, this indicated that the Au@MSN-Ter/THPP@CM NPs had tumor cell selectivity at some extent.

Next, we further utilized flow cytometry assay and confocal microscope to evaluate the intracellular behavior of Au@MSN-Ter/THPP and Au@MSN-Ter/THPP@CM NPs. As shown in Fig. 2, both confocal microscope imaging (Fig. 2 C and D) and flow cytometry analyzing results (Fig. 2 E and F) showed that the red THPP fluorescent signal represented Au@MSN-Ter/THPP and Au@MSN-Ter/THPP@CM NPs gathered in

SKOV3 cells after only 2 h co-incubation. We also noticed that, the red fluorescent positive cells and fluorescence intensity per cell were gradually increased by time in Au@MSN-Ter/THPP@CM NPs treated groups. And compared to SKOV3 cells (Supplementary Fig. 7), the red THPP fluorescent signal in OVCAR3 and NHDF cells (Supplementary Fig. 8) were less. No difference in THPP positive cells between Au@MSN-Ter/THPP and Au@MSN-Ter/THPP@CM NPs treated NHDF (Supplementary Fig. 9). Since the NPs were coated with SKOV3 cell membrane, these results indicated that the SKOV3 cell membrane coating can improve the selective cell uptake into SKOV3 cells but not other cells. Subsequently, we tested the endo/lysosome escaping ability, which is one of the crucial determinants for successful intracellular delivery. Firstly, Cy5.5 labeled Au@MSN-Ter@CM NPs were co-incubated with OVCAR3 and SKOV3 cell for scheduled 3 and 6 h, and then the cells were selectively treated with laser 980 nm for 10 min in the prior of green lysotracker and blue DAPI staining. As shown in Fig. 2 G and H, the free red fluorescent signal, which represented free Au@MSN-Ter/Cy5.5@CM NPs, were abundantly detected in both cells after 3 h and 6 h co-incubation, while most of the red fluorescent signal were merged with green fluorescence signal, which represented lysosome, except for OVCAR3 cells at 3 h' time point. These results mean that the Au@MSN-Ter/THPP@CM NPs were taken by the cells, but mass of Au@MSN-Ter/THPP@CM NPs were inside of the lysosomes. While in the laser treated groups, the red and green fluorescence signals were obviously separated in both OVCAR3 and SKOV3 cells at 3 and 6 h. This result is similarly with our previous finding and confirmed the endo/lysosome escape of Au@MSN-Ter/THPP@CM NPs, as stimulated by PTT [26].

3.3. Evaluate the ICD provoking ability of Au@MSN-Ter/THPP@CM NPs

We have shown that the Au@MSN-Ter/THPP@CM NPs can possibly induce photodynamic reaction cell death. Therefore, we further tested the ICD level by analyzing of two typical biomarkers Calreticulin (CRT) and high mobility group box 1 (HMGB1). The CRT protein is mainly expressed in ER, while under stress, the CRT is transferred on to the surface of cell membrane and exposed as an "eat-me" signal for immune system. And for HMGB1, as an activator for immune system, it is mainly located in the cell nucleus under normal condition, but it is released into extracellular matrix in stress condition [34–36]. After SKOV3 cells were treated with different NPs, the cells were separately stained with FITC labeled CRT and HMGB1 primary antibodies. Therefore, the fluorescent signal of FITC can be used to monitor the protein level and location change of CRT and HMGB1. And to better distinguish the CRT and HMGB1, we changed the green color of FITC-HMGB1 fluorescent signal to red. As shown in Fig. 3 A and C, the green CRT signal and red HMGB1 signal increased obviously in Au@MSN/THPP@CM or Au@MSN-Ter/THPP@CM NPs with 650 nm laser group, the increase was especially significant in Au@MSN-Ter/THPP@CM NPs with 650 nm laser group. Quantitative experiments with flow cytometry also revealed the same conclusion, under the irradiation of 650 nm laser, the fluorescence intensity of CRT and HMGB1 of cells treated with Au@MSN/THPP@CM NPs increased, while Au@MSN-Ter/THPP@CM NPs group showed the highest fluorescence intensity. When no laser was present, the fluorescence intensity was almost unchanged compared with the control group. (Fig. 3 B, D). These results indicated that Au@MSN/THPP@CM or Au@MSN-Ter/THPP@CM NPs treatment with 650 nm laser can significantly stimulate the CRT and HMGB1 expression. In addition, the ER targeting ligand Ter modified Au@MSN-Ter/THPP@CM NPs had better ICD provoking ability than Au@MSN/THPP@CM NPs, indicating the importance of using ER targeting.

As we have designed, we were expected to utilize the CAT, which can catalyze H₂O₂ to produce O₂ to enhance Au@MSN-Ter/THPP@CM NPs induced photodynamic reactions in the tumor cells. Therefore, we treated the SKOV3 cells with 5 mg/mL CAT and 10 mg/mL Au@MSN-Ter/THPP@CM NPs, the concentration of which were shown to be the maximum dose that would not lead to significant cell death in SKOV3

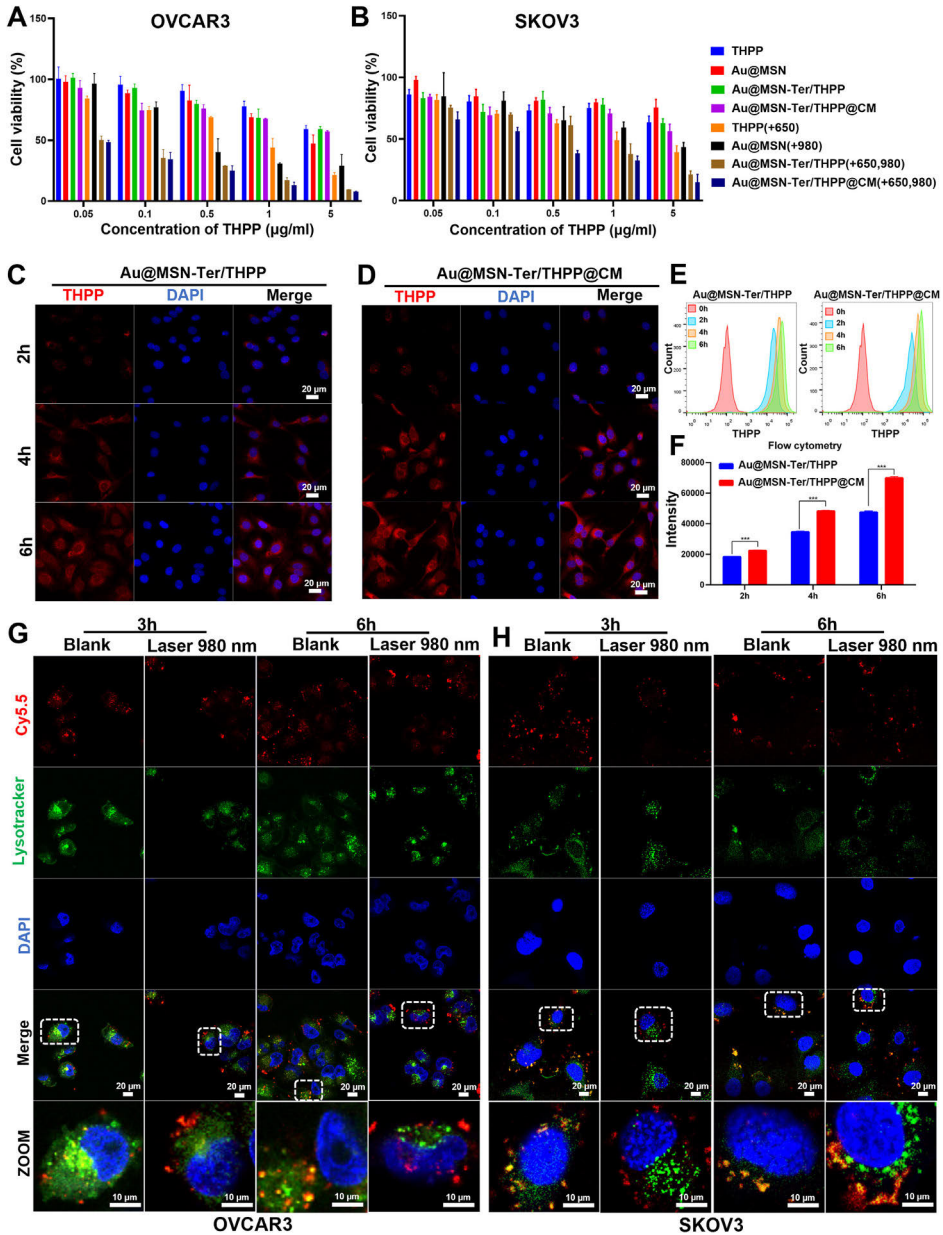


Fig. 2. Cytotoxicity and cellular uptake of different NPs. OVCAR3 (A) and SKOV3 (B) cells viability after different concentrations of various NPs for 24 h following with 650 nm laser (0.4 W/cm^2 , 5 min) and/or 980 nm laser (1 W/cm^2 , 10 min) irradiation. Confocal microscope images (C and D) and flow cytometry analysis (E and F) of various NPs' cellular uptake after 2–6 h co-incubation (Scale bar: 20 μm). G and H. Confocal microscope images of Cy5.5 labeled Au@MSN-Ter/THPP@CM NPs' lysosome escape after 3–6 h co-incubation and selectively treated with 980 nm laser (1 W/cm^2 , 10 min) irradiation. (Red: Cy5.5; Green: lysotracker; Blue: DAPI). (For interpretation of the references to color in this figure legend, the reader is referred to the Web version of this article.)

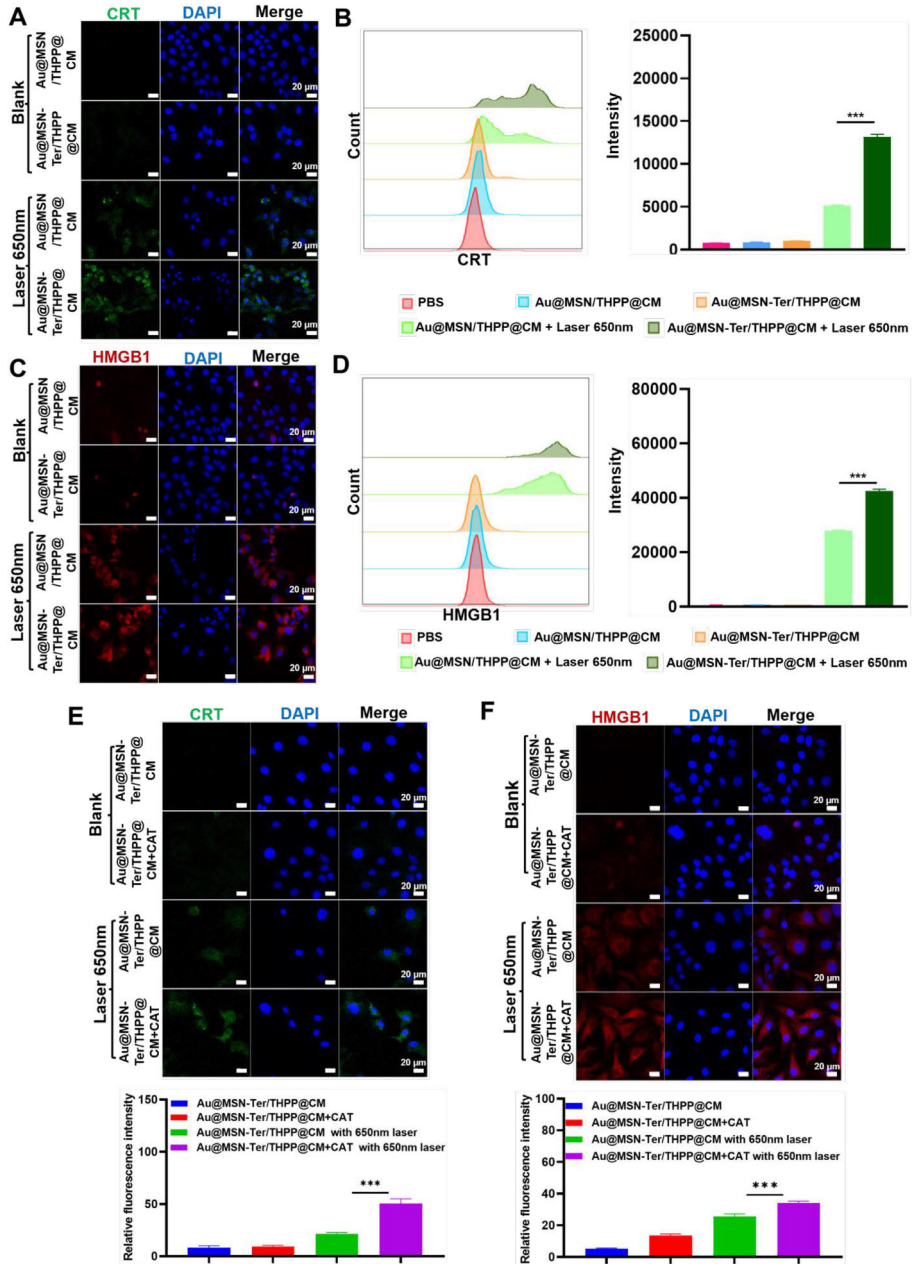


Fig. 3. Confocal microscope images of CRT and HMGB1 stained SKOV3 cells after Au@MSN/THPP@CM or Au@MSN-Ter/THPP@CM NPs treatment. Cells were stained with CRT (A) and HMGB1 (C) and imaged with confocal microscope after 24 h of Au@MSN/THPP@CM or Au@MSN-Ter/THPP@CM NPs co-incubation and following 650 nm laser (0.4 W/cm², 5 min) irradiation. Flow cytometry analysis and quantifications of CRT (B) or HMGB1 (D) positive cells after 24 h of Au@MSN/THPP@CM or Au@MSN-Ter/THPP@CM NPs co-incubation and following 650 nm laser (0.4 W/cm², 5 min) irradiation. Images of CRT (E) and HMGB1 (F) stained SKOV3 cells after treated with Au@MSN-Ter/THPP@CM NPs and selectively treated with free CAT and 650 nm laser irradiation (0.4 W/cm², 5 min). (Green: CRT; Red: HMGB1; Blue: DAPI; Scale bar: 20 μm). (For interpretation of the references to color in this figure legend, the reader is referred to the Web version of this article.)

cells (Supplementary Fig. 11), and the cells were treated with 650 nm laser irradiation. The result in Fig. 3 E and F shown that, the green CRT signal and red HMGB1 signal were only slightly increased Au@MSN-Ter/THPP@CM with 650 nm laser or Au@MSN-Ter/THPP@CM + CAT treated SKOV3 cells. And the green CRT signal and red HMGB1 signal had higher intensity in 650 nm laser and Au@MSN-Ter/THPP@CM + CAT treated SKOV3 cells. All those results indicated that the Au@MSN-Ter/THPP@CM NPs and CAT treatment can induce enhanced ICD activation under 650 nm laser irradiation.

3.4. Au@MSN-Ter/THPP@CM@GelMA and Au@MSN-Ter/THPP@CM@GelMA/CAT biomimetic nano@microgel preparation and characterization

In recent years, gelatin methacryloyl (GelMA) hydrogels have received more and more attention in the applications of drug delivery, tissue engineering and some other medical purposes owing to their excellent biocompatibility and biodegradability [17,30,37]. For example, the GelMA microspheres formed by crosslinked gelatin molecules under UV light is an ideal drug or cell carrier that can be used for cancer therapy by in situ injection and also site-specific cell transplantation [38–40]. Thereby, we further loaded the Au@MSN-Ter/THPP@CM NPs together with CAT into GelMA microsphere to form the Au@MSN-Ter/THPP@CM@GelMA/CAT biomimetic nano@microgel. We expect that the prepared biomimetic nano@microgel can be used for Ovarian cancer treatment through enhanced photodynamic reactions and photothermal combined therapy by in-situ injection. As shown in the Schematic Figure, the biomimetic nano@microgel Au@MSN-Ter/THPP@CM@GelMA/CAT was prepared on a microfluidic chip. Briefly, CAT (5 mg/mL), photocrosslinker (10 mg/mL), gelatin methacrylate (150 mg/mL) and Au@MSN-Ter/THPP@CM NPs (10 mg/mL) were firstly dispersed in PBS solution as an internal flow. Next, the mixture was flow focused by the external flow (mineral oil with 5% Span-80) to form droplet, and then cured by UV irradiation. Finally, the biomimetic nano@microgel Au@MSN-Ter/THPP@CM@GelMA/CAT was collected by centrifugation. In order to maximize the carrying capacity of the biomimetic nano@microgel, we have tried to prepare the Au@MSN-Ter/THPP@CM@GelMA/CAT microspheres with different Au@MSN-Ter/THPP@CM NPs concentrations (0, 5, 10 and 15 mg/mL). We found that 10 mg/mL was the highest Au@MSN-Ter/THPP@CM NPs' concentration that could be used for the preparation of Au@MSN-Ter/THPP@CM@GelMA/CAT microspheres, because the 15 mg/mL was too high NPs' concentration that destroyed the basic skeleton of the microgel and made it impossible to solidify. Therefore 10 mg/mL of Au@MSN-Ter/THPP@CM NP was used for the final biomimetic nano@microgel preparation. And based on cell cytotoxicity study of CAT in SKOV3 cells, we selected 5 mg/mL CAT, which was the highest concentration that did not induce considerable cell death in the test (Supplementary Fig. 11).

Compared with mechanical emulsification method, the microfluidic method that we used can produce highly monodispersed microgels and effectively avoid the leakage of NPs even under mechanical stirring or ultrasonication. The encapsulation efficiency of Au@MSN-Ter/THPP@CM NPs and CAT by Au@MSN-Ter/THPP@CM@GelMA/CAT microspheres was 89.1% and 91.5%. In addition, by controlling the flow rate of the internal and external channels, Au@MSN-Ter/THPP@CM@GelMA/CAT microspheres of different sizes could be easily prepared. As the results shown in Fig. 4 A, we first fixed the external flow (5% Span 80 in mineral oil) speed at 3 mL/h and change the internal flow (mixture of NPs, CAT and GelMA) speed, the diameter of Au@MSN-Ter/THPP@CM@GelMA/CAT microspheres could be produced with the size of 490 ± 35 , 200 ± 28 , 110 ± 18 , 55 ± 15 and $20 \pm 10 \mu\text{m}$ (the corresponding internal: external flow ratio = 1:1, 1:2, 1:4, 1:8, and 1:12). To investigate the composition of the Au@MSN-Ter/THPP@CM@GelMA/CAT microspheres, we utilized a fluorescent drug Doxorubicin (DOX) to mimetic CAT's distribution in Au@MSN-Ter/

THPP@CM@GelMA/CAT microspheres. The confocal microscope imaging results showed that the red signal of THPP in Au@MSN-Ter/THPP@CM NPs and green signal represented DOX were evenly dispersed in the microsphere (Fig. 4 B). Next, we further evaluated the stability of Au@MSN-Ter/THPP@CM@GelMA/CAT microspheres by monitoring the degradation of different sizes' Au@MSN-Ter/THPP@CM@GelMA/CAT biomimetic nano@microgels. The result in Fig. 4 G showed that, the biomimetic nano@microgels were completely degraded at 22 days (internal: external flow ratio of 1:4), 11 days (internal: external flow ratio of 1:8) and 5 days (internal: external flow ratio of 1:12), while there were still $28.2 \pm 5.2\%$ and $7.9 \pm 3.8\%$ of Au@MSN-Ter/THPP@CM@GelMA/CAT biomimetic nano@microgels left in flow ratio of 1:1 and 1:2 groups after 22 days even with laser irradiation (980 nm laser, $1 \text{ W}/\text{cm}^2$, treated for 10 min before each time point). This indicated that the degradation of Au@MSN-Ter/THPP@CM@GelMA/CAT microspheres was correlated to its size. In order to reduce the trauma of injection and maximize the sustained release time of the biomimetic nano@microgel, we chose 1:2 as the optimal flow ratio to prepare the final biomimetic nano@microgel (particle size of $200 \mu\text{m}$). And the microscopy images in Fig. 4 D showed that, the surface damage was detected in nano@microgel after 7 days, and constantly broken and missing was found after 14 and 28 days. In addition, we also evaluated the drying procedure of the GelMA microspheres. Through freeze-drying, we noticed that the water phase nucleated during the freezing process and led to increased surface pores of the GelMA microspheres, which was not good for maintaining the NPs inside and sustained the drug release. To avoid Au@MSN-Ter/THPP@CM NPs losing by the Au@MSN-Ter/THPP@CM@GelMA/CAT microspheres, we applied vacuum drying, and we managed to obtain non-porous GelMA microspheres. As shown in Fig. 4C, the dried Au@MSN-Ter/THPP@CM@GelMA/CAT microspheres had uniform size distribution and very smooth surface under SEM.

Next, we further tested the CAT and NPs' releasing from Au@MSN-Ter/THPP@CM@GelMA/CAT biomimetic nano@microgel. Because THPP can hardly dissolved in water and barely release from the NPs under aqueous condition, we measured the UV absorption of THPP to represent the releasing of NPs and detected the protein concentration of CAT in the releasing buffer by BCA kit to monitor the releasing of CAT. And in order to create a better irradiation condition that can be further used for animal study, we treated the releasing solution with 980 nm laser ($1 \text{ W}/\text{cm}^2$) for 10 min every three days. As shown in Fig. 4 E and F, the releasing of THPP and CAT were both in time dependent manner and could last up to 30 days. Furthermore, total THPP releasing was significantly increased from $65.4\% \pm 2.8\%$ to $79.7 \pm 3.8\%$ ($p < 0.001$) by 980 nm laser irradiation at 30 days' time point, while the CAT releasing increased significantly from $63.2\% \pm 2.2\%$ to $80.6 \pm 3.4\%$ ($p < 0.001$) by 980 nm laser irradiation at 30 days' time point. These results demonstrate that the biomimetic nano@microgel Au@MSN-Ter/THPP@CM@GelMA/CAT has good stability and sustained release of NPs.

3.5. Evaluating the anti-tumor effect of Au@MSN-Ter/THPP@CM@GelMA/CAT microgel in ovarian cancer cells

We have proved that the Au@MSN-Ter/THPP@CM NPs had very good capability to deliver THPP with good biocompatibility, and also evidently showed the cell proliferation inhibition ability of Au@MSN-Ter/THPP@CM NPs under both 650 nm laser and 980 nm laser irradiation. In order to further evaluate the anti-tumor effect of the Au@MSN-Ter/THPP@CM@GelMA/CAT microgel, we performed live-dead cell staining and Annexin V, PI double staining assays to test the effect of Au@MSN-Ter/THPP@CM@GelMA/CAT on cell survival in SKOV3 and OVCAR3 cells. The results in Fig. 5 showed that, the Annexin V positive cells were distinctly increased by either Au@MSN-Ter/THPP@CM@GelMA or Au@MSN-Ter/THPP@CM@GelMA/CAT treatment for 48 h, regardless of single laser (650 nm laser or 980 nm laser) treatment or double lasers treatment in both two cell lines (Fig. 5 A, B, C and D). While compared to

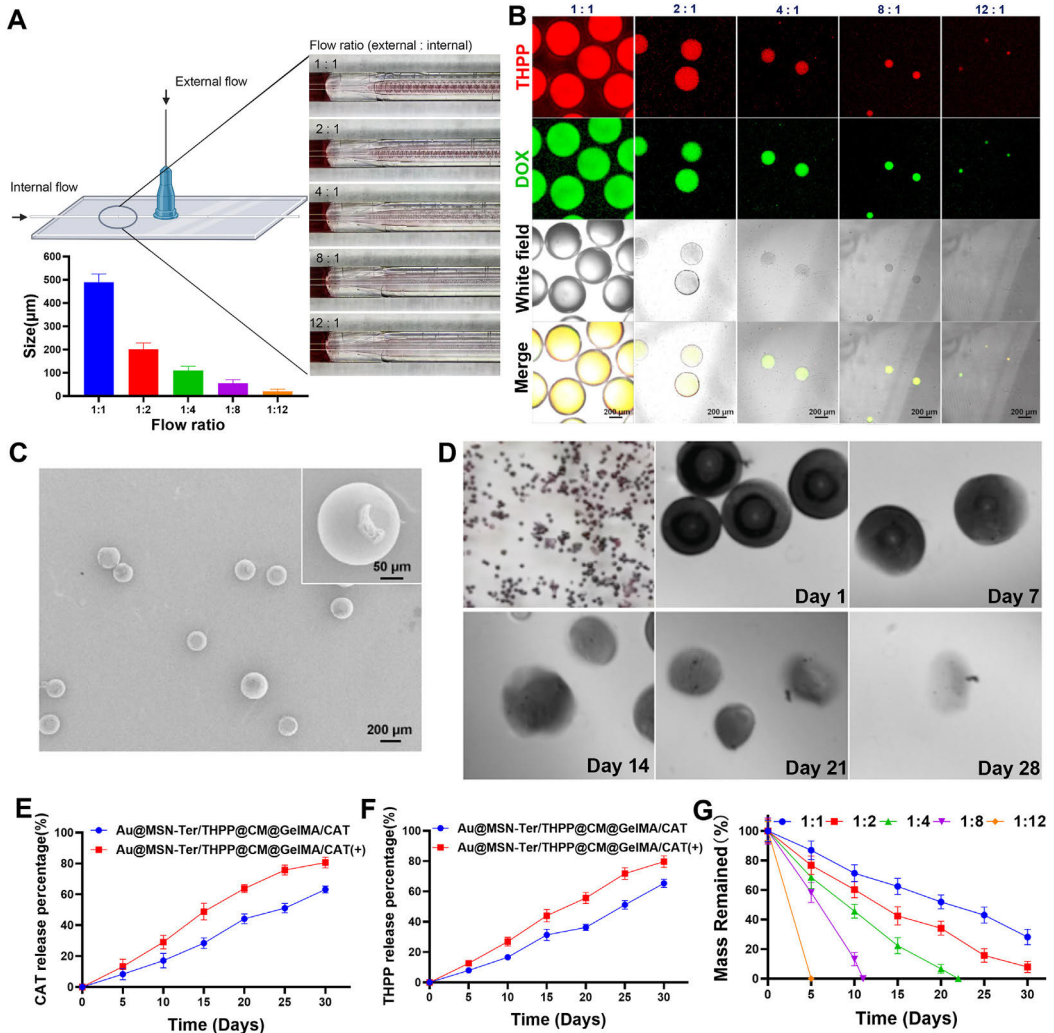


Fig. 4. Morphology and CAT/THPP releasing of Au@MSN-Ter/THPP@CM@GelMA/CAT microspheres. Illustration, particle size (A) and confocal microscope images (B) of Au@MSN-Ter/THPP@CM@GelMA/CAT microspheres with indicated external (5% Span 80 in mineral oil) and internal (mixture of NPs, DOX and GELMA) flow rate; C. SEM images of Au@MSN-Ter/THPP@CM@GelMA/CAT microspheres formed by external and internal flow rate of 2:1; D. Microscope images of Au@MSN-Ter/THPP@CM@GelMA/CAT microspheres at different time point; CAT (E) and THPP (F) releasing from Au@MSN-Ter/THPP@CM@GelMA/CAT microspheres in PBS buffer with or without laser (980 nm, 1 W/cm², 10 min); G. The degradation curve of different Au@MSN-Ter/THPP@CM@GelMA/CAT microspheres formed by different flow ratio.

single laser treated groups, Au@MSN-Ter/THPP@CM@GelMA/CAT together with both two lasers treated groups showed more significantly increased Annexin V positive cell populations in both SKOV3 and OVCAR3 cells. Most importantly, the Annexin V positive cell populations in Au@MSN-Ter/THPP@CM@GelMA/CAT and two lasers treated groups were more than Au@MSN-Ter/THPP@CM@GelMA and two lasers without Au@MSN-Ter/THPP@CM@GelMA treated groups in both SKOV3 and OVCAR3 cells. Because Annexin V is a membrane protein that can only

binding to the damaged cell membrane, thus the fluorescent signal of FITC labeled Annexin V were commonly used to detect the apoptotic cells. Therefore, our results demonstrated that the treatment of Au@MSN-Ter/THPP@CM@GelMA or Au@MSN-Ter/THPP@CM@GelMA/CAT can significantly lead to both SKOV3 and OVCAR3 cells apoptosis. And the additional laser irradiation (650 nm laser or 980 nm laser), especially the two lasers treatment was a considerable promotion factor for cell apoptosis.

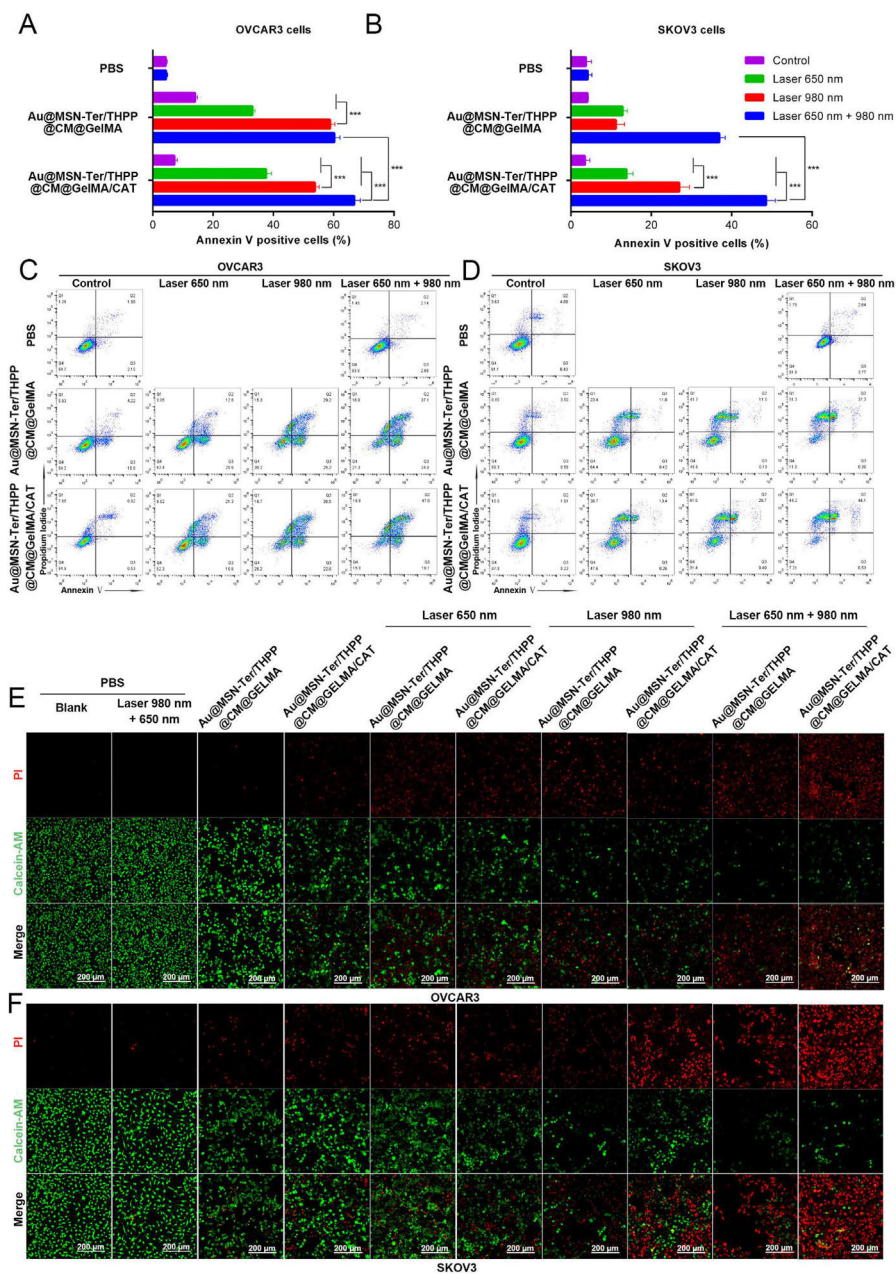


Fig. 5. Cytotoxicity of different GelMA microsphere formulations and treatments. A-D. Flow cytometry analysis of apoptotic cells by Annexin V-FITC/PI staining after co-incubation with Au@MSN-Ter/THPP@CM@GelMA or Au@MSN-Ter/THPP@CM@GelMA/CAT for 48 h and following 650 nm laser (0.4 W/cm², 5 min) and/or 980 nm laser (1 W/cm², 10 min) irradiation. E and F. Cell death analysis with confocal microscope after co-incubation with Au@MSN-Ter/THPP@CM@GelMA or Au@MSN-Ter/THPP@CM@GelMA/CAT for 48 h and following 650 nm laser (0.4 W/cm², 5 min) and/or 980 nm laser (1 W/cm², 10 min) irradiation (Red: PI; Green: Calcein-AM; Scale bar: 200 μm). (For interpretation of the references to color in this figure legend, the reader is referred to the Web version of this article.)

Since the red fluorescent nuclei dye PI can only get in to the cells with damaged membrane, while the Calcein-AM can be catalyzed in to green fluorescent Calcein and retained only in living cells. Therefore, the double staining of PI and Calcein-AM were always used to distinguish the living and dead cells. As the live-dead cell staining results in Fig. 5 E and F shown, the red PI fluorescent signal was significantly increased while the green Calcein-AM fluorescent signal was decreased in all Au@MSN-Ter/THPP@CM@GelMA or Au@MSN-Ter/THPP@CM@GelMA/CAT treated SKOV3 and OVCAR3 cells, and the additional laser treatments (either 650 nm laser and/or 980 nm laser) came to be an acceleration factor for the tendency. While in all Au@MSN-Ter/THPP@CM@GelMA or Au@MSN-Ter/THPP@CM@GelMA/CAT treated SKOV3 and OVCAR3 cells, compare to single laser (650 nm laser or 980 nm laser) treated groups, double lasers (650 nm laser and 980 nm laser) treatments were more significant in increasing the red PI fluorescent signal and decreasing the green Calcein-AM fluorescent signal. Moreover, the increasing of red PI fluorescent signal and decreasing of green Calcein-AM fluorescent signal in Au@MSN-Ter/THPP@CM@GelMA/CAT with double lasers treated groups were more obviously than Au@MSN-Ter/THPP@CM@GelMA with double lasers in both SKOV3 and OVCAR3 cells. All of these results demonstrated that both the formulations of Au@MSN-Ter/THPP@CM@GelMA and Au@MSN-Ter/THPP@CM@GelMA/CAT together with laser 650 nm and/or 980 nm treatment can lead to significant cell death and apoptosis in both OVCAR3 and SKOV3 cells. And compared to Au@MSN-Ter/THPP@CM@GelMA, Au@MSN-Ter/THPP@CM@GelMA/CAT is more efficient for inducing the cell death and apoptosis.

3.6. Evaluate the ability of ICD activation by Au@MSN-Ter/THPP@CM@GelMA/CAT in ovarian cancer cells

To further confirm the Au@MSN-Ter/THPP@CM@GelMA/CAT generated enhanced photodynamic reactions design, we detected the ROS level by a ROS indicator DCFH-DA in Au@MSN-Ter/THPP@CM@GelMA and Au@MSN-Ter/THPP@CM@GelMA/CAT treated SKOV3 cells. The DCFH-DA is a non-fluorescent molecule, which can be catalyzed and oxidized in to a strong fluorescent product DCF, thus can be used to analysis the ROS level of cells. As the results showed in Fig. 6, weak green fluorescent signal of DCF could be only observed in Au@MSN-Ter/THPP@CM@GelMA/CAT treated SKOV3 cells after 48 h. While in either Au@MSN-Ter/THPP@CM@GelMA or Au@MSN-Ter/THPP@CM@GelMA/CAT treated SKOV3 cells, the green fluorescent signal were dramatically increased by extra laser 650 nm treatment, especially in Au@MSN-Ter/THPP@CM@GelMA/CAT group (Fig. 6 A). The results evidently showed that the ROS level in either Au@MSN-Ter/THPP@CM@GelMA or Au@MSN-Ter/THPP@CM@GelMA/CAT treated SKOV3 cells were significantly increased by laser 650 nm. Therefore, we further evaluated the consequence induced by high level of ROS in SKOV3 cells.

Prolonged ER stress, which can be induced by high level of ROS is one of the leading causes for ICD triggered anti-tumor immune response [41, 42]. As shown in our design (Schematic figure), we modified the ER targeting ligand Ter on the surface of Au@MSN-Ter/THPP NPs. The Au@MSN-Ter/THPP NPs were successfully conducted to the ER once they escaped from the endo/lysosome (Supplementary Fig. 6). We believed that high level of ROS produced by the accumulated Au@MSN-Ter/THPP NPs in ER could certainly lead to irreversible ER stress under laser 650 nm irradiation. Therefore, we detected two key biomarkers of ICD to evaluate the potential ability of anti-tumor immune response provoking by Au@MSN-Ter/THPP@CM@GelMA/CAT. As shown in Fig. 6 B, C, both the fluorescent signals of CRT and HMGB1 on the cell membrane of SKOV3 cells were dramatically increased in either Au@MSN-Ter/THPP@CM@GelMA or Au@MSN-Ter/THPP@CM@GelMA/CAT treated groups with additional laser 650 nm treatment, and most obviously detected in Au@MSN-Ter/THPP@CM@GelMA/CAT plus laser 650 nm group. The increasing of both CRT and HMGB1 fluorescent signals on the cell

membrane of SKOV3 cells sufficiently indicated that the ICD status were in extremely high level in Au@MSN-Ter/THPP@CM@GelMA/CAT together with laser 650 nm treated SKOV3 cells.

3.7. Biodistribution and anti-tumor effects in ovarian cancer orthotopic implantation model

All of our previous results showed that the Au@MSN-Ter/THPP@CM@GelMA/CAT was with sustained NPs releasing and enhanced anti-tumor activity in Ovarian cancer cells synergistically with 650 nm and 980 nm lasers treatment. Moreover, the Au@MSN-Ter/THPP@CM@GelMA/CAT together with 650 nm laser treatment had great potential to provoke ICD induced anti-tumor immune response. Therefore, we further performed animal study to evaluate the possible anti-tumor activity of Au@MSN-Ter/THPP@CM@GelMA/CAT in vivo. The experiment was carried out with SKOV3 generated Ovarian cancer orthotopic implantation mice model (Fig. 7 A and Supplementary Fig. 14), and mice were randomly separated into four groups ($n \geq 6$). PBS treated group was injected with 100 μ L PBS from tail vein, NPs treated group was injected with 100 μ L Au@MSN-Ter/THPP@CM NPs in the tumor site, and two another groups were injected with 30 μ L Au@MSN-Ter/THPP@CM@GelMA/CAT (dose: equal to 2.5 mg/kg of THPP) in the tumor site. The PBS, NPs and one Au@MSN-Ter/THPP@CM@GelMA/CAT treated groups were treated lasers (10 min of 980 nm laser, 5 min of 650 nm laser) once every three days as scheduled. As shown in Fig. 7 B and Supplementary Fig. 20, after only 6 h tail vein injection of Au@MSN-Ter/THPP@CM NPs and followed double lasers treatment, the Au@MSN-Ter/THPP@CM NPs were detected in both liver and cancer tissues. And increased Au@MSN-Ter/THPP@CM NPs accumulation was found in both liver and tumor tissues, as well as in lung and kidney tissues at 24 and 48 h. In nano/microgels groups, only few Au@MSN-Ter/THPP@CM NPs were detected in the liver, while large amount of Au@MSN-Ter/THPP@CM NPs were detected in tumor tissues in Au@MSN-Ter/THPP@CM@GelMA/CAT in situ injection groups at 15 days regardless of laser treatment (Fig. 7 B). These results demonstrated that the Au@MSN-Ter/THPP@CM NPs was mainly retention in the tumor tissue after Au@MSN-Ter/THPP@CM@GelMA/CAT microsphere's intratumoral injection. While the tail vein injection of Au@MSN-Ter/THPP@CM NPs also exhibited main organs (such as liver, kidney, and lung) accumulation. Furthermore, the result of tumor weight from sacrificed mice after fifteen days treatment with different formulations and lasers showed that both Au@MSN-Ter/THPP@CM NPs and Au@MSN-Ter/THPP@CM@GelMA/CAT can significantly decrease the tumor weight under double lasers (Fig. 7C). In addition, the tumor weights in either Au@MSN-Ter/THPP@CM NPs or Au@MSN-Ter/THPP@CM@GelMA/CAT together with double lasers treated groups were obviously lower than Au@MSN-Ter/THPP@CM@GelMA/CAT only treated group, and Au@MSN-Ter/THPP@CM@GelMA/CAT together with lasers treated group exhibited the lowest tumor weight result. Subsequently, we sliced the collected tumor and organ tissues and performed HE, Ki 67 and Tumor staining assays to further evaluate the anti-tumor activity and organ toxicity of different formulations. As the result in Fig. 7 D, HE staining showed that compared to PBS treated group, cell death area of tumor tissues were strikingly increased in all different formulations treated groups, especially in Au@MSN-Ter/THPP@CM@GelMA/CAT together with lasers treated group. Correspondingly, the expression of tumor cell proliferation biomarker Ki 67 and apoptotic cells' biomarker Tumor staining were changed in the similar way as the result in HE staining. These results indicated that both formulations and treatments were effectively inhibited the tumor growth, while Au@MSN-Ter/THPP@CM@GelMA/CAT together with lasers was the best selection for the implementation of cancer treatment. And more significantly, both of the formations were non-toxic to the main organs within the used maximum formulation concentrations, because there were no obvious organ tissue damages were observed in the main organs (include heart, liver, spleen, lung and kidney) HE staining results.

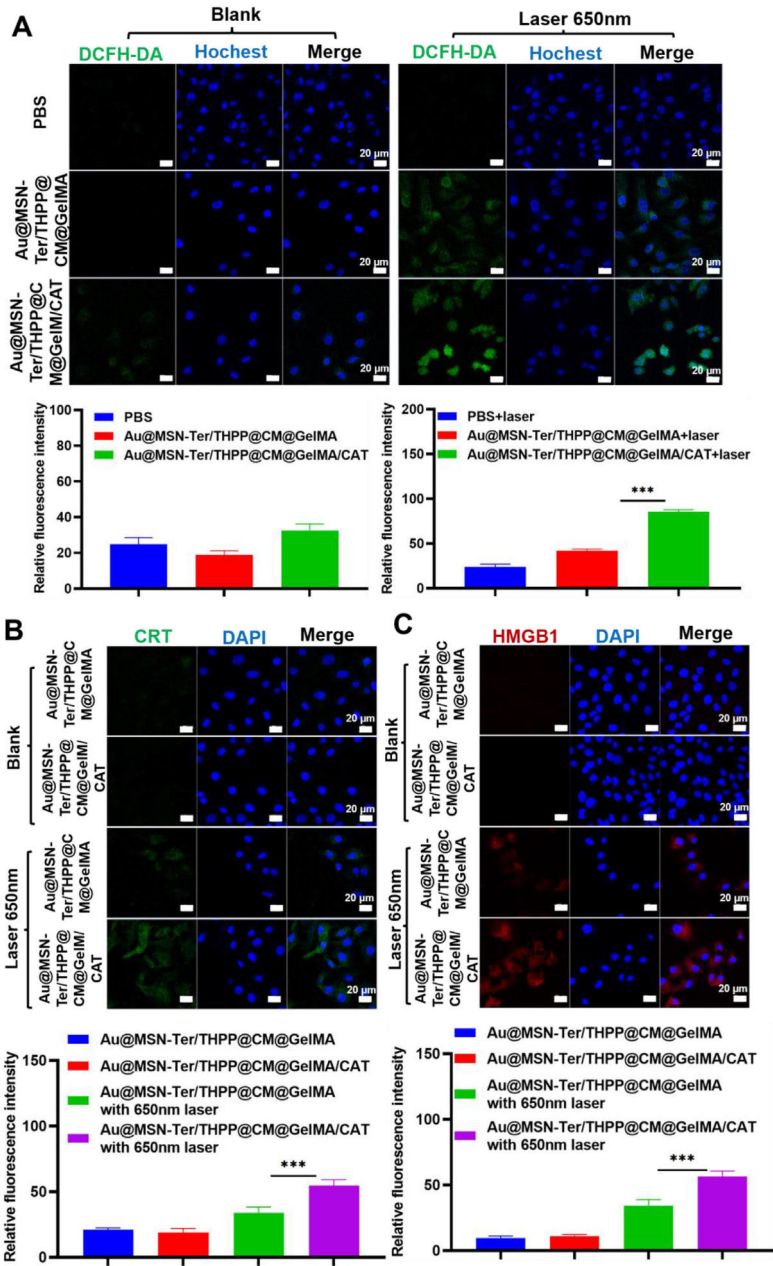


Fig. 6. Confocal microscope images of SKOV3 cell after co-incubation with Au@MSN-Ter/THPP@CM@GelMA or Au@MSN-Ter/THPP@CM@GelMA/CAT for 48 h and selectively treated with 650 nm laser (0.4 W/cm^2) for 5 min. A. Images of DCFH-DA stained SKOV3 cells and quantifications (Green: DCFH-DA; Blue: Hoechst; Scale bar: 20 μm); Images of CRT (B) and HMGB1 (C) primary antibodies stained SKOV3 cells and quantifications (Green: CRT; Red: HMGB1; Blue: DAPI; Scale bar: 20 μm). (For interpretation of the references to color in this figure legend, the reader is referred to the Web version of this article.)

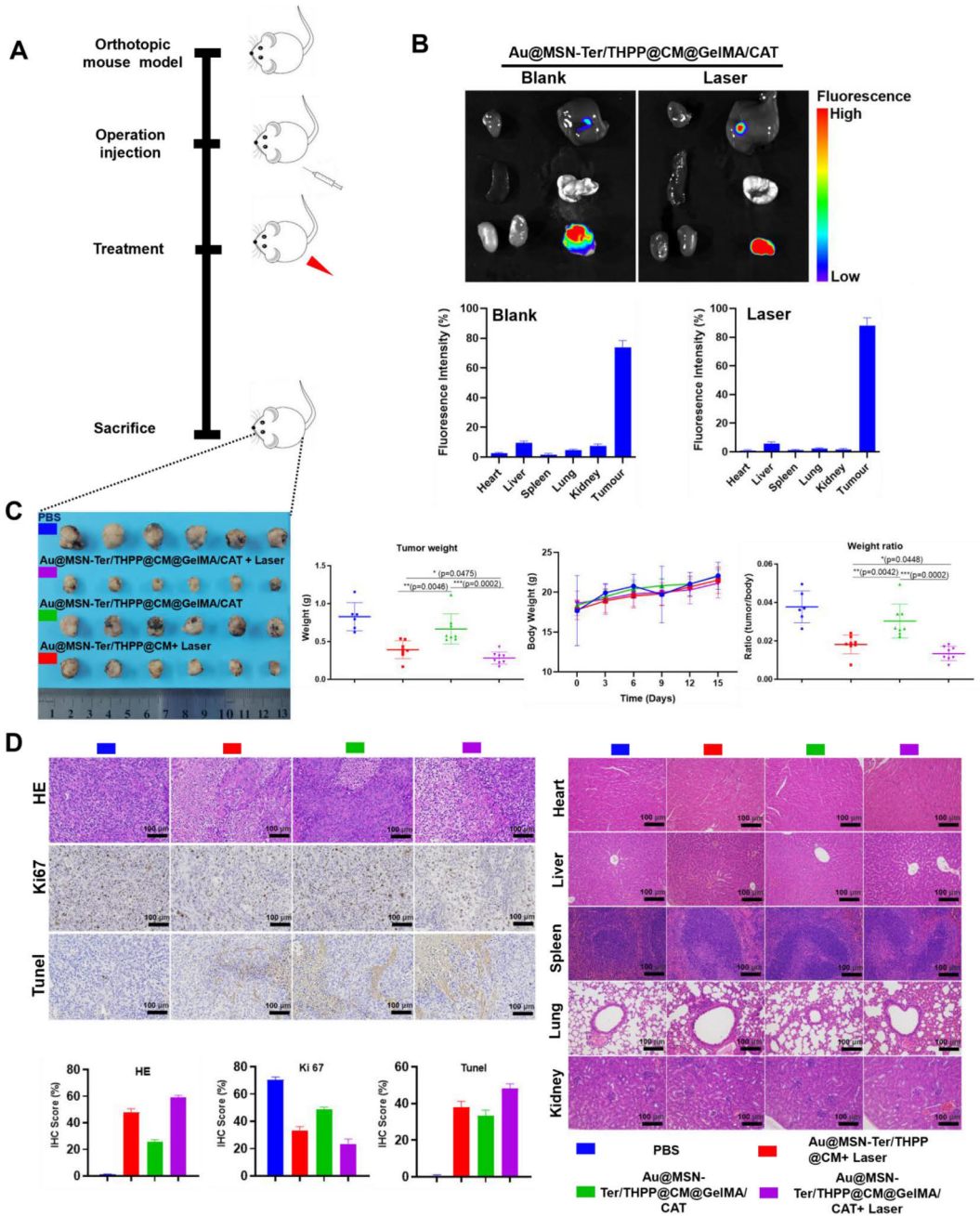


Fig. 7. Bio-imaging, tumors growth and histological analysis after different formulations of peritumoral administration. A. Illustration of animal experiment. B. Organ tissues THPP fluorescent signal captured by in vivo imaging system and quantifications (From left to right and up to down panels: Heart, liver, spleen, lung, kidney, and tumor). C. Data of tumor images, tumor weight, mice body weight and weight ratio (tumor/body) ($n \geq 6$). D. HE, Ki67 and TUNEL staining images and quantifications of tumor, and HE staining images of different organs ($n \geq 6$, $20 \times$, scale bar: $100 \mu\text{m}$).

4. Conclusion and discussion

In this study, we have developed a microfluidic method for fabricating biomimetic Au@MSN-Ter/THPP@CM@GelMA/CAT nano@microgels. These gels consist of cured GelMA microspheres and inner components including CAT and Au@MSN-Ter/THPP@CM NPs. The Au@MSN-Ter/THPP@CM NPs were found to possess excellent photo-thermal conversion ability and stability. Additionally, the Au@MSN-Ter/THPP@CM@GelMA/CAT nano@microgels demonstrated good biocompatibility and long-term tumor retention capability. Importantly, both in vitro and in vivo studies showed that Au@MSN-Ter/THPP@CM NPs and Au@MSN-Ter/THPP@CM@GelMA/CAT exhibited excellent anti-tumor activity against ovarian cancer when both 650 nm and 980 nm lasers were applied. These findings provide strong evidence for the potential of these nano@microgels as a promising therapeutic approach for ovarian cancer.

ROS provoking for cancer therapy has always been considered as a good strategy for nano-formulation drugs design [43,44]. The most common ROS include hydrogen peroxides (H_2O_2), superoxide ($\bullet O_2^-$), hydroxyl radical ($\bullet OH$) and singlet oxygen (1O_2). And among them 1O_2 is the most reactive one, which can result in most serious cell damages via reaction with organic molecules that contain double bonds [45]. In this work, we encapsulated CAT together with Au@MSN-Ter/THPP@CM NPs inside of the Au@MSN-Ter/THPP@CM@GelMA/CAT microsphere, the produced O_2 by released CAT catalyzing H_2O_2 served as good source for THPP based photodynamic reaction generated 1O_2 production. As we have proofed in Fig. 6 A, the ROS level was significantly increased in Au@MSN-Ter/THPP@CM@GelMA/CAT and laser 650 nm treated SKOV3 cells, and this further induced increasing CRT exposure and HMGB1 releasing (Fig. 6 B and C). Therefore, all of these results evidently proved the enhanced photodynamic reaction design of our Au@MSN-Ter/THPP@CM@GelMA/CAT microgel, and this is a very good strategy of enhanced ROS provoking by photodynamic reaction for cancer therapy.

The photo-thermal response has always been considered as one of the best designs for developing smart nanocarriers [46–48]. However, the results of photothermal therapy (PTT) can be easily affected by various key factors that may decrease the photothermal conversion efficiency, including NP stability, distribution, and the selected light source [49]. In our work, we developed photothermal-responsive Au-MSN NPs as nanocarriers for THPP, thereby combining PTT with PDT. The results, as shown in Figs. 2 and 5, indicate that both cell death and apoptosis were significantly increased in the groups treated with both lasers (650 nm and 980 nm) compared to those treated with a single laser, whether using Au@MSN-Ter/THPP@CM NPs or Au@MSN-Ter/THPP@CM@GelMA/CAT.

Furthermore, following intratumoral injection, the nano@microgel Au@MSN-Ter/THPP@CM@GelMA/CAT also demonstrated excellent tumor retention ability, as illustrated in Fig. 7 B. This serves as an effective solution to the problem of low accumulation of photosensitizers at the tumor site, which can reduce the amount of photosensitizer used in PDT. Moreover, the results in Fig. 7 show that enhanced anti-tumor activity can be achieved by using Au@MSN-Ter/THPP@CM@GelMA/CAT in conjunction with additional 650 nm and 980 nm laser irradiation.

In summary, the nano@microgel Au@MSN-Ter/THPP@CM@GelMA/CAT has shown great potential for inducing high levels of ROS and triggering ICD through photothermal and enhanced photodynamic reactions, both in vitro and in vivo. This newly designed biomimetic nano@microgel could be a promising candidate for in situ ovarian cancer therapy.

Author contributions

Xiaodong Ma: Conceptualization, Methodology, Software, Validation Formal analysis, Investigation, Data Curation, Writing - Original Draft, Writing - Review & Editing, Visualization. **Wenhui Zhou:** Methodology, Software, Validation Formal analysis, Investigation, Data Curation, Writing - Original Draft, Writing - Review & Editing,

Visualization. **Rong Zhang:** Resources, Funding acquisition. **Canan Zhang:** Resources, Data Curation. **Jiaqi Yan:** Resources, Writing - Original Draft. **Jing Feng:** Resources, Writing - Review & Editing. **Tingyan Shi:** Resources, Funding acquisition. **Jessica M. Rosenholm:** Resources, Writing - Review & Editing. **Xian Shen:** Resources, Writing - Review & Editing. **Hongbo Zhang:** Conceptualization, Methodology, Validation, Resources, Writing - Review & Editing, Visualization, Supervision, Project administration, Funding acquisition.

Declaration of competing interest

The authors declare that they have no known competing financial interests or personal relationships that could have appeared to influence the work reported in this paper.

Data availability

Data will be made available on request.

Acknowledgements

Imaging/Flow cytometry was performed at the Cell Imaging and Cytometry core at Turku Bioscience Centre, which is supported by Bio-center Finland. This work was supported by the Leading Talents in Scientific and Technological Innovation from Zhejiang Provincial Ten Thousand Talents Plan (Grant Nos: 2019R52021); the Key Research and Development Program of Zhejiang Province (Grant Nos: 2021C03120); the Key Research and Development Program of Wenzhou (Grant Nos: ZY2021003); the grants from National Natural Science Foundation of China (81974407 to Rong Zhang, 821732 to Tingyan Shi); Program for Outstanding Medical Academic Leader of Shanghai (LJ2019025); the Key Subject Construction Project for Medical of Shanghai (ZK2019B29); Research Fellow (Grant No. 353146), project (347897), Solutions for Health Profile (336355), InFLAMES Flagship (337531) grants from Academy of Finland; and Finland China Food and Health International Pilot Project funded by the Finnish Ministry of Education and Culture.

Appendix A. Supplementary data

Supplementary data to this article can be found online at <https://doi.org/10.1016/j.mtbio.2023.100663>.

References

- J.N. Moloney, T.G. Cotter, ROS signalling in the biology of cancer, *Semin. Cell Dev. Biol.* 80 (2018) 50–64, <https://doi.org/10.1016/j.semcdb.2017.05.023>.
- J.D. Hayes, A.T. Dinkova-Kostova, K.D. Tew, Oxidative stress in cancer, *Cancer Cell* 38 (2020) 167–197, <https://doi.org/10.1016/j.ccr.2020.06.001>.
- E. Rendra, V. Riabov, D.M. Mossel, T. Sevastyanova, M.C. Harmsen, J. Kzhyshkowska, Reactive oxygen species (ROS) in macrophage activation and function in diabetes, *Immunobiology* 224 (2019) 242–253, <https://doi.org/10.1016/j.imbio.2018.11.010>.
- J.E. Klaunig, Oxidative stress and cancer, *Curr. Pharmaceut. Des.* 24 (2018) 4771–4778, <https://doi.org/10.2174/1381612825666190215121712>.
- I.S. Harris, G.M. DeNicola, The complex interplay between antioxidants and ROS in cancer, *Trends Cell Biol.* 30 (2020) 440–451, <https://doi.org/10.1016/j.tcb.2020.03.002>.
- W. Li, J. Yang, L. Luo, M. Jiang, B. Qin, H. Yin, C. Zhu, X. Yuan, J. Zhang, Z. Luo, Y. Du, Q. Li, Y. Lou, Y. Qiu, J. You, Targeting photodynamic and photothermal therapy to the endoplasmic reticulum enhances immunogenic cancer cell death, *Nat. Commun.* 10 (2019) 3349, <https://doi.org/10.1038/s41467-019-11269-8>.
- J. Guo, Z. Yu, D. Sun, Y. Zou, Y. Liu, L. Huang, Two nanoformulations induce reactive oxygen species and immunogenetic cell death for synergistic chemo-immunotherapy eradicating colorectal cancer and hepatocellular carcinoma, *Mol. Cancer* 20 (2021) 10, <https://doi.org/10.1186/s12943-020-01297-0>.
- J. An, Y.G. Hu, K. Cheng, C. Li, X.L. Hou, G.L. Wang, X.S. Zhang, B. Liu, Y.D. Zhao, M.Z. Zhang, ROS-augmented and tumor-microenvironment responsive biodegradable nanoplatfor for enhancing chemo-sonodynamic therapy, *Biomaterials* 234 (2020), 119761, <https://doi.org/10.1016/j.biomaterials.2020.119761>.
- X. Zhu, Y. Liu, G. Yuan, X. Guo, J. Cen, Y. Gong, J. Liu, Y. Gang, In situ fabrication of MS/MnO₂ hybrid as nanozymes for enhancing ROS-mediated breast cancer

- therapy, *Nanoscale* 12 (2020) 22317–22329, <https://doi.org/10.1039/d0nr03931d>.
- [10] C. Donohoe, M.O. Senge, L.G. Arnaut, L.C. Gomes-da-Silva, Cell death in photodynamic therapy: from oxidative stress to anti-tumor immunity, *Biochim. Biophys. Acta Rev. Canc* (2019), 188308, <https://doi.org/10.1016/j.bbcan.2019.07.003>, 1872.
 - [11] M. Lan, S. Zhao, W. Liu, C.S. Lee, W. Zhang, P. Wang, Photosensitizers for photodynamic therapy, *Adv Healthc Mater* 8 (2019), e1900132, <https://doi.org/10.1002/adhm.201900132>.
 - [12] J. Chen, T. Fan, Z. Xie, Q. Zeng, P. Xue, T. Zheng, Y. Chen, X. Luo, H. Zhang, Advances in nanomaterials for photodynamic therapy applications: status and challenges, *Biomaterials* 237 (2020), 119827, <https://doi.org/10.1016/j.biomaterials.2020.119827>.
 - [13] N. Yang, W. Xiao, X. Song, W. Wang, X. Dong, Recent advances in tumor microenvironment hydrogen peroxide-responsive materials for cancer photodynamic therapy, *Nano-Micro Lett.* 12 (2020) 15, <https://doi.org/10.1007/s40820-019-0347-0>.
 - [14] M. Wang, M. Chang, Q. Chen, D. Wang, C. Li, Z. Hou, J. Lin, D. Jin, B. Xing, Au2Pt-PEG-C6e nanoformulation with dual nanzyme activities for synergistic chemodynamic therapy/phototherapy, *Biomaterials* 252 (2020), 120093, <https://doi.org/10.1016/j.biomaterials.2020.120093>.
 - [15] L. Song, B. Chen, Z. Qin, X. Liu, Z. Guo, H. Lou, H. Liu, W. Sun, C. Guo, C. Li, Temperature-dependent CAT-like RGD-BPNS@SMFN nanoplaform for PTT-PDT self-synergistic tumor phototherapy, *Adv Healthc Mater* (2021), e2102298, <https://doi.org/10.1002/adhm.202102298>.
 - [16] Q. Zhang, L. Wu, S. Liu, Q. Chen, L. Zeng, X. Chen, Q. Zhang, Moderating hypoxia and promoting immunogenic photodynamic therapy by HER-2 nanobody conjugate nanoparticles for ovarian cancer treatment, *Nanotechnology* 32 (2021), <https://doi.org/10.1088/1361-6528/ac07d1>.
 - [17] J. Yan, Y. Wang, M. Ran, R.A. Mustafa, H. Luo, J. Wang, J.H. Smatt, J.M. Rosenholm, W. Cui, Y. Lu, Z. Guan, H. Zhang, Peritumoral microgel reservoir for long-term light-controlled triple-synergistic treatment of osteosarcoma with single ultra-low dose, *Small* 17 (2021), e2100479, <https://doi.org/10.1002/smll.202100479>.
 - [18] C. Sabu, C. Rejo, S. Kotta, K. Pramod, Bioinspired and biomimetic systems for advanced drug and gene delivery, *J. Contr. Release* 287 (2018) 142–155, <https://doi.org/10.1016/j.jconrel.2018.08.033>.
 - [19] J. Zhou, A.V. Kroll, M. Holay, R.H. Fang, L. Zhang, Biomimetic nanotechnology toward personalized vaccines, *Adv. Mater.* 32 (2020), e1901255, <https://doi.org/10.1002/adma.201901255>.
 - [20] Z. Chen, Z. Wang, Z. Gu, Bioinspired and biomimetic nanomedicines, *Acc. Chem. Res.* 52 (2019) 1255–1264, <https://doi.org/10.1021/acs.accounts.9b00079>.
 - [21] W. Zhang, C. Gong, Z. Chen, M. Li, Y. Li, J. Gao, Tumor microenvironment-activated cancer cell membrane-liposome hybrid nanoparticle-mediated synergistic metabolic therapy and chemotherapy for non-small cell lung cancer, *J. Nanobiotechnol.* 19 (2021) 339, <https://doi.org/10.1186/s12951-021-01085-y>.
 - [22] H.S. Kim, Y.M. Shin, S. Chung, D. Kim, D.B. Park, S. Baek, J. Park, S.Y. Kim, D.H. Kim, S.W. Yi, S. Lee, J.B. Lee, J.Y. Ko, G.I. Im, M.L. Kang, H.J. Sung, Cell-membrane-derived nanoparticles with notch-1 suppressor delivery promote hypoxic cell-packing and inhibit angiogenesis acting as a two-edged sword, *Adv. Mater.* 33 (2021), e2101558, <https://doi.org/10.1002/adma.202101558>.
 - [23] R.H. Fang, A.V. Kroll, W. Gao, L. Zhang, Cell membrane coating nanotechnology, *Adv. Mater.* 30 (2018), e1706759, <https://doi.org/10.1002/adma.201706759>.
 - [24] F. Oroojalian, M. Beygi, B. Baradaran, A. Mokhtarzadeh, M.A. Shahbazi, Immune cell membrane-coated biomimetic nanoparticles for targeted cancer therapy, *Small* 17 (2021), e2006484, <https://doi.org/10.1002/smll.202006484>.
 - [25] Y. Yang, K. Wang, Y. Pan, L. Rao, G. Luo, Engineered cell membrane-derived nanoparticles in immune modulation, *Adv. Sci.* 8 (2021), e2102330, <https://doi.org/10.1002/advs.202102330>.
 - [26] L.R. Zhang, X.D. Ma, W.H. Zhou, Q.W. Wu, J.Q. Yan, X.Y. Xu, B. Ghimire, J.M. Rosenholm, J. Feng, D.Q. Wang, H.B. Zhang, Combination of photothermal, prodrug and tumor cell camouflage technologies for triple-negative breast cancer treatment, *Mater Today Adv* 13 (2022), <https://doi.org/10.1016/j.mtaadv.2021.100199>, ARTN 100199.
 - [27] Y. Hao, Y. Chen, X. He, Y. Yu, R. Han, Y. Li, C. Yang, D. Hu, Z. Qian, Polymeric nanoparticles with ROS-responsive prodrug and platinum nanzyme for enhanced chemophotodynamic therapy of colon cancer, *Adv. Sci.* 7 (2020), 2001853, <https://doi.org/10.1002/advs.202001853>.
 - [28] H. Deng, Z. Zhou, W. Yang, L.S. Lin, S. Wang, G. Niu, J. Song, X. Chen, Endoplasmic reticulum targeting to amplify immunogenic cell death for cancer immunotherapy, *Nano Lett.* 20 (2020) 1928–1933, <https://doi.org/10.1021/acs.nanolett.9b05210>.
 - [29] P. Sarbadhikary, B.P. George, H. Abrahamse, Recent advances in photosensitizers as multifunctional theranostic agents for imaging-guided photodynamic therapy of cancer, *Theranostics* 11 (2021) 9054–9088, <https://doi.org/10.7150/thno.62479>.
 - [30] K. Yue, G. Trujillo-de Santiago, M.M. Alvarez, A. Tamayol, N. Annabi, A. Khademhosseini, Synthesis, properties, and biomedical applications of gelatin methacryloyl (GelMA) hydrogels, *Biomaterials* 73 (2015) 254–271, <https://doi.org/10.1016/j.biomaterials.2015.08.045>.
 - [31] R.L. Siegel, K.D. Miller, H.E. Fuchs, A. Jemal, Cancer statistics, 2021, *CA A Cancer J. Clin.* 71 (2021) 7–33, <https://doi.org/10.3322/caac.21654>.
 - [32] K.C. Kurnit, G.F. Fleming, E. Lengyel, Updates and new options in advanced epithelial ovarian cancer treatment, *Obstet. Gynecol.* 137 (2021) 108–121, <https://doi.org/10.1097/AOG.0000000000004173>.
 - [33] J.M. Lee, L. Minasian, E.C. Kohn, New strategies in ovarian cancer treatment, *Cancer* 125 (Suppl 24) (2019) 4623–4629, <https://doi.org/10.1002/ncr.32544>.
 - [34] D.V. Krysko, A.D. Garg, A. Kaczmarek, O. Krysko, P. Agostinis, P. Vandenabeele, Immunogenic cell death and DAMPs in cancer therapy, *Nat. Rev. Cancer* 12 (2012) 860–875, <https://doi.org/10.1038/nrc3380>.
 - [35] W. Jiang, W. Dong, M. Li, Z. Guo, Q. Wang, Y. Liu, Y. Bi, H. Zhou, Y. Wang, Nitric oxide induces immunogenic cell death and potentiates cancer immunotherapy, *ACS Nano* (2022), <https://doi.org/10.1021/acsnano.1c09048>.
 - [36] P. Liu, L. Zhao, F. Loos, K. Inbarren, S. Lachkar, H. Zhou, L.C. Gomes-da-Silva, G. Chen, L. Bezi, G. Boncompain, F. Perez, L. Zitvogel, O. Kepp, G. Kroemer, Identification of pharmacological agents that induce HMGB1 release, *Sci. Rep.* 7 (2017), 14915, <https://doi.org/10.1038/s41598-017-14848-1>.
 - [37] A.G. Kurian, R.K. Singh, K.D. Patel, J.H. Lee, H.W. Kim, Multifunctional GelMA platforms with nanomaterials for advanced tissue therapeutics, *Bioact. Mater.* 8 (2022) 267–295, <https://doi.org/10.1016/j.bioactmat.2021.06.027>.
 - [38] Z. Luo, W. Sun, J. Fang, K. Lee, S. Li, Z. Guo, M.R. Dokmeci, A. Khademhosseini, Biodegradable gelatin methacryloyl microgels for transdermal drug delivery, *Adv Healthc Mater* 8 (2019), e1801054, <https://doi.org/10.1002/adhm.201801054>.
 - [39] J. Cheng, Z. Chen, C. Liu, M. Zhong, S. Wang, Y. Sun, H. Wen, T. Shu, Bone mesenchymal stem cell-derived exosome-loaded injectable hydrogel for minimally invasive treatment of spinal cord injury, *Nanomedicine* 16 (2021) 1567–1579, <https://doi.org/10.2217/nmm.2021-0025>.
 - [40] S. Xiao, T. Zhao, J. Wang, C. Wang, J. Du, L. Ying, J. Lin, C. Zhang, W. Hu, L. Wang, K. Xu, Gelatin methacrylate (GelMA)-Based hydrogels for cell transplantation: an effective strategy for tissue engineering, *Stem Cell Rev Rep* 15 (2019) 664–679, <https://doi.org/10.1007/s12015-019-09893-4>.
 - [41] J. Fucikova, O. Kepp, L. Kasikova, G. Petroni, T. Yamazaki, P. Liu, L. Zhao, R. Spisek, G. Kroemer, L. Galluzzi, Detection of immunogenic cell death and its relevance for cancer therapy, *Cell Death Dis.* 11 (2020) 1013, <https://doi.org/10.1038/s41419-020-03221-2>.
 - [42] L. Galluzzi, A. Buque, O. Kepp, L. Zitvogel, G. Kroemer, Immunogenic cell death in cancer and infectious disease, *Nat. Rev. Immunol.* 17 (2017) 97–111, <https://doi.org/10.1038/nri.2016.107>.
 - [43] M. Horie, Y. Tabei, Role of oxidative stress in nanoparticles toxicity, *Free Radic. Res.* 55 (2021) 331–342, <https://doi.org/10.1080/10715762.2020.1859108>.
 - [44] B. Yang, Y. Chen, J. Shi, Reactive oxygen species (ROS)-Based nanomedicine, *Chem. Rev.* 119 (2019) 4881–4985, <https://doi.org/10.1021/acs.chemrev.8b00626>.
 - [45] P. Di Mascio, G.R. Martinez, S. Miyamoto, G.E. Ronsein, M.H.G. Medeiros, J. Cadet, Singlet molecular oxygen reactions with nucleic acids, lipids, and proteins, *Chem. Rev.* 119 (2019) 2043–2086, <https://doi.org/10.1021/acs.chemrev.8b00554>.
 - [46] Q. Zhang, Q. Guo, Q. Chen, X. Zhao, S.J. Pennycook, H. Chen, Highly efficient 2D NIR-II photothermal agent with fenton catalytic activity for cancer synergistic photothermal-chemodynamic therapy, *Adv. Sci.* 7 (2020), 1902576, <https://doi.org/10.1002/advs.201902576>.
 - [47] Q.W. Chen, X.H. Liu, J.X. Fan, S.Y. Peng, J.W. Wang, X.N. Wang, C. Zhang, C.J. Liu, X.Z. Zhang, Self-mineralized photothermal bacteria hybridizing with mitochondria-targeted metal-organic frameworks for augmenting photothermal tumor therapy, *Adv. Funct. Mater.* 30 (2020), <https://doi.org/10.1002/adfm.201909806>.
 - [48] C.X. Wang, B. Wu, Y.T. Wu, X.Y. Song, S.S. Zhang, Z.H. Liu, Camouflaging nanoparticles with brain metastatic tumor cell membranes: a new strategy to traverse blood-brain barrier for imaging and therapy of brain tumors, *Adv. Funct. Mater.* 30 (2020), <https://doi.org/10.1002/adfm.201909369>.
 - [49] H.P. Lee, A.K. Gaharwar, Light-responsive inorganic biomaterials for biomedical applications, *Adv. Sci.* 7 (2020), 2000863, <https://doi.org/10.1002/advs.202000863>.

Biomimeration of in vitro transcribed messenger RNA by organic frameworks for gene supplementary and restoring expression (Manuscript)

Wenhui Zhou, Chang Liu, Jiaqi Yan, Xiaoyu Xu, Jessica M. Rosenholm, Tapani Viitala, Jing Feng*, Hongbo Zhang*

Exploiting the warburg effect: Co-delivery of metformin and FOXK2 siRNA for ovarian cancer therapy

Wenhui Zhou, Xiaodong Ma, Jianpeng Xiao, Xiaohui He, Chang Liu, Xiaoyu Xu, Tapani Viitala, Jing Feng*, Hongbo Zhang*. *Small Science* **2024**; 2300192.

Exploiting the Warburg Effect: Co-Delivery of Metformin and FOXK2 siRNA for Ovarian Cancer Therapy

Wenhui Zhou, Xiaodong Ma, Jianpeng Xiao, Xiaohui He, Chang Liu, Xiaoyu Xu, Tapani Viitala, Jing Feng,* and Hongbo Zhang*

Ovarian cancer remains a significant health issue worldwide, often facing limitations in treatment due to side effects and drug resistance. Tumor cells typically undergo the "Warburg effect," preferring glycolysis, which leads to their rapid growth and survival. Metformin, a widely used diabetes medication, targets 5' adenosine monophosphate-activated protein kinase (AMPK), reducing glycolysis and thereby slowing tumor growth. Additionally, forkhead box protein K2 (FOXK2), a transcription factor often found in excess in many tumors, promotes glycolysis and tumor development. Delivering metformin and FOXK2 siRNA directly to the tumor site in the body is challenging due to the metformin's poor water solubility and the fragile nature of siRNA. To address this, zirconium and 5,10,15,20-tetra(4-pyridyl)porphyrin nanoparticles loaded with FOXK2 siRNA, enveloped in cell membrane, co-encapsulated with metformin in gelatin methacrylate microspheres (ZrTCP@siFOXK2@CM/Met@GelMA) hydrogel microspheres are developed for effective dual delivery. These microspheres facilitate targeted drug delivery, photothermal therapy with near-infrared light, and interference with glucose metabolism. These results show that infrared light combined with metformin and FOXK2 siRNA successfully activates the AMPK pathway, reducing ovarian cancer growth. This method offers a promising new direction in treatment, utilizing the complex metabolic characteristics of ovarian cancer to achieve better results.

1. Introduction

Ovarian cancer ranks among the deadliest gynecological malignancies, casting a significant shadow over women's health globally.^[1] Despite the marked progress in surgical procedures and supplementary treatments, handling this malignancy continues to be a daunting task. The key challenges include the adverse side effects from therapeutic interventions and the inexorable emergence of drug resistance during chemotherapy regimens.^[2-6] This underscores the urgent need for innovative therapies that accurately target the core processes behind tumor growth and survival.

The unique metabolism of tumor cells, mainly known for glycolysis or the "Warburg effect," has always intrigued cancer researchers.^[7] Within this metabolic shift, cells predominantly lean toward glycolysis over oxidative phosphorylation, even in oxygen-rich environments. This grants cancer cells distinct advantages, encompassing swift proliferation, heightened metastatic propensities, and

W. Zhou, J. Feng
Shanghai Fengxian District Central Hospital
Shanghai 201499, China
E-mail: fengjing@cuhk.edu.cn

W. Zhou, X. Ma, C. Liu, X. Xu, T. Viitala, H. Zhang
Pharmaceutical Sciences Laboratory
Åbo Akademi University
20520 Turku, Finland
E-mail: hongbo.zhang@abo.fi

X. Ma, C. Liu, X. Xu, T. Viitala, H. Zhang
Turku Bioscience Centre
University of Turku and Åbo Akademi University
20520 Turku, Finland


J. Xiao, J. Feng
The Third School of Clinical Medicine
Southern Medical University
Guangzhou 510630, China

X. He, J. Feng
School of Laboratory Medicine and Biotechnology
Southern Medical University
Guangzhou, Guangdong Province 510515, China

X. He, J. Feng
Department of Laboratory Medicine & Central Laboratory
Shanghai Fengxian District Central Hospital
Shanghai 201499, China

X. He, J. Feng
Longgang District People's Hospital of Shenzhen
Shenzhen 518172, China

T. Viitala
Drug Research Program
Division of Pharmaceutical Chemistry and Technology
Faculty of Pharmacy
University of Helsinki
00014 Helsinki, Finland

 The ORCID identification number(s) for the author(s) of this article can be found under <https://doi.org/10.1002/smcs.202300192>.

© 2023 The Authors. Small Science published by Wiley-VCH GmbH. This is an open access article under the terms of the Creative Commons Attribution License, which permits use, distribution and reproduction in any medium, provided the original work is properly cited.

DOI: 10.1002/smcs.202300192

resilience against programmed cell death.^[8,9] At the heart of this metabolic tale stands 5' adenosine monophosphate-activated protein kinase (AMPK), the guardian of cellular energy equilibrium. Attuned to cellular energy variations, AMPK deftly calibrates both glycolytic and mitochondrial processes, maintaining a balanced energetic state.^[10,11] AMPK's role in thwarting tumorigenic trajectories and its suppressive impact on cell growth and protein genesis is well established.^[12,13] This narrative spotlight shifts to metformin, a preeminent medication for type 2 diabetes. Exemplifying notable anticancer virtues, metformin's therapeutic principle hinges on AMPK activation, tempering the glycolytic enthusiasm intrinsic to tumor cells. By modulating AMPK dynamics, metformin not only curtails protein synthesis and cell proliferation but also rebuffs the glycolytic axis, underscoring its potent candidacy in cancer combat.^[14–17]

Interlaced within this metabolic tapestry is the transcription factor forkhead box protein K2 (FOXK2). With conspicuous over-expression across varied tumors, FOXK2 emerges as a pivotal nexus in glycolytic oversight.^[18] Cutting-edge studies underscore FOXK2's commanding role in steering enzymes and pathways integral to glycolysis, affirming its stature as both a glycolytic champion and a catalyst for tumorigenesis.^[19,20] This revelation promotes a rejuvenated lens on FOXK2, beyond just a diagnostic lighthouse, positioning it as a promising therapeutic target. In light of metformin's robust glycolytic inhibition and FOXK2's glycolytic affinities, a harmonized approach looms on the horizon. Melding metformin's action with FOXK2 silencing offers a tantalizing prospect, potentially unveiling a transformative paradigm in targeting the glycolytic trajectory for refined cancer therapy.

However, despite the optimism surrounding recent advances, significant hurdles persist in the targeted delivery of metformin and siFOXK2 RNA for maximizing cancer treatment efficacy. While metformin, in tandem with chemotherapy drugs, has shown promising therapeutic outcomes,^[21–23] the required cytotoxic concentration for cancer cells remains prohibitively high. Achieving this optimal concentration in tumor tissues through standard means, like intravenous injections, is daunting. Conversely, siRNAs, such as siFOXK2 RNA, with their transformative potential in gene silencing, grapple with multiple challenges.^[24–26] The innate instability of siRNA molecules stands out as a primary concern. Compounding this is the biological membrane barrier, which restricts the efficient delivery of these sequences into target cells, a predicament more pronounced within the intricate tumor microenvironments. Consequently, this barrier has become a significant roadblock for the broader adoption of nucleotide-based treatments.^[27] Therefore, crafting a precise co-delivery system for metformin and FOXK2 siRNA is crucial for tapping into their synergistic therapeutic potential against cancer.

Capitalizing on the synergistic therapeutic benefits of FOXK2 siRNA and metformin, we employed microfluidic technology to craft the zirconium and 5,10,15,20-tetra(4-pyridyl)porphyrin nanoparticles loaded with FOXK2 siRNA, enveloped in cell membrane, co-encapsulated with metformin in gelatin methacrylate microspheres (ZrTCP@siFOXK2@CM/Met@GelMA) hydrogel microspheres, heralding a new paradigm in enhanced treatment.^[28,29] Central to this pioneering approach is the GelMA substrate, lauded for its outstanding biocompatibility and precision in drug release.^[30] This deliberate integration is crucial in

overcoming the inherent barriers of reaching optimal therapeutic concentrations of metformin within tumor tissues, a feat seldom achieved through conventional delivery methods.^[31] By engineering GelMA microspheres tailored for intratumoral administration, we champion localized drug delivery, curtailing systemic side effects and bolstering therapeutic efficacy.^[32] Encapsulated within these microspheres are both metformin and the ingeniously designed ZrTCP@siFOXK2@CM nanoparticles (NPs). These NPs represent a confluence of the metallic zirconium (Zr) and the photosensitizing agent 5,10,15,20-tetra(4-pyridyl)porphyrin (TCPP), giving rise to the versatile ZrTCP metal-organic frameworks (MOFs).^[33] Characterized by their porous construct, these MOFs excel in siRNA encapsulation and are further sheathed with a tumor-cell-sourced membrane, enhancing their tumor-targeting ability.^[34–36] But their ingenuity stretches further. At the heart of their design lies the TCPP component, which, when stimulated by near-infrared light, triggers a photodynamic reaction, releasing reactive oxygen species (ROS) within the tumor milieu.^[37,38] This cascade of ROS serves a twofold purpose: direct cytotoxic effects causing cellular membrane damage and consequent cell death, and strategic interference with glucose metabolism.^[39–42] Such intervention enhances the precision targeting of metformin and FOXK2 siRNA on these metabolic pathways, accentuating their collective antitumor prowess.

The synthesized ZrTCP NPs, with impressive dispersity in ethanol solution, presented an approximate particle size of 104.5 ± 8.4 nm. The tumor-cell-membrane-coated NPs showcased high cellular uptake efficiency and superior lysosome escape potential. In conjunction with metformin, ZrTCP@siFOXK2@CM NPs exhibited heightened cytotoxicity, especially under infrared light, significantly impacting SKOV3 and OVCAR3 ovarian cancer cells. Upon exposure to infrared light, these NPs notably raised cellular ROS levels, and their synergistic use with metformin prominently activated the AMPK signaling pathway in SKOV3 cells. In vivo studies, the GelMA microspheres, ZrTCP@siFOXK2@CM/Met@GelMA, demonstrated impressive tumor tissue retention and significant tumor suppression under laser irradiation. In sum, our work introduces a pioneering therapeutic strategy, leveraging the metabolic vulnerabilities of ovarian cancer for enhanced treatment outcomes.

2. Results

2.1. FOXK2 Silencing-Induced Cell Death in Ovarian Cancer is Enhanced by Metformin

To explore the role of the FOXK2 gene in ovarian cancer, we analyzed its expression in 30 types of pan-cancer and adjacent non-tumor tissues using The Cancer Genome Atlas (TCGA) database. Our results (Figure 1A) revealed a significant overexpression of FOXK2 in ovarian cancer tissues, with markedly lower expression in the adjacent non-tumor tissues. This differential expression pattern indicates that FOXK2 may serve as an oncogene in ovarian cancer and suggests that it could be a potential therapeutic target. The broad pan-cancer analysis contextualized these

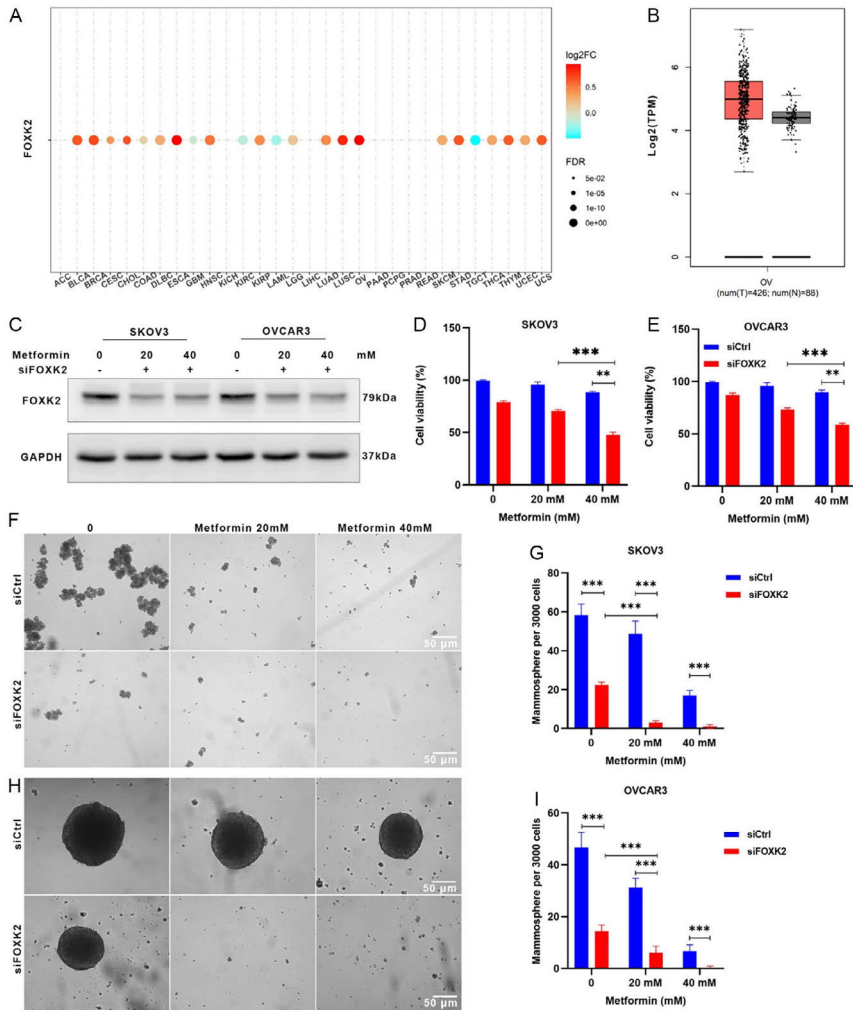


Figure 1. Metformin intensified the inhibitory effect of FOXK2 siRNA on the proliferation and mammosphere formation of SKOV3 and OVCAR3 cells. A,B) FOXK2 expression across Cancer Genome Atlas (TCGA) cancers (A) and ovary cancers (B) from TCGA database ($P < 0.05$). C) Expression of FOXK2 in SKOV3 and OVCAR3 cells tested by western blot assay; cell viability of D) SKOV3 and E) OVCAR3 cells after treatment of siFOXK2 and metformin for 48 h tested by Cell Counting Kit-8 (CCK-8) assay ($n = 3$). Data are presented as the mean \pm standard deviation (SD) from three independent experiments. F–I) Representative images and quantification of mammospheres formed from SKOV3 (F,G) and OVCAR3 (H,I) cell lines after treatment of siFOXK2 and metformin for 24 h (scale bar = 50 μm). Statistical significance among groups in (D,E,G,I) was determined by one-way analysis of variance (ANOVA), $*P < 0.05$, $**P < 0.01$, $***P < 0.001$, and $****P < 0.0001$.

findings, reinforcing the specificity of the role of FOXK2 in ovarian cancer within the larger oncological landscape (Figure 1B).

To further elucidate the functional significance of FOXK2 in ovarian cancer, we silenced its expression in SKOV3 and OVCAR3 cells using siRNA. Post transfection, we observed a pronounced decrease in cell viability (Figure 1C–E) and tumor

sphere-forming ability (Figure 1F–I), reflecting the importance of FOXK2 in ovarian cancer progression. Subsequent incubation with 20–40 mM of metformin further weakened the cells' survival and sphere-forming ability. These findings highlight a potential synergistic effect between FOXK2 silencing and metformin, offering insights into novel therapeutic strategies for ovarian cancer.

Collectively, our study illuminates the pivotal role of FOXK2 in the progression of ovarian cancer. By demonstrating its over-expression in tumors and its functional importance in cell survival and growth, we have identified FOXK2 as a promising therapeutic target. The synergistic effects of FOXK2 silencing and metformin treatment lay the groundwork for innovative treatment modalities in ovarian cancer. Further studies are required to translate these findings into clinically effective interventions.

2.2. Synthesis and Characterization of ZrTCP@siFOXK2@CM NPs

In our study, we ingeniously utilized the photosensitizer TCP (TCPP) as a ligand and, through a nanoscale self-assembly process, reacted it with Zr ions to synthesize ZrTCP NPs (Scheme 1). These NPs displayed a fusiform shape, with a diameter of approximately 104 nm and a negative charge (Figure 2A–C). In a subsequent step, we successfully loaded FOXK2 siRNA into these NPs by means of self-adsorption, thereby creating ZrTCP@siFOXK2 NPs. Interestingly, this procedure did not significantly alter the NP size, but the surface charge was markedly reduced to -27.8 mV. Quantitative analysis revealed that the loading capacity of the ZrTCP@siFOXK2 NPs could reach up to 100 mg g^{-1} . To further enhance the protective effect of the NPs for siRNA and targeting specificity to tumor cells, we isolated and purified the cell membrane from SKOV3 cells. Through overnight stirring, we prepared biomimetic NPs with cell-membrane coating, termed ZrTCP@siFOXK2@CM. These cell-membrane-coated NPs maintained an elliptical shape, but exhibited clear membrane structures on their surface (Figure 2B). Significantly, the particle size of the

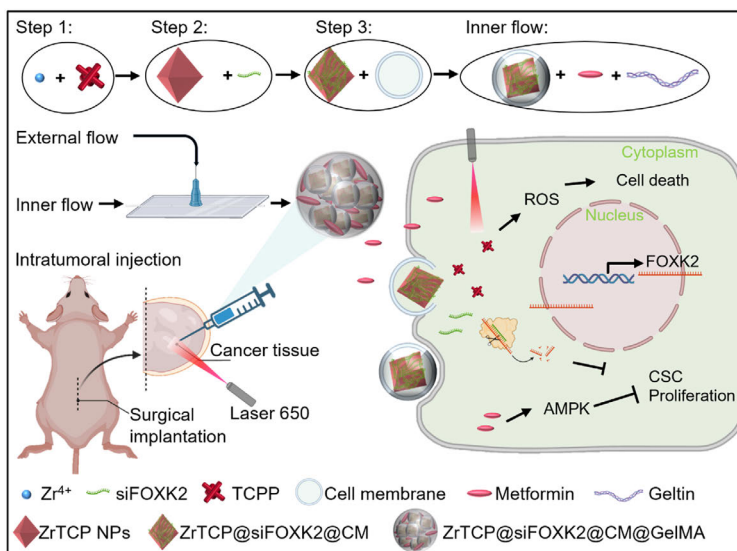
cell-membrane-coated NPs increased to 125.3 nm, and the surface charge further decreased to -34.6 mV (Figure 2D).

In conclusion, our fabricated ZrTCP@siFOXK2 NPs, as well as ZrTCP@siFOXK2@CM, possess appropriate size and physical morphology, coupled with a high siRNA loading capacity. Theoretically, these attributes confer feasibility for intracellular siRNA delivery, positioning them as promising vectors for targeted gene silencing applications. These findings provide a novel insight into NP engineering and underscore the potential of ZrTCP@siFOXK2@CM NPs for therapeutic interventions in oncological research.

2.3. Cellular Interaction of ZrTCP@siFOXK2@CM NPs and Ovary Cancer Cells

Building upon previous results, we sought to further validate the feasibility of ZrTCP@siFOXK2 NPs as siRNA intracellular delivery carriers. To this end, ZrTCP@siCtrl-Cy5.5 and ZrTCP@siCtrl-Cy5.5@CM NPs were synthesized using Cy5.5-labeled control siRNA, and subsequently incubated with logarithmically growing SKOV3 cells over a period of 2–6 h. Observations revealed that both types of NPs exhibited intracellular aggregation as early as 2 h post-incubation, with a time-dependent increase in Cy5.5 red fluorescence (Figure 3A,B). Remarkably, cell-membrane-coated ZrTCP@siCtrl-Cy5.5@CM demonstrated enhanced intracellular accumulation compared to its non-coated counterpart (Figure 3A,B and S4, Supporting Information), supporting the hypothesis that membrane-coating augments NP uptake and intracellular delivery efficiency.

In a subsequent experiment, we employed green lysosomal fluorescent dye LysoTracker to investigate the lysosomal escape capability of ZrTCP@siCtrl-Cy5.5@CM NPs within SKOV3



Scheme 1. Schematic representation of the preparation process for ZrTCP@siFOXK2@CM/Met@GelMA microgel and its antitumor mechanism.

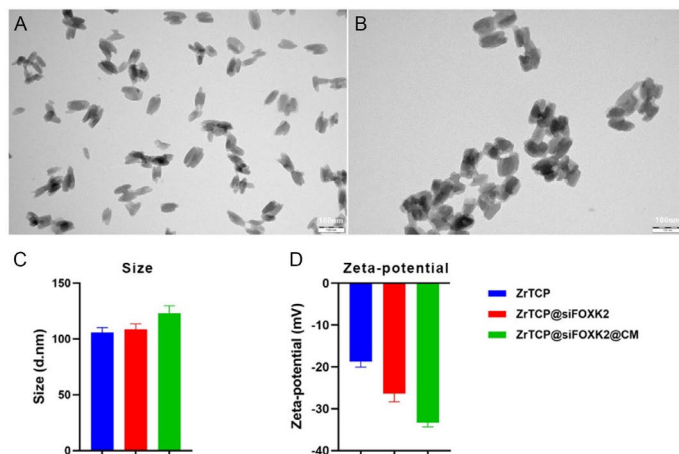


Figure 2. Morphology and characteristics of ZrTCP@siFOXK2 and ZrTCP@siFOXK2@CM nanoparticles (NPs). A,B) Representative images of ZrTCP (A) and ZrTCP@siFOXK2@CM (B) NPs captured by transmission electron microscopy (scale bar = 100 nm); C) size and D) zeta-potential of ZrTCP, ZrTCP@siFOXK2, and ZrTCP@siFOXK2@CM NPs measured by dynamic light scattering. Data are presented as the mean \pm SD from three independent experiments, statistical significance among groups was determined by one-way ANOVA, * $P < 0.05$, ** $P < 0.01$, *** $P < 0.001$, and **** $P < 0.0001$.

cells (Figure 3C–E). The data revealed minimal colocalization between lysosomal green fluorescence and the red fluorescence of ZrTCP@siCtrl-Cy5.5@CM, regardless of incubation time (Figure 3D–F). This suggested that ZrTCP@siCtrl-Cy5.5@CM NPs could either efficiently escape lysosomal compartments or enter cells via pathways independent of the lysosomal route.

Finally, the cytotoxicity profile of ZrTCP@siFOXK2 and ZrTCP@siFOXK2@CM NPs was explored. The findings indicated a notable reduction in cell survival rates to 72.3% and 69.8% for SKOV3 and OVCAR3 cells, respectively, after 48 h incubation at $2 \mu\text{g mL}^{-1}$ (Figure 3F,G). Moreover, survival rates were further reduced to 20.3% and 25.6% with ZrTCP@siFOXK2@CM, emphasizing its superior inhibitory effect. A caveat emerged with the observation that higher concentrations of ZrTCP@siCtrl exerted significant cytotoxic effects, revealing a potential underlying toxicity of the ZrTCP NPs themselves.

In summary, the current study affirms the promising characteristics of ZrTCP NPs in cellular uptake and lysosomal escape, with cell-membrane-coating serving as an effective strategy for enhancing efficiency. Additionally, the significant inhibitory effects of ZrTCP@siFOXK2 NPs on SKOV3 and OVCAR3 cell proliferation were elucidated, with further enhancement observed upon membrane encapsulation. These collective insights underline the potential of ZrTCP NPs for targeted siRNA delivery, indicating their potential applicability in therapeutic strategies for ovarian cancer.

2.4. Synthesis and Characterization of ZrTCP@siFOXK2@CM@GelMA Microgel

Building on the initial findings, we extended our investigation to determine the synergistic effect of ZrTCP@siFOXK2 NPs with

metformin, given that prior studies confirmed the ability of metformin to enhance the inhibitory effect of FOXK2 siRNA on ovarian cancer cells. ZrTCP@siFOXK2 and ZrTCP@siFOXK2@CM NPs were incubated with logarithmically growing SKOV3 and OVCAR3 cells at a concentration of $1 \mu\text{g mL}^{-1}$, in conjunction with 20–30 mM of metformin. Following 48 h of incubation, a significant reduction in cell survival rates was observed in both ZrTCP@siFOXK2 and ZrTCP@siFOXK2@CM NP-treated groups relative to the ZrTCP@siCtrl control group (Figure 4A,B). More remarkably, the addition of metformin further significantly decreased the survival rates, with the lowest rates attained in the 30 mM metformin and ZrTCP@siFOXK2@CM combination group, reaching 27.1% and 32.5% for SKOV3 and OVCAR3 cells, respectively. These results strongly indicate that ZrTCP@siFOXK2 NPs and metformin exert a synergistic inhibition on tumor cell proliferation.

Subsequently, in an effort to optimize the administration of ZrTCP@siFOXK2@CM NPs and metformin, enhance drug utilization efficiency, and mitigate potential toxicity, we utilized microfluidic technology to encapsulate ZrTCP@siFOXK2@CM NPs and metformin within GelMA to create injectable, slow-degrading GelMA microgel beads suitable for in situ tumor injection (Figure 4C). As depicted in Figure 4C, an aqueous solution containing $2 \mu\text{g mL}^{-1}$ of ZrTCP@siFOXK2@CM NPs, 30 mM metformin, GelMA, and cross-linking agents was used as the inner phase (Flow 1), and a 5% Span80 mineral oil solution was employed as the outer phase (Flow 2). By manipulating the flow rate ratio between Flow 1 and Flow 2, we successfully fabricated ZrTCP@siFOXK2/Met@CM@GelMA microbeads ranging from 70 to 200 μm in diameter (Figure 4D,E). We selected the 70 μm ZrTCP@siFOXK2@CM/Met@GelMA microbeads for subsequent experiments.

Interestingly, the release profile of metformin from the ZrTCP@siFOXK2@CM/Met@GelMA microgel revealed a

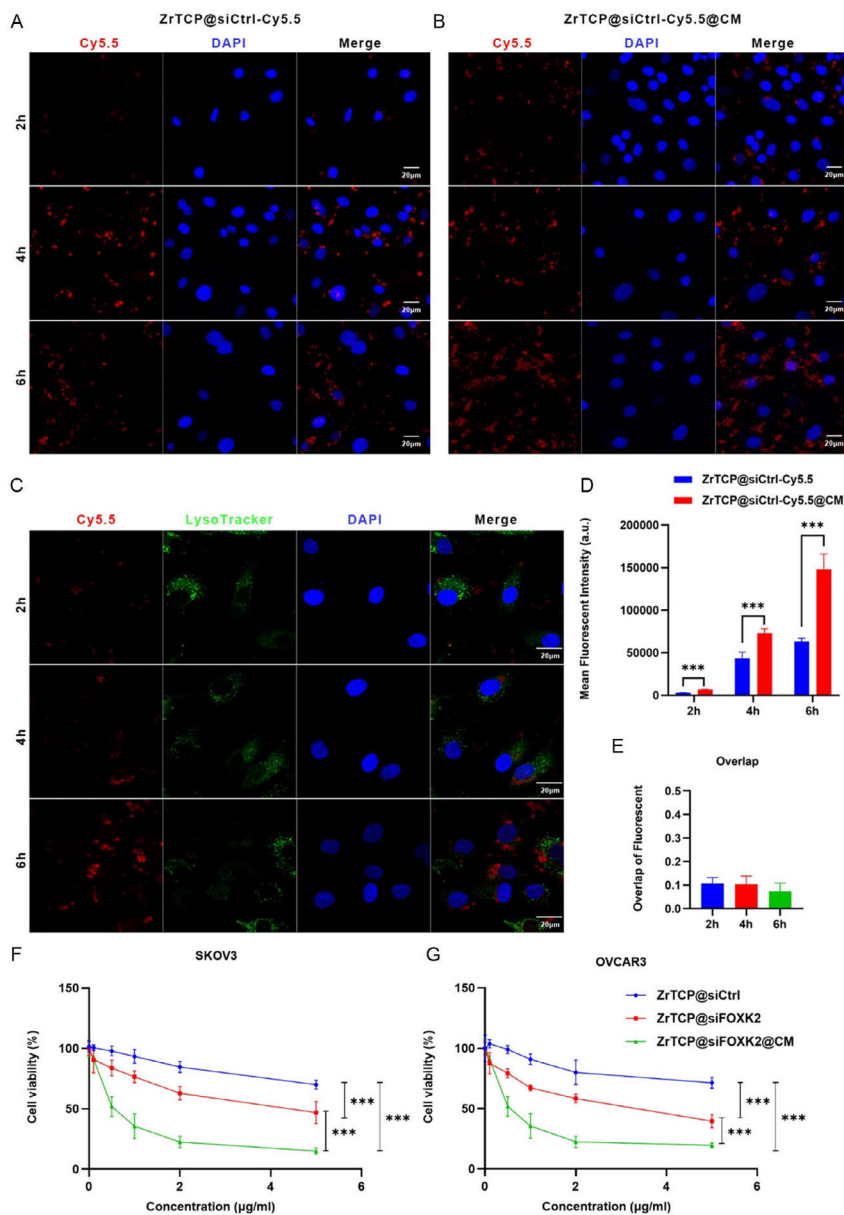


Figure 3. Confocal imaging, fluorescence intensity, and cellular viability of SKOV3 and OVCAR3 cells post-NP uptake. A,B) Representative confocal microscopy images of SKOV3 cells after uptake of ZrTCP@siCtrl-Cy5.5 (A) and ZrTCP@siCtrl-Cy5.5@CM (B) NPs (scale bar: 20 µm). C) Representative confocal microscopy images of ZrTCP@siCtrl-Cy5.5@CM NPs colocalized with lysosomes after endocytosis (red: ZrTCP@siCtrl-Cy5.5@CM NPs; green: lysosome; blue: nucleus; scale bar: 20 µm). D) Quantitative data on the mean fluorescent intensity of SKOV3 cells following uptake of ZrTCP@siCtrl-Cy5.5 and ZrTCP@siCtrl-Cy5.5@CM NPs ($n = 3$). E) Overlap of the fluorescent signal from ZrTCP@siCtrl-Cy5.5@CM NPs with that of the lysosome following uptake ($n = 3$). F,G) Cell viabilities of SKOV3 (F) and OVCAR3 (G) cells after treatment of ZrTCP@siCtrl, ZrTCP@siFOXK2, and ZrTCP@siFOXK2@CM NPs for 48 h measured by CCK-8 assay ($n = 3$). Data are presented as the mean \pm SD from three independent experiments, statistical significance among groups was determined by one-way ANOVA, $*P < 0.05$, $**P < 0.01$, $***P < 0.001$, and $****P < 0.0001$.

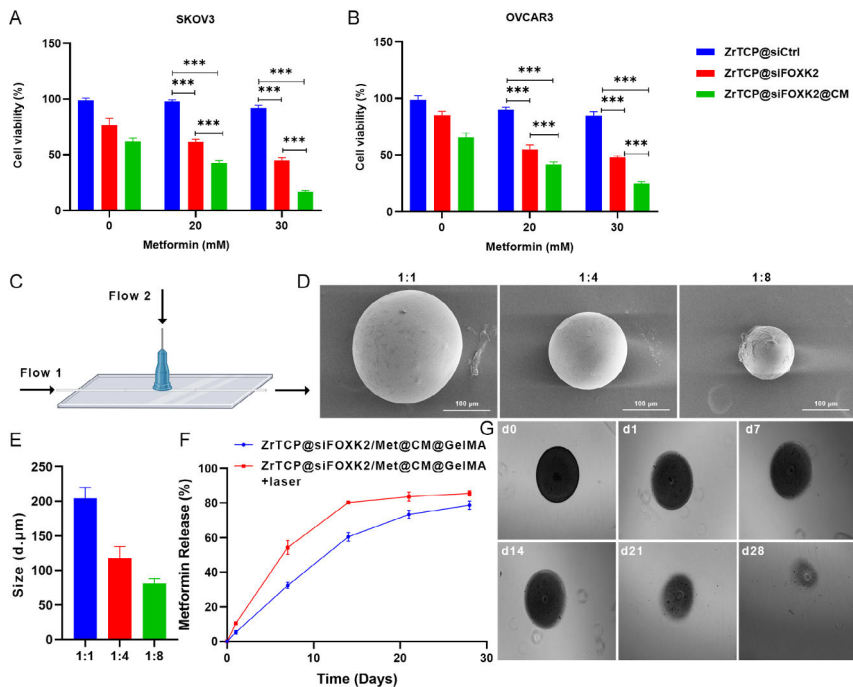


Figure 4. Preparation and characterization of ZrTCP@siFOXK2/Met@CM@GelMA microgel. A,B) Cell viabilities of SKOV3 (A) and OVCAR3 (B) cells after 48 h of treatment with ZrTCP@siCtrl, ZrTCP@siFOXK2, or ZrTCP@siFOXK2@CM NPs combined with metformin, as measured by the CCK-8 assay ($n = 3$). C) Schematic of microfluidics chip for ZrTCP@siFOXK2/Met@CM@GelMA microgel preparation. D) Representative images of ZrTCP@siFOXK2/Met@CM@GelMA microgel prepared with different flow 1:flow 2 flow speed ratio (scale bar: 100 μm). E) Size of ZrTCP@siFOXK2/Met@CM@GelMA microgel formed at different flow 1:flow 2 flow speed ratio ($n = 3$). F) Metformin release profile of ZrTCP@siFOXK2/Met@CM@GelMA microgel in deionized water with or without 650 nm laser irradiation (0.5 W cm^{-2} , 5 min every 3 days) ($n = 3$). G) Representative images showing the degradation of ZrTCP@siFOXK2/Met@CM@GelMA microgel in deionized water. Data in (A,B,E,F) are presented as the mean \pm SD from three independent experiments, statistical significance among groups was determined by one-way ANOVA, * $P < 0.05$, ** $P < 0.01$, *** $P < 0.001$, and **** $P < 0.0001$.

continuous release over 28 days, with a maximum release of 78.6% (Figure 4F). This correlated with observable, gradual collapse of the microbeads, culminating in complete degradation at 28 days (Figure 4G). When exposed to 650 nm laser irradiation, the release rate of metformin significantly accelerated, reaching a maximum release of 80.8% after 14 days. Based on these findings, we inferred that the ZrTCP@siFOXK2/Met@CM@GelMA microgel exhibits excellent sustained-release efficiency for both metformin and ZrTCP@siFOXK2/Met@CM NPs. The enhanced release upon 650 nm laser irradiation is likely attributed to the photosensitive material TCPP within the ZrTCP NPs, which responded to the laser, stimulating release through photodynamic reactions.

In conclusion, this part of the study demonstrated the synergistic antitumor effect of ZrTCP@siFOXK2 NPs with metformin and introduced a novel microgel delivery system, facilitating controlled, sustained release. The promising release characteristics, augmented by light-triggered responsiveness,

underscore the potential of ZrTCP@siFOXK2/Met@CM@GelMA microgels for localized cancer therapy. Further studies will be essential to assess the in vivo efficacy and safety profile of this innovative therapeutic approach.

2.5. Laser Irradiation Elevated ZrTCP@siFOXK2@CM@GelMA Microgel-Mediated Cell Death at Cellular Level

Continuing from the aforementioned research, we sought to further validate the tumor-suppressing efficacy of our synthesized GelMA microspheres at the cellular level. By employing techniques such as calcein-acetoxymethyl ester/propidium iodide (calcein AM/PI) live/dead cell staining and flow cytometric analysis, we examined the apoptosis levels in SKOV3 and OVCAR3 cells under various GelMA microsphere formulations, both with and without laser irradiation. As depicted in the corresponding Figure 5A,B, in comparison with the phosphate-buffered saline (PBS) group, the cells treated with $1 \mu\text{mL}^{-1}$ NPs of

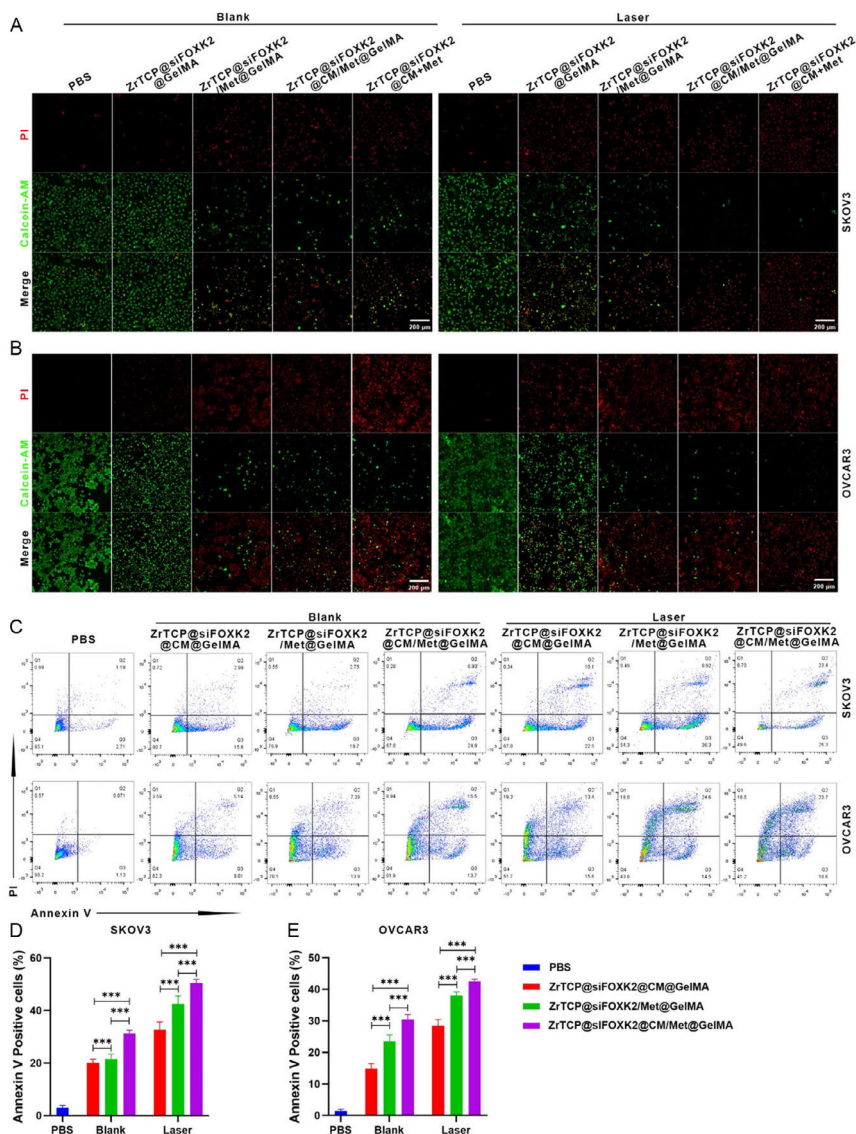


Figure 5. ZrTCP@siFOXK2@CM@GelMA microgel-induced cell death in SKOV3 and OVCAR3 cells. A,B) Representative confocal microscopy images of SKOV3 (A) and OVCAR3 (B) cells after treatment of PBS, ZrTCP@siFOXK2@GelMA, ZrTCP@siFOXK2/Met@GelMA, ZrTCP@siFOXK2@CM/Met@GelMA, or ZrTCP@siFOXK2@CM + Met for 48 h and combined with/without 650 nm laser irradiation (0.5 W cm^{-2} , 5 min) (red: PI; green: calcein AM; scale bar: 200 μm). C) Apoptotic cells and D,E) quantification data after 48 h of treatment, analyzed by flow cytometry. Data in (D,E) are presented as the mean \pm the standard error of the mean (S.E.M.) from three independent experiments, statistical significance among groups was determined by one-way ANOVA, $*P < 0.05$, $**P < 0.01$, $***P < 0.001$, and $****P < 0.0001$.

ZrTCP@siFOXK2/Met@GelMA, ZrTCP@siFOXK2@CM/Met@GelMA, and ZrTCP@siFOXK2@CM@GelMA + 30 mM free metformin for 48 h displayed a significant increase in red

fluorescent PI-labeled dead cells, with a concomitant substantial reduction in green fluorescent calcein-AM-labeled live cells. Following the addition of 650 nm laser irradiation, the SKOV3

and OVCAR3 cells incubated with ZrTCP@siFOXK2GelMA exhibited a marked increase in red fluorescent signals representing dead cells and a significant reduction in green fluorescent signals representing live cells. Moreover, regardless of additional laser exposure, the groups treated with metformin-containing ZrTCP@siFOXK2/Met@CM@GelMA and ZrTCP@siFOXK2@CM@GelMA + 30 mM free metformin showed even more dead cells and fewer live cell signals.

Further deepening our analysis, we utilized flow cytometry to provide additional clarity regarding the antitumor effects of ZrTCP@siFOXK2/Met@CM@GelMA. As demonstrated in Figure 5C–E, following the treatment of SKOV3 and OVCAR3 cells for 48 h with ZrTCP@siFOXK2@CM@GelMA, ZrTCP@siFOXK2/Met@GelMA, and ZrTCP@siFOXK2@CM/Met@GelMA, there was a marked increase in Annexin-V-positive apoptotic cell populations. This effect was further amplified under the influence of 650 nm laser irradiation. The ZrTCP@siFOXK2@CM/Met@GelMA + laser irradiation group displayed the highest Annexin-V-positive cell populations,

measuring 52.3% and 42.6% in SKOV3 and OVCAR3 cells, respectively. In summary, these findings further delineate the cellular-level antitumor effects of ZrTCP@siFOXK2@CM/Met@GelMA and confirm the synergistic antitumor efficacy when combined with 650 nm laser irradiation.

2.6. Biodistribution and in Vivo Safety of ZrTCP@siFOXK2@CM NPs and ZrTCP@siFOXK2/Met@CM@GelMA Microgel

Continuing from our previous findings, we delved into evaluating the in vivo antitumor efficacy of our formulated ZrTCP@siFOXK2@CM/Met@GelMA GelMA hydrogel. Initially, using a mouse xenograft model, we assessed the in vivo distribution and organ toxicity of both ZrTCP@siFOXK2@CM NPs and the ZrTCP@siFOXK2/Met@CM@GelMA microgel. As evident from Figure 6A,B, the in vivo imaging of small animals post tail vein injection of 100 μL of 5 mg mL^{-1} ZrTCP@siFOXK2@CM NPs revealed a substantial NP

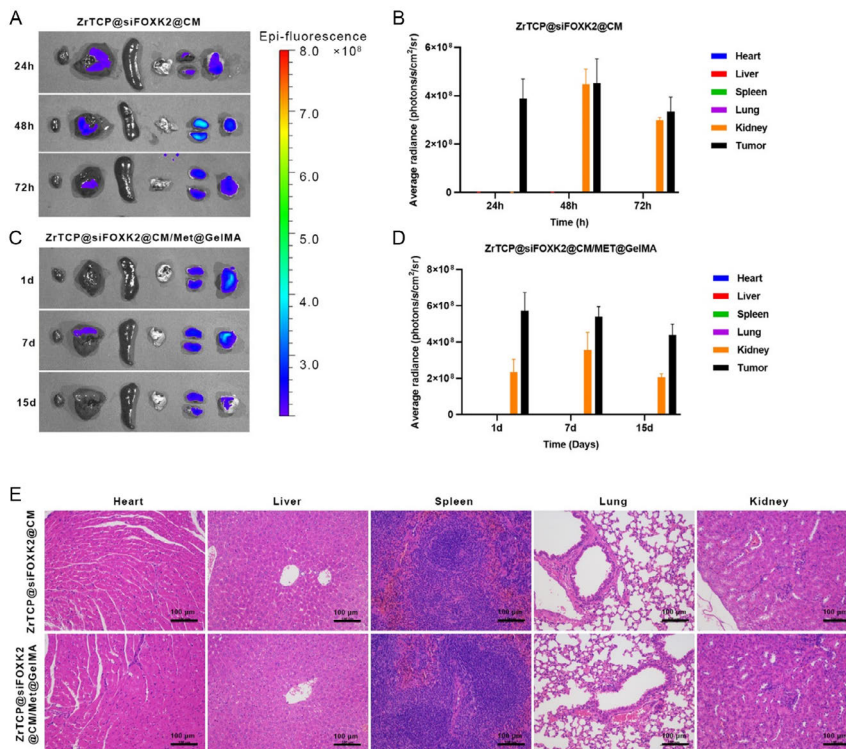


Figure 6. Biodistribution and organotoxicity in a nude mouse xenograft tumor model. A–D) Fluorescence imaging of main organs (L–R: heart, liver, spleen, lung, kidney, tumor) in tumor-bearing nude mice post-intravenous injection of ZrTCP@siFOXK2@CM (A,B) and post-intratumoral injection of ZrTCP@siFOXK2@CM/Met@GelMA (C,D) using the in vivo imaging system. E) Hematoxylin and eosin (H&E)-stained sections of main organs from tumor-bearing nude mice 7 days after intravenous injection of ZrTCP@siFOXK2@CM and intratumoral injection of ZrTCP@siFOXK2@CM/Met@GelMA ($n = 3$, scale bar: 100 μm). Data in (B,D) are presented as the mean \pm S.E.M. from three independent experiments, statistical significance among groups was determined by one-way ANOVA, * $P < 0.05$, ** $P < 0.01$, *** $P < 0.001$, and **** $P < 0.0001$.

aggregation in tumor tissues within a mere 24 h. Concurrently, significant NPs were also detected in the liver and kidneys of the mice, with a persistent presence even after 72 h. In stark contrast (Figure 6C,D), when the tumor tissue was directly injected with an equivalent amount of ZrTCP@siFOXK2/Met@CM@GelMA microgel, the signal from ZrTCP@siFOXK2@CM NPs was predominantly localized within the tumor tissue, enduring for at least 15 days.

Subsequently, mice injected with ZrTCP@siFOXK2@CM NPs for 72 h and those administered with ZrTCP@siFOXK2/Met@CM@GelMA microgel intra-tumorally for 15 days were euthanized to obtain primary organ (heart, liver, spleen, lungs, kidneys) tissue samples. Histopathological examinations from hematoxylin and eosin (H&E)-stained sections (Figure 6E) demonstrated that neither the tail vein injection of ZrTCP@siFOXK2@CM NPs nor the intratumoral injection of ZrTCP@siFOXK2/Met@CM@GelMA microgel-induced any significant pathological damage in the major organs. This data confirms that tail vein injection of ZrTCP@siFOXK2@CM NPs, apart from tumor tissues, results in aggregation in both the liver and kidneys. In contrast, *in situ* injection of the ZrTCP@siFOXK2/Met@CM@GelMA microgel into the tumor displayed some degree of aggregation in kidney tissues, though without evident damage to the primary organs (heart, liver, spleen, lungs, kidneys) in either scenario.

2.7. Antitumor Efficacy of the ZrTCP@siFOXK2@CM@GelMA Microgel in Ovarian Cancer Models

Expanding on our previous observations, we further explored the *in vivo* antitumor efficacy of ZrTCP@siFOXK2@CM NPs and ZrTCP@siFOXK2/Met@CM@GelMA gel using the SKOV3 xenograft model in nude mice. Mice bearing SKOV3 xenografts were grouped into eight distinct categories, with each group undergoing a different treatment regimen as outlined: Group 1: mice received a tail vein injection of 100 μ L PBS on the first day. Group 2: a tail vein injection of metformin in PBS at 0.2 mg kg⁻¹ was administered on the first day. Groups 3 and 6: a tail vein injection of a mixture solution of ZrTCP@siFOXK2@CM NPs and metformin was administered on the first day. Groups 4 and 7: an intratumoral injection of ZrTCP@siFOXK2/Met@GelMA gel at 5 mg kg⁻¹ was given on the first day. Groups 5 and 8: an intratumoral injection of ZrTCP@siFOXK2/Met@CM@GelMA gel at 5 mg kg⁻¹ was given on the first day. From the second day onward, Groups 6–8 underwent *in situ* laser irradiation (650 nm, 0.25 W cm⁻² for 5 min) every other day. Mice were monitored bi-daily for weight and tumor growth, with euthanization occurring when the maximum tumor diameter reached 2 cm. Following euthanization, tumor and primary organ tissues (heart, liver, spleen, lungs, kidneys) were harvested for histological (H&E) and immunohistochemical examination.

As depicted in Figure 7A,B, when compared to the PBS control and the metformin injection groups, the ZrTCP@siFOXK2/Met@CM@GelMA (Group 5), ZrTCP@siFOXK2/Met@CM+laser (Group 6), ZrTCP@siFOXK2/Met@GelMA+laser (Group 7), and ZrTCP@siFOXK2/Met@CM@GelMA+laser (Group 8) groups all exhibited significant inhibition of tumor growth. Notably, the tumor growth inhibition capability

of Groups 6–8 was markedly superior to that of Group 5, but no discernible differences were observed among them. H&E results (Figure 7C) indicated varying degrees of necrosis in tumor tissues from Groups 3–8. Evaluated by necrotic area, the percentage of tumor necrosis was significantly higher in Groups 5–8, with respective figures of 45%, 55%, 65%, and 80%, in stark contrast to the 12% observed in Group 4 (Figure 7E). Furthermore, immunohistochemical findings for tumor tissues revealed a substantial decline in the proliferation index Ki67 in Groups 4–8 (Figure 7G and S7, Supporting Information) coupled with a significant increase in the apoptosis index terminal deoxynucleotidyl transferase dUTP nick end labeling (TUNEL) (Figure 7H and S8, Supporting Information) when juxtaposed with Groups 1–3. Additionally, tumor tissue FOXK2 gene expression levels were assessed (Figure 7D,F). Using the PBS-treated group as the benchmark (100%), FOXK2 gene expression in Groups 3–8 was 90%, 65%, 60%, 70%, 58%, and 40%, respectively. In comparison with control Groups 1 and 2, a significant reduction in FOXK2 gene expression was observed across Groups 3–8.

Collectively, these findings underscore the capability of combined treatments—tail vein injection of ZrTCP@siFOXK2@CM NPs and metformin mixture with laser therapy, intratumoral injections of either ZrTCP@siFOXK2/Met@GelMA with laser or ZrTCP@siFOXK2/Met@CM@GelMA with or without laser—to notably inhibit tumor growth and induce tumor tissue apoptosis. Moreover, tail vein injection of ZrTCP@siFOXK2@CM NPs or intratumoral injections of ZrTCP@siFOXK2/Met@GelMA or ZrTCP@siFOXK2/Met@CM@GelMA effectively diminished the FOXK2 gene expression in tumor tissues.

3. Discussion

The challenge of managing ovarian cancer is magnified by its heterogeneity, its tendency to remain asymptomatic in initial stages, and the evolution of chemoresistance during the therapeutic course. These barriers emphasize the pressing need for refined therapeutic strategies targeting the unique susceptibilities of ovarian cancer cells. A burgeoning body of research has pinpointed metabolic reprogramming as a distinct hallmark of cancer cells, opening avenues for specialized therapeutic interventions.^[43–45]

The antidiabetic medication, metformin, has garnered attention for its promising anticancer capabilities.^[46] Its mechanism, notably through modulating mitochondrial oxidative phosphorylation and orchestrating the AMPK signaling pathway, offers intriguing therapeutic possibilities.^[47] Our findings robustly suggest that the antiproliferative prowess of metformin is heightened when combined with FOXK2 siRNA. The forkhead box (FOX) family of transcription factors, with FOXK2 in particular, stands out as instrumental in metabolic reprogramming and resilience under metabolic duress.^[18,19,48] These features nominate them as compelling therapeutic contenders. Yet, bridging the chasm between *in vitro* observations and *in vivo* therapeutic triumphs demands an astute approach to drug delivery.

The quandaries inherent to the targeted conveyance of therapeutic agents, especially siRNAs, are well chronicled. These nucleic acid derivatives often grapple with obstacles like rapid

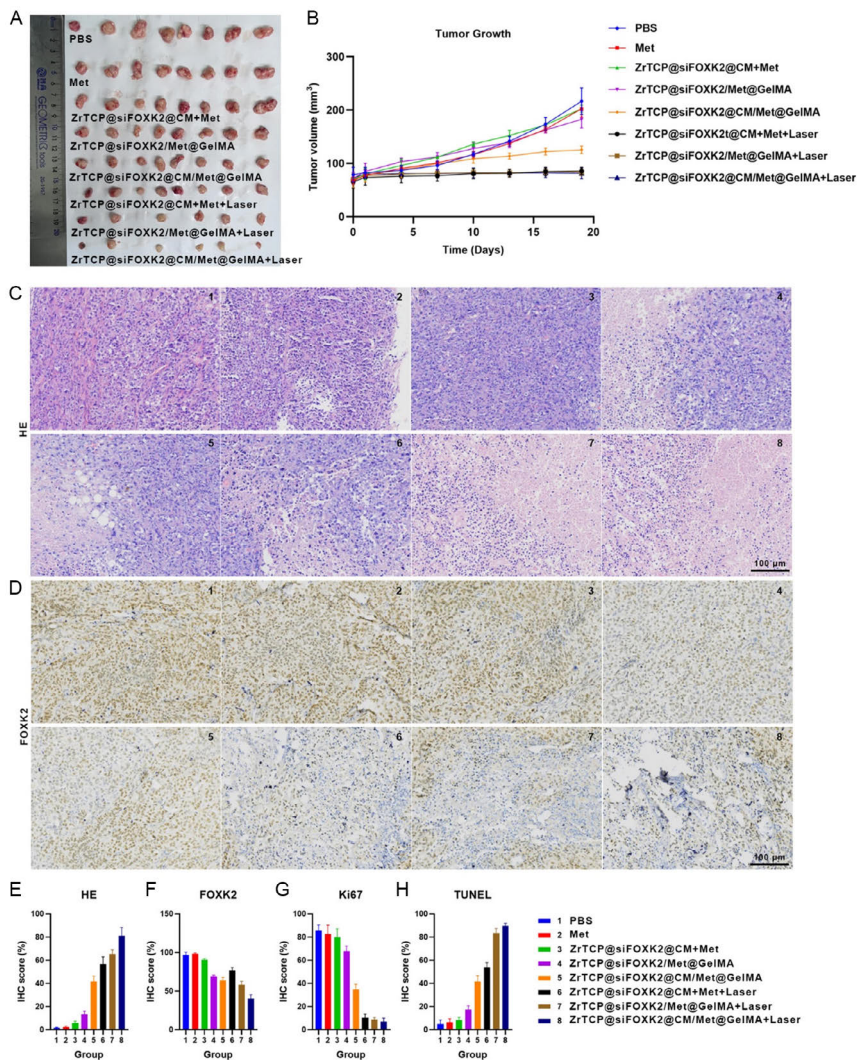


Figure 7. Antitumor effects of ZrTCP@siFOXK2@CM NPs and ZrTCP@siFOXK2@CM/Met@GelMA microgel in SKOV3 xenograft tumor model. A) Photos of tumors from SKOV3-xenograft-bearing nude mice post 18 days of various treatments, alongside B) the tumor growth curve ($n \geq 6$). C) H&E sections and D) FOXK2 immunohistochemistry (IHC) staining of tumor tissues from SKOV3-xenograft-bearing nude mice following different treatments ($n = 3$; scale bar: 100 μm). E–H) IHC scores for tumor tissue staining: E) H&E, F) FOXK2, G) Ki67, and H) TUNEL ($n = 3$). Data in (B, E–H) are presented as the mean \pm S.E.M. from three independent experiments; statistical significance among groups was determined by one-way ANOVA, $*P < 0.05$, $**P < 0.01$, $***P < 0.001$, and $****P < 0.0001$.

degradation, hindered cellular entry, and erratic biodistribution.^[26,49] Our innovative methodology encases FOXK2 siRNA within biomimetic ZrTCP NPs, and these loaded NPs are subsequently incorporated alongside metformin into GelMA microspheres. This approach directly addresses the mentioned challenges. Existing literature extols the virtues of NPs for

superior cellular entry and amplified therapeutic potential, particularly for siRNA delivery.^[50] The biomimetic design of our NPs augments tumor specificity, thereby curtailing off-target repercussions and systemic toxicity.^[51]

In a pivotal innovation, our strategy harnesses near-infrared light exposure to the TCPP component within the ZrTCP

NPs, invoking a photodynamic reaction analogous to traditional photodynamic therapy.^[52] This therapeutic cascade culminates in the localized generation of ROS that can expedite cancer cell destruction. Merging this controllable, dynamic tactic with our distinctive therapeutic concoction substantially bolsters cancer cell mortality rates.

In summary, the intricate synergy of metformin, FOXK2 siRNA, and the TCPP-activated photodynamic capabilities of ZrTCP NPs formulates a comprehensive strategy. This approach adeptly targets the metabolic vulnerabilities of ovarian cancer cells while fine-tuning the precision of drug delivery. Our findings, though promising, underscore the necessity for deeper exploration. This includes recognizing the current study's limitations, particularly in safety assessment. The lack of extensive long-term toxicity data and in-depth blood chemistry analysis marks a significant oversight. Future research endeavors should focus on these areas, integrating thorough long-term toxicity studies and detailed blood chemistry evaluations. Such comprehensive investigations are pivotal not only for a complete understanding of the ZrTCP NPs' safety profile but also for refining dosing protocols, uncovering potential resistance mechanisms, and anticipating adverse reactions, thereby enhancing the clinical efficacy and safety of our approach.

4. Conclusion

Our research presents a cutting-edge therapeutic strategy tailored for ovarian cancer treatment. The convergence of metformin, FOXK2 siRNA, and light-activated ZrTCP NPs encapsulated within GelMA microspheres offers an unprecedented targeting precision. This holistic approach not only addresses the metabolic vulnerabilities of the tumor, but also ensures the targeted delivery of therapeutic agents, maximizing their efficacy while minimizing collateral damage. Future studies and clinical trials could further refine this method, making it a frontline therapy for ovarian cancer and potentially revolutionizing the landscape of cancer therapeutics.

5. Experimental Section

The experimental methods and main materials are detailed in Supporting Information.

Animal Experiments: All animal experiments were conducted in compliance with the guidelines and protocols of the Institutional Animal Care and Use Committee of China and were approved by the Institutional Animal Care and Use Committee of The Chinese University of Hong Kong, Shenzhen (No. CUHKSZ-AE2021013). Additionally, all experimental procedures also adhered to the European Union's respective guidelines for the accommodation and care of animals.

Supporting Information

Supporting Information is available from the Wiley Online Library or from the author.

Acknowledgements

W.Z., X.M., and J.X. contributed equally to this work. The authors extend their heartfelt gratitude to the Hubei Key Laboratory of Embryonic Stem

Cell Research and the Hubei Provincial Clinical Research Center for Umbilical Cord Blood Hematopoietic Stem Cells at Taihe Hospital, Hubei University of Medicine, Shiyan, 44200, China, for their invaluable assistance in the analysis of TCGA data. Cell imaging and flow cytometry were carried out at the Turku Bioscience Centre's cell imaging and cytometry core, which is supported by Biocenter Finland. This work was supported by grants from China Postdoctoral Science Foundation (grant no. 2021M700830), the National Natural Science Foundation of China (grant no. 82201287), the Research Fellow grant (grant no. 353146), the project grant (grant no. 347897) from the Academy of Finland, the Solutions for Health Profile (grant no. 336355), and the InFLAMES Flagship (grant no. 337531). The authors also acknowledge funding from the Finland China Food and Health International Pilot Project, sponsored by the Finnish Ministry of Education and Culture, and the Medical and Health Technology Public Relations Project of Shenzhen Longgang District Science and Technology Innovation Special Fund (LGKCYLWS2022001 to J.F.).

Conflict of Interest

The authors declare no conflict of interest.

Data Availability Statement

The data that support the findings of this study are available from the corresponding author upon reasonable request.

Keywords

FOXK2 siRNA, metformin, microfluidic technology, ovarian cancer therapy, Warburg effect

Received: September 6, 2023
Revised: November 25, 2023
Published online: January 29, 2024

- [1] R. L. Siegel, K. D. Miller, N. S. Wagle, A. Jemal, *CA-Cancer J. Clin.* **2023**, *73*, 17.
- [2] V. Rodriguez-Freixinos, H. J. Mackay, K. Karakasis, A. M. Oza, *Expert Opin. Pharmacother.* **2016**, *17*, 1063.
- [3] A. Chandra, C. Pius, M. Nabeel, M. Nair, J. K. Vishwanatha, S. Ahmad, R. Basha, *Cancer Med.* **2019**, *8*, 7018.
- [4] S. Tendulkar, S. Dodamani, *Anti-Cancer Agents Med. Chem.* **2021**, *21*, 668.
- [5] C. Guo, C. Song, J. Zhang, Y. Gao, Y. Qi, Z. Zhao, C. Yuan, *Genes Dis.* **2022**, *9*, 668.
- [6] M. Song, M. Cui, K. Liu, *Eur. J. Med. Chem.* **2022**, *232*, 114205.
- [7] M. G. Vander Heiden, L. C. Cantley, C. B. Thompson, *Science* **2009**, *324*, 1029.
- [8] M. V. Libertini, J. W. Locasale, *Trends Biochem. Sci.* **2016**, *41*, 211.
- [9] O. Warburg, *Science* **1956**, *123*, 309.
- [10] R. A. Cairns, I. S. Harris, T. W. Mak, *Nat. Rev. Cancer* **2011**, *11*, 85.
- [11] D. G. Hardie, F. A. Ross, S. A. Hawley, *Nat. Rev. Mol. Cell Biol.* **2012**, *13*, 251.
- [12] B. Faubert, G. Boily, S. Izreig, T. Griss, B. Samborska, Z. Dong, F. Dupuy, C. Chambers, B. J. Fuerth, B. Viollet, O. A. Mamer, D. Avizonis, R. J. DeBerardinis, P. M. Siegel, R. G. Jones, *Cell Metab.* **2013**, *17*, 113.
- [13] C. K. Keerthana, T. P. Rayginia, S. C. Shifana, N. P. Anto, K. Kalimuthu, N. Isakov, R. J. Anto, *Front. Immunol.* **2023**, *14*, 1114582.

- [14] J. M. Evans, L. A. Donnelly, A. M. Emslie-Smith, D. R. Alessi, A. D. Morris, *BMJ [Br. Med. J.]* **2005**, 330, 1304.
- [15] R. J. Shaw, K. A. Lamia, D. Vasquez, S. H. Koo, N. Bardeesy, R. A. Depinho, M. Montminy, L. C. Cantley, *Science* **2005**, 310, 1642.
- [16] G. Zhou, R. Myers, Y. Li, Y. Chen, X. Shen, J. Fenyk-Melody, M. Wu, J. Ventre, T. Doebber, N. Fujii, N. Musi, M. F. Hirshman, L. J. Goodyear, D. E. Moller, *J. Clin. Invest.* **2001**, 108, 1167.
- [17] J. J. Shank, K. Yang, J. Ghannam, L. Cabrera, C. J. Johnston, R. K. Reynolds, R. J. Buckanovich, *Gynecol. Oncol.* **2012**, 127, 390.
- [18] X. Liu, N. Tang, Y. Liu, J. Fu, Y. Zhao, H. Wang, H. Wang, Z. Hu, *Leuk. Res.* **2023**, 132, 107343.
- [19] G. Nestal de Moraes, L. D. T. Carneiro, R. C. Maia, E. W. Lam, A. D. Sharrocks, *Cancers* **2019**, 11, 393.
- [20] X. Shi, A. M. Wallis, R. D. Gerard, K. A. Voelker, R. W. Grange, R. A. DePinho, M. G. Garry, D. J. Garry, *J. Cell Sci.* **2012**, 125, 5329.
- [21] I. Pernicova, M. Korbonits, *Nat. Rev. Endocrinol.* **2014**, 10, 143.
- [22] G. Tossetta, *Int. J. Mol. Sci.* **2022**, 23, 12893.
- [23] T. Tsakiridis, G. R. Pond, J. Wright, P. M. Ellis, N. Ahmed, B. Abdulkarim, W. Roa, A. Robinson, A. Swaminath, G. Okawara, M. Wierzbicki, M. Valdes, M. Levine, *JAMA Oncol.* **2021**, 7, 1333.
- [24] W. Alshaer, H. Zureigat, A. Al Karaki, A. Al-Kadash, L. Gharaibeh, M. M. Hatmal, A. A. Aljabali, A. Awidi, *Eur. J. Pharmacol.* **2021**, 905, 174178.
- [25] P. E. Saw, E. W. Song, *Sci. China: Life Sci.* **2020**, 63, 485.
- [26] L. Wu, W. H. Zhou, L. H. Lin, A. H. Chen, J. Feng, X. M. Qu, H. B. Zhang, J. Yue, *Bioact. Mater.* **2022**, 7, 292.
- [27] M. I. Sajid, M. Moazzam, S. Kato, K. Yeseom Cho, R. K. Tiwari, *Pharmaceuticals* **2020**, 13, 294.
- [28] Y. Liu, G. Yang, Y. Hui, S. Ranaweera, C. X. Zhao, *Small* **2022**, 18, 2106580.
- [29] D. Zhang, W. Li, Y. Shang, L. Shang, *Eng. Regener.* **2022**, 3, 258.
- [30] J. He, Y. Sun, Q. Gao, C. He, K. Yao, T. Wang, M. Xie, K. Yu, J. Nie, Y. Chen, Y. He, *Adv. Healthcare Mater.* **2023**, 12, 2300395.
- [31] Z. Li, K. Xu, L. Qin, D. Zhao, N. Yang, D. Wang, Y. Yang, *Adv. Mater.* **2023**, 35, 2203890.
- [32] N. M. Munoz, M. Williams, K. Dixon, C. Dupuis, A. McWatters, R. Avritscher, S. Z. Manrique, K. McHugh, R. Murthy, A. Tam, A. Naing, S. P. Patel, D. Leach, J. D. Hartgerink, S. Young, P. Prakash, P. Hwu, R. A. Sheth, *J. Immunother. Cancer* **2021**, 9, e001800.
- [33] Y. Bai, Y. Dou, L. H. Xie, W. Rutledge, J. R. Li, H. C. Zhou, *Chem. Soc. Rev.* **2016**, 45, 2327.
- [34] Y. Yang, K. Wang, Y. Pan, L. Rao, G. Luo, *Adv. Sci.* **2021**, 8, 2102330.
- [35] W. Zhao, X. Hou, O. G. Vick, Y. Dong, *Biomaterials* **2019**, 217, 119291.
- [36] J. Cao, X. Li, H. Tian, *Curr. Med. Chem.* **2020**, 27, 5949.
- [37] B. Yang, Y. Chen, J. Shi, *Chem. Rev.* **2019**, 119, 4881.
- [38] H. P. Lee, A. K. Gaharwar, *Adv. Sci.* **2020**, 7, 2000863.
- [39] C. Lennicke, H. M. Cocheme, *Mol. Cell* **2021**, 81, 3691.
- [40] C. Gorrini, I. S. Harris, T. W. Mak, *Nat. Rev. Drug Discovery* **2013**, 12, 931.
- [41] Y. Zhao, X. Hu, Y. Liu, S. Dong, Z. Wen, W. He, S. Zhang, Q. Huang, M. Shi, *Mol. Cancer* **2017**, 16, 79.
- [42] W. Zhou, X. Ma, J. Wang, X. Xu, O. Koivisto, J. Feng, T. Viitala, H. Zhang, *Smart Med.* **2022**, 1, e20220036.
- [43] I. Martinez-Reyes, N. S. Chandel, *Nat. Rev. Cancer* **2021**, 21, 669.
- [44] L. K. Boroughs, R. J. DeBerardinis, *Nat. Cell Biol.* **2015**, 17, 351.
- [45] G. J. Yoshida, *J. Exp. Clin. Cancer Res.* **2015**, 34, 111.
- [46] M. Foretz, B. Guigas, B. Viollet, *Nat. Rev. Endocrinol.* **2023**, 19, 460.
- [47] Y. Wang, H. An, T. Liu, C. Qin, H. Sesaki, S. Guo, S. Radovick, M. Hussain, A. Maheshwari, F. E. Wondisford, B. O'Rourke, L. He, *Cell Rep.* **2019**, 29, 1511.
- [48] Y. Zhang, Y. Wang, G. Zhao, E. J. Tanner, M. Adli, D. Matei, *J. Clin. Invest.* **2022**, 132, e151591.
- [49] A. Gupta, J. L. Andresen, R. S. Manan, R. Langer, *Adv. Drug Delivery Rev.* **2021**, 178, 113834.
- [50] R. J. Mosley, B. Rucci, M. E. Byrne, *J. Mater. Chem. B* **2023**, 11, 2078.
- [51] B. T. Luk, L. Zhang, *J. Controlled Release* **2015**, 220, 600.
- [52] R. Zhu, Q. He, Z. Li, Y. Ren, Y. Liao, Z. Zhang, Q. Dai, C. Wan, S. Long, L. Kong, W. Fan, W. Yu, *Acta Biomater.* **2022**, 153, 442.

Boosting glioblastoma therapy with targeted pyroptosis induction

Xinggang Fang, Zhuo Chen, **Wenhui Zhou**, Tongfei Li, Man Wang, Yujiu Gao, Shinan Ma, Ying Feng, Shiming Du, Peimin Lan, Hanyu Chen, Jiarui Wei, Sisi Zhang, Zixiang Li, Xinglin Liu, Hongbo Zhang*, Xingrong Guo*, Jie Luo*. *Small* **2023**; 2207604

Boosting Glioblastoma Therapy with Targeted Pyroptosis Induction

Xinggong Fang, Zhuo Chen, Wenhui Zhou, Tongfei Li, Man Wang, Yujiu Gao, Shinan Ma, Ying Feng, Shiming Du, Peimin Lan, Hanyu Chen, Jiarui Wei, Sisi Zhang, Zixiang Li, Xinglin Liu, Hongbo Zhang,* Xingrong Guo,* and Jie Luo*

Glioblastoma (GBM) is a highly aggressive cancer that currently lacks effective treatments. Pyroptosis has emerged as a promising therapeutic approach for cancer, but there is still a need for new pyroptosis boosters to target cancer cells. In this study, it is reported that Aloe-emodin (AE), a natural compound derived from plants, can inhibit GBM cells by inducing pyroptosis, making it a potential booster for pyroptosis-mediated GBM therapy. However, administering AE is challenging due to the blood-brain barrier (BBB) and its non-selectivity. To overcome this obstacle, AE@ZIF-8 NPs are developed, a biomineralized nanocarrier that releases AE in response to the tumor's acidic microenvironment (TAM). Further modification of the nanocarrier with transferrin (Tf) and polyethylene glycol-poly (lactic-co-glycolic acid) (PEG-PLGA) improves its penetration through the BBB and tumor targeting, respectively. The results show that AE-NPs (Tf-PEG-PLGA modified AE@ZIF-8 NPs) significantly increase the intracranial distribution and tumor tissue accumulation, enhancing GBM pyroptosis. Additionally, AE-NPs activate antitumor immunity and reduce AE-related toxicity. Overall, this study provides a new approach for GBM therapy and offers a nanocarrier that is capable of penetrating the BBB, targeting tumors, and attenuating toxicity.

1. Introduction

As a grade IV glioma, glioblastoma (GBM) is the most common and deadly intracranial malignant tumor which has high mortality and morbidity rates and a low effective cure rate.^[1,2,3] Surgical therapy is the preferred treatment, but the complete resection is difficult and resulting in a high recurrence rate especially in invasive growth GBM cases.^[4] In addition, the creative structure of the blood-brain barrier (BBB) fairly restricted the using of traditional chemotherapies for GBM therapy.^[5] And the suppressed immune microenvironment also worsens the prognosis of GBM.^[6] Thus, new therapies for GBM are still highly demanded.

Pyroptosis, which is a programmed cell death depending on the activation of gasdermin family (GSDMs), the activation of which further induces cell

X. Fang, Z. Chen, J. Luo
Clinical College of Traditional Chinese Medicine
Taihe Hospital
Hubei University of Chinese Medicine
Wuhan, Hubei 430065, P. R. China
E-mail: yueli@taihehospital.com

X. Fang, Z. Chen, Y. Gao, S. Ma, Y. Feng, S. Du, S. Zhang, Z. Li, X. Guo, J. Luo
Department of Neurosurgery
Hubei Key Laboratory of Embryonic Stem Cell Research
Hubei Clinical Research Center for Umbilical Cord Blood Hematopoietic Stem Cells
Taihe Hospital
Hubei University of Medicine
Shiyan, Hubei 442000, P. R. China
E-mail: gxrld@hbm.u.edu.cn

X. Fang, P. Lan, H. Chen
Department of Integrated Chinese and Western Medicine
Taihe Hospital
Hubei University of Medicine
Shiyan, Hubei 442000, P. R. China

W. Zhou, H. Zhang
Pharmaceutical Sciences Laboratory
Åbo Akademi University
20520 Turku, Finland
E-mail: hongbo.zhang@abo.fi


W. Zhou, H. Zhang
Turku Bioscience Centre
University of Turku and Åbo Akademi University
20520 Turku, Finland

T. Li, J. Wei
School of Basic Medical Sciences
Hubei University of Medicine
Shiyan, Hubei 442000, P. R. China

M. Wang
Pharmacy intravenous admixture service
Taihe Hospital

Hubei University of Medicine
Shiyan, Hubei 442000, P. R. China

X. Liu
Institute of Biomedicine
Hubei University of Medicine
Shiyan, Hubei 442000, P. R. China

 The ORCID identification number(s) for the author(s) of this article can be found under <https://doi.org/10.1002/smll.202207604>.

© 2023 The Authors. Small published by Wiley-VCH GmbH. This is an open access article under the terms of the Creative Commons Attribution License, which permits use, distribution and reproduction in any medium, provided the original work is properly cited.

DOI: 10.1002/smll.202207604

membrane pore-forming and GSDMs N-terminal fragment release, causing intracellular and extracellular osmotic pressure imbalance, cell swelling and rupture, and then leakage of cytoplasmic pro-inflammatory cytokines, resulting in cell death.^[7,8] More importantly, depend on membrane ruptures and cellular contents release, cytotoxic lymphocytes were activated to kill tumor cells, which was closely involved in anticancer immune response and rising as a very promising method for cancer treatment.^[9] As an important pyroptosis pathway, activation of caspase-3/gasdermin E (CASP3/GSDME) can further trigger the activation of host immune system,^[10] which stimulates a “cold” tumor microenvironment to be an immunogenic “hot” tumor microenvironment,^[8] and showed significant inhibitory effects on multiple tumors, such as breast cancer, melanoma, gastric cancer, lung cancer, hepatocellular carcinoma, etc.^[11,12] And lots of effort have been done to utilize the pyroptosis pathway as target for cancer therapy. For example, many chemotherapeutic drugs, such as doxorubicin and cisplatin have been shown to have the potential to induce pyroptosis. However, the drug-related side effects and drug resistance are still the main problems. Therefore, the finding of new novel pyroptosis activator still has a promising contribution for GBM immunotherapy.

Aloe-emodin (AE), an anthraquinone derivative extracted from a variety of natural plants has aroused increased attention for cancer therapy during recent years because of its wide range of pharmacological effects, which include antiviral, antibacterial, antiallergic, antiosteoporosis, antidiabetic, neuroprotective, and antitumors by induction of DNA damage, cell cycle arrest, and inhibit cell migration.^[13,14] In this work, we found that AE suppressed GBM cells in a time- and concentration-dependent manner, and the mechanism studies investigated that this antitumor effect may arise from the activation of the CASP3/GSDME pyroptosis pathway. Thus, AE may act as a pyroptosis booster for GBM therapy. Moreover, our analyzing results from the Cancer Genome Atlas (TCGA) database showed that GSDME, which is a key modulator for pyroptosis is highly expressed in GBM relative to adjacent tissues (Figure 2F,G). Therefore, targeting GSDME by AE might serve as a good strategy for GBM treatment via immunotherapy.

However, similar to other fat soluble drugs, poor water solubility, as well as BBB penetration, and nonselection remain the main obstacles to applying AE in GBM treatment. In recent years, multiple strategies have been reported to improve BBB penetration or tumor targeting, such as polymeric nanoparticles, nanoemulsions, liposomes, micelles, and exosomes,^[15] such strategies partially improved BBB penetration or tumor targeting. But as an intracranial tumor, GBM treatment faces the dual challenges of BBB and tumor targeting. Notably, GSDME is also expressed in normal brain, and nonselective activation of GSDME have the risk of normal brain injury, thus an ideal drug delivery carrier for intracranial tumors needs to have both BBB penetration, tumor targeting, and tumor acid microenvironment (TAM) controlled release ability. To meet the requirements, we first biomimetic AE with zeolitic imidazolate framework nanoparticles (ZIF-8 NPs), which are zinc ions and dimethylimidazole composed metal-organic framework (MOF) based NPs and have been widely used for biomolecular intracellular delivery

owing to their easy preparation, good biocompatibility, and acidic microenvironments responsive degradation.^[16] Therefore, ZIF-8 NPs may serve as a good method for improving the solubility and tumor targeting of AE. Moreover, since Zn^{2+} is a positive regulator for both innate immunity and adaptive immunity,^[17] we supposed that the released Zn^{2+} during ZIF-8 NPs degradation in GBM cancer cells is also a good factor for improving the suppressed immune microenvironment. Thereby, the immune response induced by pyroptosis of GBM cells will be enhanced.

It was reported that Poly (lactic-co-glycolic acid) (PLGA) polymer is with good biocompatibility, biodegradability, and no toxicity,^[18] thus is widely used to improve BBB permeability both in vitro and in vivo, however, they are readily cleared by the reticuloendothelial system (RES) through protease-mediated phagocytosis.^[19] But the remarkable thing is that PLGA modified with polyethylene glycol (PEG) prolongs circulation time in vivo and improves water solubility and stability.^[20,21] Therefore, to increase the blood circulation time, BBB penetration ability, as well as minimize the non-selected cytotoxicity of AE loaded ZIF-8 NPs (AE@ZIF-8 NPs), we further coated AE@ZIF-8 NPs with transferrin (Tf) modified PEG-PLGA polymer (Tf-PEG-PLGA). Tf is a ligand of Tf receptor (TfR), which is highly expressed in the endothelium of brain capillaries and tumor tissue.^[22,23] Thus, by targeting the TfR of brain capillaries endothelium cells and tumor cells, we expect that the AE-NPs will first cross the BBB and enter the brain in an efficient active transport mode,^[23] and then realizing the enrichment in GBM tumor cells. On the whole, ZIF-8 NPs can provide a good solution for in vivo administration of AE and also act as an immune response regulator, and Tf-PEG-PLGA polymer coating enable the AE-NPs across the BBB and finally accumulating in the GBM tumor cells.

Our data demonstrated that, AE induced GBM tumor cells death in a time and concentration dependent manner by activation of CASP3/GSDME pyroptosis pathway. By loading AE in ZIF-8 NPs, TAM targeted AE release was realized. And the Tf-PEG-PLGA polymer coating significantly increased the intracranial distribution and tumor enrichment, therefore, boosted pyroptosis in the tumor cells and enhanced antitumor effects of AE@ZIF-8 NPs. Furthermore, AE-NPs also enhanced microglia GBM infiltration and M1 subtype polarization, increased CD8+ T cell expression, prolonged the survival rate of tumor-bearing mice, and reduced AE-related hepatotoxicity and nephrotoxicity. In summary, our work offers a new strategies for GBM targeted therapy, and the newly constructed AE loaded Tf-PEG-PLGA coated ZIF-8 nanoparticles (AE@ZIF-8/Tf-PEG-PLGA NPs, AE-NPs) can be served as an effective, safe, and BBB penetrative pyroptosis booster for intracranial tumor therapy.

2. Results

2.1. AE Inhibited Proliferation and Induced Pyroptosis in GBM Cells

Previous studies have shown that AE is a natural monomeric compound with antitumor effects (Figure 1A).^[24] However,

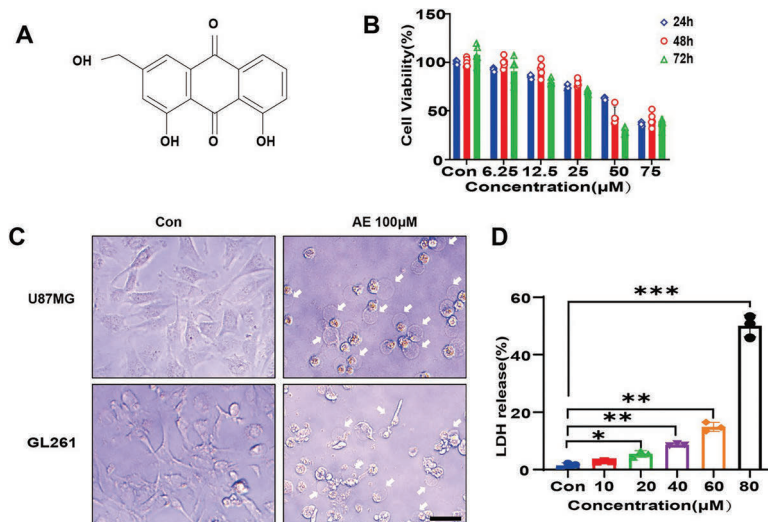


Figure 1. AE induced pyroptosis in GBM cells. A) Chemical structure of AE. B) Cell viability was tested by CCK-8 in AE-treated GL261 cells. All values are presented as mean \pm SD ($n = 4$). C) Representative photographs of U87MG and GL261 cells treated with AE for 60 h. The white arrows indicate pyroptotic cells (scale bar: 200 μ m). D) LDH release of U87MG cells treated with AE for 60 h. Data are presented as mean \pm SD ($n = 3$); * $P < 0.05$, ** $P < 0.01$, *** $P < 0.001$ (one-way ANOVA and Bonferroni's multiple comparisons test).

its role in anti-glioma is currently not very clear. To explore the potential anti-GBM activity, we administered AE to GBM human cell line U87MG and GBM mouse cell line GL261. Cell Counting Kit 8 (CCK-8) assay showed that AE suppressed GBM cells in a time- and concentration-dependent manner (Figure 1B; and Figure S1, Supporting Information), and the morphology of AE-treated GBM cells showed pyroptosis-specific features, such as cell membrane swelling and blebbing (Figure 1C), suggesting that AE may induced GBM cells pyroptosis. Because pyroptosis is accompanied with lactate dehydrogenase (LDH) extracellular release,^[25] to further confirm AE-induced pyroptosis, we next measured LDH release from AE treated U87MG cells, and showed that LDH release was increased with the increasing of AE concentration (Figure 1D). These results indicated that, AE inhibited cell proliferation and induced pyroptosis in GBM cells.

2.2. AE Activated the CASP3/GSDME Pyroptosis Pathway in GBM Cells

Pyroptosis is mainly activated through the caspase-1/gasdermin D (CASP1/GSDMD) pathway or CASP3/GSDME pathway.^[26] To clarify the mechanism of AE-mediated pyroptosis, AE-GBM network pharmacology analysis was performed. A Venn diagram with the overlapping targets related to AE and GBM identified 44 promising targets for GBM treatment of AE (Figure 2A). The network of these 44 targets was analyzed with the STRING database (Figure 2B), and the PPI network showed 44 nodes and 473 edges. We

next analyzed each node and screened out the first 20 targets with node degrees greater than 23. These targets included AKT1, ALOX5, AKT2, BCL2L1, CASP3, CASP9, CDK2, and CDK6. Among them, CASP3 is one of the core intersection targets (Figure 2C). Since CASP3 is the key protein of CASP3/GSDME pyroptosis pathway, we speculated that AE may induce GBM pyroptosis through the CASP3/GSDME pathway. And this was confirmed by *in vitro* studies with AE inducing CASP3 and GSDME activation but not GSDMD (Figure 2D,E), which is similar to cisplatin, a classic pyroptosis-inducer, and this activation can be inhibited by z-VAD-FMK (Figure S2, Supporting Information). Furthermore, we found that AE increasing the expression of GSDME at mRNA (Figure S3, Supporting Information) and protein levels (Figure S4, Supporting Information).

A previous report showed that GSDME expression determines whether pyroptosis is dominant in the antitumor process induced by chemotherapeutic drugs.^[27] We next analyzed the expression of GSDME in GBM cell lines and tumor tissues by western blot (WB) and TCGA database. The analyzing result from the TCGA database (<http://ualcan.path.uab.edu/index.html>) showed that, compared to other tumors and normal brain tissue, GSDME was higher expressed in GBM (Figure 2F,G). And the WB showed that GSDME was negatively expressed in HMO6 (human microglia cell line) cells, and higher expressed in human GBM cell lines U87MG, DBTRG, and then HepG2, Hela, A549, even in mouse cells. Most importantly, GSDME is higher expressed GBM cell line GL261 than microglia cell line BV2 (Figure 2H). These results suggesting that GSDME is a good target for anti-GBM therapy by activating of the CASP3/GSDME pyroptosis pathway.

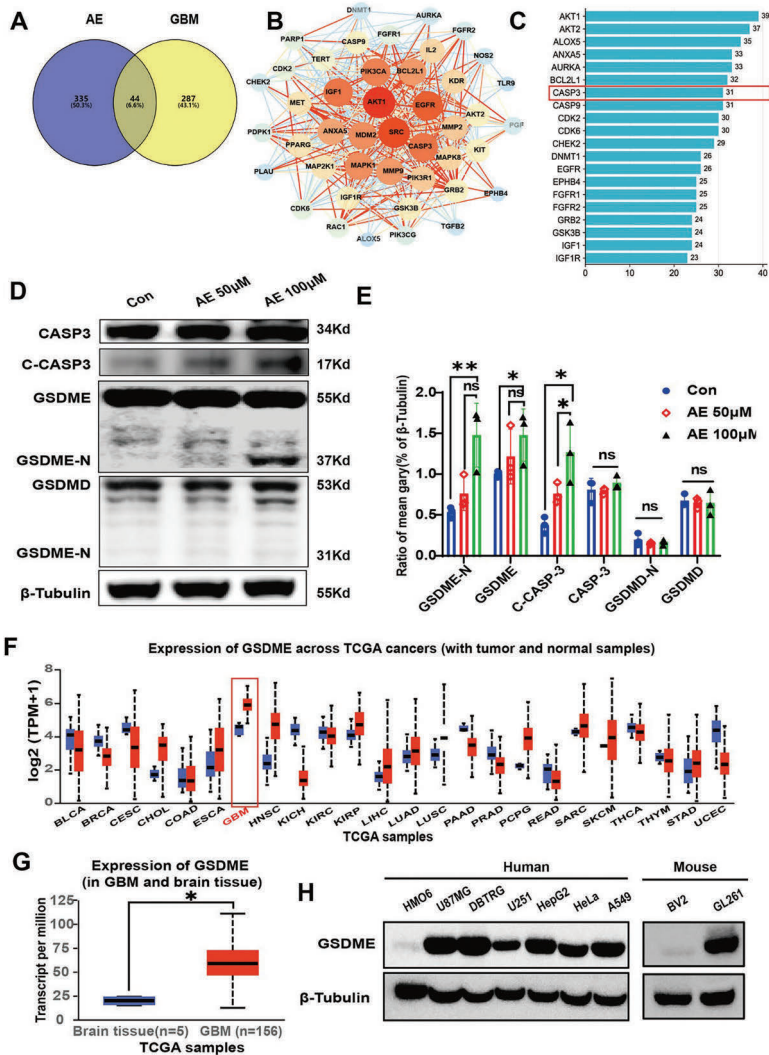
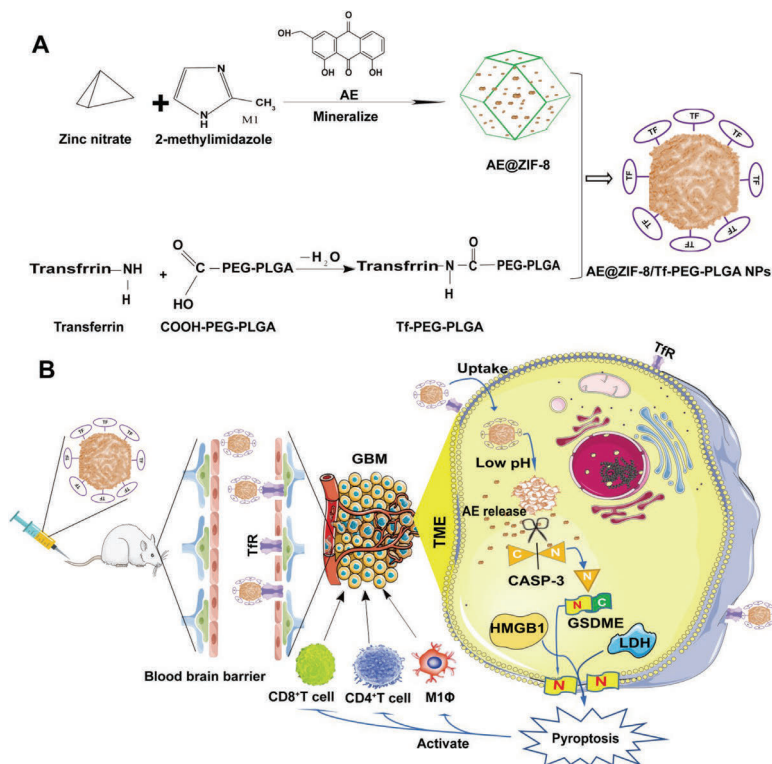


Figure 2. AE activated the CASP3/GSDME pyroptosis pathway in GBM cells. A) 44 intersection targets of AE and GBM illustrated by Venn diagram. B) Cytoscape-based PPI analysis construction (intensity of the node color is proportional to the amounts of linked proteins). C) Bar plot of the top 20 targets in the PPI network. CASP3 is one of the core intersection targets. D) The expression of CASP3, cleaved caspase-3 (C-CASP3), GSDME, and GSDME-N terminal (GSDME-N), GSDMD, GSDMD-N terminal (GSDMD-N), biomarkers of pyroptosis, was assayed by WB. E) Quantitatively analyzed CASP3, C-CASP3, GSDME, GSDME-N, GSDMD, GSDMD-N by the mean gray value. All the data are presented as the mean \pm SD from three independent experiments ($n = 3$); * $P < 0.05$, (one-way ANOVA and Bonferroni's multiple comparisons test). F) Expression of GSDME across TCGA cancers from TCGA database. G) Expression of GSDME in GBM and brain tissue from TCGA database (* $P < 0.05$). H) Expression of GSDME in different tumor cell lines and normal cell lines, tested by western blot.

2.3. Characterization and Acidic Microenvironment Responsiveness of AE-NPs

Previous studies have shown that lack of selectivity distribution and poor water solubility in vivo can lead to low efficacy

and off-target side effects.^[28,29] To improve the intracranial distribution and tumor enrichment of AE, AE-NPs were constructed by a two-step method (Scheme 1A). First, AE@ZIF-8 nanoparticles were synthesized by encapsulating AE during the mineralization of zinc nitrate and 2-methylimidazole. Sub-



Scheme 1. Preparation (A), in vivo delivery, and anti-GBM mechanism (B) schematic diagram of AE@ZIF-8/Tf-PEG-PLGA NPs (AE-NPs).

sequently, AE@ZIF-8 NPs were coated with Tf-PEG-PLGA polymer. The appearances of blank ZIF-8, AE@ZIF-8, and AE-NPs were shown in **Figure 3A**. During the formation of AE@ZIF-8, increasing AE dosage increased the particle size, and UV-absorption peak (255 nm) (**Figure S5A,C**, Supporting Information), while the average ζ potential was decreased (**Figure S5B**, Supporting Information). However, a stable UV-absorption curve could not be formed with AE concentrations of 20 mg (**Figure S5C**, Supporting Information). Therefore, 10 mg AE was selected for the final AE@ZIF-8 NPs formulation and subsequent experiments. The AE loading degree was 43.2%, AE encapsulation rate of AE@ZIF-8 is 32.6%, and the hydrodynamic size of AE@ZIF-8 measured by dynamic light scattering (DLS) was 155.1 ± 42.41 nm (**Figure 3B**), while the size measured by transmission electron microscopy (TEM) was 38.87 ± 4.71 nm (**Figure S8**, Supporting Information), and the surface zeta potential was 20.3 ± 7.95 mV (**Figure 3C**) in methanol. Next, AE-NPs were prepared according to an established protocol, while the increased ratio of AE@ZIF-8 NPs to Tf-PEG-PLGA polymer decreased the particle size (**Figure S6A**, Supporting Information), but the surface zeta potential, UV-vis absorption and AE loading degree were increased (**Figure S6B–D**, Supporting Information). The transferrin conjugation degree decreased significantly when the dosage ratio was higher than 7:3 (**Figure S6E**,

Supporting Information), thus a volume ratio of 7:3 was chosen for final AE-NPs preparation and subsequent experiments. Then hydrodynamic size of AE-NPs measured by DLS was 199 ± 85 nm (**Figure 3B**), and remains stable for 96 h (**Figure 3G**), while the size measured in the TEM image was 46.52 ± 6.43 nm (**Figure S8**, Supporting Information), the surface zeta potential was 13.8 ± 6.49 mV (**Figure 3C**), the AE loading rate was 15.43% (**Figure S6D**, Supporting Information), AE encapsulation rate of AE-NPs is 22.5%. Because the normal brain interstitial space is 38–68 nm,^[30] and the tumor tissue intercellular space is 7–100 nm,^[31] these suggests that our prepared AE-NPs can freely pass through the brain interstitial and tumor cell space. In addition, characterization data were expanded in biological solutions of normal saline containing 1% F127 (1% F127 NS) and 1% F127 NS with 10% FBS (1% F127 NS+10% FBS), in biological solutions, particles size are increased and zeta potential were decreased (**Figure S7A–C**, Supporting Information). This may be protein in biological solutions adsorbed on the nanoparticles' surface changed the characterization.

When blank ZIF-8 NPs, AE@ZIF-8 NPs, and AE-NPs were detected by TEM, the surface of AE-NPs had a prominent Tf-PEG-PLGA coating (amaranth arrows in **Figure 3E**). The Fourier transform infrared (FTIR) spectrum of AE-NPs also revealed new absorption peaks between 1500 and 1700 cm^{-1}

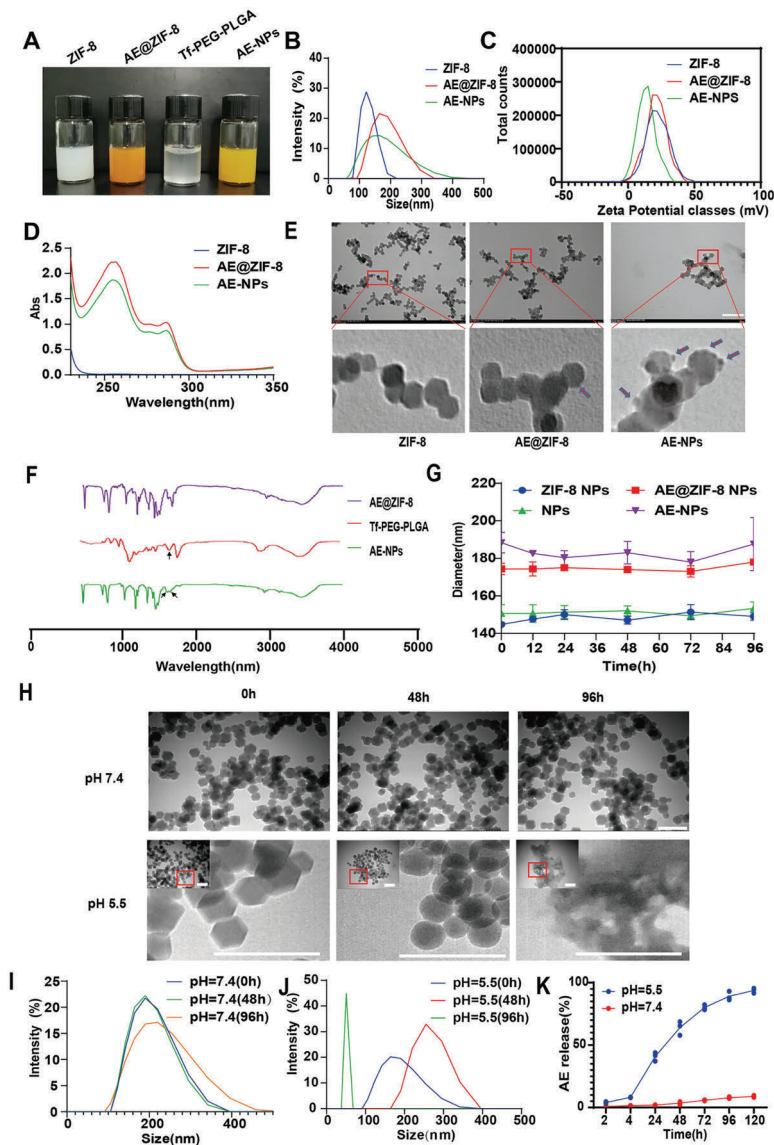


Figure 3. Characterizations and acid-microenvironmental response of AE-NPs. A) Appearance. B) Size results from DLS. C) Zeta potential. D) UV–vis absorption spectra. E) TEM images (scale bar: 200 nm). F) FTIR spectra of AE@ZIF-8, Tf-PEG-PLGA, and AE-NPs, arrow point to stretching vibration peak of $-\text{CO}-\text{NH}-$ from the amide bonds of transferrin connect to PEG-PLGA and contained in Tf. G) Stability of different nanoparticles within 96 h. H) Morphology of AE-NPs in response to pH 7.4 and pH 5.5 for 48 and 96 h (Scale bar: 200 nm). I, J) Size of AE-NPs in pH 7.4 and pH 5.5 solutions at different time points. K) AE cumulative release profiles in 1% F127 NS, pH 7.4, and 5.5 from AE-NPs ($n = 3$).

compared with the spectrum of AE@ZIF-8 (Figure 3F). These may be resulted by the stretching vibration peak of $-\text{CO}-\text{NH}-$ from the amide bonds of transferrin to PEG-PLGA, suggesting that AE-NPs were successfully prepared.

The acidic environment-responsive degradation ability makes ZIF-8 NPs are efficient carriers to target tumors and intracellular environment.^[16,32] To test whether the Tf-PEG-PLGA polymer coating could interfere the pH responsive properties

of ZIF-8 NPs, we further performed pH degradation assay. Our experiments showed that the AE-NPs were stable in a neutral environment (pH = 7.4) but degraded with AE released in an acidic environment (pH = 5.5) (Figure 3H–K). These results suggest that AE-NPs react with the acidic microenvironment.

2.4. NPs Elevated Intracellular Uptake and AE-Mediated GBM Pyroptosis In Vitro

To evaluate the cellular uptake of AE-NPs by GBM cells, we encapsulated the fluorescent dye indocyanine green in ZIF-8 particle (ICG@ZIF-8) and Tf-PEG-PLGA polymer coated ZIF-8 NPs (ICG-NPs) (Figure S9, Supporting Information). Flow cytometry analysis showed that ICG, ICG@ZIF-8, and ICG-NPs (ICG concentration equilibrated to 3 $\mu\text{g mL}^{-1}$) entered U87MG cells in a time-dependent manner (Figure 4A). The proportion of ICG positive cells and their fluorescence intensity were significantly higher in ICG-NPs groups than ICG and ICG@ZIF-8 groups at each time point (Figure 4B). Therefore, we speculate that Tf-PEG-PLGA polymer coated ZIF-8 NPs increased intracellular uptake of ICG by U87MG cells. We next treated U87MG cells with ICG, ICG@ZIF-8, and ICG-NPs for 6 h (ICG concentration equilibrated to 3 $\mu\text{g mL}^{-1}$). Laser scanning confocal microscopy (LSCM) showed that the fluorescence intensity of the ICG-NPs groups was significantly enhanced in ICG-NPs treated groups (Figure 4C), confirming increased uptake.

Since Tf-PEG-PLGA polymer coated ZIF-8 NPs increased the intracellular uptake of cargo, we were wondering if the antitumor effect of AE was also enhanced by Tf-PEG-PLGA polymer coated ZIF-8 NPs. Therefore, we next treated U87 MG cells with AE and AE-NPs for 24 h and cell viability was measured. AE encapsulation with NPs exhibited a significantly higher inhibitory effect (Figure 4D). To investigate whether elevated cellular uptake impacts the cell death mechanism, we next observed AE and AE-NPs treated U87MG cells with a confocal high-intensity imaging analysis system. The results showed that pyroptosis occurred within 24 h in the AE-NPs treated group but took over 60 h in the AE group (Figure 4E), that was confirmed by the GSDME cleavage in AE-NPs group but not AE group in 24 h (Figure 4F). This suggests that the encapsulation of AE by Tf-PEG-PLGA polymer coated ZIF-8 NPs further increased the anti-GBM cells effect via enhanced pyroptosis.

2.5. AE-NPs Increased Intracranial Distribution and Tumor Enrichment of AE In Vivo

The main challenge for chemotherapeutic drugs in GBM treatment is BBB penetration and tumor targeting. Therefore, free ICG, ICG@ZIF-8, ICG-NPs were prepared as nanotracers to evaluate the biodistribution, BBB penetration, and tumor targeting capability of Tf-PEG-PLGA coated ZIF-8 NPs in vivo. As scheduled, C57BL/6J mice were first treated with ICG, ICG@ZIF-8, and ICG-NPs through the tail vein (ICG was normalized to 3 mg kg^{-1}), and then optical live imaging was performed to detect the biodistribution of ICG in brain and main organs at each time points. The results showed that compared with ICG

and ICG@ZIF-8, ICG-NPs had a superior intracranial enrichment within 15 min and with obvious intracranial retention after 24 h (Figure 5A,B), liquid chromatography-mass spectrometry (LC-MS) quantification further confirmed there was a higher AE concentration in AE-NPs group in brain than other groups within 2 h (Figure 5D; and Figure S10, Supporting Information). Organ distribution showed that Tf-PEG-PLGA coated ZIF-8 NPs prolonged the retention time in the body. Our study also showed that, compared with free ICG, ICG@ZIF-8 exhibited lower brain distribution in early time, but had a longer detention time (Figure 5A–C). These findings indicated that loading with Tf-PEG-PLGA coated ZIF-8 NPs enhanced the ability of the cargo enter into the brain, and prolonged residence time. Subsequently, to evaluate tumor targeting ability, cryosections of tumor bearing brain from ICG and ICG-NPs treated mice were prepared. The results showed that ICG-NPs were remarkably enriched in tumor tissue (Figure 5E; and Figure S11, Supporting Information), LC-MS quantification further confirmed that the tumor tissue of AE-NPs group had higher AE concentration (Figure 5D; and Figure S10, Supporting Information). These findings suggested that Tf-PEG-PLGA coated ZIF-8 NPs enhanced intracranial distribution and tumor targeting.

2.6. AE-NPs Enhanced AE-Mediated Antitumor Effects In Vivo

To further evaluate the antitumor effect of AE-NPs, in vivo assay on GL261 orthotopic GBM mouse model was performed. Upon inoculation and tumor establishment, animals were randomly divided into four groups, and 1% F127 NS, AE, Tf-PEG-PLGA polymer coated ZIF-8 NPs (NPs), AE@ZIF-8 AE-NPs were administered through the tail vein every 2 days. Body weight, tumor luciferase expression, and mental status were measured weekly (Figure 6A). The results showed that after 1 week administration, the fluorescence of GBM in the control (Con) group, NPs group, and AE group increased continuously, especially in the Con group. In contrast, it was decreased in the AE-NPs group (Figure 6B,C). Compared with the other three groups, AE-NPs showed a stronger effect on tumor volume and weight reduction. Furthermore, compared to the control group, NPs also reduced tumor volume and weight (Figure 6D,E), which may be attributed to the cytotoxic effect of ZIF-8 NPs.^[16,33] Although NPs and AE have similar effects on tumor volume and weight reduction, the AE group showed increased tumor necrosis in histopathology (Figure 6F).

Finally, hematoxylin and eosin staining (HE), Ki-67 staining and WB assays were performed to clarify mechanism of AE-NPs act on GBM. HE staining showed that tumor necrosis was happened in all groups, but more obvious in AE, AE@ZIF-8, and AE-NPs groups (Figure 6F). Ki-67 staining is a biomarker of proliferation, immunohistochemical results showed that AE-NPs treated GBM tissue displayed lower Ki-67 expression (Figure 6G,H), and supporting inhibited proliferation. At the end of the administration, the terminal survival rate was better in the AE-NPs group than in the other 4 groups (Figure 6I). Together these results suggest that AE-NPs promote necrosis, inhibit of GBM growth, and ameliorated the prognosis. Subsequently, to further confirm the antitumor mechanism at

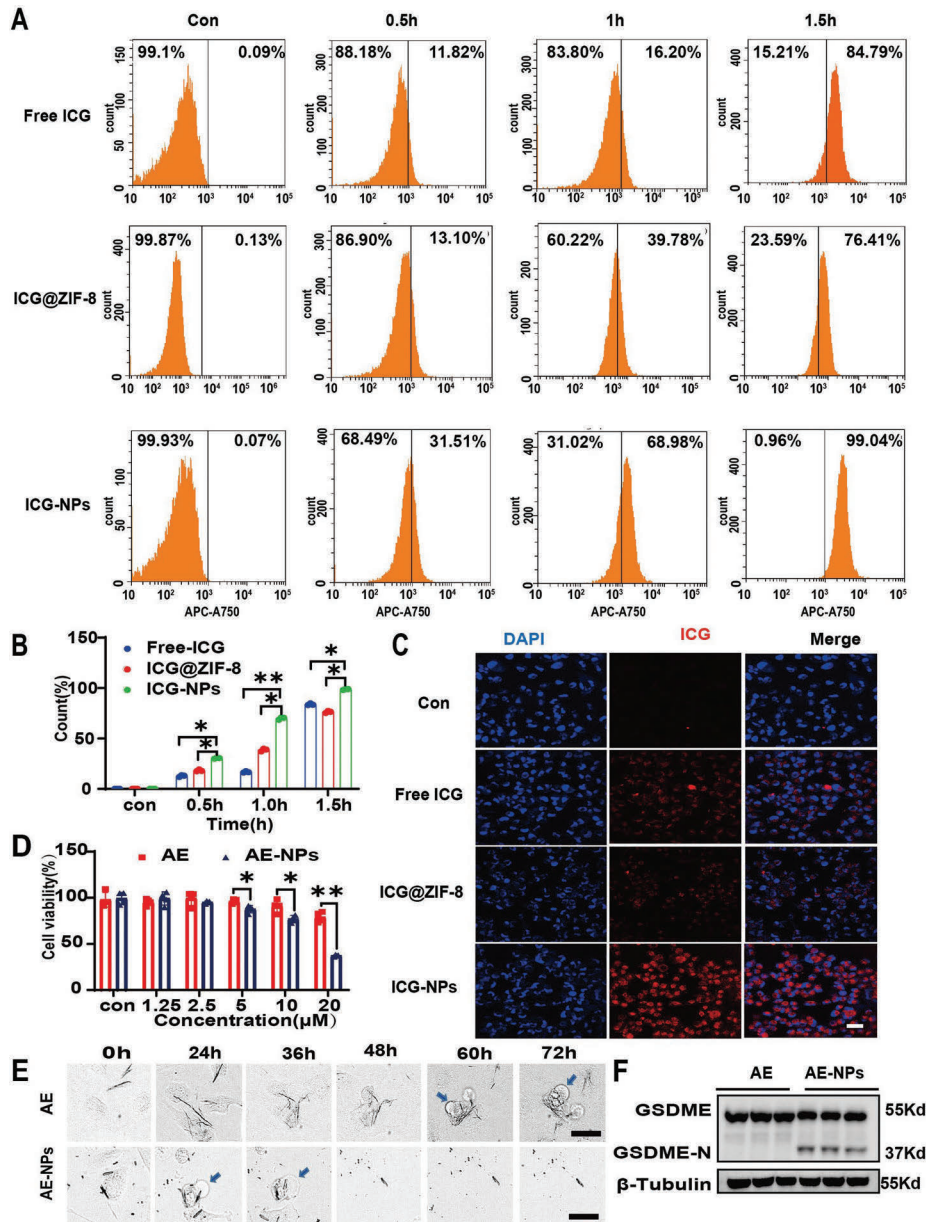


Figure 4. AE-NPs enhanced intracellular uptake and AE-mediated GBM cell pyroptosis in vitro. A,B) ICG, ICG@ZIF-8, and ICG-NPs intracellular uptake by U87MG for 0.5, 1, and 1.5 h, ICG was normalized to $3 \mu\text{g mL}^{-1}$ assessed by flow cytometry. Data are presented as the mean \pm SD from three independent experiments; * $P < 0.05$, ** $P < 0.01$ (one-way ANOVA and Bonferroni's multiple comparisons test) ($n = 3$). C) Confocal microscopy images of ICG, ICG@ZIF-8, and ICG-NPs (ICG was normalized to $3 \mu\text{g mL}^{-1}$) intracellular uptake by U87MG cells for 6 h (scale bar: $200 \mu\text{m}$). D) Cytotoxicity on U87MG of AE and AE-NPs for 24 h, test by CCK-8. All data are presented as the mean \pm SD ($n = 3$), * $P < 0.05$, ** $P < 0.01$ (two-tailed t -test). E) Confocal high-intensity imaging of U87MG cells treated with AE and AE-NPs (AE was normalized to $20 \mu\text{M}$) at different time points. Green arrows indicate pyroptotic cells (scale bar: $200 \mu\text{m}$). F) Expression of GSDME-N terminal in U87MG cells after AE and AE-NPs treated for 24 h (AE was normalized to $20 \mu\text{M}$), tested by WB.

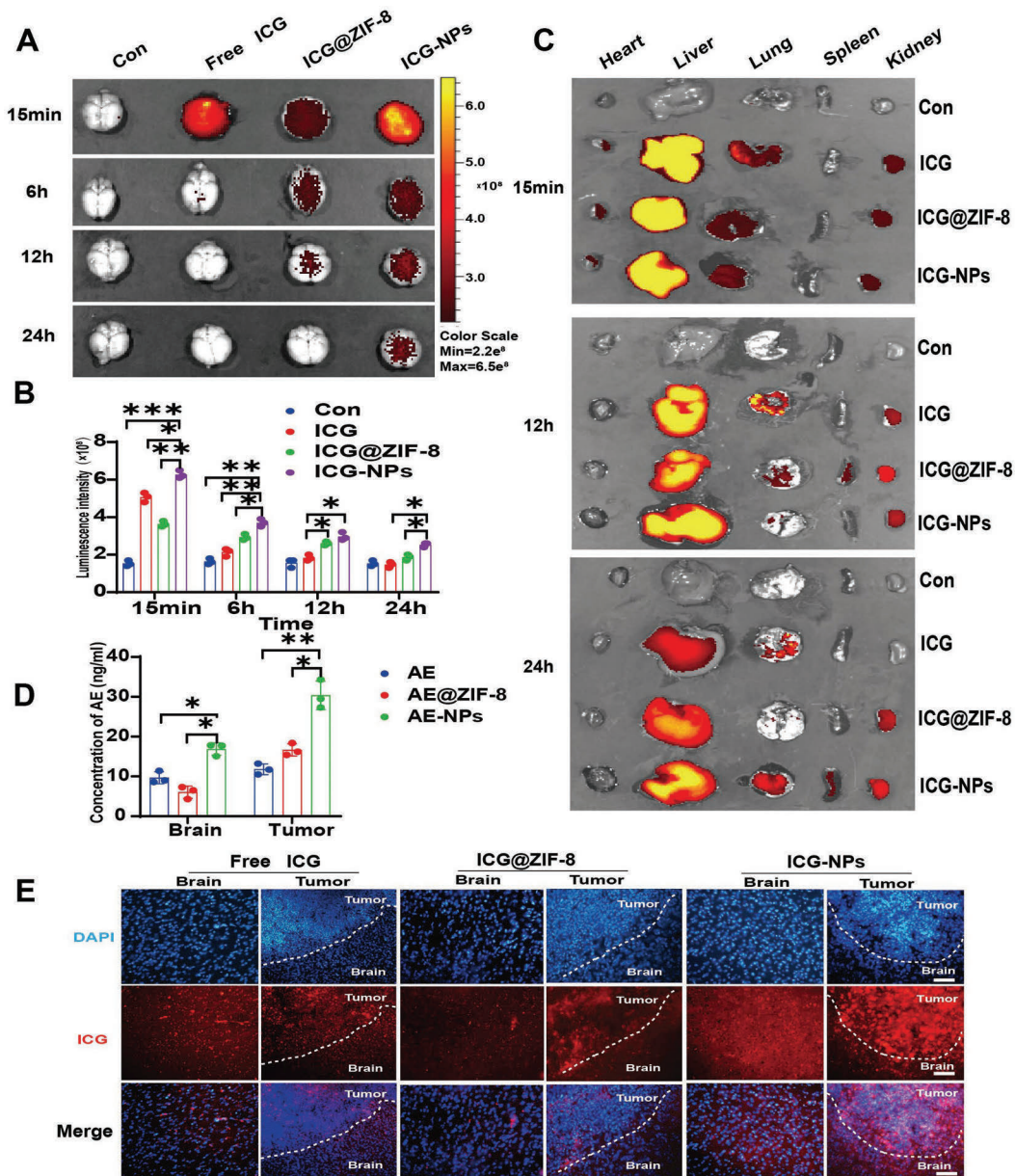


Figure 5. AE-NPs improved the intracranial distribution and tumor enrichment in vivo. Optical live imaging detection (A) and quantification (B) of the intracranial distribution of ICG from ICG, ICG@ZIF-8, and ICG-NPs treated mice for 15 min, 6 h, and 12 h. ICG was normalized to 3 mg kg⁻¹. Data are presented as the mean ± SD from three independent experiments. **P* < 0.05, ***P* < 0.01, ****P* < 0.001 (one-way ANOVA and Bonferroni's multiple comparisons test). C) Organ distribution of ICG from ICG, ICG@ZIF-8 and ICG-NP treated mice in different time point. D) Quantitation of AE concentration in brain and tumors from tumor bearing mice of different treatment by LC-MS. AE was normalized to 8 mg kg⁻¹. Data are presented as the mean ± SD from three independent experiments; **P* < 0.05, ***P* < 0.01 (one-way ANOVA and Bonferroni's multiple comparisons test). E) Brain distribution of ICG (red) from ICG, ICG@ZIF-8, and ICG-NP-treated GBM bearing mice for 6 h. ICG was normalized to 3 mg kg⁻¹ and assayed by cryosection with confocal microscopy (scale bar: 200 μm).

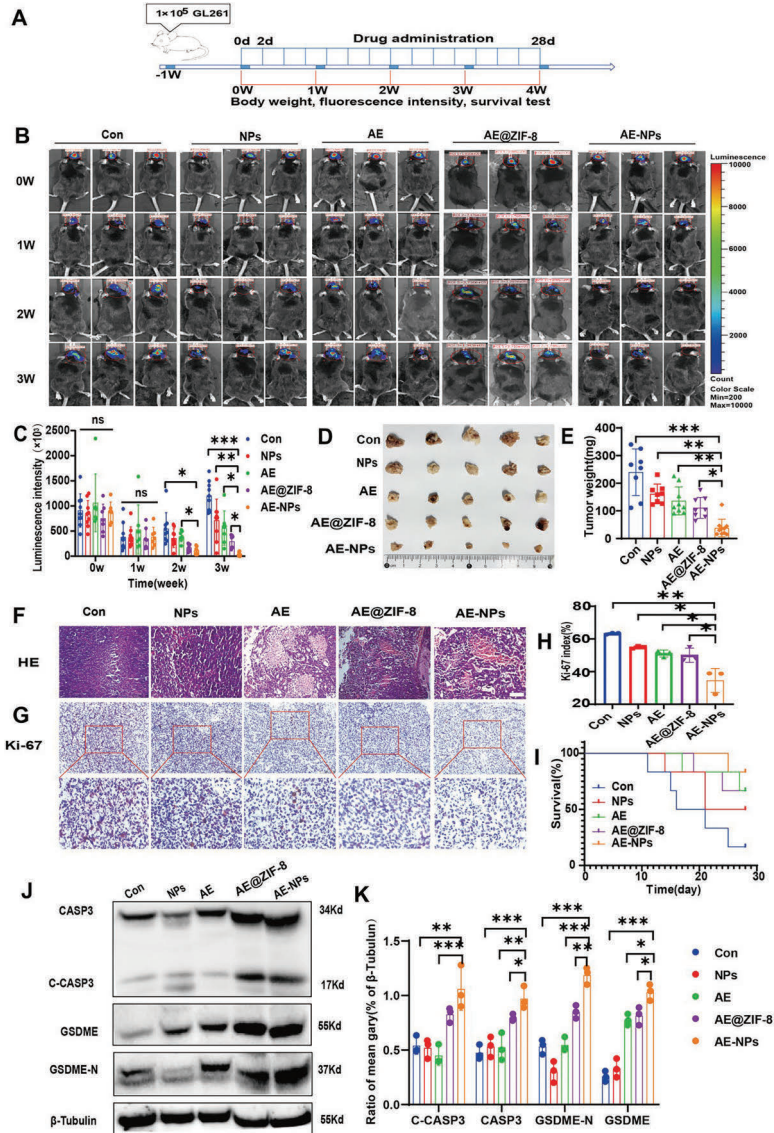


Figure 6. NPs enhanced the antitumor effects of AE in vivo. A) Administrative protocol in vivo. B) Fluorescent staining of GL261 tumor-bearing mice treated with 1% F127 NS (Con), NPs, AE, AE@ZIF-8, and AE-NPs at different time points, AE normalized to 8 mg kg^{-1} . C) Quantitative analysis of tumor fluorescence. Data are presented as mean \pm SD, 8 to 10 mice per group, $*P < 0.05$, $***P < 0.01$, $****P < 0.001$ (one-way ANOVA and Bonferroni's multiple comparisons test). D) Photographs of tumors from different treatments. E) Change curves of tumor weight after different treatments, data are presented as mean \pm SD, 8 to 10 mice per group, $*P < 0.05$, $**P < 0.01$, $***P < 0.001$ (one-way ANOVA and Bonferroni's multiple comparisons test). F) H&E staining of tumor tissues after different treatments. G,H) The expression of Ki-67 was detected by IHC staining of tumor tissues after different treatments (scale bar: $100 \mu\text{m}$), data in (H) are presented as mean \pm SD, $n = 3$ mice, $*P < 0.05$, $**P < 0.01$, $***P < 0.001$ (one-way ANOVA and Bonferroni's multiple comparisons test). I) Survival curves of mice after different treatments ($n = 6$ mice); Western blot (J) and quantitative analysis (K) of pyroptosis biomarkers CASP-3, C-CASP3, GSDME, and GSDME-N in tumor tissues from different treatments by mean gray value. Data in (K) are presented as mean \pm SD, $n = 3$, $*P < 0.05$, $**P < 0.01$, $***P < 0.001$ (one-way ANOVA and Bonferroni's multiple comparisons test).

molecular level, we measured the pyroptosis key biomarkers CASP3, C-CASP3, GSDME, and GSDME-N in tumor tissues from different treatments by western blotting. Compared with the other three groups, AE-NPs significantly enhanced the activation of CASP3 and GSDME (Figure 6J,K). At the same time, AE@ZIF-8 displayed pyroptosis activation ability, this might be induced by AE@ZIF-8 enrichment in tumor tissue.

2.7. AE-NPs Regulated GBM Immune Microenvironment

The above experiments confirmed that AE-NPs activated CASP3/GSDME pyroptosis pathway *in vitro* and *in vivo*. As an immunogenic death model, pyroptosis has the potential to activate intrinsic and adaptive immunity to amplify antitumor effect. Therefore, immune cells CD8⁺ T cells, CD4⁺ T cells, Treg cells (FoxP3⁺), macrophage, and their M1 subtype (anti-inflammatory and antitumor subtype, CD86⁺) were examined by flow cytometry (FCM) and immunofluorescence. CD8⁺ T cell is critical immune cells in antitumor immunity. Therefore, flow cytometry was performed to identify the infiltration level of CD8⁺ T cells in tumor tissues from different treatment. The results showed that compare with con group, CD8 expression levels were improved in AE, AE@ZIF-8, and AE-NPS group, especially in the AE-NPs group (the ratio of CD8⁺ T cells to CD3⁺ T cells is increased from 31% to 64%) (Figure 7A,E). Immunofluorescence also showed pronounced CD8⁺ T cells expression (Figure S13A, Supporting Information). Since CD8⁺ T cells are main immune cells that perform tumor killing *in vivo*, their elevated expression suggest enhanced immune killing effect, but at the same time, the expression of PD-1 was elevated (Figure S13A, Supporting Information). The traditional view is that PD-1 expressed on CD8⁺ T cell act as an inhibitory receptor mediates immune tolerance, but it was also reported that PD-1 expressed during the early stage of CD8⁺ T cell activation after antigen stimulation. Thus, the elevated PD-1 may come from CD8⁺ T cell activation,^[34,35] but the exact role needs to be further explored. CD4⁺ T is an important immune cell, CD4⁺ T cells and their subtype Treg cells (FoxP3⁺, mediated immune tolerance) are also detect. Even immunofluorescence showed no significant differences in each group (Figure S13B, Supporting Information), the FCM showed that compare with con group, the CD4⁺ T increased from 71.45% to 86.18% in AE-NPs group, and with no significant difference in Treg cells (Figure 7B,E,F). The function of tumor-associated macrophages is complex, but M1 subtype (M1Φ) infiltration are conducive to their antitumor effects.^[36] FCM showed the ratio of F4/80⁺ CD86⁺ cells to F4/80⁺ cell is increased from 54% in Con group to 71% in AE-NPs group (Figure 7C,G). Immunofluorescence also showed more obvious Iba1⁺ and CD 86⁺ cell expression in tumor of AE-NPs group (Figure S13C, Supporting Information), that suggests more macrophage infiltration and M1 subtype expression. Furthermore antitumor immunity relate cytokines IFN-γ, HMGB1, TNF-α are also measured by qPCR, as shown in Figure 7HJ, compare with control group, the expression of IFN-γ, HMGB1, TNF-α mRNA are increased 6–17 fold in AE-NPs group, this verified the activation of the immune microenvironment.

2.8. AE-NPs Relieved AE-Related Hepatotoxicity and Nephrotoxicity

Similar to many chemotherapeutics, hepatotoxic, and nephrotoxic effects of high concentration AE have been previously reported.^[28,37] Meanwhile, high concentrations and unmodified ZIF-8 NPs also has noticeable toxic reactions.^[16,33] Therefore, it was necessary to evaluate the safety of the newly constructed AE-NPs. Thus, CCK-8 *In vivo*, body weight, blood biochemical, and histopathological assays on tumor bearing mouse were performed. Despite a noticeable GBM inhibitory effect with the blank NPs *in vivo* (Figure 6B,E,F), low dosage of zinc nitrate, 2-methylimidazole, ZIF-8, TF-PEG-PLGA, and blank NPs did not show noticeable cytotoxicity *in vitro* (Figure 8A). As the concentration continues to increase a certain concentration, zinc nitrate (above 40 μg mL⁻¹), ZIF-8 (above 80 μg mL⁻¹), and NPs (above 80 μg mL⁻¹) all affected cell viability (Figure S15, Supporting Information). Blood biochemical analysis showed that the liver injury biomarkers alanine aminotransferase (ALT), aspartate aminotransferase (AST) (Figure 8B,C), and the renal injury biomarker BUN (Figure 8E) were increased in the AE, AE@ZIF-8, and NPs treated groups, while γGT (Figure 8D) and CRE (Figure 8F) were unchanged. Surprisingly, no significant changes in ALT, AST, or BUN were observed in AE-NPs-treated mice. Moreover, the histopathology by HE staining showed that focal necrosis was detected in the liver from the AE treated group, but not in the NPs and AE-NPs treated groups (Figure 8G). These results indicated that liver and kidney injury caused by AE and NPs were significantly reduced by AE-NPs. This is likely the result of enhanced tumor targeting, which reduce drug-related off-target toxicity and side effects.^[38] Within 4 weeks, mice in control and NPs group had a body weight loss, but not obvious in AE@ZIF-8 and AE-NPs groups (Figure S12, Supporting Information). For health mice, within 4 weeks, NPs did not affect the body weight (Figure S16A, Supporting Information), organ pathology (Figure S16C, Supporting Information). But there is a slight elevation of ALT on NPs group, and there is no statistic difference in AST, γGT, Cr, BUN (Figure S16B, Supporting Information). Moreover, no mouse death during the experiment, shown acceptable security.

3. Discussion

BBB permeability, tumor targeting, and drug toxicity are the main hurdles for chemotherapeutic drugs applied in GBM treatment. Using nanocarriers for drug delivery provides an opportunity to overcome these challenges. Herein, AE-NPs were generated and proven superior to AE alone by the following: 1) Improved BBB permeability; 2) Enhanced tumor targeting and antitumor effects; 3) Reduced drug toxicity.

Improving BBB permeability is key in the treatment of intracranial diseases. The BBB refers to the barrier between the blood and brain formed by the capillary endothelium and glial cells, selectively allowing oxygen and nutrients to enter the central nervous system (CNS), while preventing toxins, microorganisms, and most drugs.^[39,40] Although GBM may lead to the disruption of the BBB and enhanced permeability and retention effect (EPR), the barrier remains effective against drugs.^[41]

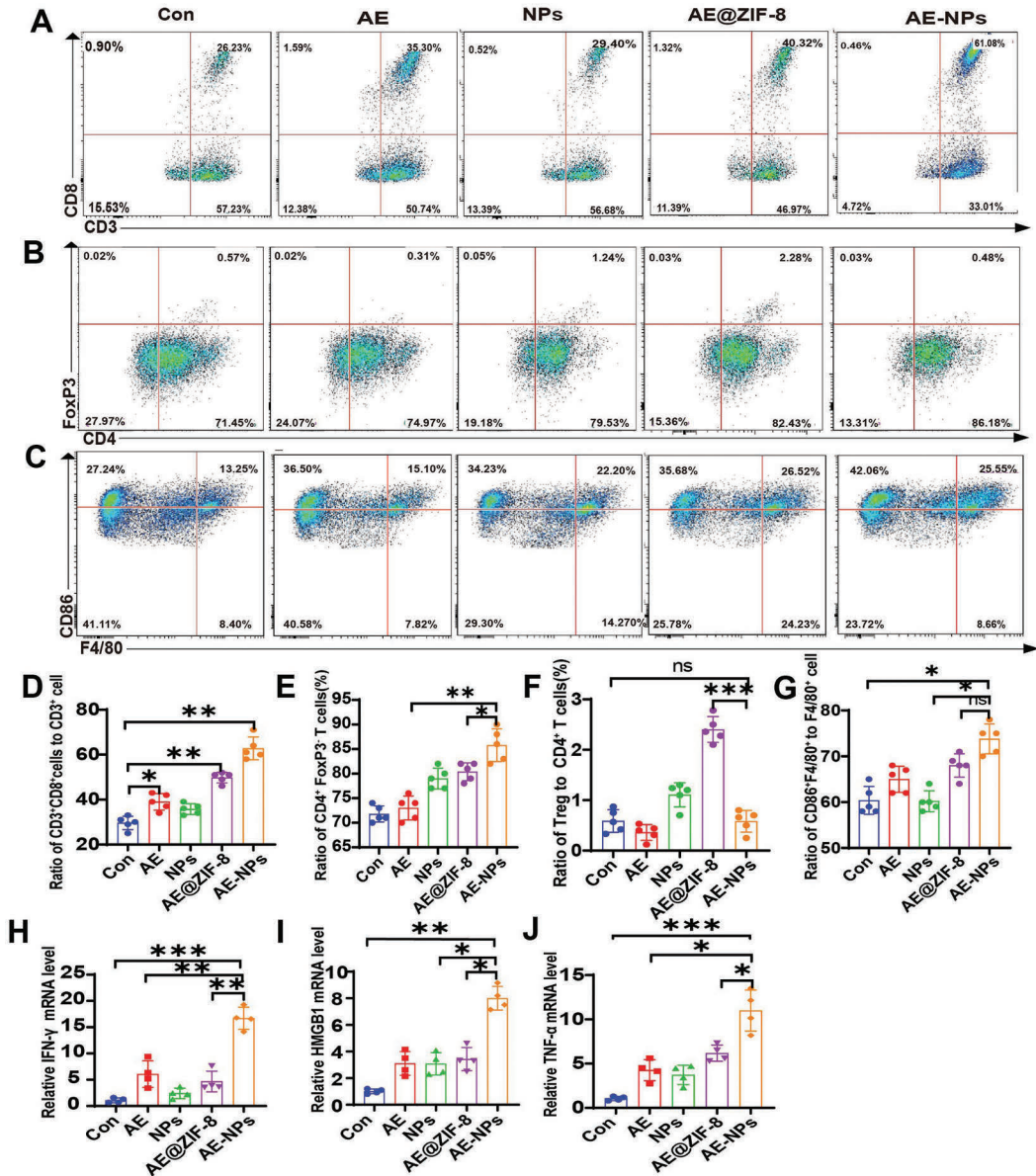


Figure 7. AE-NPs regulate GBM immune microenvironment. Flow cytometry assay of CD8⁺ T cell (A), CD4⁺ T and Treg cell (B), macrophage and M1 subtype (C) infiltration in the tumor tissue after different treatments, $n = 5$ mice. D–G) Quantitative analysis of flow cytometry. Data are presented as mean \pm SD, $n = 5$ mice, $^{*}P < 0.05$, $^{**}P < 0.01$, $^{***}P < 0.001$ (one-way ANOVA and Bonferroni's multiple comparisons test). H–J) The expression of IFN- γ (H), HMGB1 (I), TNF- α mRNA in GBM tissue after different treatment, assayed by qPCR. All data are represented as means \pm SD ($n = 5$); $^{*}P < 0.05$, $^{**}P < 0.01$, $^{***}P < 0.001$ compared with the control group (one-way ANOVA and Bonferroni's multiple comparisons test).

As the tumor deteriorates and progresses, the tumor membrane ruptures, and the structure of the BBB and its functions will also be changed,^[42,43] eventually leading to 98% of small

molecules and almost all macromolecules being insulated from the CNS.^[44] These factors lead to the failure of most clinical drugs for the treatment of GBM. Significantly, in this work, our

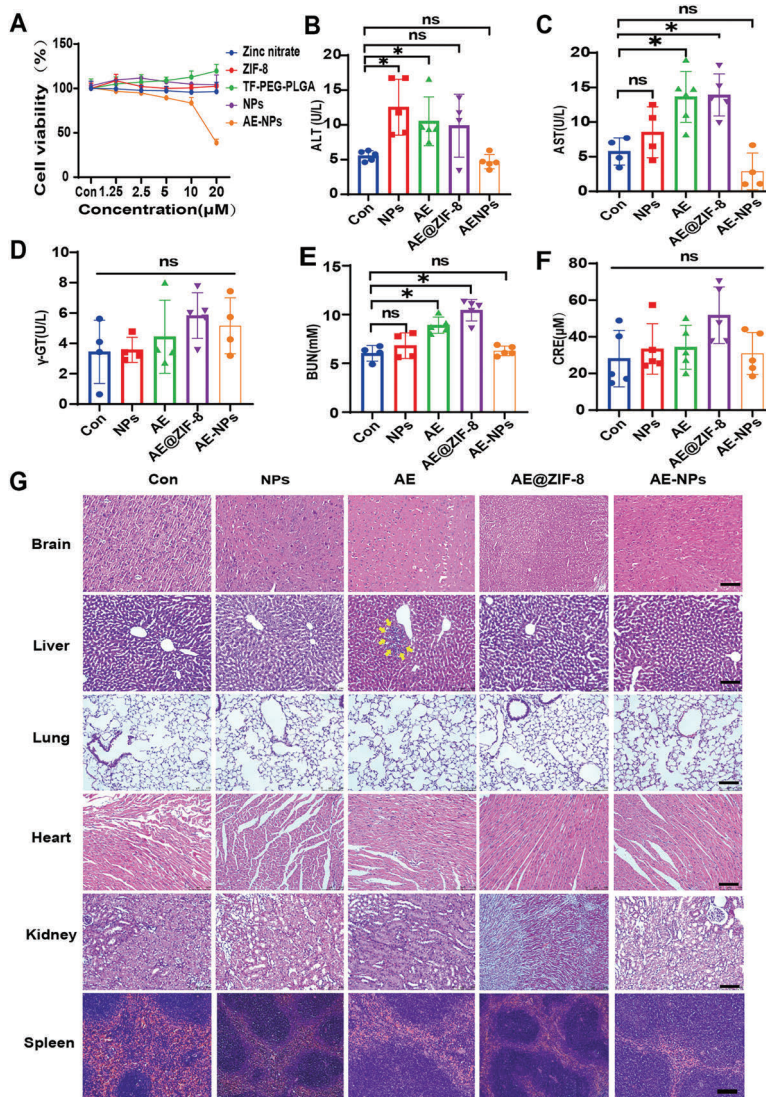


Figure 8. AE-NPs relieved hepatotoxicity and nephrotoxicity. A) Cytotoxicity of zinc nitrate, ZIF-8, TF-PEG-PLGA, NPs, and AE-NPs on U87MG cells was measured by CCK-8 ($n = 3$); ALT (B), AST (C), γ -GT (D), CRE (E), and BUN (F) values in mouse serum after different treatments. All values are presented as mean \pm SD, 4–6 mice per group, * $P < 0.05$, ** $P < 0.01$ (one-way ANOVA and Bonferroni's multiple comparisons test). C) HE staining of the pivotal organs after different treatments. The yellow arrow points to the lesion zone (scale bar: 100 μ m).

constructed AE-NPs improved the BBB penetration, which probably because the TF-PEG-PLGA coating prolonged the blood circulation time and altered BBB penetration mode.

Enhanced tumor targeting is beneficial for antitumor effects and reducing drug-related toxicity and side effects.^[38] Constructed AE-NPs achieved tumor targeting and enrichment (Figure 5D,E), likely related to TFR are highly expressed in

tumor tissue, hence Tf can anchor the nanoparticles to tumor tissue and improve tumor enrichment. Furthermore, the ability of ZIF-8 NPs responded degradation in acidic tumor microenvironment also has a synergistic effect to improve the tumor targeting effect.^[16]

In this study, we found that AE acts as a pyroptosis inducer. Additionally, we observed that AE at a concentration of IC50

(48.7 μM , U87MG) significantly inhibited the activity of U87 cells after 48 h (Figure 1B). However, there was no significant activation of CASP3 and GSDME (Figure 2D), suggesting that AE-induced pyroptosis may not be the only mechanism underlying its anti-GBM effects. Moreover, we found that AE-induced pyroptosis in U87MG cells is concentration-dependent, with high doses inducing GBM pyroptosis but not low doses (Figure 2D).

Our research also shows that tumor-targeted delivery of AE-NPs enhances AE enrichment in GBM (Figure 5D,E). This concentration difference makes the induction of tumor tissue pyroptosis feasible (Figure 6J), while minimizing pyroptosis in normal brain tissue, which is considered one of the reasons for the side effects of chemotherapy drugs.^[27] This advantage supports our decision to choose AE as a pyroptosis-inducing agent.

The materials used in this study have been shown to be safe in previous studies, but high concentrations and unmodified ZIF-8 NPs can have noticeable toxic reactions.^[16,33] These are mainly derived from the rapid degradation of ZIF-8 NPs.^[33] It was reported that unmodified ZIF-8 NPs could kill not only cells but also animals, however, such toxic reactions can be alleviated by appropriate modification.^[33] We utilized ZIF-8 NPs as drug carriers in this study, and the coating of Tf-PEG-PLGA polymer did not show increased cytotoxicity on GBM cells (Figure 8A). Although ALT, AST, and BUN levels were elevated by NPs, the organ toxicity of AE-NPs was not obvious (Figure 8B,C,E). At the same time, the NPs showed an obvious inhibitory effect and necrosis-promoting effect on GBM cells (Figure 6F), meanwhile no pathological damage to the brain and vital organs was observed (Figure 8G). These results suggest that Tf-PEG-PLGA coated ZIF-8 NPs suppress GBM without obvious toxic side effects, which likely attributed to the modification of Tf-PEG-PLGA anchoring ZIF-8 NPs in tumor tissue. The acidic microenvironment promotes ZIF-8 NPs degradation, and the cytotoxic effect is restricted to tumor tissue.

Immunosuppressive tumor microenvironment, which suppress immune responses and support tumor growth is one of the biggest hurdles to effective therapy for GBM.^[45] Pyroptosis of the GSDME pathway has good prospects in antitumor therapy because it can mediate both cell death and antitumor immune activation. Couple with pyroptosis, intracellular antigens (such HMGB1, IL-1 β) released, promote DC maturation, initiate T-cell clone, enhance tumor killing effect, pyroptosis is considered as a new tumor immunotherapy.^[46] At present, there are limited reports on anti-GBM by promote pyroptosis. Herein, the targeted delivery of AE by NPs to GBM enhanced AE-mediated GBM pyroptosis in vivo (Figure 6J,K). Furthermore, AE-NPs also enhanced CD8⁺ T cells, CD4⁺ T cells, macrophage M1 subtype GBM infiltration, and increased the expression of IFN- γ , HMGB1, TNF- α mRNA level (Figure 7). Therefore, our research may offer a new strategies for GBM immunotherapy.

Despite the big advantages of Aloe-emodin for cancer therapy, the hepatotoxicity and nephrotoxicity brought by high concentration of AE are also main problems for its clinical application. It was reported that these defects were mainly caused by high concentration of AE induced FAS death, mitochondrial damage, endoplasmic reticulum stress provoking, and DNA damage.^[37,47,48] Our study showed that AE signifi-

cantly inhibited GBM cells and GBM growth both in vitro and in vivo (Figures 1B,6B–E; and Figure S1, Supporting Information), but it was accompanied by elevated liver and kidney injury serologic markers (ALT, AST, BUN) and histopathological injury of the liver (Figure 8B,C,G). These observations are consistent with previous reports of hepatotoxicity and nephrotoxicity. However, when AE was encapsulated by NPs, there were no significant differences in blood biochemical changes (Figure 8B,C,E) or histopathological (Figure 8G) injury compared to control groups, indicating that NPs encapsulation effectively alleviated AE-related hepatotoxicity and nephrotoxicity. This may be attributed to enhanced tumor targeting, but the in-depth mechanism needs further exploration.

4. Conclusion

In summary, AE was proved as a pyroptosis booster to suppress GBM through the CASP3/GSDME pathway both in vitro and in vivo. By loaded with a pH responsive and BBB penetrating nanocarrier, improved BBB penetration, tumor targeting, enhanced antitumor efficacy, and reduced toxicity effect were realized. In addition, AE-NPs have also been proved to enhance CD8⁺ T, CD4⁺T, macrophage M1 subtype GBM infiltration, prolong the survival rate of tumor-bearing mice. Overall, our study provides a new strategy for the treatment of GBM and provides a BBB-penetrating, tumor-targeting, high-efficiency, and attenuated drug carrier for intracranial tumor therapy.

5. Experimental Section

Main Materials: Aloe-emodin (AE, 99%, Chengdu Alpha). Zinc nitrate hexahydrate ($\text{Zn}(\text{NO}_3)_2 \cdot 6\text{H}_2\text{O}$, 99.998%, Aladdin), *N*-hydroxy succinimide (NHS, 98%, Aladdin), *N*-(3-Dimethylaminopropyl)-*N*'-ethylcarbodiimide hydrochloride (EDC-HCl, 98%, Aladdin), 2-methylimidazole ($\text{C}_4\text{H}_8\text{N}_2$, 98%, Aladdin), transferrin (95%, Aladdin). Indocyanine green (ICG, 75%, Macklin), PLGA20k-PEG5k-COOH was purchased from Xi'an Ruixi Biological Technology Co. Ltd. (Xi'an, China). Recombinant anticlaved caspase-3 antibody, recombinant anti-DFNA5/GSDME N-terminal antibody, anti-Iba1 antibody, Anti-CD4 antibody (EPR19514), PD-1 antibody, and anti-Ki67 antibody were purchased from Abcam Plc Co., Ltd. (Cambridge, UK). CD86(B7-2(D-6)) antibody, CD8- α (D-9) were obtained from SantaCruz (Dallas, USA), PE antimouse CD8a were purchased from Biolegend (CA, USA). PE Rat Anti-Mouse F4/80(T45-2342), PE-Cy7 Rat Anti-Mouse CD86(GL1), APC-Cy7 Rat Anti-Mouse CD45(30-F11), PE-Cy7 Hamster Anti-Mouse CD3e(145-2C11), APC Rat Anti-Mouse CD4(RM4-5), PE Rat anti-Mouse Foxp3(R16-715), were purchased from BD Pharmingen (NJ, USA). FoxP3 Monoclonal Antibody were purchased from eBioscience (CA, USA), Donkey anti-Goat IgG-AlexaFluor 488, Donkey anti-Rabbit IgG-Alexa Fluor 594 (Shanghai, China), β -Tubulin rabbit monoclonal antibody, FITC-labeled goat anti-rabbit IgG, horseradish peroxidase-labeled goat anti-rabbit IgG (H+L), and LDH Release Assay Kit were purchased from Beyotime Biotechnology Co., Ltd. (Shanghai, China). And alanine aminotransferase (ALT) assay kit, creatinine (CRE) assay kit, aspartate aminotransferase (AST) assay kit, blood urea nitrogen (BUN) assay kit, γ glutamyl transferase (γ GT) assay kit were purchased from Nanjing Jiancheng Bioengineering Research Institute Co., Ltd. (Nanjing, China).

Synthesis of AE@ZIF-8 NPs: AE-loaded ZIF-8 NPs (AE@ZIF-8 NPs) were prepared by a self-assembly method.^[19,49] First, 75 mg of zinc nitrate was added to 2.5 mL of methanol and sonicated to dissolve with a 120 W ultrasonic bath for 2 min (solution A). Meanwhile, 165 mg of 2-methylimidazole and aloe-emodin (0, 2, 6, 10, 20 mg) were dissolved in

5 mL of methanol and sonicated with a 120 W ultrasonic bath for 5 min (solution B). Subsequently, solution B was stirred for 5 min at 250 rpm under room temperature. Next, solution A was dropped into solution B under 250 rpm stirring condition. After that, the mixture was continue stirred in the dark at room temperature for 1 h, and then kept for another 1 h at 4 °C. Finally, the mixture was centrifuged at 12 000 rpm for 10 min, washed with methanol three times to obtain AE@ZIF-8 nanoparticles, and resuspended in 5 mL methanol or normal saline (NS) containing 1% poloxamer (F127) (1% F127 NS) for further experiments.

Preparation of Tf-PEG-PLGA: Tf was conjugated to PEG-PLGA by a two-step EDC/NHS coupling method.^[50] With the catalysis of EDC/NHS, the —COOH of COOH-PEG-PLGA interacts with —NH₂ from Tf to generate amide bonds, thereby obtaining Tf-modified PEG-PLGA (Tf-PEG-PLGA) (Scheme 1A). Briefly, 10 mg COOH-PEG-PLGA was dissolved in 4.5 mL methanol in a 120 W ultrasonic bath for 5 min, then 250 μL of EDC·HCl (1 mg mL⁻¹) and 250 μL of NHS (1 mg mL⁻¹) were added and magnetically stirred at room temperature for 4 h at 250 rpm. Then, 200 μL of transferrin aqueous solution (1 mg mL⁻¹) was added dropwise, stirred in the dark for 2 h, and incubated for overnight at 4 °C.

Preparation of AE-NPs: The above AE@ZIF-8 NPs methanol solution was mixed with Tf-PEG-PLGA methanol solution in volume ratios of 5:5, 6:4, 7:3, 8:2, and 9:1 at room temperature with magnetic stirring at 250 rpm for 4 h in the dark. The samples were centrifuged at 12 000 rpm for 10 min, and the precipitate was taken to obtain the final AE-NPs product, which was washed twice with methanol. Then, the NPs were resuspended in 75% ethanol, soaked for 30 min to remove bacteria, and washed twice with 1% F127 NS.

Characterizations of ZIF-8 NPs, AE@ZIF-8 NPs, and AE-NPs: Dynamic light scattering (DLS) and transmission electron microscopy (TEM) were used to detect the size of nanoparticles. For detection nanoparticle size and zeta potential, the NPs were distributed in methanol, 1% F127NS, and 1% F127NS+10% FBS, respectively, and analyzed by a Malvern laser particle size analyzer (DTS1070, Malvern, UK). The stability of nanoparticles was evaluated by hydrodynamic particle size at 0, 12, 24, 48, 72, and 96 h. The structure and morphology of blank ZIF-8 NPs, AE@ZIF-8 NPs, and AE-NPs were observed by TEM (HITACHI, Japan) with an accelerating voltage of 80 kV. TEM samples were tweezers held on carbon-coated copper grids (200 mesh; Ted Pella, Inc., USA), immersed in a particle solution, removed, and air-dried prior to imaging. The size from TEM was analyzed with ImageJ software. Each picture was marked with 100 nanoparticles, three pictures were recorded, and the detection results were imported to Origin 2021 software to obtain the size. Furthermore, the successful encapsulation of AE and ICG into Tf-PLGA-PEG coated ZIF-8 NPs was detected through remarkable absorption at 255 and 780 nm by UV–vis absorption spectroscopy (Puxi General Instrument Co., Ltd. China). The coating of Tf-PEG-PLGA on ZIF-8 NPs was confirmed by FTIR spectra and TEM images.

Drug Loading Degree and Efficiency Detection: The content of AE was detected by UV–vis absorption at 255 nm. A 200 μL sample was dropped into a cuvette containing 2.8 mL methanol solution with a pH of 1.5. According to the standard curve, the content of AE in the sample was calculated. AE loading degree (LD, %) = amount of encapsulated AE/weight of nanoparticles; AE encapsulation rate (%) = amount of encapsulated AE/total input amount of AE. the connection efficiency of transferrin was calculated by a BCA kit, Tf loading efficiency (LE, %) = weight of transferrin in nanoparticles/total input amount of transferrin.

In Vitro Release and pH-Responsive Analysis: AE-NPs were dispersed into 1.0 mL of 1% F127 NS (pH = 7.4; pH = 5.5) and shaken at 37 °C gently in dark. The solution was first centrifuged at 12 000 rpm for 10 min, and then 900 μL of supernatant was withdrawn and analyzed by a UV spectrophotometer at 255 nm at indicated time points. Then, 900 μL of fresh medium was added and sonicated until dispersed well. Calculate cumulative release rates at selected time intervals. The alternative sample disposal method is as above. At selected time intervals, the appearance of AE-NPs from different pH values was observed by TEM, and size was test by Malvern laser particle size analyzer.

Cells and Animals: U87MG, DBTRG, U251, HeLa, HepG2, A549, HMO6, BV2 cells were purchased from ATCC (American Type

Culture Collection) and stored in the laboratory and cultured in DMEM containing 10% FBS, 1% penicillin–streptomycin solution, 2 mM l-glutamine, and maintained at 37 °C with 5% CO₂ humidity. GL261-Luc was purchased from Shanghai Yansheng Industrial Co., Ltd (Shanghai, China), and used as the transplanted tumor model. GL261-Luc cells were stored as recommended by ATCC, cultured and cryopreserved according to the manufacturer's protocol. C57BL/6 mice were purchased from Laboratory Animal Center of Hubei University of Medicine (Hubei, China) and bred according to the Guide for the Care and Use of Laboratory Animals of the National Institutes of Health. The experimental protocol of this study was reviewed and approved by the Laboratory Animal Welfare Ethics Review Committee of Hubei University of Medicine (Hubei University of Medicine Animal (welfare) No. 2022-Experiment 015).

Cell Viability Assay: CCK-8 was used to detect the cell viability. U87MG and GL261 cells were seeded in 96-well plates at a density of 4000 cells per well. Twelve hours later, cell culture medium containing gradient concentrations of AE was administered and cocultured, 0.1% DMSO was used as the control (Con), and 10 μL of CCK-8 solution was added to each well at 24, 48, and 72 h and incubated in an incubator (37 °C, 5% CO₂) for 2 h. The absorbance at 450 nm was measured using a SpectraMax 190 microplate reader (Molecular Devices, USA).

Screening of AE-Related Targets: Swiss Target Prediction database was used to query AE targets and related target genes. Then, the Pharm Mapper database was applied to restrict the species to human, and the Target Net database was used to identify potential target genes. After merging the targets of each database, the duplicate data were deleted, and the aloeo-emodin-related targets were uniformly transformed using the UniPort protein standardization database.

Collection of Targets of GBM: Using “Glioblastoma” as the keyword, the related targets were screened by the OMIM database, Gene Cards database, and TTD database. Targets were selected according to the principle of a Gene Cards database relevance score > 5, and the published literature was found to supplement the unscreened targets. After merging three disease database targets, the repeat values were deleted to obtain the final target for interaction with glioblastoma.

Construction of the AE-GBM Target Protein–Protein Interaction (PPI) Network: After merging and compiling the search results from the database, duplicate targets were removed. The intersection between the predicted targets of AE active ingredients and the retrieval results of glioblastoma-related target genes was determined, and the common targets were screened as possible targets of AE in GBM. The Venny 2.1.0 to map GBM-related targets and active ingredient targets in the form of Venn diagrams was applied. The intersection targets were uploaded to the STRING database (version 11.5) to construct the PPI network, and the key targets were subsequently screened and analyzed subsequently, the scoring condition was set to >0.40, and the selected target proteins were limited to “Homo sapiens.” Then, the key protein targets were visually analyzed by Cytoscape3.7.2 software. The function of the plug-in “Analysis Network” was used for analysis, and the key targets were sorted by “Degree.” In the PPI network, the edges represent protein–protein associations, more lines suggesting greater correlation.^[51] Databases and software used in the network pharmacology analysis were list at Table S1 (Supporting Information).

LDH Release: LDH release was detected by an LDH Release Assay Kit. U87 cells were first seeded into 96-well plate at the density of 5000 cells per well and incubated for 24 h. After that, a gradient concentration of AE was added into the cells and cocultured for 48 h. The supernatant from each well was collected into a new 96-well plate to detect the level of LDH release by the LDH Release Assay Kit, and the absorbance at 490 nm of the supernatant was detected by a SpectraMax 190 microplate reader (Molecular Devices, USA).

qPCR Assay: Total RNA was extracted from AE treated U87MG, GL261 cells and tumor tissue after different treatment by Trizol, using an ABScript II Reverse Transcriptase kit (RK21400, ABclonal, China) to reverse-transcribe and synthesize cDNA. The obtained cDNA was used as a template for subsequent qPCR experiments. Primer sequences used in this work were listed in Table S2 (Supporting Information).

Confocal High-Content Imaging: U87MG cells were seeded into 24-well plates, 3000 cells per well. Then, the cells were treated with AE and AE-NPs, the AE concentrations were equilibrated to 50 μM , 0.2% DMSO was used as a control, and the Operetta CLS confocal high-content imaging analysis system (Perkin Elmer, USA) was used for detection. There were 8 detection views in each well, taking pictures once per hour (200X), and observing for 72 h.

Body Distribution: ICG-NPs were prepared as nanotrackers, and the distribution of NPs *in vivo* was analyzed by optical live imaging and cryosections. C57BL/6J mice were treated with ICG and ICG-NPs through the tail vein, and the dosage of ICG was normalized to 3 mg kg⁻¹. At selected time intervals, the mice were anesthetized and sacrificed. The fluorescence expression of the brain and vital organs was examined under a fluorescence imaging system (Calliper, USA). For cryosections, tumor-bearing mice were administered and treated in the same way as above, brain (with tumor) were taken for cryosections (10 μm), the nuclei were stained with DAPI after fixation, and the drug distribution was observed under a fluorescence microscope (Leica DMI6000B, Leica, Germany). The distribution of AE in brain and tumor was detected by liquid chromatography-mass spectrometry (LC-MS): Tumor bearing mice were injected with AE, AE@ZIF-8, and AE-NPs (the amount of AE was balanced to 8 mg kg⁻¹) through tail vein, and the tumor bearing brain tissue was obtained in 2 h, then brain and tumor were separated and weighed, Homogenized in normal saline, 1, 8-dihydroxy-anthraquinone was used as the internal standard, methanol was added, and all supernatants were dried with nitrogen. The precipitation was redissolved with the initial mobile phase (10% methanol +90% 2 mM ammonium acetate), vortexed for 5 min, centrifuged, and 5 μL supernatant was taken for detection. Calibration standards and quality control (QC) samples were prepared and extracted same as the samples. The analysis was performed using a Waters ACQUITY UPLC system (Waters, Milford, MA) and a Micromass Quattro Micro API mass spectrometer (Waters, Milford, MA). Chromatographic separation was performed on an ACQUITY UPLC BEH C18 Column (2.1 \times 100 mm; 1.7 μm), maintained at 45 °C. The flow rate was maintained at 300 $\mu\text{L min}^{-1}$. The initial flow conditions were 90% solvent A (2 mM ammonium acetate) and 10% solvent B (methanol). The gradient elution program was as follows: 0–0.5 min, 10% B; 0.5–1.2 min, 10–35% B; 1.2–3.5 min, 35–70% B; 3.5–4.2 min, 70–90% B; 4.2–5.2 min, 90% B; 5.2–5.5 min, 90–10% B; and 5.5–6.0 min, 10% B. The mass spectrometer was operated under multiple reaction monitoring (MRM) mode with negative electrospray ionization. Mass spectrometer was operated using the following parameters: Electrospray ion source, gas temperature, 400 °C; gas flow, 800 L h⁻¹; capillary 3 Kv.

Blood Biochemical Examination: Blood was collected by cardiac puncture after anesthesia at the end of the treatment, and serum was collected by centrifugation. ALT, AST, Cr, γ -GT, and BUN assay kits were used to assay ALT, AST, Cr, γ -GT, and BUN.

HE Staining and Immunohistochemistry: Paraffin sections from tumor tissue and vital organs (brain, heart, spleen, liver, lung, and kidney) were dewaxed, rehydrated, and antigen repaired. The paraffin sections were stained with eosin and hematoxylin for HE. For IHC staining, the paraffin sections were incubated in 3% hydrogen peroxide for 12 min at room temperature. And then blocked with 5% BSA for 40 min, stained with 1:200 anti-Ki67 antibody (ab15580, Abcam, USA) overnight at 4 °C, and secondary antibody were incubated for 1 h at 37 °C, Diaminobenzidine was applied for coloration for 3 min at room temperature, the nucleus was stained by hematoxylin.

Flow Cytometry: The tumors were harvested from the GBM-bearing mice after different treatment. Then homogenized in DMEM containing collagenase IV at 37 °C. The tumor-infiltrating immune cells were collected by centrifugation (3000 rpm, 15 min), and resuspended in PBS containing 2% FBS and nonspecific antibody binding was blocked with CD16/CD32. After strain with FIXABLE VIABILITY DYE EF506. CD8⁺T cells were labeled with CD45, CD3, and CD8 antibodies, CD4⁺T cells were labeled with CD45, CD3, and CD4 antibodies, and Treg cells were further labeled with FoxP3 antibody base on CD4⁺ T cells. M1 Φ was labeled with CD45, F4/80, and CD86 antibodies, FoxP3 were stained using a

Transcription Factor Buffer Set. Gating strategy for flow cytometry were showed in Figure S14 (Supporting Information). The cells were measured with a flow cytometer (Sony 3800, Japan) and analyzed using SA3800 Software Version 2.0.4.14073.

Statistical Analysis: All experiments were repeated at least three independent times, and data were expressed as the mean \pm SD. Statistical analysis was performed using a 2-tailed Student's *t*-test or one-way ANOVA and Bonferroni's multiple comparisons test when multiple groups were evaluated. *P* values < 0.05 were considered significant differences.

Supporting Information

Supporting Information is available from the Wiley Online Library or from the author.

Acknowledgements

X.F., Z.C., and W.Z. contributed equally to this work. This work was supported by the National Natural Science Foundation of China (Nos. 81671831, 82073232, 81700769, and 81641028), Guiding project of Scientific Research Plan of Education Department of Hubei Province (No. B2022131), Hubei health commission youth talents project (No. WJ2021F023), the Hubei Science & Technology Department Foundation (Nos. 2020CFB558 and 2018ACA162), the Key Projects of Hubei Education (No. D20202103), the Department of Biomedical Research Foundation, Hubei University of Medicine (No. HBMUPI201803), the Advantages Discipline Group (medicine) Project in Higher Education of Hubei Province (Nos. 2022XKQT3 and 2022XKQY1), and the Scientific Research Project of Shiyang Science and Technology Bureau (Nos. 21Y06 and 21Y38).

Conflict of Interest

The authors declare no conflict of interest.

Data Availability Statement

The data that support the findings of this study are available from the corresponding author upon reasonable request.

Keywords

aloe-emodin, blood–brain barrier, glioblastoma, pyroptosis, tumor target

Received: December 5, 2022

Revised: April 1, 2023

Published online: April 17, 2023

- [1] M. L. Goodenberger, R. B. Jenkins, *Cancer Genet.* **2012**, *205*, 613.
- [2] M. Carlberg, L. Hardell, *Biomed Res. Int.* **2017**, *2017*, 9218486.
- [3] L. P. Ganipineni, F. Danhier, V. Préat, *J. Controlled Release* **2018**, *281*, 42.
- [4] A. F. Hottinger, R. Stupp, K. Homicsko, *Chin. J. Cancer* **2014**, *33*, 32.
- [5] D. H. Upton, C. Ung, S. M. George, M. Tsoli, M. Kavallaris, D. S. Ziegler, *Theranostics* **2022**, *12*, 4734.
- [6] Z. Chen, D. Hambardzumyan, *Front. Immunol.* **2018**, *9*, 1004.
- [7] P. Broz, V. M. Dixit, *Nat. Rev. Immunol.* **2016**, *16*, 407.

- [8] Z. Zhang, Y. Zhou, S. Zhao, L. Ding, B. Chen, Y. Chen, *Adv. Sci.* **2022**, 9, 2203583.
- [9] Z. Li, F. Mo, Y. Wang, W. Li, Y. Chen, J. Liu, T. J. Chen-Mayfield, Q. Hu, *Nat. Commun.* **2022**, 13, 6321.
- [10] P. Yu, X. Zhang, N. Liu, L. Tang, C. Peng, X. Chen, *Signal Transduct. Target Ther.* **2021**, 6, 128.
- [11] Y. Tan, Q. Chen, X. Li, Z. Zeng, W. Xiong, G. Li, X. Li, J. Yang, B. Xiang, M. Yi, *J. Exp. Clin. Cancer Res.* **2021**, 40, 153.
- [12] Y. Fang, S. Tian, Y. Pan, W. Li, Q. Wang, Y. Tang, T. Yu, X. Wu, Y. Shi, P. Ma, Y. Shu, *Biomed. Pharmacother.* **2020**, 121, 109595.
- [13] C. Giuliani, B. Altieri, C. Bombelli, L. Galantini, G. Mancini, A. Stringaro, *Langmuir* **2015**, 31, 76.
- [14] H. Z. Lee, C. J. Lin, W. H. Yang, W. C. Leung, S. P. Chang, *Cancer Lett.* **2006**, 239, 55.
- [15] X. Li, J. Tsibouklis, T. Weng, B. Zhang, G. Yin, G. Feng, Y. Cui, I. N. Savina, L. I. Mikhailovska, S. R. Sandeman, C. A. Howel, S. V. Mikhailovsky, *J. Drug Target* **2017**, 25, 17.
- [16] J. Yan, C. Liu, Q. Wu, J. Zhou, X. Xu, L. Zhang, D. Wang, F. Yang, H. Zhang, *Anal. Chem.* **2020**, 92, 11453.
- [17] C. Wang, R. Zhang, X. Wei, M. Lv, Z. Jiang, *Adv. Immunol.* **2020**, 145, 187.
- [18] N. Katila, R. Duwa, S. Bhurtel, S. Khanal, S. Maharjan, J. H. Jeong, S. Lee, D. Y. Choi, S. Yook, *J. Controlled Release* **2022**, 346, 1.
- [19] D. R. Owens, N. A. Peppas, *Int. J. Pharm.* **2006**, 307, 93.
- [20] S. M. Jusu, J. D. Obayemi, A. A. Salifu, C. C. Nwazojie, V. Uzonwanne, O. S. Oduanya, W. O. Soboyejo, *Sci. Rep.* **2020**, 10, 14188.
- [21] P. Rafiei, A. Haddadi, *Int. J. Nanomed.* **2017**, 12, 935.
- [22] K. B. Johnsen, A. Burkhart, L. B. Thomsen, T. L. Andresen, T. Moos, *Prog. Neurobiol.* **2019**, 181, 101665.
- [23] E. Ryschich, G. Huszty, H. P. Knaebel, M. Hartel, M. W. Büchler, J. Schmidt, *Eur. J. Cancer* **2004**, 40, 1418.
- [24] N. özenver, M. Saeed, L. Ö. Demirezer, T. Efferth, *OncoTargets Ther.* **2018**, 9, 17770.
- [25] Y. Xiao, T. Zhang, X. Ma, Q. C. Yang, L. L. Yang, S. C. Yang, M. Liang, Z. Xu, Z. J. Sun, *Adv. Sci.* **2021**, 8, 2101840.
- [26] J. Ding, K. Wang, W. Liu, Y. She, Q. Sun, J. Shi, H. Sun, D. C. Wang, F. Shao, *Nature* **2016**, 535, 111.
- [27] Y. Wang, W. Gao, X. Shi, J. Ding, W. Liu, H. He, K. Wang, F. Shao, *Nature* **2017**, 547, 99.
- [28] X. Dong, Y. Zeng, Y. Liu, L. You, X. Yin, J. Fu, J. Ni, *Phytother. Res.* **2020**, 34, 270.
- [29] R. Chen, J. Zhang, Y. Hu, S. Wang, M. Chen, Y. Wang, *Am. J. Chin. Med.* **2014**, 42, 275.
- [30] R. G. Thorne, C. Nicholson, *Proc. Natl. Acad. Sci. USA* **2006**, 103, 5567.
- [31] S. K. Hobbs, W. L. Monsky, F. Yuan, W. G. Roberts, L. Griffith, V. P. Torchilin, R. K. Jain, *Proc. Natl. Acad. Sci. USA* **1998**, 95, 4607.
- [32] H. Zheng, Y. Zhang, L. Liu, W. Wan, P. Guo, A. M. Nyström, X. Zou, *J. Am. Chem. Soc.* **2016**, 138, 962.
- [33] L. Su, Q. Wu, L. Tan, Z. Huang, C. Fu, X. Ren, N. Xia, Z. Chen, X. Ma, X. Lan, Q. Zhang, X. Meng, *ACS Appl. Mater. Interfaces* **2019**, 11, 10520.
- [34] D. Sugiura, T. Maruhashi, I. M. Okazaki, K. Shimizu, T. K. Maeda, T. Takemoto, T. Okazaki, *Science* **2019**, 364, 558.
- [35] E. Ahn, K. Araki, M. Hashimoto, W. Li, J. L. Riley, J. Cheung, A. H. Sharpe, G. J. Freeman, B. A. Irving, R. Ahmed, *Proc. Natl. Acad. Sci. USA* **2018**, 115, 4749.
- [36] Z. Zheng, J. Zhang, J. Jiang, Y. He, W. Zhang, X. Mo, X. Kang, Q. Xu, B. Wang, Y. Huang, *J. Immunother. Cancer* **2020**, 8, 1.
- [37] F. Nesslany, S. Simar-Meintières, H. Ficheux, D. Marzin, *Mutat. Res.-Fundam. Mol. Mech. Mutagen.* **2009**, 678, 13.
- [38] K. Bouzinab, H. S. Summers, M. Stevens, C. J. Moody, N. R. Thomas, P. Gershkovich, N. Weston, M. B. Ashford, T. D. Bradshaw, L. Turyanska, *ACS Appl. Mater. Interfaces* **2020**, 12, 12609.
- [39] N. J. Abbott, A. A. Patabendige, D. E. Dolman, S. R. Yusuf, D. J. Begley, *Neurobiol. Dis.* **2010**, 37, 13.
- [40] H. K. Kimelberg, M. Nedergaard, *Neurotherapeutics* **2010**, 7, 338.
- [41] R. K. Oberoi, K. E. Parrish, T. T. Sio, R. K. Mittapalli, W. F. Elmquist, J. N. Sarkaria, *Neuro Oncol.* **2016**, 18, 27.
- [42] N. S. Ningaraj, M. Rao, K. Hashizume, K. Asotra, K. L. Black, *J. Pharmacol. Exp. Ther.* **2002**, 301, 838.
- [43] C. Zhan, W. Lu, *Curr. Pharm. Biotechnol.* **2012**, 13, 2380.
- [44] C. A. René, R. J. Parks, *Pharmaceutics* **2021**, 13, 492.
- [45] H. J. Kim, J. H. Park, H. C. Kim, C. W. Kim, I. Kang, H. K. Lee, *Nat. Commun.* **2022**, 13, 6211.
- [46] J. X. Fan, R. H. Deng, H. Wang, X. H. Liu, X. N. Wang, R. Qin, X. Jin, T. R. Lei, D. Zheng, P.-H. Zhou, Y. Sun, X.-Z. Zhang, *Nano Lett.* **2019**, 19, 8049.
- [47] X. Dong, J. Fu, X. Yin, C. Qu, C. Yang, H. He, J. Ni, *Cell. Physiol. Biochem.* **2017**, 42, 685.
- [48] S. Zhu, J. Jin, Y. Wang, Z. Ouyang, C. Xi, J. Li, Y. Qiu, J. Wan, M. Huang, Z. Huang, *Food Chem. Toxicol.* **2012**, 50, 1149.
- [49] Y. Pan, Y. Liu, G. Zeng, L. Zhao, Z. Lai, *Chem. Commun.* **2011**, 47, 2071.
- [50] A. Halder, P. Mukherjee, S. Ghosh, S. Mandal, U. Chatterji, A. Mukherjee, *Mater. Today: Proc.* **2018**, 5, 9698.
- [51] D. Szklarczyk, A. L. Gable, K. C. Nastou, D. Lyon, R. Kirsch, S. Pyysalo, N. T. Doncheva, M. Legeay, T. Fang, P. Bork, L. J. Jensen, C. von Mering, *Nucleic Acids Res.* **2020**, 49, D605.

ISBN 978-952-12-4381-3